An exploration of shape memory polymers and (nano) composites for packaging applications.

BARWOOD, Michael.

Available from the Sheffield Hallam University Research Archive (SHURA) at:

http://shura.shu.ac.uk/19326/

A Sheffield Hallam University thesis

This thesis is protected by copyright which belongs to the author.

The content must not be changed in any way or sold commercially in any format or medium without the formal permission of the author.

When referring to this work, full bibliographic details including the author, title, awarding institution and date of the thesis must be given.

Please visit http://shura.shu.ac.uk/19326/ and http://shura.shu.ac.uk/information.html for further details about copyright and re-use permissions.

Learning and Information Services
Adsetts Centre, City Campus
Sheffield S1 1WD

102 040 939 8

Sheffield Hallam University
Learning and Information Services
Adsetts Centre, City Campus
Sheffield S1 1WD

REFERENCE

ProQuest Number: 10694207

All rights reserved

INFORMATION TO ALL USERS
The quality of this reproduction is dependent upon the quality of the copy submitted.

In the unlikely event that the author did not send a complete manuscript
and there are missing pages, these will be noted. Also, if material had to be removed,
a note will indicate the deletion.

ProQuest 10694207

Published by ProQuest LLC (2017). Copyright of the Dissertation is held by the Author.

All rights reserved.
This work is protected against unauthorized copying under Title 17, United States Code
Microform Edition © ProQuest LLC.

ProQuest LLC.
789 East Eisenhower Parkway
P.O. Box 1346
Ann Arbor, MI 48106 – 1346

An Exploration of Shape Memory Polymers and (Nano)composites for Packaging Applications

Michael Barwood

A thesis submitted in partial fulfilment of the requirements of
Sheffield Hallam University
for the degree of Doctor of Philosophy

June 2012

Declaration

The Work described in this thesis was carried out by the author in the Materials and Engineering Research Institute at Sheffield Hallam University, between October 2008 and June 2012. The author declares that this work has not been submitted for any other degree. The work is original except where acknowledged by reference.

Author:

(Michael Barwood)

Supervisors:

(Prof Chistopher Breen)

(Dr Francis Clegg)

Acknowledgements

I would like to thank both my supervisors, Prof Chris Breen and Dr Francis Clegg, for their advice, enthusiasm and guidance throughout this project. I would also like to thank my industrial sponsor Chesapeake Plc., especially Carol Hammond and Bill Marwick for aiding me with the project and helping me to see the potential of SMP.

I would also like to thank HiFi films Ltd, Lambson Ltd., Dr David Guemi, CTP, and SUN Chemicals who were all generous enough to provide free samples of their products for use in this research project, without whom this project would not have achieved what it did.

Finally I am very thankful to my family, friends and colleagues who all supported me throughout this research project, providing a lot of help, advice, encouragement and especially laughter over the last three and a half years.

Abstract

Shape memory polymers, SMP, are gaining considerable interest in research and industry due to their novel properties and vast potential. SMP belong to an emerging class of materials known as 'smart polymers', and have the intriguing ability to be moulded into a temporary shape, store that temporary shape and, when activated by an external stimulus, recover its original shape. SMP have currently been used for a wide range of applications including SMP stents, catheters, smart clothing, composite tooling and biodegradable sutures.

This project aims to develop an understanding of how SMP can be of use in the packaging industry, exploring several types of thermoset and thermoplastic based SMP for packaging applications. The fundamental aspects of SMP, the methods to tailor the mechanical and thermal properties and the quantification of the shape memory effect are also considered.

Initially photopolymerised thermoset shape-memory networks, class I SMP, with tailorable thermomechanics were investigated. Tertiary butylacrylate (tBA) and polyethylene glycol dimethacrylate (PEGDMA) were copolymerized to create networks with adjustable glass transition temperatures (T_g) and rubbery modulus values ranging from -18 to 39 °C and 0.7 to 25.0 MPa, respectively. The networks were characterised for homogeneity, thermal, mechanical and shape memory properties. The adjustable T_g had a great impact on the shape memory effect however the varying rubbery modulus had no significant effect.

Previously incorporation of clay into polymers has shown to dramatically increase the mechanical, barrier and fire resistant properties of a wide range of polymers. At addition levels of 1 to 5 wt% no significant changes occurred to the mechanical abilities of the tBA-co-PEGDMA networks, although there was a minor improvement of the rubbery modulus at 1 wt% clay loading. There was a significant increase in initial shape memory recovery, at 1 wt% clay loading, but no improvement in total shape memory recovery. Alternatives to tBA-co-PEGDMA were also studied; these include i-bornylacrylate, IBoA, i-bornylmethacrylate, IBoMA, and tertiary butylmethacrylate, tBMA, in co-PEGDMA networks, which were also explored for their SMP packaging potential. The IBoA, IBoMA and tBMA-co-PEGDMA networks also had adjustable T_g and rubbery modulus values ranging from -20 to 53 °C and 2.0 to 22.0 MPa, -11 to 93 °C and 4.0 to 30.0 MPa and -11 to 74 °C and 1.0 to 30.0 MPa, respectively.

Thermoplastic polyurethane, PU, PU-co-PVC blends, class IV SMP, and their nanocomposites were also evaluated as SMP packaging materials. As clay content was increased, 1 to 5 wt%, in the SMP PU, there was a significant shift of the soft segment (SS) Tg from -29 to -10 °C, respectively, but only a minor improvement in the rubbery modulus. There was no significant effect on the shape memory ability. As PVC was blended with PU the SS T_g shifted from -29 to 1 °C, and the PU initial modulus dropped dramatically from 2414 to 493 MPa. On any addition of PVC the shape memory recovery time was extended. As clay was increased, 1 to 5 wt%, in the PU-co-PVC blend the overall modulus was reduced with no other significant effects apart from a minor increase in intensity and shift to lower temperatures of the PU/PVC/Lap 1 tan δ peak. As clay increased the time for the initial shape recovery of the polymer blends decreased, from 12.5 to 8.0 seconds, however there was no effect on the overall return time, ca. 15 seconds.

Table of Contents

Declaration i

Acknowledgements ii

Abstract iii

List of Abbreviation and Formula x

List of Chemical and Material Structures xiii

Chapter 1: Literature Review 1

1. Literature review 2
  - 1.1. Introduction 2
    - 1.1.1. What is a Shape Memory Material 2
    - 1.1.2. Discovery of SMP 3
    - 1.1.3. Shape Memory Polymer Definition and Mechanism 5
    - 1.1.4. Other Shape Memory Materials 7
  - 1.2. Classification of Shape Memory Polymers Class I to IV 9
    - 1.2.1. Covalently Cross-Linked Glassy Thermoset Networks (Class I) 10
    - 1.2.2. Covalently Cross-Linked Semi-Crystalline Networks (Class II) 11
    - 1.2.3. Physically Cross-Linked Glassy Copolymers (Class III) 12
    - 1.2.4. Physically Cross-Linked Semi-Crystalline Block Copolymers (Class IV) 14
  - 1.3. Advantages of Shape Memory Polymers Compared to Shape Memory Alloys 15
  - 1.4. Shape Memory Testing Methods 16
    - 1.4.1. Cyclic Thermo-Mechanical Characterisation 16
    - 1.4.2. Bending Test for the Determination of SME 18
    - 1.4.3. Other Shape Memory Tests - Hot-Stage Microscope 19
  - 1.5. SMP Composites and Blends 19
    - 1.5.1. Filler Materials 20
    - 1.5.2. SMP Blends 26
  - 1.6. Triple or Multiple Shape Memory Polymers 26
  - 1.7. Biodegradable SMP 28
  - 1.8. Applications of SMP 30
  - 1.9. References 32

Chapter 2: Theory of Techniques Used 39

2. Theory of Techniques Used 40
  - 2.1. Characterisation Techniques 40
    - 2.1.1. X-ray Diffraction (XRD) 40

2.1.2. Attenuated Total Reflectance Fourier Transfer Infrared Spectroscopy (ATR-FTIR) .. 43
2.1.3. Differential Scanning Calorimetry (DSC) 47
2.1.4. Thermogravimetric Analysis (TGA) 50
2.1.5. Dynamic Mechanical Analysis (DMA) 53
2.1.6. Shape Memory Effect (SME) 57
2.2. References 60
Chapter 3: Evaluation of tert-Butyl Acrylate as Potential Packaging SMP 62
3. Introduction 63
3.1. Experimental 66
3.1.1. Materials 66
3.1.2. C10A Clay Washing 66
3.1.3. Sample Preparation 66
3.1.3.1. tBA-co-PEGDMA 66
3.1.3.2. tBA-co-PEGDMA C10A 67
3.1.3.3. Coated Substrate Sample Preparation 67
3.1.4. Photopolymerisation Methods 68
3.1.5. Techniques 69
3.1.5.1. Swelling Test 69
3.1.5.2. X-Ray Diffraction 69
3.1.5.3. ATR-FTIR Spectroscopy 69
3.1.5.4. Thermogravimetric Analysis 70
3.1.5.5. Dynamic Mechanical Analysis 70
3.1.5.6. Unconstrained Shape Memory Effect Evaluation 70
3.2. tBA-co-PEGDMA Results and Discussion 72
3.2.1. Polymer Network Structure 72
3.2.1.1. Swelling Test 72
3.2.1.2. ATR-FTIR Spectroscopy 73
3.2.2. Thermal Results 76
3.2.2.1. Thermogravimetric Analysis 76
3.2.3. Mechanical Properties 78
3.2.3.1. Dynamic Mechanical Analysis 78
3.2.4. Shape Memory Effect Testing 81
3.2.4.1. Unconstrained Shape Memory Effect Evaluation 81
3.3. tBA-co-PEGDMA Summary 85
3.4. t/P/C10A Results and Discussion 86

3.4.1. C10A Dispersal 86

3.4.1.1. X-Ray Diffraction 86

3.4.1.2. ATR-FTIR Spectroscopy 87

3.4.2. Mechanical Properties 91

3.4.2.1. Dynamic Mechanical Analysis 91

3.4.3. Shape Memory Effect Testing 94

3.4.3.1. Unconstrained Shape Memory Effect Evaluation 94

3.5. t/P/C10A Summary 97

3.6. Coated Substrate Results and Discussion 98

3.6.1. C10A Dispersal 98

3.6.1.1. X-Ray Diffraction 98

3.6.2. Shape Memory Effect Testing 99

3.6.2.1. Unconstrained Shape Memory Effect Evaluation 99

3.7. Conclusion 103

3.8. References 104

Chapter 4: Evaluation of Isobornyl Acrylate, Isobonyl Methacrylate and tert-Butyl Methacrylate as Potential Packaging SMP 107

4. Introduction 108

4.1. Experimental 112

4.1.1. Materials 112

4.1.2. IBoA, IBoMA and tBMA Network Sample Preparation 112

4.1.3. Coated Substrate Sample Preparation 113

4.1.4. IBoA, IBoMA and tBMA Network Photopolymerisation Method 114

4.1.5. Coated Substrate Photopolymerisation Method 114

4.1.6. Techniques 115

4.1.6.1. ATR-FTIR Spectroscopy 115

4.1.6.2. Coated Substrate Cure Assessment 115

4.1.6.3. Dynamic Mechanical Analysis 115

4.1.6.4. Unconstrained Shape Memory Effect Evaluation 115

4.2. IBoA, IBoMA and tBMA Network; Results and Discussion 116

4.2.1. Network Structure 116

4.2.1.1. ATR-FTIR spectroscopy 116

4.2.2. Mechanical Properties 121

4.2.2.1. Dynamic Mechanical Analysis 121

4.2.3. Shape memory properties 129

4.2.3.1. Unconstrained Shape Memory Effect Evaluation 129

4.3. IBoA, IBoMA and tBMA Network Summary 139

4.4. C00 to C17 I90/P10 network; Results and discussion 143

4.4.1. Network Polymerisation 143

4.4.1.1. Photopolymerisation in Air 143

4.4.2. Mechanical Properties 145

4.4.2.1. Dynamic Mechanical Analysis 145

4.4.3. Shape Memory Properties 148

4.4.3.1. Unconstrained Shape Memory Effect Evaluation 148

4.5. C00 to C17 I90/P10 Network Summary 148

4.6. D00 to D06 I90/P10 Network; Results and Discussion 150

4.6.1. Mechanical Properties 150

4.6.1.1. Dynamic Mechanical Analysis 150

4.7. D00 to D06 I90/P10 Networks Summary 154

4.8. D07 I90/P10 Network; Results and discussion 155

4.8.1. Mechanical Properties 155

4.8.1.1. Dynamic Mechanical Analysis 155

4.8.2. Shape Memory Properties 157

4.8.2.1. Unconstrained Shape Memory Effect Evaluation 157

4.9. D07 I90/P10 Network Summary 158

4.10. D07 IM80/P20 to IM70/P30 Networks Results and Discussion 159

4.10.1. Networks Mechanical Properties 159

4.10.1.1. Dynamic Mechanical Analysis 159

4.10.2. Shape Memory Properties 161

4.10.2.1. Unconstrained Shape Memory Effect Evaluation 161

4.11. D07 IM80/P20 to IM70/P30 Networks Summary 164

4.12. Coated Substrate Results and Discussion 165

4.12.1. Shape Memory Properties 165

4.12.1.1. Unconstrained Shape Memory Effect Evaluation 165

4.13. Conclusion 168

4.14. References 170

Chapter 5: Evaluation of Polyurethane Composites as SMP 173

5. Introduction 174

5.1. Experimental 180

5.1.1. Materials 180

5.1.2. Sample Preparation 180
5.1.2.1. Clay Delamination Procedure 180
5.1.2.2. Solution Casting 181
5.1.3. Characterisation Methods 182
5.1.3.1. X-Ray Diffraction 182
5.1.3.2. ATR-FTIR Spectroscopy 182
5.1.3.3. Thermogravimetric Analysis 182
5.1.3.4. Differential Scanning Calorimetry 183
5.1.3.5. Dynamic Mechanical Analysis 183
5.1.3.6. Unconstrained Shape Memory Effect Evaluation 183
5.2. Results and Discussion 185
5.2.1. Homogeneity 185
5.2.1.1. X-Ray Diffraction 185
5.2.1.2. ATR-FTIR Spectroscopy 186
5.2.2. Thermoanalytical Results 190
5.2.2.1. Thermogravimetric Analysis 190
5.2.2.2. Differential Scanning Calorimetry 193
5.2.3. Mechanical Results 197
5.2.3.1. Dynamic Mechanical Analysis 197
5.2.4. Shape Memory Properties 200
5.2.4.1. Unconstrained Shape Memory Effect Evaluation 200
5.3. Conclusions 204
5.4. References 205
Chapter 6: Exploration of Polyurethane/PVC Blends and Composites as SMP 209
6. Introduction 210
6.1. Experimental 213
6.1.1. Materials 213
6.1.2. Elasthane/PVC Blends Preparation 213
6.1.3. PU/PVC 0 to 5 wt% Laponite Composites Preparation 214
6.1.4. Techniques 215
6.2. PU/PVC Blend Results 216
6.2.1. Homogeneity 216
6.2.1.1. ATR-FTIR Spectroscopy 216
6.2.2. Thermoanalytical Results 218
6.2.2.1. Thermogravimetric Analysis 218

6.2.2.2. Differential Scanning Calorimetry 221
6.2.3. Mechanical Properties 225
6.2.3.1. Dynamic Mechanical Analysis: 225
6.2.4. Shape Memory Effect Testing 228
6.2.4.1. Unconstrained Shape Memory Effect Evaluation 228
6.3. PU/PVC Blend Summary 233
6.4. PU/PVC/Lap Composite Results 234
6.4.1. Homogeneity 234
6.4.1.1. X-Ray Diffraction 234
6.4.1.2. ATR-FTIR Spectroscopy 235
6.4.2. Thermoanalytical Results 239
6.4.2.1. Thermal Gravimetric Analysis 239
6.4.2.2. Differential Scanning Calorimetry 242
6.4.3. Mechanical Properties 245
6.4.3.1. Dynamic Mechanical Analysis 245
6.4.4. Shape Memory Effect Testing 249
6.4.4.1. Unconstrained Shape Memory Effect Evaluation 249
6.5. Conclusions 252
6.6. References 253
Chapter 7: Conclusions and Future Work 257
7. Conclusions 258
7.1. Future Work 263
Appendix 265
A1. Award and presentation in seminar and conferences: 266
A2. Conference and seminars attended: 267

List of Abbreviation and Formula

Several abbreviations and formulations are used in this thesis, and are listed below.

Abbreviation / Formulation	Full Term
ΔC_p	Heat of fusion
Al_2O_3	Alumina
AM	acrylamide
ATR-FTIR	Attenuated total reflectance Fourier transfer infrared spectroscopy
BDO	1,4-butanediol
BDOB	Benzoylbenzyl-N,N-dimethyl-N octadecylammonium bromide
BMA	Butyl methacrylate
C10A	Cloisite 10A
C30B	Cloisite 30B
CB	Carbon black
CNF	Carbon nanofiber
CNT	Carbon nano-tubes
DEA	Methyl diethanolamine
DMA	Dynamic mechanical analysis
DMAc	N,N-dimethylacetamide
DMPA	2,2-dimethoxy-2-phenylacetophenone
DSC	Differential scanning calorimetry
DTG	Derivative thermogram
E	Elastic modulus
E′	Storage modulus
E″	Loss modulus
EDB	Ethyl (4-dimethylmino) benzoate
EHA	2-Ethylhexyl 4-(dimethylamino)benzoate
EOC	Ethylene-1-octene copolymers
F_d	Dynamic or oscillatory force
F_s	Static or clamping force
FWHM	Full width at half maximum
H_2O	Water
H_C	Heat capacity
HDPE	High-density polyethylene
HS	Hard segment
Hz	Hertz
IBoA	Isobornyl acrylate
IBoMA	Isobornyl methacrylate
ITX	Isopropylthioxanthone
LVDT	Linear variable differential transformer
MA	Methyl acrylate
M-C15A	Dimethyl dehydrogenated tallow quaternary ammonium modified Cloisite 15A
M-C20A	Dimethyl dehydrogenated tallow quaternary ammonium modified Cloisite 20A
M-C30B	Bis-2-hydroxyethyl-methyl tallow quaternary ammonium chloride

Abbreviation / Formulation	Full Term
	modified C30B
MCT	Mercury cadmium telluride
MDI	4,4 -methylene bisphenyl diisocyanate
MERI	Materials and engineering research institute
MMA	Methyl methacrylate
MMT	Montmorillonite
MT	Martensitic transformation
PCL	Polycaprolactone
PCO	Polycyclooctene
PEG	Poly(ethylene glycol)
PEGDMA	Poly(ethylene glycol) dimethacrylate
PET	Polyethylene terephthalate
PFSA	Perfluorosulphonic acid ionomer
PGD	Poly-glycerol-dodecanoate
PLA	Poly-L-lactide
PLGA	Poly glycolic acid
POSS	Polyhedral oligomeric silsesquioxane
PPDO	Poly(p-dioxanone)
PRT	Platinum resistance thermometer
PTFE	Polytetrafluoroethylene
PTMO	Polytetramethylene oxide
PU	Polyurethane
PVA	Polyvinyl alcohol
PVAc	poly(vinyl acetate)
PVC	poly(vinyl chloride)
PVDF	poly(vinylidene fluoride)
q	Equilibrium swelling ratio
R_f	Shape fixity rate
R_r	Strain recovery rate
SBS	Styrene-butadiene-styrene
Si_3N_4	Silicone nitride
SiC	Silicon carbide
SMA	Shape memory alloy
SMC	Shape memory ceramics
SME	Shape memory effect
SMG	Shape memory gels
SMP	Shape memory polymer
SS	Soft segment
StA	Stearyl acrylate
STBS	Styrene-trans-butadiene-styrene
StMA	Stearyl methacrylate
T	Temperature
t	Time
tBA	tert-butyl acrylate
tBMA	tert-butyl methacrylate

Abbreviation / Formulation	Full Term
T_c	Crystallisation/re-crystallisation temperature
TEA	Triethanolamine
TEM	Transmission electron microscopy
T_g	Glass transition temperature
TGA	Thermogravimetric analysis
THCL	Dehydrochlorination
T_{high}	High temperature
T_{low}	Low temperature
T_m	Melting transition temperature
TPO-L	Ethyl (2,4,6-trimethylbenzoyl)-phenyl phosphinate
T_{trans}	Transition temperature
UV	Ultraviolet radiation
W_i	Initial weight
W_s	Equilibrium, swollen, weight
wt%	Weight %
XRD	X-ray diffraction
ZrO_2	Zirconia
θ_{final}	Final angle
θ_{fixed}	Fixed angle
$\theta_i(t)$	Angle at specific interval
θ_{max}	Maximum angle

List of Chemical and Material Structures

Several chemicals and materials are used in this thesis, the most frequently used are listed below.

Chemical / Material Abbreviation	Chemical / Material Structure
DEA	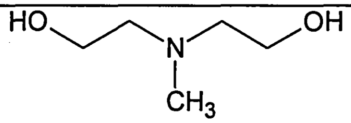
DMPA	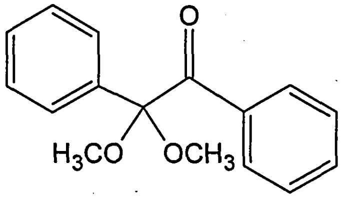
EDB	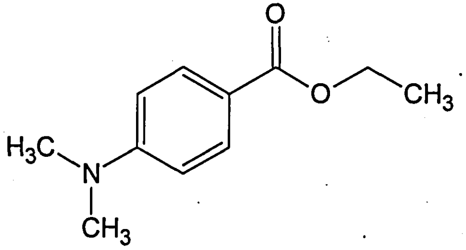
EHA	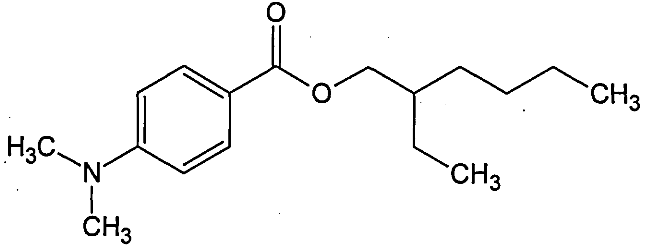
IBoA	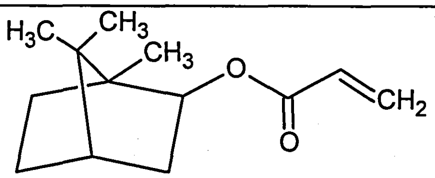
IBoMA	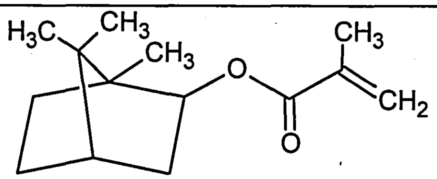
ITX	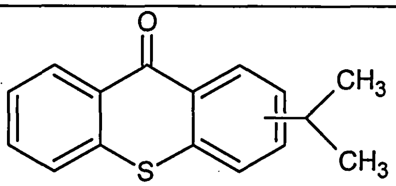
PEGDMA	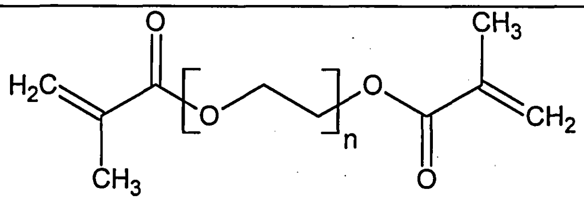

Chemical / Material Abbreviation	Chemical / Material Structure
PET	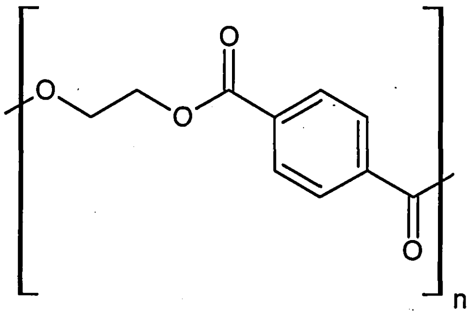
PTFE	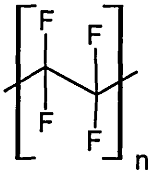
PU	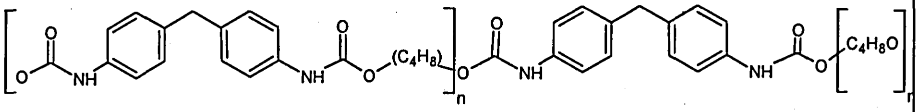
PVC	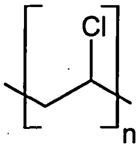
tBA	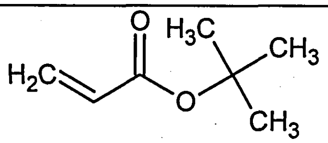
tBMA	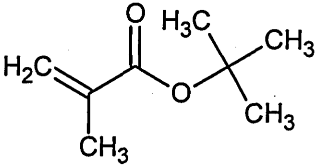
TEA	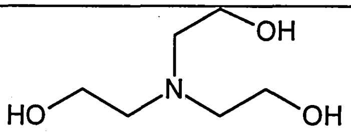
TPO-L	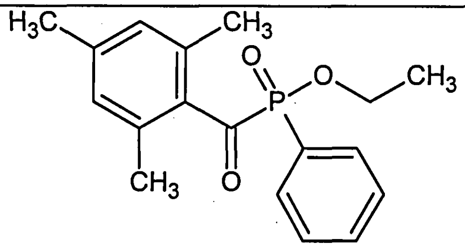

1. Literature review

1.1. Introduction

1.1.1. What is a Shape Memory Material

Shape memory polymers, SMP, are a class of smart material that respond dynamically to environmental stimuli. Due to this intriguing property research on smart materials is actively growing both in academic and industrial sectors. Although the term 'smart material' is conventionally used, all materials, to some degree, are responsive and thus in the same sense 'smart', therefore a further category of smart materials were classified, very smart' materials.

Very smart materials have the ability to respond reversibly to changes in the surrounding environment and contribute an optimal or useful response by either changing their geometry or physical, mechanical, or electromagnetic properties. The underlying concept of very smart materials is that they have their own way of sensing an external stimulus, resulting in them changing their properties.

Shape memory materials belong to this class of very smart materials having the ability to memorize a macroscopic, permanent, shape, be deformed via external stress and fixed into another temporary, dormant shape under specific conditions of temperature and stress. This temporary shape can then be induced to relax back to the original, stress-free condition by thermal, electrical, or other environmental stimulus.

The most common shape memory materials are thermally-responsive, this means that a thermal change is required to deform the material and another thermal change is required for it to recover back to the original shape. The temperature change is typically known as the transition temperature, T_{trans}, either a glass transition temperature, T_g, or melting transition temperature, T_m, of the material figure 1.1.

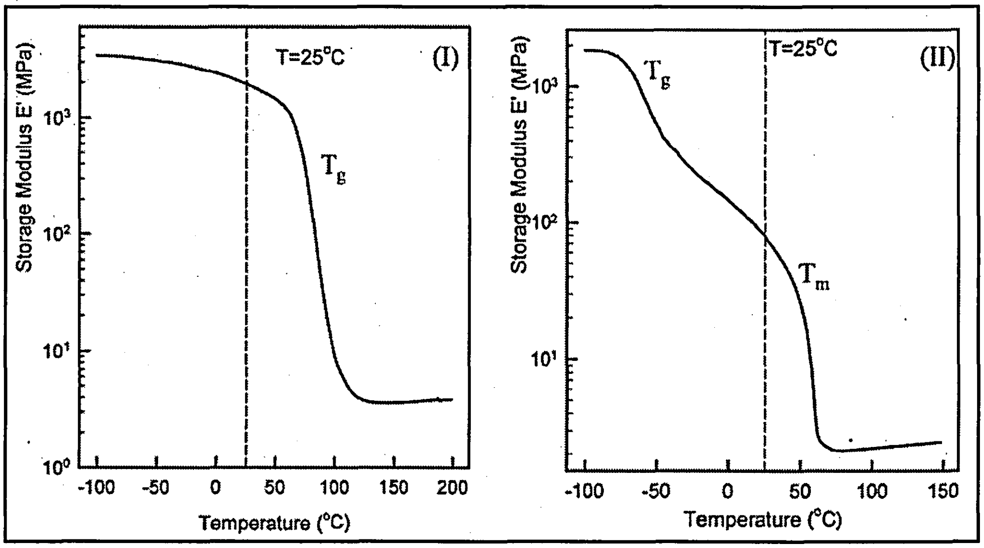

Figure 1.1: Temperature dependent storage modulus of a generic SMP where (I) T_g is T_{trans} and (II) T_m is T_{trans} (Liu et al., 2007).

1.1.2. Discovery of SMP

Shape memory materials were initially discovered, although not fully recognised, when gold and cadmium were combined together to form an alloy, AuCd, in 1932 by a Swedish researcher, A. Ölander (Olander, 1932), who found that the alloy exhibited pseudoelastic behaviour. However it was not until 1947 when Bystrom and Almin carried out a series of x-ray investigations that different phases were identified in the AuCd alloy depending on composition. Finally in 1951 Chang and Read discovered that the Au-47.5 at. % Cd alloy composition displayed shape memory effect, SME, thus making this the first real discovery of shape memory alloys, SMA (Otsuka and Wayman, 2002). After the AuCd SMA discovery many other SMAs were developed but these were not widely publicized until the discovery of Ti-Ni alloy, named Nitinol, by Buehler et al., (1963) after which its potential applications were quickly realized.

SMA can achieve SME by alternating between two separate phases, the martensite and austenite phases. This movement from one phase to another is known as martensitic transformation, MT, it is a diffusionless phase transformation in solids in which atoms move cooperatively, often via a shear-like mechanism.

During SME the SMA starts in the relaxed state, the martensite phase, at lower temperatures, where it is relatively soft and easily deformable. The molecular structure of this phase is referred to as 'twinned', referring to the ability to rearrange the atomic planes without causing permanent deformation. When this phase is deformed, maximum 6 to 8 %, by an external force, typically 50 to 200 MPa is required, MT occurs. The external force activating MT causes a shear-like mechanism to occur shifting the twinned martensite phase to the deformed martensite phase. The latter is a stable structure and is maintained as the temporary shape at low temperatures. When the SME is activated, i.e. when the temperature is increased, the deformed martensite phase becomes unstable, reverse transformation occurs and the unstable deformed martensite structure shifts to the stronger austenite phase. The phase change shows a SME, generating ca. 150 to 300 MPa recovery stress as it returns from the temporary shape back to the original shape, as the austenite and martensite phases are the same shape but have different orientations. Upon cooling the austenite phase relaxes back to the resting twinned martensite configuration, figure 1.2 (Otsuka and Wayman, 2002).

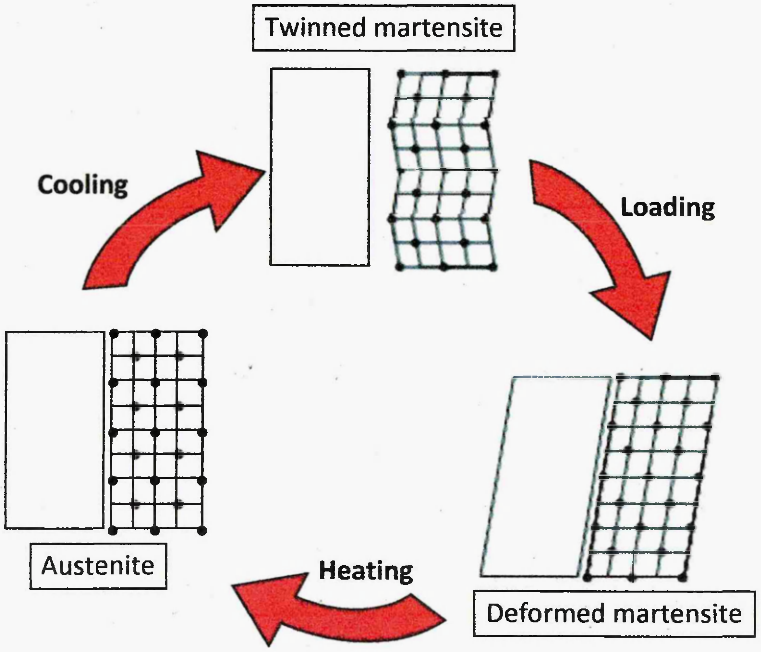

Figure 1.2: SME of a generic SMA, macroscopic and microscopic views.

As well as SMA there are several other classes of shape memory materials including SMP, shape memory ceramics, SMCs, and shape memory gels, SMG, with the two major categories being SMAs and SMP.

1.1.3. Shape Memory Polymer Definition and Mechanism

The other main group of shape memory materials are the SMP. SMP were first introduced in the 1980s, with the development of polynorbornene SMP in 1984 by the Nippon Zeon company in Japan. This SMP had very limited processability, therefore several companies strived to form new SMP, however these too suffered from poor processability. The discovery of polyurethane, PU, based SMP in the late 1980s overcame these processability problems and demonstrated superior mechanical properties, leading to modern day SMP (Huang et al., 2010).

SMP are generally defined, on a macro level, as a polymer material that has the ability to memorize a permanent shape, and be deformed into a temporary, fixed, shape by specific external conditions of temperature and stress. A SMP can remain in its temporary shape remaining dormant until activated by an external stimulus such as heat (Liff et al., 2007), electricity (Mohr et al., 2006), light (Jiang et al., 2006), or other environmental stimuli, whereupon it relaxes to its stress-free, permanent shape, figure 1.3. This movement from temporary to permanent shape is associated with the elastic strain stored during the prior deformation (Lui et al., 2007).

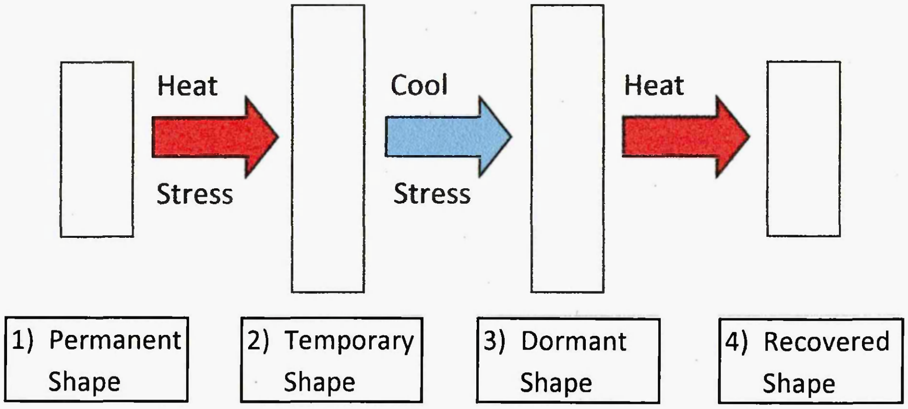

Figure 1.3: Unconstrained SME of a thermally activated SMP.

On a micro level SMP can be described as elastic polymer networks that consist of netpoints and switching segments that act as stimuli-sensitive switches. The netpoints determine the permanent shape of the polymer network and can be of chemical or physical origin while the typically amorphous switching segments allow storage of the temporary shape.

In a linear SMP, in the amorphous state, the polymer chains take up a completely random distribution within the polymer matrix. The conformation of the polymer chains would be in random, highly coiled structures, in states of high entropy, which can be shown by the Boltzmann equation, equation 1.1.

$$S = k_B \ln W$$

Equation 1.1: The Boltzmann equation, W = probability of chain conformation, S = entropy, k = Boltzmann constant.

When the SMP is heated past T_{trans} of the switching segment, the SMP can be deformed, with external stress, as the switching segment becomes flexible; displaying rubbery elasticity, equation 1.2.

$$G = v\mathrm{k_B T} = \rho RT/M_c$$

Equation 1.2: Classic prediction of rubber elasticity theory, where G, the elastic shear modulus, is proportional to both cross-link density and temperature. v = number density of network chains, ρ = mass density, R universal gas constant and M_C = molecular weight between cross-links.

This results in an entropic elastic behaviour of the polymer network, going from high entropy to low entropy as the external stress causes the switching segments to align. During the deformation, due to external stress, the netpoints behave as anchors for the switching segments, stopping them from sliding past each other. When the SMP is cooled below the T_{trans} of the switching segments, whilst maintaining external stress, the switching segments lose their flexibility and are fixed into position, by the freezing of the Brownian motion, storing the temporary shape. While in the temporary shape the stress of the deformation is stored in the form of an unfavourable entropic state. When reheated to the T_{trans} of the switching segments, the SMP polymer chains relax, regaining the favourable high entropy state. This relaxation causes the SMP to return to its original shape that was maintained by the netpoints, figure 1.4 (Behl and Lendlein, 2007).

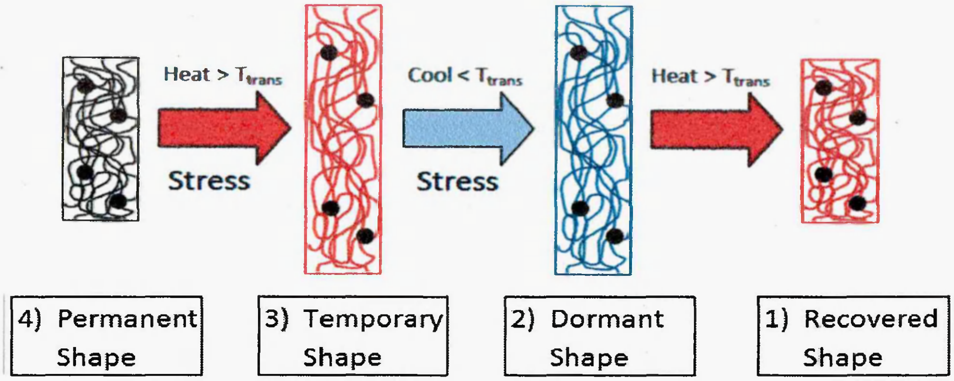

Figure 1.4: Molecular mechanism of a physically cross-linked thermally activated SMP. Black circles represent netpoints.

1.1.4. Other Shape Memory Materials

Some mica glass-ceramics show a shape memory effect, these are known as shape memory ceramics, SMCs. The SMCs show a typical shape recovery of ca. 0.5 % after high-temperature plastic deformation, cooling under load to room temperature, and then reheating causing recovery. SMCs have a heterostructure, from which the SME arises, containing a volume fraction of 0.4 to 0.6 mica as the principle crystalline phase which is dispersed in a continuous glassy phase. The SME occurs from the elastic energy that is imparted into the rigid matrix; this is possible when the temperature is elevated to ca. 573 K, allowing the mica to be deformed plastically by basal slipping and the plastic strain becoming stored in the crystalline constituent. The energy stored in the crystalline constituent is retained when the SMC is cooled as the drop in temperature prevents dislocations occurring in the mica. This causes a viscous plastic strain reversal in the dispersed crystalline phase on reheating, generating a shape memory response.

The SME is not only limited to mica glass-ceramics as β-spodumene glass-ceramics and $2ZnO\text{-}B_2O_3$ glass-ceramics as well as sintered ceramics containing very little glass phase, including mica ($KMg_3AlSi_3O_{10}F_2$), silicone nitride (Si_3N_4), silicone carbide (SiC), zirconia (ZrO_2) and alumina (Al_2O_3), also exhibit shape memory behaviour. The major difference between these and mica glass-ceramics is that the recoverable strain is smaller ca. 0.1 %.

Certain ZrO_2 ceramics have been shown to demonstrate a SME mechanism similar to that of SMAs, the transition from a tetragonal to a monoclinic structure occurs as a martensitic phase transition, as with SMAs, which is induced thermally or by the application of stress. Ceramics which undergo this type of transition are commonly referred to as martensitic ceramics. The recovery or transformation from the monoclinic, temporary shape, to the tetragonal symmetry of the permanent shape, can occur thermoelastically, which is why martensitic ceramics show a thermoresponsive SME (Lendlein and Kelch, 2002).

Contractile polymeric gels, commonly referred to as intelligent gels or SMG, have been the source of great interest over the last 20 years. Many publications have appeared from several research groups including Li and Tanaka (1992), Osada and Ross-Murphy (1993), and Shibayama and Tanaka (1993) as well as more recently from Mitsumata et al., (2001), Guan et al., (2005) and Chaterji et al., (2007). SMG are a hybrid of an elastic cross-linked network with a liquid filled interstitial space, they can easily change their dimensions resulting in a shrinking or swelling response to even small changes in the environmental conditions i.e. temperature, light, solvent concentration, electric field, pH, biochemical elements and even stress. These SMGs can be tailored to respond to any one or even several of these external stimuli depending on the desired purpose.

An examples of a thermoresponsive SMG includes cross-linked poly(vinylalcohols), while others e.g. copolymerised acrylic acid and stearyl acrylate cross-linked with methylene bisacrylamide demonstrate a temperature dependence in their mechanical properties. These SMG show their shape memory ability by behaving like tough polymers while below 25 °C, and like soft rubber while above 50 °C. The softening causes a dramatic decrease of elastic modulus by ca. three orders of magnitude, an indicator of SME (Tsai et al., 2008). In order to store a temporary shape within SMG, heating to above the T_{trans} and the application of an external force is required. The external force needs to be maintained while the SMG is then being cooled below the T_{trans} fixing the temporary shape. The permanent shape can then be restored when the external force is removed and it is heated above the T_{trans} (Lendlein and Kelch, 2002).

Due to SMGs unique chemo-mechanical system that is capable of conversion between chemical energy and mechanical work and able to undergo shape memory ability, it has been suggested that they are able to provide actuating power capacities comparable to that of human muscles. However this application has several drawbacks including the SMG's undesirable chemical and mechanical hysteresis.

1.2. Classification of Shape Memory Polymers Class I to IV

Although SMP are often referred to as a single group of materials they are in themselves a diverse group, and can be further categorized by their different fixing mechanisms and origin of their permanent shape elasticity. It is generally accepted that there are four sub-categories of SMP including I) covalently cross-linked glassy thermoset networks, II) covalently cross-linked semi-crystalline networks, III) physically cross-linked glassy copolymers and IV) physically cross-linked semi-crystalline block copolymers. Each type of SMP, class I to IV, has a different shape-fixing and shape-recovery mechanism, figure 1.5.

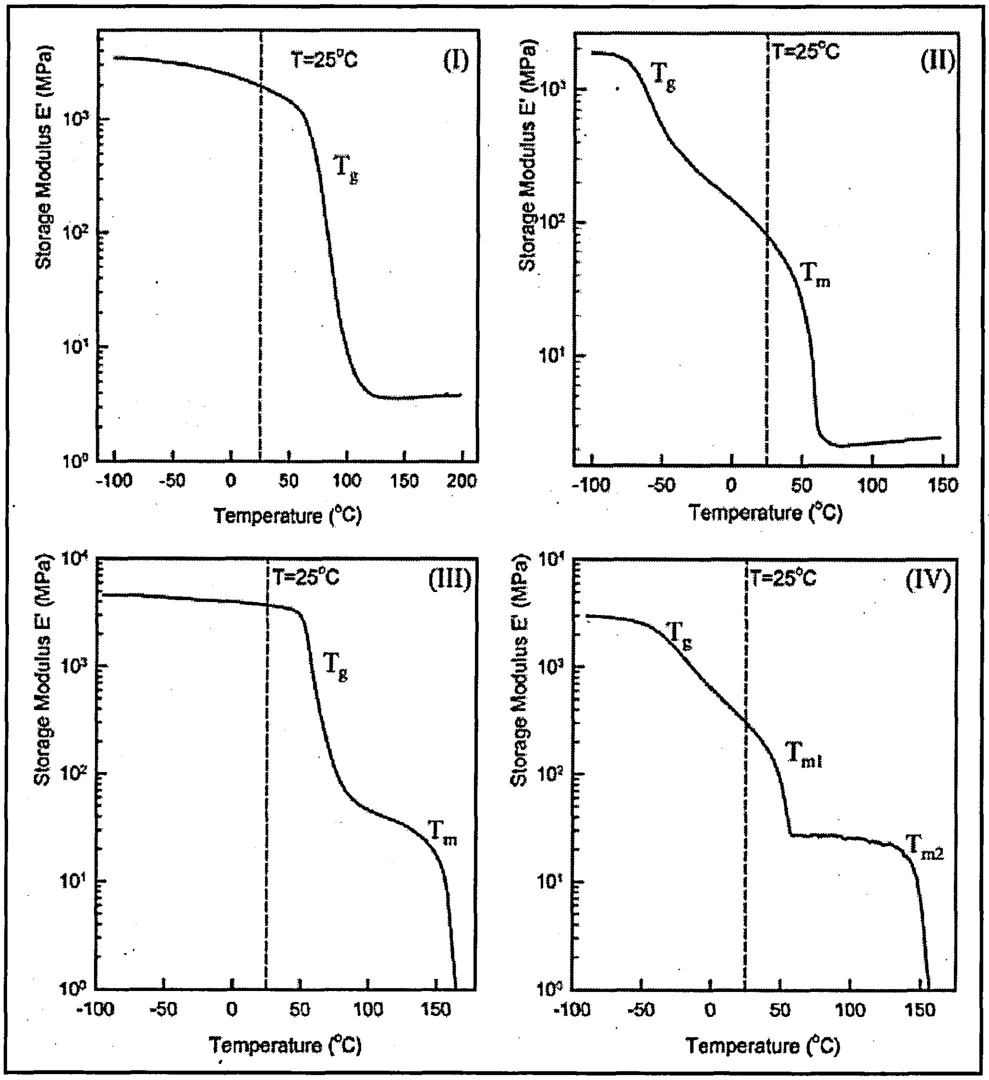

Figure 1.5: Temperature variation of the storage modulus for different types of SMP, I) covalently cross-linked glassy thermoset networks, II) covalently cross-linked semi-crystalline networks, III) physically cross-linked glassy copolymers and IV) physically cross-linked semi-crystalline block copolymers. Each class displays different shape-

fixing and shape recovery mechanisms depicted as a function of their individual dynamic mechanical behaviour (Liu et al., 2007).

1.2.1. Covalently Cross-Linked Glassy Thermoset Networks (Class I)

Class I SMP, figure 1.5 (I), are generally regarded as the simplest type of SMP, they are cross-linked glassy polymers featuring a sharp transition temperature with rubbery elasticity (a plateau in the E' value) above T_g derived from covalent cross-links. The T_g governs the shape memory behaviour, with the temporary shape commonly being formed at T_g or above and fixed by cooling below T_g. SMP class I materials have many attractive features including an excellent degree of shape fixing and recovery, primarily due to the high modulus below T_g and excellent rubbery elasticity above T_g as well as the absence of molecular slippage between chains due to cross-linking. The SMP system is highly tuneable with regard to work capacity, being dependent on the extent of covalent cross-linking. The permanent shape is set during the processing stage, either casting or moulding, by the covalent bonds of the three-dimensional network causing the re-shaping of the material post-processing to be difficult (Liu et al., 2007).

The most common examples of this class include epoxy-based SMP, thermoset polyurethanes, PU, and various random copolymers including chemically cross-linked vinylidine consisting of two vinylidine monomers and natural oils, with high degrees of unsaturation, polymerised with styrene and divinylbenzene. Other examples are summarised in table 1.1.

Typically epoxy-based SMP show fixing and recovery, when quantified, of ca. 95 to 100 % and are available commercially i.e. Veriflex. Alti et al., (2009) has previously reported on the shape memory properties of Veriflex, which demonstrated a shape fixing ability of 97 to 98 % when deformed at 75% strain and an unconstrained shape recovery of 100 % when heated above T_g (Rousseau, 2008).

Thermoset PUs are typically formed by using excess diisocyanate or by using a cross-linker like glycerin or trimethylol propane (Ratna and Karger-Kocsis, 2008). Buckley et al. (2007) have previously reported a thermosetting PU using 1,1,1-trimethylol propane as a cross-linker where an improvement in creep, an increase in recovery temperature and recovery window, were achieved. PU with cross-links in the hard or soft segments have been reported by Lee et al., (2009) who found that good shape fixity and recovery could be achieved depending on the positions and number of the cross-links. Other thermoset PU with hybrid cross-linking have also been shown to exhibit shape recovery of almost 100% (Xu et al., 2006).

Liu and Mather (2002) have reported that chemically cross-linked methyl methacrylate, MMA, and butyl methacrylate, BMA, show a single, sharp T_g that is tuneable between the T_g, of the homopolymers, 110 and 20 °C respectively, by varying the composition. It was also found that the work capacity, dictated by the rubbery modulus, is adjustable to accommodate various applications by varying the extent of cross-link density (Ratna and Karger-Kocsis, 2008).

Aside from chemically cross-linked polymers, certain polymers with T_g above room temperature and with ultra-high molecular weights, $>10^6$ g mol^{-1}, may also be included in this group due to the lack of flow above the T_g as well as exhibiting good shape fixity by vitrification. These types of polymer have a large number of entanglements per chain (>25) which form physical cross-links that give excellent elasticity above the T_g, however this makes thermal processing difficult, requiring a solvent-based process to be used. These characteristics cause this group of polymers to essentially behave as covalently cross-linked glassy thermoset SMP (Lendlein and Kelch, 2002).

Material	Transition Temperature, °C	Special Features
Polynorbornene	40	Sharp T_g
Thermosetting PU	0 to 150	Can be moisture activated
High MW poly(MMA)	105	Easily deformable below T_g
Poly(MMA)-co-poly(BMA)	20 to 110	Optically transparent
Co-polyester	48 to 66	Biodegradable

Table 1.1: Summary of the Class I shape memory thermosets with $T_{trans} = T_g$.

1.2.2. Covalently Cross-Linked Semi-Crystalline Networks (Class II)

In the class II SMP T_{trans} is the T_m, typically of the semi-crystalline networks, which can provide a sharper recovery event. The temporary shape is fixed by crystallisation instead of being fixed by vitrification. Therefore the temporary shape is deformed and fixed when the sample is heated above the T_m of the crystalline regions and subsequently cooled below their crystallization temperature. However as with class I SMP the permanent shape is established by chemical cross-linking and cannot be reshaped after processing (Rousseau, 2008). When compared to glassy SMP, the class II materials are commonly more compliant below T_{trans} with a stiffness that correlates to the degree of crystallinity, thus indirectly to the extent of cross-linking. With class II SMP a larger range of shape fixity and recovery can be attained and the range depends entirely on the composition of the network.

Examples of class II SMP include cross-linked polycyclooctene, PCO, with almost 100 % shape fixity and recovery (Liu et al., 2002), cross-linked ethylene vinyl acetate rubbers with 30 to 95% recovery depending on their composition (Li et al., 1999) and cross-linked polyethylene systems commonly used as heat shrink materials with shape fixing and recoveries of up to 96 and 94 %, respectively (Khonakdar et al., 2007, Li et al., 1998). Other examples of class II SMP are summarised in table 1.2.

Class II SMP can be tailored with regards to shape fixity and recovery, allowing optimal performance to be achieved for desired applications. However as the temporary shape is achieved by crystallisation, the polymers intrinsically show large thermal hysteresis between melting and crystallisation transition temperatures. This means during the fixing and recovery stage of the SME testing cycle the SMP loses its ability to fully store a temporary shape or fully recover the original shape. In order to achieve a good shape memory cycle, class II SMP require cooling to much lower temperatures than the relative T_{trans}, when compared to class I SMP, in order to allow full crystallisation and therefore good shape fixity (Liu et al., 2007).

Material	Transition Temperature, °C	Special Features
Polycaprolactone (PCL)	54 to 58	Undergoes no chain scission
PCO / crystalline polyalkylene polymer blend	58	Selective cross-linking
PCO	45	Fast shape recovery
PCL-co-butyl acrylate	45	UV polymerised
Polyethylene	ca. 120	Allows E-beam cross-linking

Table 1.2: Summary of the Class II shape memory thermosets with $T_{trans} = T_m$.

1.2.3. Physically Cross-Linked Glassy Copolymers (Class III)

The shape memory behaviour of class III SMP is attributed to the T_g of the soft segment regions, therefore a temporary shape can by formed when the soft segments in the SMP are heated above the T_g and fixed when cooled below the T_g. The permanent shape of the network is provided by the physical cross-linking of the hard segments via molecular interactions i.e. van der Waals and dipole-dipole interactions as well as hydrogen bonding. This allows the hard segments to withstand moderately high temperatures without being destroyed (Rousseau, 2008). As class III SMP are physically cross-linked, they have an advantage over class I and II SMP, being processable above the T_m of the hard domains which allows the permanent shape to be changed (Liu et al., 2007).

The majority of examples of class III SMP are physically cross-linked PUs, multi-block copolymers consisting of alternating oligomeric sequences of hard and soft segments. The class III PUs are generally synthesised by reacting a diisocyanate with a diol, triol or polyol, with reported shape fixity and recovery ratios varying from 80 to 90 % and 75 to 100 %, respectively (Rousseau, 2008).

Other class III SMP include melt-miscible blends of poly(vinyl acetate), PVAc, and poly(lactic acid), PLA, a form of phase-separated block co-polymer, which was found to have elasticity similar to rubber at temperatures above T_m. The temporary shape could easily be formed with external force and fixed by cooling below the T_m (Mather et al., 2007). Jeon et al., (2000) formed a class III SMP from norbornene copolymerised with a polyhedral oligosilsesquioxane hybrid monomer, the copolymer was found to have fairly high strain recovery with enhanced thermal stability compared to poly(norbornene). Another class III SMP, poly(MMA) blended with poly(vinyldiene fluoride), PVDF, was also found to show shape memory properties (Campo and Mather, 2005). A summary of physically cross-linked block copolymers and blends are summarised in table 1.3.

Overall class III SMP, generally, have a lower shape memory performance, regarding fixity and recovery, compared to SMP classes I and II, primarily caused by the loss of physical cross-link integrity during mechanical deformation. However class III SMP do exhibit a modulus below T_{trans} comparable to class I SMP.

Materials	Hard Segments	Soft Segments	Transition type	Transition Temperature °C
Aramid/PCL blend	Aramid	PCL or poly (tetrahydrofuran)	T_m	0 to 35
Poly(ketone-co-alcohol)	Micro-crystalline segments	Amorphous polyketone	T_g	-
PLA -co-poly(glycolide-co-caprolactone) multi-block copolymer	PLA crystalline domain	Amorphous copolymer	T_g	40 to 50
PVDF and PVAc blends	PVDF crystals	PVDF/PVAc amorphous regions	T_g	20 to 35
Polyhedral oligomeric silsesquioxane (POSS) telechelic	POSS domain	Poly(ethylene glycol)	T_m	55

Table 1.3: Summary physically cross-linked block copolymers and blends

1.2.4. Physically Cross-Linked Semi-Crystalline Block Copolymers (Class IV)

Although similar in structure to class III SMP, class IV are physically cross-linked semi-crystalline block copolymers whose shape memory behaviour, T_{trans}, arises from the T_m of the soft segments rather than the T_g. Retention of the permanent shape is attributed to the physical cross-linking between hard segments through molecular interactions in the crystalline regions (Rousseau, 2008). The most common examples of class IV SMP are PUs, similar to SMP class III, predominantly formed from polycaprolactone, PCL, diol soft segments, and methylene diisocyanate hard segments, occasionally with butandiol as a chain extender (Cao and Jana, 2007, Lin and Chen, 1998). The class IV SMP PUs have been described in the literature to have shape fixity and recoveries of 65 to 96 % and 56 to 100 %, respectively, depending on composition (Lin and Chen, 1998). Other examples include styrene-trans-butadiene-styrene, STBS, triblock copolymers, these are strongly segregated ABA-type triblock copolymers which have demonstrated 96 % shape fixity and 98 % shape recoveries. Class IV SMP, like class III SMP, can be processed after the permanent shape is fixed (Fei and Cavicchi, 2010). A summary of physically cross-linked block copolymers and blends are summarised in table 1.3.

As with class III SMP class IV SMP can be tailored to reach optimal properties dependent on the application, reaching levels comparable to those of SMP class I and II, however it was observed that large amounts of irrecoverable strain generally occurs during the first completed shape memory cycle which then occurs through every other shape memory cycle until an equilibrium is reached. Therefore in order to optimize the shape memory behaviour of class IV SMP several cycles, or training, of the SME is required (Rousseau, 2008).

1.3. Advantages of Shape Memory Polymers Compared to Shape Memory Alloys

Overall SMP, when compared to other shape memory materials such as SMAs, possess several advantages including high elastic deformation, the ability to be elongated by more than 1000 %, low cost, low density, potential biocompatibility and biodegradability, a broad range of application temperatures that can be tailored, tuneable stiffness, and have less complicated processing and programming (Lendlein and Kelch, 2002). A comparison of the key differences between a typical SMP and SMA are summarised in table 1.4 (Liu et al., 2007).

Property	Shape Memory Polymer	Shape Memory Alloy
Density, g cm^{-3}	0.9 - 1.1	6 - 8
Extent of deformation, %	Up to 1000 %	< 8 %
Young's modulus at $T < T_{trans}$, GPa	0.01 - 3	83
Young's modulus at $T > T_{trans}$, GPa	$0.1 – 10 \times 10^{-3}$	28 – 41
Stress required for deformation, MPa	1 - 3	50 – 200
Stress produced during recovery, MPa	1 - 3	150 – 300
Critical temperatures, °C	-10 – 100	-10 – 100
Transition breath, °C	10 – 50	5 - 30
Recovery speeds	< 1s – several minutes	< 1s
Thermal conductivity, W m^{-1} K^{-1}	0.15 – 0.30	18
Biocompatibility and biodegradability	Potentially both	Not biodegradable
Processing conditions	< 200 °C, low pressure	> 1000 °C, high pressure
Corrosion performance	Excellent	Excellent
Cost	< £14 per kilogram	~ £355 per kilogram

Table 1.4: Comparison of the properties of SMP and SMAs.

Each type of shape memory material, SMP, SMA, SMG and SMC however does have distinct application uses due to their intrinsic mechanical, viscoelastic, and optical properties that allow them to be suitable for different, selected purposes.

1.4. Shape Memory Testing Methods

In order to quantify a SME there are several different methods that can be used. In the literature there has not been an agreed method of shape memory quantification with it depending on the equipment available and type of deformation the SMP sample will typically undergo during its use in practical applications.

1.4.1. Cyclic Thermo-Mechanical Characterisation

The SME can be quantified by utilising a cyclic thermo-mechanical measurement. This is carried out by means of a tensile testing rig equipped with a thermochamber, which allows different test protocols to be carried out. The experimental test protocols generally allow the programming of cold drawing at $T < T_{trans}$ or the temporary heating of the test piece to $T > T_{trans}$ and to control the stress and strain applied to a sample. Typical test protocols include 1) heating the test sample up to a temperature, T_{high}, above the T_{trans}, and stretching it to the maximum strain, ε_{max}. 2) cooling the sample down below the T_{trans} while maintaining constant strain, ε_{max}, to a set temperature, T_{low}, thus fixing the temporary shape. 3) reducing the distance between the clamps holding the specimen thus taking the sample to a stress-free state, 0 % strain, 4) heating the sample to a temperature T_{high}, greater than T_{trans}, so that the sample contracts and restores the permanent shape, 5) repeating the cycle as required. The results of the thermocyclic measurement are often presented as an $\varepsilon - \sigma$ curve (σ = tensile stress), figure 1.6.

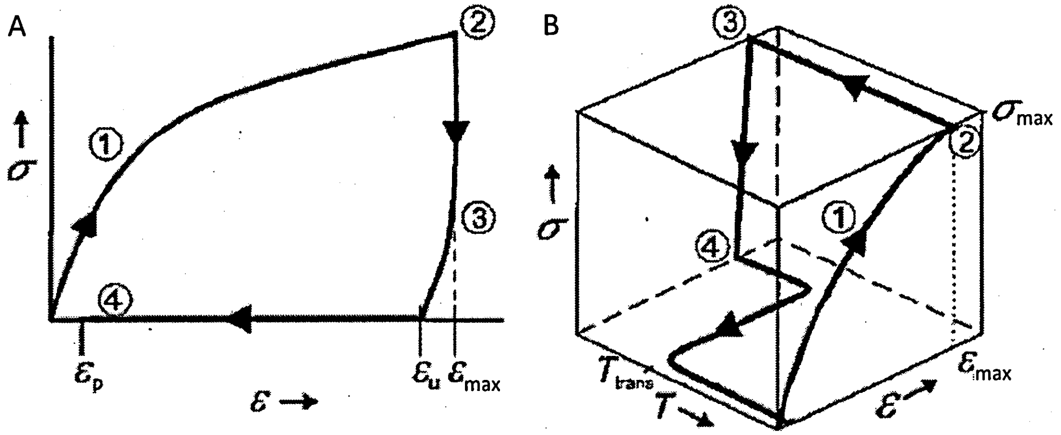

Figure 1.6: Schematic diagram of a standard SMP that has undergone cyclic thermomechanical investigation for two different tests: a) ε – σ diagram 1) SMP is stretched to ε_{max} at T_{high}, 2) SMP cooled to T_{low} while maintaining ε_{max}, 3) the distance between the clamps is reduced resulting in a stress-free state, 4) at ε = 0 % SMP heated to T_{high}. b) ε - T - σ diagram 1) SMP is stretched to ε_{max} at T_{high}, 2) SMP cooled to T_{low} with a cooling rate, K_{cool} = dT/dt, while σ_{max} is kept constant, 3) distance between the clamps is reduced resulting in a stress-free state, σ = 0 MPa is reached, 4) SMP is heated to T_{high} with a heating rate K_{heat} = dT/dt at σ = 0 MPa (Lendlein and Kelch, 2002).

Using the ε – σ curve it is possible to determine the elastic modulus, E, at T_{high}, E(T_{high}), found from the initial slope in the measurement range 1, figure 1.6 A. The value of E for the stretched sample at T_{low}, E(T_{low}) can also be determined from the slope in measurement 3, figure 1.6 A. Shape memory quantities e.g. strain recovery rate, R_r and shape fixity rate, R_f, can also be extrapolated from the traces.

The R_r quantifies the ability of the SMP to memorize its permanent shape and is a measure of how much strain is recovered during the shape-memory transition. There are several ways in which this may be calculated, however there are two main routes, equation 1.3.

$$R_r(N) = \left(\frac{\varepsilon_{max} - \varepsilon_p(N)}{\varepsilon_{max} - \varepsilon_p(N-1)}\right) \times 100\%$$

Equation 1.3: Equation employed by Tobushi et al., (1996) to calculate R_r where $R_r(N)$ and $\varepsilon_p(N)$ denote strain recovery and residual strain in the Nth cycle, respectively.

The other equation for calculating R_r is attributed to Kim et al., (1996), equation 1.4. When N = 1, equation 1.3 reduces to equation 1.4.

$$R_r(N) = \left(\frac{\varepsilon_{max} - \varepsilon_p(N)}{\varepsilon_{max}}\right) \times 100\%$$

Equation 1.4: Kim et al., equation for calculating R_r.

The R_f describes the ability of the SMP switching segments to fix and store the mechanical deformation applied during the programming stage. The R_f is produced by the ratio of the strain in the stress-free state after the removal of the tensile stress and ε_{max}, equation 1.5.

$$R_f = \frac{\varepsilon_u}{\varepsilon_{max}} \times 100\%$$

Equation 1.5: Equation to calculate the R_f.

1.4.2. Bending Test for the Determination of SME

The most common alternate to the thermomechanical cyclic tensile test, which requires specialised equipment, is the bending test for the determination of the SME, figure 1.7. The bending test is a much simpler and easier approach and has been used by Lin and Chen (1998), Liu et al., (2002) and Li and Larock (2002) in order to establish the SME of SMP.

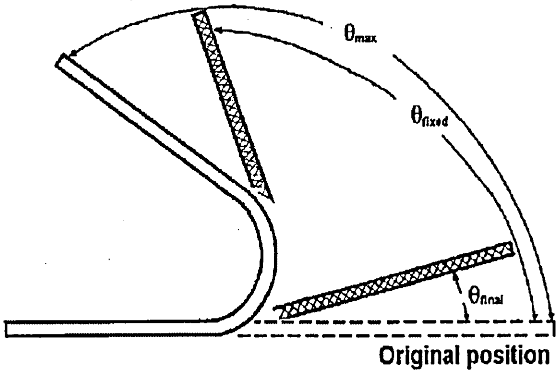

Figure 1.7: Schematic illustration of the key parameters obtained during a SMP bending test.

The bending test is typically carried out on a thin strip of SMP. The typical procedure involves 1) deforming, bending, the SMP to a given angle, θ_{max}, at a set temperature , commonly above T_{trans}, 2) while deformed the sample is cooled to below the T_{trans}, 3) the external force is removed and any recovery the sample undergoes is recorded, θ_{fixed}. 4) the sample is heated to a constant temperature > T_{trans} the sample gradually recovers its original shape allowing a series of angles, $\theta_i(t)$, to be recorded as a function of time, t, 5) when recovery is complete the final angle, θ_{final}, can be recorded. 6) with the $\theta_i(t)$ angles recorded, the R_f and R_r can be calculated, equation 1.6.

$$\text{A) } \boldsymbol{R_f} = \frac{\theta_{fixed}}{\theta_{max}} \times \mathbf{100\%}$$

$$\text{B) } \boldsymbol{R_r} = \left(\frac{\theta_{fixed}-\theta_{final}}{\theta_{fixed}}\right) \times \mathbf{100\%}$$

$$\text{C) } \boldsymbol{R_r(T)} = \left(\frac{\theta_{max}-\theta_i(t)}{\theta_{max}}\right) \times \mathbf{100\%}$$

Equation 1.6: Equations to calculate A) R_f, B) R_r and C) $R_r(T)$, denoting the sample recovery when heated to a set temperature.

1.4.3. Other Shape Memory Tests - Hot-Stage Microscope

Aside from the previous methods of assessing SME there are several others including the hot-stage microscope method adopted by Ma et al., (1998) and Li et al., (1998) and the dynamic mechanical analyser method developed by Gall et al., (2002). Another technique is the heat shrinkage test described by Lendlein and Kelch (2002). However even though the heat-shrinkage process has been agreed to be analogous to a thermally induced SME, there is still some debate about where the border between heat-shrinkage polymers and SMP actually occurs. This test is therefore not widely used to assess SME (Lendlein and Kelch, 2002, Hu, 2007).

1.5. SMP Composites and Blends

Although SMP are superior to SMAs in some respects, table 1.4, SMP have some substantial shortcomings including low mechanical strength and shape recovery stress, when compared to SMAs. This is due to intrinsically lower modulus of the SMP, therefore in order to improve this many authors including Li et al., (2000), Cao and

Jana (2007), and Gunes et al., (2008), have incorporated high modulus inorganic or organic fillers into the SMP matrix (Meng and Hu, 2009).

1.5.1. Filler Materials

1.5.1.1. Clays

One of the main fillers utilised to improve the properties of polymers are clays, this is due to their high capacity for cation exchange, useful swelling properties, high adsorption capacities, low cost, high modulus and relative ease of procurement.

Clays are difficult to define precisely, but the term 'clay' implies a natural, earthy, fine-grained material which develops plasticity when mixed with water. Clays are the product of weathering of rocks formed by hydrothermal action, or due to being deposited as sediment with particle sizes ranging from micro- to nano-meters.

On a molecular level clays are crystalline in structure with the composition being determined by the atomic arrangement and combination of each clay layer, or platelet.

The atomic structure of a clay platelet typically contains two structural units forming atomic lattices. One unit consists of six closely packed oxygen or hydroxyl atoms with an embedded aluminium, iron, or magnesium atom in the centre forming an octahedral coordination, figure 1.8, (Grim, 1968).

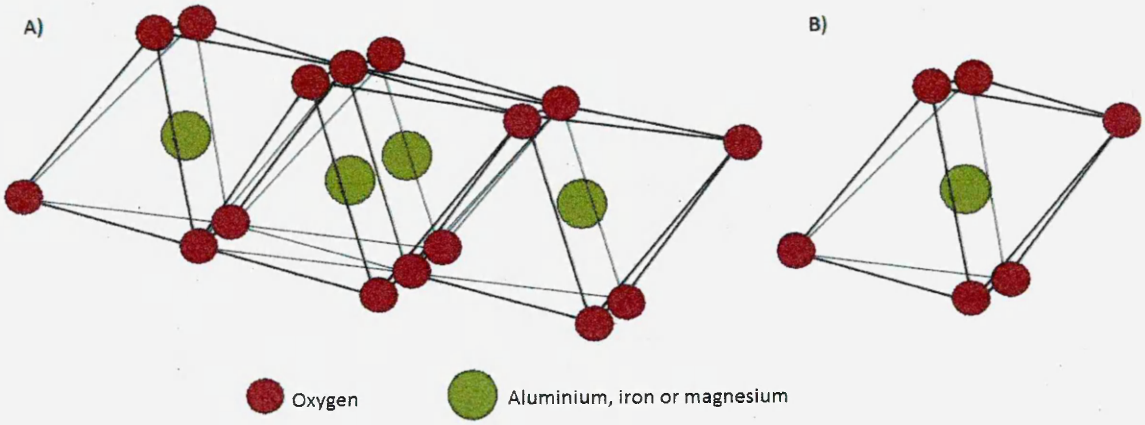

Figure 1.8: Diagrammatic representation of A) the sheet structure of the octahedral units and B) a single octahedral unit (Grim, 1968).

The second unit is formed of silica tetrahedra, where a silicon ion is in the centre of four oxygen or hydroxyl ions which have a tetrahedral coordination, figure 1.9.

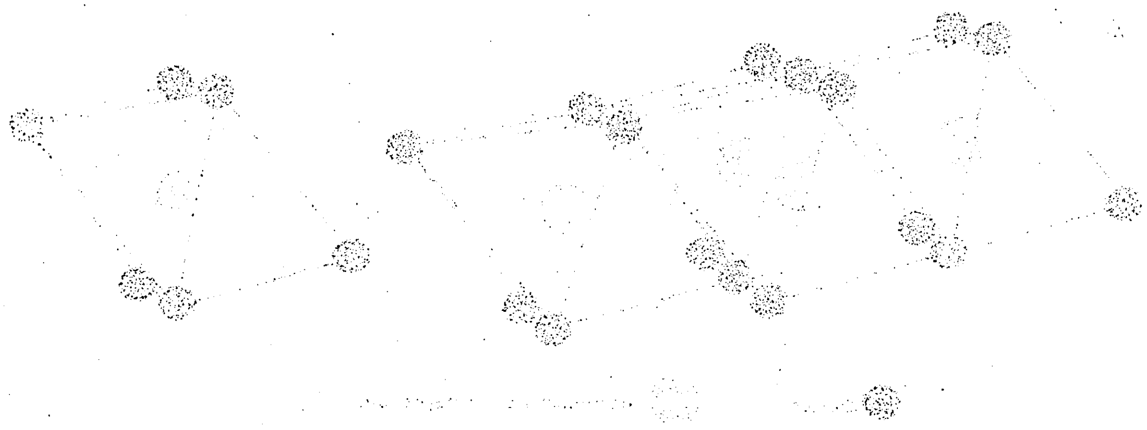

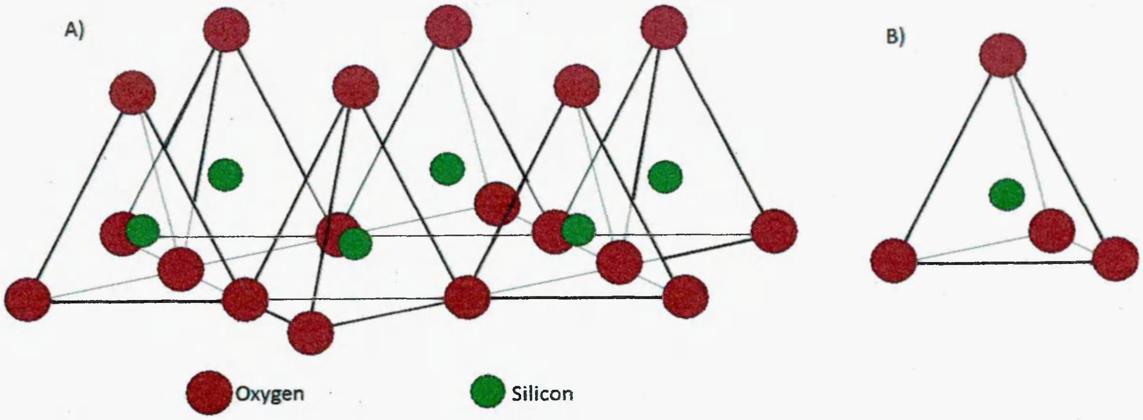

Figure 1.9: Diagrammatic representation of A) the sheet structure of the tetrahedral units, typically arranged in a hexagonal network and B) a single tetrahedral unit (Grim, 1968).

The hexagonal arrangement of the silica tetrahedra causes a hexagonal void to appear in the centre of each arrangement, known as the ditrigonal cavity. In this formation the oxygen atoms either become external, such as hydroxyl groups, or form bonds to an octahedral sheet.

The octahedral and tetrahedral sheets are superimposable and can be fused to one another by the sharing of oxygen atoms, with the fused sheets forming a clay layer. The clay layers naturally arrange into regular stacks which have a large surface area and high aspect ratios, figure 1.10, (Grim, 1968).

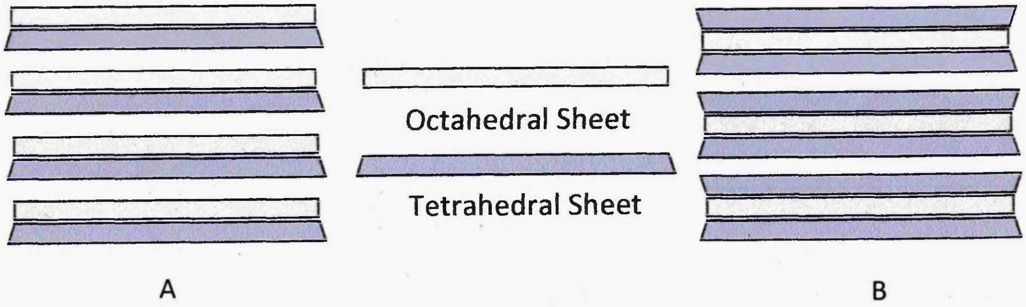

Figure 1.10: Diagrammatic representation of clay layers forming regular stacks, A) a 1:1 clay e.g. kaolin and B) a 2:1 clay, e.g. montmorillonite.

The classification of clays reflects the combination of sheets in a layer e.g. a Kaolin clay is formed from one silica tetrahedral sheet fused to an octahedral sheet (1:1), figure 1.10 A, whereas e.g. a smectite clay is formed by fusing one octahedral sheet between

two silica tetrahedral sheets (2:1), figure 1.10 B. Other 1:1 clays include Dickite and Nacrite, while other 2:1 clays include hectorite, Vermiculites, Mica and Talc. Smectite clays are most often used to form polymer composites as they have the ability to swell in solvents and readily undergo cation exchange.

Isomorphous substitution involves the replacement of the inter-layer ions with ions of a similar size but lower charge e.g. Al^{3+} would be replaced by Mg^{2+} in an octahedral sheet while Si^{4+} would be replaced by Al^{3+} in a tetrahedral sheet. This leaves a net negative charge and causes the exchange cations to be sorbed between the clay layers in order to make the structure electrically neutral. The number of exchange cations that clay can contain is quantified via the cation exchange capacity; this is the measurable quantity that is related to the layer charge of the clay.

The distance between the clay platelets in the stack is known as the d-spacing, figure 1.11.

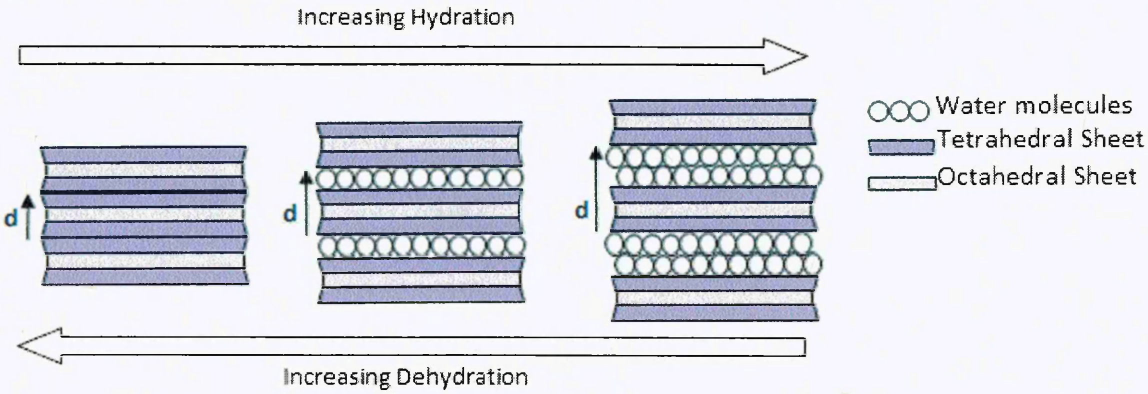

Figure 1.11: The swelling of clay platelets and resulting increase in d-spacing.

The swelling ability of the clay depends largely on the strength of the bonding between the clay platelets, i.e. van der Waal's or small ionic forces. The weaker the interaction the easier it is for water and polar molecules to be absorbed into the clay gallery, increasing swelling, (Delpennino, 1981). Hence a Na^{+}-clay will swell more than a Ca^{2+}-clay. By measuring the d-spacing, the state of clay platelet dispersion can be calculated. This is very important when forming a polymer composite, figure 1.12.

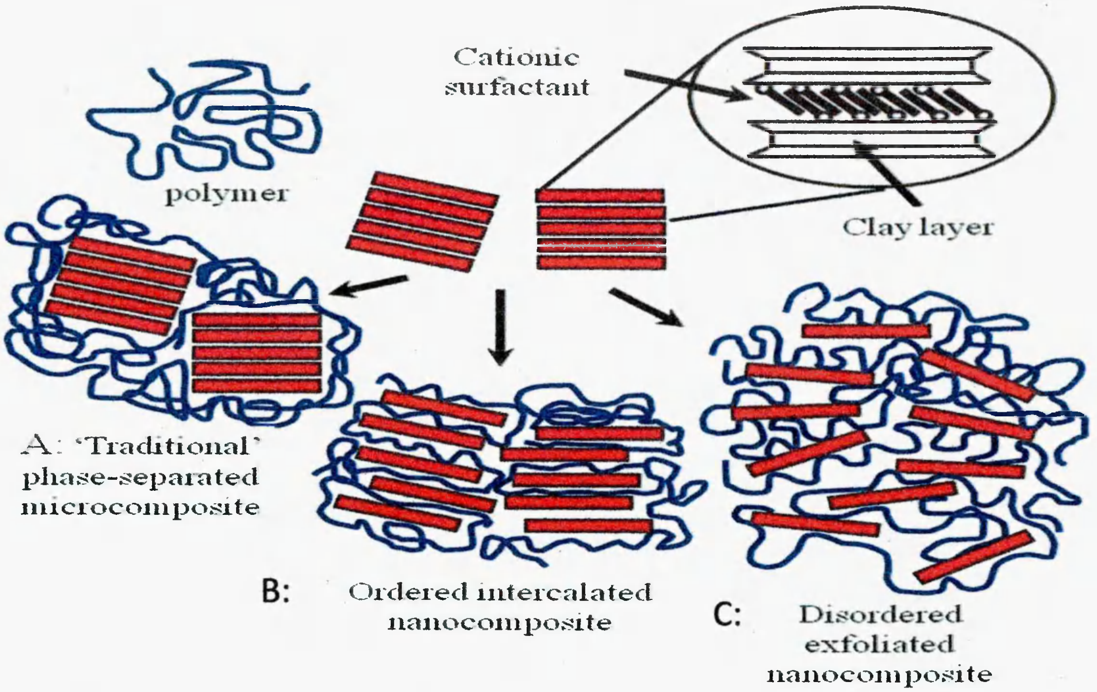
Cationic surfactant
polymer
Clay layer
A: 'Traditional' phase-separated microcomposite
B: Ordered intercalated nanocomposite
C: Disordered exfoliated nanocomposite

Figure 1.12: General dispersed states of polymer swelled clays. A, small d-spacing, B, moderate d-spacing and C, large d-spacing (Doppers et al., 2004).

Exfoliated clays, figure 1.12 C, have been extensively used to improve the thermal, mechanical and barrier properties of polymers. It has been suggested by several authors that clay, used to prepare functional nanocomposites, can (in some circumstances) improve shape memory properties (Meng and Hu, 2009). Gunes et al., (2008), has shown that when Cloisite$^{©}$ 30B, C30B, was exfoliated in a SMP PU with a 33 wt% hard segment content, there was an overall improvement to shape fixity, recovery stress and recovery ratio. There were also improvements to both tensile modulus and stretching stress, with the best results observed being when the nanoclay was at 1 wt%. Liff et al., (2007) used a novel solvent-exchange approach to exfoliate unmodified Laponite into a commercial SMP PU, Elasthane 80A, to preferentially reinforce the hard microdomains. It was found that the exfoliated Laponite caused an increase in stiffness and toughness along with an increase in rubbery modulus that was predicted to increase the shape memory restoring force without changing the T_g. Utilising up to 5 wt% C30B Coa and Jana., (2007) found that when exfoliated into a SMP PU, the room temperature tensile properties were dependent on the competing influence of reduced soft segment crystallinity and clay content. The tensile modulus at temperatures > T_m of the soft segment increased with clay content and at 1 wt% there was a 20 % increase in the magnitude of the shape recovery stress.

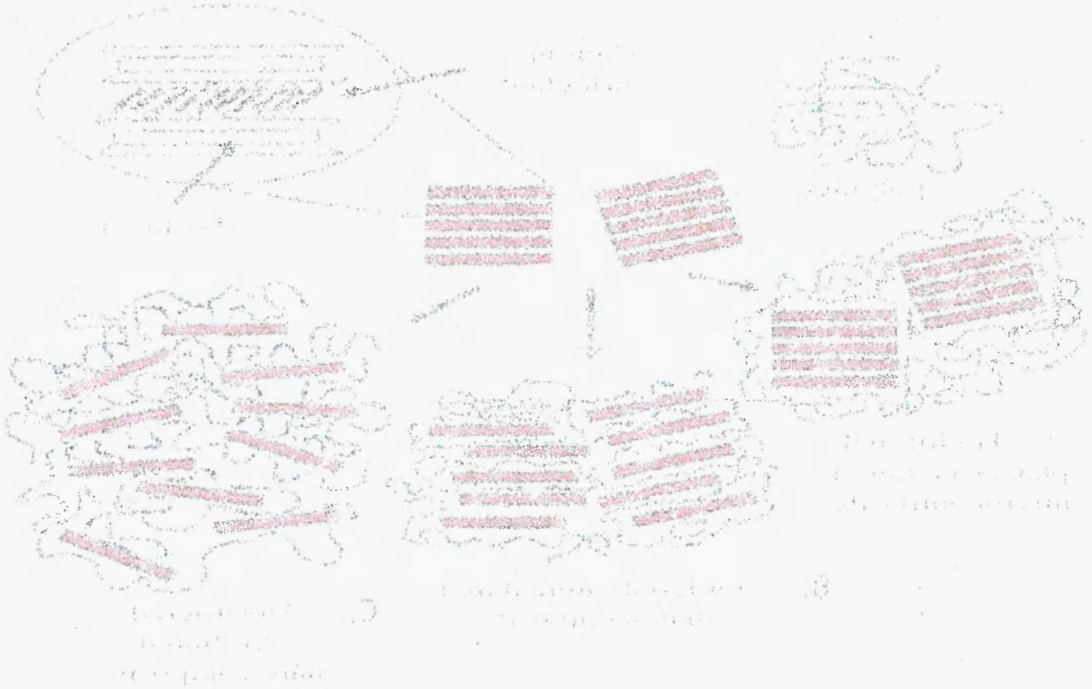

1.5.1.2. Carbon Black

SMP blended with carbon black, CB, have been formed primarily for applications in the field of electronics as polymer conductors, semi-conductors and the media for heat transference devices (Meng and Hu, 2009). Experiments carried out by Li et al., (2000) and Gunes et al., (2008, 2010) have shown that CB is not very effective in improving the mechanical strength or shape recovery stress of SMP. Li et al. (2000), investigating the possibility of creating a SMP PU/CB composite containing good electrical conductivity and shape memory ability, found that CB reduced the shape recovery of the permanent shape as well as the speed of recovery with increasing CB content. Gunes et al., (2008) while also attempting to form SMP PU/CB composites, found similar results, however they observed that at above 5 wt% CB loading shape memory ability was lost entirely. Gunes et al., did find that the SMP PU/CB composite became electrically conductive beyond a CB loading of about 3 wt% and that at 5 wt% an increased tensile modulus was observed.

1.5.1.3. Microfibers

It has been proposed by Meng and Hu (2009) that chopped and continuous, especially continuous, microfibers and fabrics are comparable to micro-and nano-sized particles to improve the mechanical strengths of SMP. Liang et al., (1997) and Ohki et al., (2004) found that reinforcing thermoplastic SMP with chopped fibreglass, unidirectional Kevlar fibre and woven fibreglass causes an increase in stiffness and shape recovery stress. Other results presented by Wei et al., (1998) demonstrated that epoxy SMP are also enhanced by the incorporation of carbon fibre, glass fibre and Kevlar fibre. However Zheng and Ni, (2007) previously found that the direction of the carbon fibre reinforcement in the SMP laminates is crucial to the influence on the shape memory ability.

1.5.1.4. Silica/Silicon Carbide

Incorporation of silica or silicon carbide, SiC, into SMP matrixes has been reported by several authors, including Liu et al., (2003), Cho and Lee (2004), Gunes et al., (2008) and Jang et al., (2009). It was found overall that silica as a filler material can improve the elastic modulus of SMP; however it has been shown to deteriorate the SME even at low loading. Liu et al., found that the inclusion up to 20 wt% of SiC nano-particles in an SMP resin caused an increase in the modulus and attainable recovery force without causing major changes to the T_g. Cho and Lee found that SMP PU samples containing 10 wt% silica, obtained from tetraethoxysilane, showed increase breaking stress, elongation-at-break, and modulus, as well as shape recovery of 80 % and greater. However Gunes et al., found that there were only minor improvements to tensile modulus and deformation stress, and decreases to shape fixity and shape recovery stress, with no significant change in recovery ratio until SiC reached 5 wt% loading. Finally Jang et al., used 3-aminopropyltriethoxysilane and nano-sized silica particles to act as physical cross-links and reinforcing filler for a SMP PU. It was found that the PU with silica particles modulus was significantly increased compared with uncross-linked PU and PU cross-linked by 3-aminopropyltriethoxysilane Si–O–Si bonds in the absence of silica particles. It was shown that up to 99 % shape fixity and recovery could be achieved compared to the unfilled SMP PUs 95 % fixity and 55 % recovery.

1.5.1.5. Carbon nano-tubes

Carbon nano-tubes, CNT, are nano materials with exceptional mechanical strength with high elastic modulus and aspect ratios making them effective as fillers in SMP, where improvement of the mechanical strength and shape recovery stress is desired, table 1.4. Yoo et al., (2006) incorporated CNTs into a SMP PU forming a nanocomposite. The CNTs enhanced the mechanical properties and caused the SMP PU to become electroactive, allowing almost full shape recovery when a 50 V electric field was applied. Ni et al., (2007) utilised vapour grown carbon fibres to form CNTs and incorporated them into a SMP PU, Diary MS4510, at varying weight fractions. It was found that the Young's modulus and the yield stress increased with increasing CNT content, at any temperature, and after several cycles of training the SMP can achieve a shape fixity and recoverability of ca. 90 %. It was also found that at 3.3 wt% CNT loading twice the amount of recovery stress was generated compared to the pure SMP. Miaudet et al., (2007) produced a CNT reinforced SMP polyvinyl alcohol, PVA, utilising a coagulation spinning technique. The CNT reinforcement allowed a 1:2 order of magnitude greater maximal recovery stress to be generated compared to conventional SMP producing shape memory recovery stresses close to those of SMAs, table 1.4.

1.5.2. SMP Blends

As mentioned previously SMP have some weak points and attempts to compensate for this by introducing filler materials is well established, however another approach is by blending polymers together. In the SMP field, polymer blending is carried out to achieve two general targets, 1) tune or improve the properties of an original SMP, including T_{trans}, mechanical properties and shape memory properties, 2) create new shape memory materials where one polymer will form the reversible phase while the other forms the fixing phase (Meng and Hu, 2009). Several authors have attempted to tune or improve SMP properties by blending a SMP with another polymer. Jeong et al., (2001) blended a SMP PU with a phenoxy resin, a miscible polymer, forming a tuneable, content dependent T_{trans}, occurring between the T_g of the PU soft segments and the T_g of the phenoxy resin. Other authors blended a crystalline polymer and an amorphous polymer in order to create new novel SMP, with the crystalline polymer acting as the cross-linking structure and the amorphous polymer providing the switch. Mather et al., (2007) blended together a crystalline polymer i.e. PVDF, polyethylene-co-vinyl acetate or PVC with an amorphous polymer i.e. atactic poly(MMA), PVAc and other poly alkyl methacrylates to form novel SMP. The blending of crystalline polymers with other crystalline polymers has also been carried out by Behl et al., (2009), blending together poly(p-dioxanone), PPDO, and PCL with a poly(alkylene adipate) mediator as a compatibilizer, in order to create new SMP. Varying the content of the two crystalline polymers allows the mechanical properties to be smoothly adjusted, with the PPDO providing the hard segment determining the permanent shape and the PCL providing the soft segment determining the T_{trans}. Another method of forming a novel SMP is the blending of an elastomer with a crystalline or amorphous polymer. Zhang et al., (2009) blended a tri-block copolymer, styrene-butadiene-styrene, SBS, with an immiscible PCL, in order to create a new SMP with tuneable properties. The SBS polymer phase acted as the fixing phase providing the memory of the permanent shape while the PCL acted as the reversible phase providing the T_{trans}.

1.6. Triple or Multiple Shape Memory Polymers

SMP do not always have dual shape memory abilities i.e. original and individual temporary shape. Some materials e.g. poly(octadecyl vinyl ether) with butyl acrylate

(Reyntjens et al., 1999), poly(ethylene-co-vinyl acetate) (Li et al., 2011), and poly(ethylene glycol) monomethyl ether monomethacrylate, using PCL dimethacrylate as a cross-linker, can demonstrate triple SME i.e. store two individual temporary shapes and the original shape (Behl et al., 2009).

The majority of research into two-way shape memory research has been to achieve a SME where heating to two different temperatures will cause two different shapes to be recovered. Bellin et al., (2007) reported that using poly(ethylene glycol) monomethyl ether monomethacrylate using PCL dimethacrylate as a cross-linker can demonstrate the two-way SME. In this system there are two T_{trans}, the T_m of A and the T_m of B one is provided by the crystallizable PCL chain segments while the second results from grafted crystallizable poly(ethylene glycol), PEG, side chains. In order to program two temporary shapes, the two-way SMP needs to be heated to a temperature above the highest $T_{trans(B)}$, deformed into temporary shape 2, and fixed by cooling to the lower $T_{trans(A)}$, deformed a second time to temporary shape 1, and cooled to below $T_{trans(A)}$ to fix and store the second temporary shape. Bellin et al., found that two temporary shapes could be stored individually, and recovered before returning to the original shape, the overall process showed complete shape recovery.

Other types of SMP can store multiple temporary shapes. This is achieved at the molecular level, with the maximum number of temporary shapes that can be memorized typically correlating directly to the number of individual reversible phases, with their individual T_{trans} values, in the polymer e.g. high-density polyethylene, HDPE, ethylene-1-octene copolymers, EOC, combined with a short-chain branched polyethylene (Meng and Hu, 2009). Kolesov and Radusch (2008), found that the HDPE-co-EOC combined with short-chain branched polyethylene possessed multiple crystallization and melting points which could be used as T_{trans}, allowing for triple- and quadruple- SME with the appropriate programming regime. Depending on composition the SMP could display an overall shape fixity between 76 to 97 % and a shape recovery between 93 to 98 %. The SMP blends were reported to have good potential for further development and successful application.

Another, atypical, multi-shape SMP, perfluorosulphonic acid ionomer, PFSA, has recently been reported by Xie (2010). PFSA has a single broad reversible phase transition, but exhibits dual-, triple-, and quadruple- SME. This has been suggested to occur because the polymer memorizes not just the imparted strain applied during deformation, but also the thermomechanical history previously applied. Therefore multiple temporary shapes can be achieved by applying multiple deformations within the T_g range. The shape memory ability has been reported to display shape recovery values of 93%, for up to 3 fixed temporary shapes, while the shape fixity for the first and second temporary shapes are around 60% the third shape demonstrated a 96% fixity.

1.7. Biodegradable SMP

Biodegradability is an important material property that has become very popular in recent years (Gross and Karla, 2002). One of the first reports of biodegradability and SME was carried out by Lendlein and Langer (2002) who reported on PCL-based biodegradable SMP. Biodegradable SMP have quickly become an area of research interest, especially for potential biomedical applications as there would be no need to remove implants in follow-up surgery as it would degrade within a predefined time period (Behl and Lendein, 2007). Biodegradable SMP are primarily produced from polyglycolide, PLA and PCL, and have been used as biodegradable SMP sutures (Lendlein and Langer, 2002), stents (Venkatraman et al., 2006) and tissue scaffolds (Migneco et al., 2009).

Many PCL-based biodegradable SMP products have been reported. It been suggested that it is the most suitable SMP material for biomedical applications due to having an easily tailored T_{trans}. It has been shown that PCL, as a switching segment, can easily be adjusted to physiological temperature, 37 to 40 °C, by carefully selecting the molecular weight of PCL, hard segment and soft/hard phase compositions (Ratna and Karger-Kocsis, 2008).

PCL can be formed into either a SMP network (Lendlein et al., 2005) or, by using the PCL diols, figure 1.13, can be reacted with a diisocyanate, and potentially a chain extender, to make a SMP PU (Wang et al., 2006), figure 1.14.

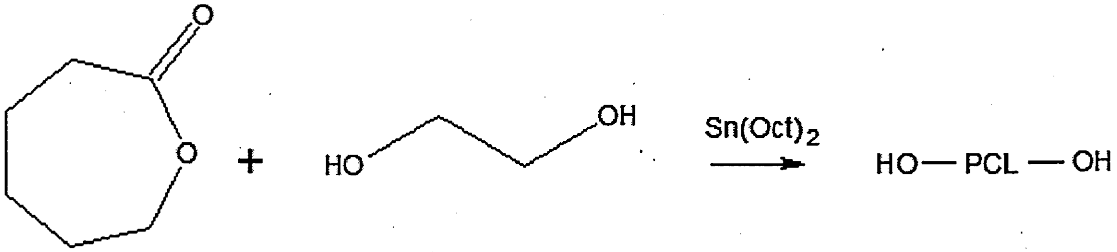
O
O
+
HO
OH
Sn(Oct)2
HO— PCL —OH

Figure 1.13: General reaction mechanism for the synthesis of PCL-diols (Ratna and Karger-Kocsis, 2008).

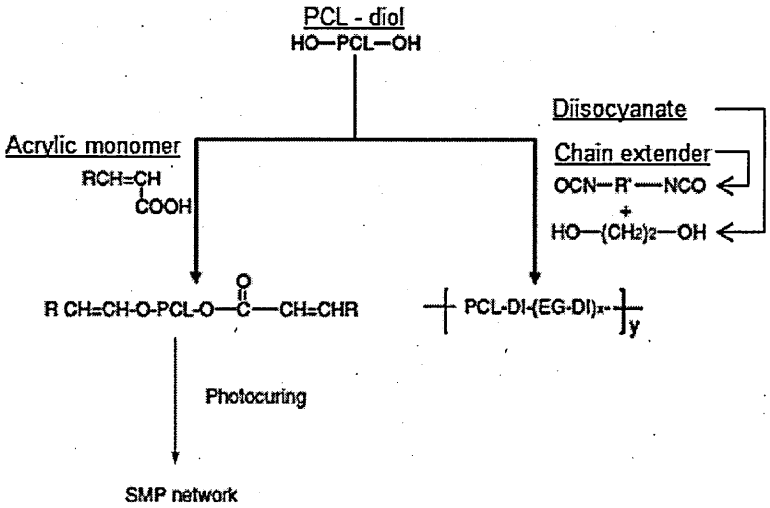
PCL - diol
HO—PCL—OH
Acrylic monomer
RCH=CH
COOH
Diisocyanate
Chain extender
OCN—R'—NCO
+
HO—(CH2)2—OH
R CH=CH-O-PCL-O—C—CH=CHR
O
PCL-DI-(EG-DI)x
y
Photocuring
SMP network

Figure 1.14: Schematic of the basic synthetic strategies for production of biodegradable PCL-based SMP (Ratna and Karger-Kocsis, 2008).

Lendlein et al., (2005) found that PCL-based dimethacrylates can show a variety of shape fixities, 86 to 96 % and recoveries, 93 to 99 %, depending on the MW of the PCL, 1500 to 10,000. Another SMP PU, synthesised from PCL 2,4-toluene diisocyanate and ethylene glycol, was reported by Ping et al., (2005). The SMP PU had an adjustable T_{trans}, T_m of PCL, in the range of 37 to 42 °C displaying shape recoveries of 94 to 100 %. Nagata et al., (2005) synthesised a multi-block copolymer by a poly-condensation of a PCL diol, MW = 3,000, and PEG, MW = 3,000, with 4,4'-(adipoyldioxy)dicinnamic acid dichloride as a chain extender. The polymer networks are formed after UV exposure in the absence of photoinitiators. The extent of network formation, gel content, is dependent on the UV irradiation exposure time. When studying the SME it was found that the best shape memory properties were achieved when a gel content of 57 % was achieved, providing shape fixity of 100 % and shape recovery of 88 %. It has been reported that when combining PCL and PEG exceptional properties can be achieved with regard to hydrophobicity and degradability, with degradability increasing with increasing PEG content (Ratna and Karger-Kocsis, 2008).

PCL-based biodegradable SMP do have some limitations typically including inadequate strength above the T_{trans} for certain practical mechanical applications as well as a low biodegradability rate. In order to overcome the limitations of PCL Wang et al., (2007), synthesised a copolymer, prepared from L-lactide and ε-caprolactone, 2,4-toluene diisocyanate, and 1,4-butanediol, in order to enhance the mechanical ability of PCL above the $T_{trans.}$ It was found that when the SMP was deformed at $T_g + 5$ °C and fixed at $T_g - 15$ °C, the shape-recovery ratios were more than 93 % at a tensile elongation of 150 % or a compression of 2- fold. However further investigation of random copolymers of PLA and PCL is required to overcome their limits (Ratna and Karger-Kocsis, 2008).

1.8. Applications of SMP

With the property of triggered responses, there are potential applications for SMP that exist in practically every avenue of life, ranging from self-repairing car bodies (Ikematu et al., 1993), Kitchen utensils (Lendlein and Kelch, 2002), switches to sensors (Synder et al., 2010), intelligent packaging (Behl et al., 2010), toys (Ikematu et al., 1993) and tools (Tong, 2004). However the majority of recent literature has been concerning the use of SMP in biomedical applications including SMP sutures (Lendlein and Langer, 2002), stents (Venkatraman et al., 2006), catheters (Liu et al., (2006), micro-actuators (Maitland et al., 2002) and tissue scaffolds (Migneco et al., 2009).

Venkatraman et al., (2006) used PLA, and poly glycolic acid, PLGA, polymers to form a biodegradable SMP stent to replace the existing Igaki–Tamai stents for use in coronary or peripheral vascular applications. It was found that the recovery temperature, biocompatibility and the time for recovery were all superior to the existing stent and that full biodegradation would take ca. 1 to 2 months.

Maitland et al., (2002) developed a SMP micro-actuator that was laser-activated and used for treating ischemic stroke. The device was fabricated using commercially available thermoplastic SMP MM6520, $T_{trans} = T_g$ of the soft segment, 65 °C, and MM5520, $T_{trans} = T_g$ of the soft segment, 55°C. The intention of the device was to be inserted by minimally invasive surgery into the blood vessel with a thrombus, locate the thrombus and insert a SMP straight wire, temporary shape, into it. A laser would be used to activate the SMP which would return it to its original shape, a cone-shaped coil, trapping the thrombus, allowing it to be removed.

Biodegradable SMP tissue scaffolds have been formed using Poly-Glycerol-Dodecanoate, PGD, by Migneco et al., (2009). It was found that the polymer T_{trans}, was the T_g, ca. 32 °C, and at body temperature, 37 °C, it showed shape memory abilities. The SMP maintained its deformed shape well when deformed below T_{trans}. When PGD was deformed above T_{trans} it could not fully maintain its temporary shape when the temperature was below the T_{trans}, unless cooled rapidly after deformation. It was also found that a complete shape recovery could be achieved in ca. 20 seconds when unconstrained SME testing was carried out in water at 40 °C.

Lendlein and Langer (2002) used a PCL-based SMP PU to form a biodegradable SMP suture. The thermoplastic SMP was extruded as a monofilament; this was sterilized and deformed, extended, by 200 % before being applied to animal test subjects. It was found that at room temperature ca. 23 °C, the suture held its deformed shape but when heated to body temperature, 37 °C and above the suture showed shape memory recovery, generating a force of 1.6 N, able to keep the wound closed.

Overall the future outlook of the SMP area is extensive with many new applications being identified with ever increasing new SMP materials.

1.9. References

ATLI, BILIM, GANDHI, FARHAN and KARST, GREG, (2009). Thermomechanical characterization of shape memory polymers. Journal of Intelligent Material Systems and Structures, 20 (1), 87-95.

BEHL, M., RAZZAQ, M.Y., and LENDLEIN, A., (2010). Multifunctional shape-memory polymers. Advanced Materials, 22 (31), 3388-3410.

BEHL, M., and LENDLEIN, A., (2007). Shape-memory polymers. Materials Today, 10 (4), 20-28.

BEHL, M., et al. (2009). Shape-memory capability of binary multiblock copolymer blends with hard and switching domains provided by different components. Soft Matter, 5 (3), 676-684.

BELLIN, I., KELCH, S., and LENDLEIN, A., (2007). Dual-shape properties of triple-shape polymer networks with crystallizable network segments and grafted side chains. Journal of Materials Chemistry, 17 (28), 2885-2891.

BUCKLEY, C.P., PRISACARIU, C., and CARACULACU, A., (2007). Novel triol-crosslinked polyurethanes and their thermorheological characterization as shape-memory materials. Polymer, 48 (5), 1388-1396.

BUEHLER, J.W., GILFRICH and R.C., WILEY, 1963. Effects of low-temperature phase changes on the mechanical properties of alloys near composition TiNi,. Journal of Applied Physics 34 p 475.

CAMPO, C.J., and MATHER, P.T., (2005). PVDF : PMMA shape memory blends: Effect of short carbon fiber addition. Abstracts of papers of the American Chemical Society, 230, U3760-U3761.

CAO, F., and JANA, S.C., (2007). Nanoclay-tethered shape memory polyurethane nanocomposites. Polymer, 48 (13), 3790-3800.

CHATERJI, S, IL, K.K., and PARK, K., (2007). Smart polymeric gels: Redefining the limits of biomedical devices. Progress in Polymer Science, 32 (8-9), 1083-1122.

CHEN, J.S., et al. (2002). Study of the interlayer expansion mechanism and thermal-mechanical properties of surface-initiated epoxy nanocomposites. Polymer, **43** (18), 4895-4904.

CHO, J.W., and LEE, S.H., (2004). Influence of silica on shape memory effect and mechanical properties of polyurethane-silica hybrids. European Polymer Journal, 40 (7), 1343-1348.

DELPENNINO, U., et al. (1981). Interlayer water and swelling properties of monoionic montmorillonites. Journal of Colloid and Interface Science, **84** (2), 301-309.

DOPPERS, L.M., BREEN, C., and SAMMON, C., (2004). Diffusion of water and acetone into poly(vinyl alcohol)-clay nanocomposites using ATR-FTIR. Vibrational Spectroscopy, **35** (1-2), 27-32.

FEI, P., and CAVICCHI, K.A., (2010). Synthesis and characterization of a poly(styrene-block-methylacrylate-random-octadecylacrylate-block-styrene) shape memory ABA triblock copolymer. Acs Applied Materials & Interfaces, 2 (10), 2797-2803.

GRIM, E.R., (1968) Clay mineralogy. New York: McGraw-Hill Book Company

GROSS, R.A., and KALRA, B., (2002). Biodegradable Polymers for the Environment. Science, 297 (5582), 803-807.

GUAN, J.J., et al. (2005). Self-folding of three-dimensional hydrogel microstructures. Journal of Physical Chemistry B, 109 (49), 23134-23137.

GUNES, I.S., CAO, F., and JANA, S.C., (2008). Effect of thermal expansion on shape memory behavior of polyurethane and its nanocomposites. Journal of Polymer Science Part B-Polymer Physics, 46 (14), 1437-1449.

GUNES, I.S., CAO, F., and JANA, S.C., (2008). Evaluation of nanoparticulate fillers for development of shape memory polyurethane nanocomposites. Polymer, 49 (9), 2223-2234.

GUNES, I.S., et al. (2010). Analysis of non-covalent interactions between the nanoparticulate fillers and the matrix polymer as applied to shape memory performance. Journal of Materials Chemistry, 20 (17), 3467-3474.

HU J.L., (2007). Shape memory polymers and textiles. Cambridge: Woodhead publishing limited.

HUANG, W.M., et al. (2010). Thermo-moisture responsive polyurethane shape-memory polymer and composites: A review. Journal of Materials Chemistry, 20 (17), 3367-3381.

IKEMATU, T., KISHIMOTO Y., and MIYAMOTO, K., (1993). Shape memory polymer resin composition and the shape memorizing molded product thereof. Japan Patent 5189110.

JANG, M.K., HARTWIG, A., and KIM, B.K., (2009). Shape memory polyurethanes cross-linked by surface modified silica particles. Journal of Materials Chemistry, 19 (8), 1166-1172.

JEON, H.G., MATHER, P.T., and HADDAD, T.S., (2000). Shape memory and nanostructure in poly(norbornyl-POSS) copolymers. Polymer International, 49 (5), 453-457.

JEONG, H.M., AHN, B.K., and KIM, B.K., (2001). Miscibility and shape memory effect of thermoplastic polyurethane blends with phenoxy resin. European Polymer Journal, 37 (11), 2245-2252.

JIANG, H.Y., KELCH, S., and LENDLEIN, A., (2006). Polymers move in response to light. Advanced Materials, 18 (11), 1471-1475.

KIM, B.K., LEE, S.Y., and XU, M., (1996). Polyurethanes having shape memory effects. Polymer, 37 (26), 5781-5793.

KOLESOV, I.S., and RADUSCH, H.J., (2008). Multiple shape-memory behavior and thermal-mechanical properties of peroxide cross-linked blends of linear and short-chain branched polyethylenes. Express Polymer Letters, 2 (7), 461-473.

LENDLEIN, A., and KELCH, S., (2002). Shape-memory polymers. Angewandte Chemie-International Edition, 41 (12), 2034-2057.

LENDLEIN, A., et al. (2005). Shape-memory polymer networks from oligo(epsilon-caprolactone)dimethacrylates. Journal of Polymer Science Part A-Polymer Chemistry, 43 (7), 1369-1381.

LENDLEIN, A., and LANGER, R., (2002). Biodegradable, elastic shape-memory polymers for potential biomedical applications. Science (New York, N.Y.), 296 (5573), 1673-1676.

LI, F.K., and LAROCK, R.C., (2002). New soybean oil-styrene-divinylbenzene thermosetting copolymers. v. shape memory effect. Journal of Applied Polymer Science, 84 (8), 1533-1543.

LI, F.K., et al. (1999). Shape memory effect of ethylene/vinyl acetate copolymers. Journal of Applied Polymer Science, 71 (7), 1063-1070.

LI, F.K., et al. (1998). Shape memory effect of polyethylene nylon 6 graft copolymers. Polymer, 39 (26), 6929-6934.

LI, F.K., et al. (2000). Polyurethane/conducting carbon black composites: Structure, electric conductivity, strain recovery behavior; and their relationships. Journal of Applied Polymer Science, 75 (1), 68-77.

LI, J., RODGERS, W., and XIE, T., (2011). Semi-crystalline two-way shape memory elastomer. Polymer, 52 (23), 5320-5325.

LI, Y. and TANAKA, T. (1992). Phase transitions of gels. Annual Review of Materials Science, 22 (1), 243-277.

LIANG, C., ROGERS, C.A., and MALAFEEW, E. (1997). Investigation of shape memory polymers and their hybrid composites (reprinted from proceedings of the second joint Japan/US conference on adaptive structures, Nov, p789-802). Journal of Intelligent Material Systems and Structures, 8 (4), 380-386.

LIFF, S.M., KUMAR, N. and MCKINLEY, G.H. (2007). High-performance elastomeric nanocomposites via solvent-exchange processing. Nature Materials, 6 (1), 76-83.

LIN, J.R., and CHEN, L.W., (1998). Study on shape-memory behavior of polyether-based polyurethanes. I. influence of the hard-segment content. Journal of Applied Polymer Science, 69 (8), 1563-1574.

LIN, J.R., and CHEN, L.W., (1998). Study on shape-memory behavior of polyether-based polyurethanes. II. influence of soft-segment molecular weight. Journal of Applied Polymer Science, 69 (8), 1575-1586.

LIU, C and MATHER, P.T., 2002. Proceedings of the annual technical conference - society of plastics engineers, 60th (Vol. 3), Society of Plastics Engineers, Brookfield, CT, USA, pp. 2685 2689.

LIU, C. et al. (2002). Chemically cross-linked polycyclooctene: Synthesis, characterization, and shape memory behavior. Macromolecules, 35 (27), 9868-9874.

LIU, C., QIN, H. and MATHER, P.T., (2007). Review of progress in shape-memory polymers. Journal of Materials Chemistry, 17 (16), 1543-1558.

LIU, Y.P., et al. (2004). Thermomechanics of shape memory polymer nanocomposites. Mechanics of Materials, 36 (10), 929-940.

MA, D.Z., et al. (1998). Compositional heterogeneity, thermostable, and shape memory properties of ethylene oxide-ethylene terephthalate segmented copolymer with long soft segment. Journal of Applied Polymer Science, 69 (5), 947-955.

MAITLAND, D.J., et al. (2002). Photothermal properties of shape memory polymer micro-actuators for treating stroke. Lasers in Surgery and Medicine, 30 (1), 1-11.

MATHER, P.T., LIU, C., CAMPO, C.J, (2007). Blends of amorphous and semicrystalline polymers having shape memory properties. Patent 7371799.

MENG, Q.H., and HU, J.L., (2009). A review of shape memory polymer composites and blends. Composites Part A-Applied Science and Manufacturing, 40 (11), 1661-1672.

MIAUDET, P., et al. (2007). Shape and temperature memory of nanocomposites with broadened glass transition. Science (New York, N.Y.), 318 (5854), 1294-1296.

MIGNECO, F., et al. (2009). Poly(glycerol-dodecanoate), a biodegradable polyester for medical devices and tissue engineering scaffolds. Biomaterials, 30 (33), 6479-6484.

MITSUMATA, T., GONG, J.P., and OSADA, Y., (2001). Shape memory functions and motility of amphiphilic polymer gels. Polymers for Advanced Technologies, 12 (1-2), 136-150.

MOHR, R., et al. (2006). Initiation of shape-memory effect by inductive heating of magnetic nanoparticles in thermoplastic polymers. Proceedings of the National Academy of Sciences of the United States of America, 103 (10), 3540-3545.

NAGATA, M., and SATO, Y., (2005). Synthesis and properties of photocurable biodegradable multiblock copolymers based on poly(epsilon-caprolactone) and poly(L-lactide) segments. Journal of Polymer Science Part A-Polymer Chemistry, 43 (11), 2426-2439.

NI, Q., et al. (2007). Shape memory effect and mechanical properties of carbon nanotube/shape memory polymer nanocomposites. Composite Structures, 81 (2), 176-184.

OHKI, T., et al. (2004). Mechanical and shape memory behavior of composites with shape memory polymer. Composites Part A-Applied Science and Manufacturing, 35 (9), 1065-1073.

OLANDER, A., (1932), J. Amer. Chem. Soc. 54: 3819.

OSADA, Y., and ROSSMURPHY, S.B., (1993). Intelligent gels. Scientific American, 268 (5), 82-87.

OTSUKA and WAYMAN, 1998. Shape memory materials, Cambridge University Press.

PING, P., et al. (2005). Poly(epsilon-caprolactone) polyurethane and its shape-memory property. Biomacromolecules, 6 (2), 587-592.

RATNA, D., and KARGER-KOCSIS (2008). Recent advances in shape memory polymers and composites: A review. Journal of Materials Science, 43 (1), 254-269.

REYNTJENS, W.G., DU PREZ, F.E., and GOETHALS, E.J., (1999). Polymer networks containing crystallizable poly(octadecyl vinyl ether) segments for shape-memory materials. Macromolecular Rapid Communications, 20 (5), 251-255.

ROUSSEAU, I.A., (2008). Challenges of shape memory polymers: A review of the progress toward overcoming SMP's limitations. Polymer Engineering and Science, 48 (11), 2075-2089.

SHIBAYAMA, M., and TANAKA, T., (1993). Volume phase-transition and related phenomena of polymer gels. Advances in Polymer Science, 109 , 1-62.

SNYDER, R., et al. (2010). Shape memory polymer sensors for tracking cumulative environmental exposure. Industrial and Commercial Applications of Smart Structures Technologies 2010, 7645, 76450C.

TOBUSHI, H., et al. (1996). Thermomechanical properties in a thin film of shape memory polymer of polyurethane series. Smart Materials & Structures, 5 (4), 483-491.

TONG, T.H., (2004). Shape memory styrene copolymer. Patent US6759481 B2.

TSAI, Y., et al. (2008). Shape memory effects of poly(ethylene terephthalate-co-ethylene succinate) random copolymers. European Polymer Journal, 44 (2), 550-554.

VENKATRAMAN, S.S., et al. (2006). Biodegradable stents with elastic memory. Biomaterials, 27 (8), 1573-1578.

WANG, W., et al. (2007). Biodegradable polyurethane based on random copolymer of L-lactide and epsilon-caprolactone and its shape-memory. Journal of Applied Polymer Science, 104 (6), 4182-4187.

WANG, W., et al. (2007). Biodegradable polyurethane based on random copolymer of L-lactide and epsilon-caprolactone and its shape-memory. Journal of Applied Polymer Science, 104 (6), 4182-4187.

WEI, Z.G., SANDSTROM, R., and MIYAZAKI, S., (1998). Shape memory materials and hybrid composites for smart systems: Part II shape-memory hybrid composites. Springer Netherlands. Journal of Materials Science, 33 (15), 3763-3783 .

WEI, Z.G., SANDSTRORÖM, R., and MIYAZAKI, S., (1998). Shape-memory materials and hybrid composites for smart systems: Part I shape-memory materials. Springer Netherlands. Journal of Materials Science, 33 (15), 3743-3762 .

XIE, T., (2010). Tunable polymer multi-shape memory effect. Nature, 464 (7286), 267-270.

XU, J.W., SHI, W.F., and PANG, W.M., (2006). Synthesis and shape memory effects of Si-O-Si cross-linked hybrid polyurethanes. Polymer, 47 (1), 457-465.

XUE, L., DAI, S., and LI, Z., (2010). Biodegradable shape-memory block co-polymers for fast self-expandable stents. Biomaterials, 31 (32), 8132-8140.

YOO, H.J., et al. (2006). Polyurethane-carbon nanotube nanocomposites prepared by in-situ polymerization with electroactive shape memory. Journal of Macromolecular Science Part B-Physics, 45 (4), 441-451.

ZHANG, H., et al. (2009). A novel type of shape memory polymer blend and the shape memory mechanism. Polymer, 50 (6), 1596-1601.

Chapter 2: Theory of Techniques Used

2. Theory of Techniques Used

2.1. Characterisation Techniques

The following techniques in this thesis were used to characterise all polymers, polymer blends and polymer (nano)composites samples.

2.1.1. X-ray Diffraction (XRD)

2.1.1.1. XRD Theory

X-ray diffraction, XRD, is a technique used to analyse the crystal structure of a crystalline material using x-rays. X-rays are a high frequency, ca. 10^{18} Hz, form of electromagnetic radiation that is produced when atoms of any substance are struck by high-speed electrons.

When fixed wavelength, monochromatic, x-rays strike a material and have the same magnitude as the atomic spacing in the material they are scattered in all directions. Most of the radiation scattered from one atomic layer cancels out the radiation scattered from the others, but some x-rays hit certain crystallographic planes at specific angles and become reinforced rather than being annihilated, figure 2.1. This effect of x-ray reinforcement is known as diffraction, and has to satisfy Bragg's law, equation 2.1 (Askeland et al., 2011).

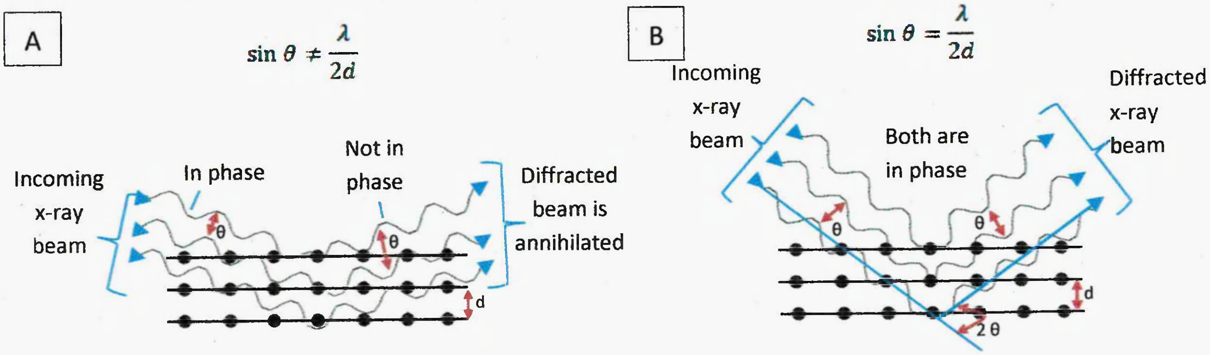
A
$\sin\theta \neq \frac{\lambda}{2d}$
Incoming x-ray beam
In phase
Not in phase
Diffracted beam is annihilated
θ
θ
d
B
$\sin\theta = \frac{\lambda}{2d}$
Incoming x-ray beam
Both are in phase
Diffracted x-ray beam
θ
θ
d
2θ

Figure 2.1: The A) destructive and B) constructive interference between x-rays and crystalline materials, with reinforcement occurring at angles which satisfy Bragg's law.

$$n\lambda = 2d_{hkl}\sin\theta$$

Equation 2.1: Bragg's law, where n = integer, λ= wavelength of x-rays, d_{hkl} = interplanar spacing, or d-spacing, between the planes that cause constructive reinforcement of the beam and θ = angle between the diffracted beam and original beam direction.

The Bragg equation can be rearranged so that the d-spacing may be calculated, equation 2.2.

$$d_{hkl} = n\lambda / 2 \sin \theta$$

Equation 2.2: Re-arrangement of the Bragg equation to calculate d-spacing.

The expressions used to describe the d-spacing i.e. d_{001}, are derived from the separation of the crystal planes in the material being analysed. As the incident beam is rotated around the material it will encounter different planes of regular crystalline forms, these planes give rise to a set of indices according to their position in the material.

XRD analysis is dependent on many factors including sample position and alignment and sample thickness, area and homogeneity.

2.1.1.2. XRD Analysis

X-rays are created in an x-ray tube that is kept under vacuum. Inside the x-ray tube electrons are produced by a glowing tungsten filament (cathode). These high-energy electrons are then accelerated by voltages of ca. 15 to 60 kV in order to bombard a metal target e.g. copper, table 2.1, which acts an anode.

Material	Wavelength, Å
Molybdenum	0.711
Copper	1.541
Cobalt	1.790
Iron	1.937
Chromium	2.291

Table 2.1: Summary of x-ray wavelength produced by various metals.

The most commonly used metal target is copper and is predominantly used in this thesis. The lowest angle of diffraction, the lowest theta angle, which copper tubes can use is 2 °. This means that the largest d-spacing that a copper tube can detect is 44.2 Å.

In this thesis XRD was carried out using the Bragg-Brentano geometry, figure 2.2 A. The sample e.g. PU clay (nano)composite, was prepared and exposed to monochromatic x-rays, if crystals or aggregates of crystals with planes orientated to satisfy Bragg's law are present, a diffracted beam will be produced. The diffracted beam of the sample was collected in the detector. By moving the x-ray detector and incident x-rays different 2θ angles were recorded producing characteristic diffraction patterns, figure 2.2 B (Askeland et al., 2011).

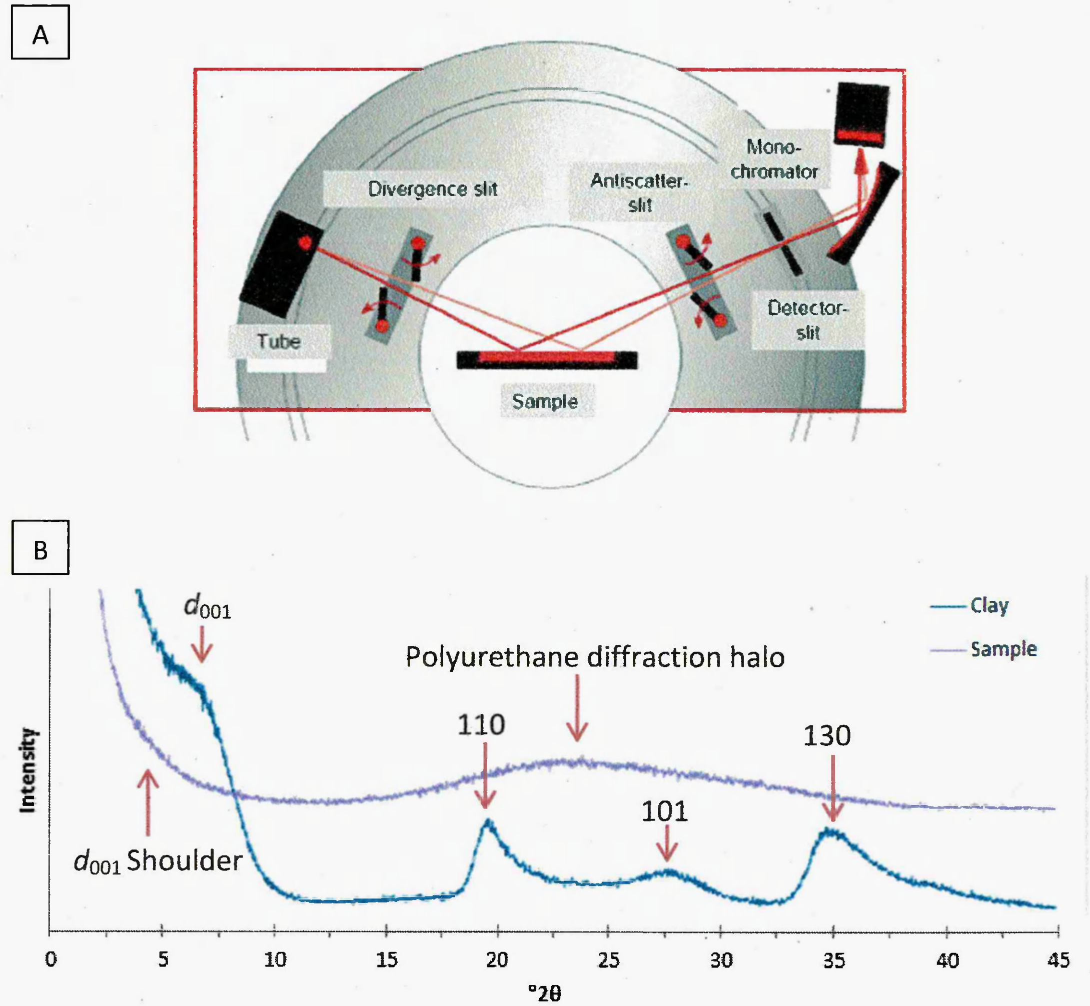

Figure 2.2: A) Diagram of a diffractometer (X-ray fluorescence analysis RoHS, 2012*)*, and B) an example of a polyurethane clay (nano)composite diffraction pattern from a Cu x-ray source. The XRD trace of the clay powder displayed peaks that correspond to the d001, 110, 101, and 130 reflections with d-spacings of 14.7, 4.7, 3.3 and 2.6 Å, respectively.

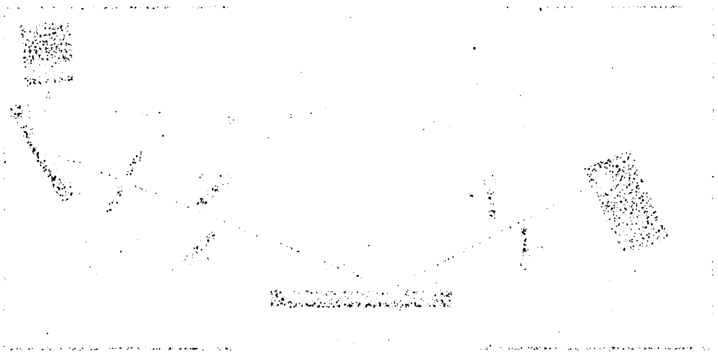

XRD is a non-destructive technique that can be conducted, typically, in a short amount of time, ca. 30 to 60 minutes per sample, on bulk, thin film or powdered materials without the need for extensive sample preparation.

When the wavelength of the x-rays is known, the diffraction pattern allows the interplanar spacing of clay to be determined, which can be used to identify the level of clay platelet dispersion within a polymer host.

2.1.2. Attenuated Total Reflectance Fourier Transfer Infrared Spectroscopy (ATR-FTIR)

2.1.2.1. ATR-FTIR Theory

The energy of a molecule can consist as translational, rotational, vibrational and electronic energy.

These energy contributions can be considered separately, with the electronic energy transitions giving rise to absorptions or emissions in the ultraviolet and visible regions of the electromagnetic spectrum, pure rotation giving rise to absorption in the microwave region or the far infrared and molecular vibrations give rise to absorption bands in most of the infrared region of the spectrum (Colthup et al., 1990).

Electromagnetic radiation is characterised by its wavelength, λ, its frequency, ν, and its wavenumber, $\bar{\nu}$, where the wavenumber is expressed as cm^{-1}. The $\bar{\nu}$ is related to other parameters by equations 2.3 and 2.4.

$$\bar{\nu} = \frac{\nu}{(c/n)}$$

Equation 2.3: The relationship between wavenumber and c, the velocity of light in a vacuum (2.998×10^{10} cm/sec), and (c/n), the velocity of light in a medium whose reflective index is n, in which the wavenumber is measured. The frequency ν is independent of the medium and is expressed in cycles per second (sec^{-1}) or Hertz (Hz) (Colthup et al., 1990).

$$\bar{\nu} = \frac{1}{\lambda}$$

Equation 2.4: The relationship between the wavenumber and the wavelength, expressed in cm.

In terms of these units, the ultraviolet, visible, infrared and microwave regions of the electromagnetic spectrum assume certain values, table 2.2 (Colthup et al., 1990).

Region	λ, cm	$\bar{\nu}$, cm^{-1}	ν, Hz
Ultraviolet (far)	1.0×10^{-6} to 2.0×10^{-5}	1×10^{6} to 50,000	3.0×10^{16} to 1.5×10^{15}
Ultraviolet (near)	2.0×10^{-5} to 3.8×10^{-5}	50,000 to 26,300	1.5×10^{15} to 7.9×10^{14}
Visible	3.8×10^{-5} to 7.8×10^{-5}	26,300 to 12,800	7.9×10^{14} to 3.8×10^{14}
Infrared (near)	7.8×10^{-5} to 2.5×10^{-4}	12,800 to 4000	3.8×10^{14} to 1.2×10^{14}
Infrared (middle)	2.5×10^{-4} to 5.0×10^{-3}	4000 to 200	1.2×10^{14} to 6.0×10^{12}
Infrared (far)	5.0×10^{-3} to 1.0×10^{-1}	200 to 10	6.0×10^{12} to 3.0×10^{11}
Microwave	1.0×10^{-1} to 1.0×10^{2}	10 to 0.01	1.0×10^{12} to 3.0×10^{8}

Table 2.2: Values for λ, $\bar{\nu}$ and ν for different regions of the electromagnetic spectrum.

In this thesis ATR-FTIR, is used to characterise polymers, polymer blends and polymer (nano)composites. FTIR is based on the Michelson interferometer and a mathematical procedure developed by Fourier which transforms the time domain to the frequency domain, figure 2.3.

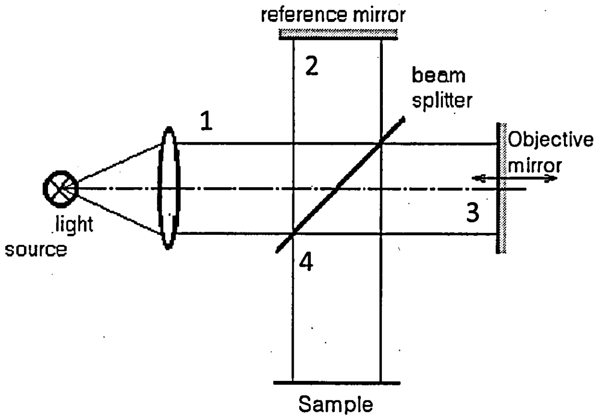

Figure 2.3: Schematic illustration of a Michelson interferometer. 1) The radiation from the light source e.g. a mercury lamp, is directed towards a beam splitter made from infrared transparent material e.g. KBr. 2) Approximately half the light is reflected by the beam splitter onto a fixed mirror, the reference mirror, that reflects it back to the beam splitter. Any light not reflected by the beam splitter continues through and impacts a continuously moving mirror, the objective mirror. 3) The light is reflected off the objective mirror, which is moving at a known velocity, back to the beam splitter where it recombines with the light reflected off the fixed mirror and back to the beam

splitter. 4) The recombined radiation is then directed to the sample and towards the detector, most commonly a liquid nitrogen cooled mercury cadmium telluride, MCT, detector.

FTIR has several advantages over the traditional dispersive techniques to record an infrared spectrum. Some of these advantages include the multiplex, Jacquinot, advantage where all frequency elements impact the detector at the same time allowing an infrared spectrum to be produced very rapidly. The throughput, Fellgett, advantage where there is no need for slits to be used, therefore the amount of radiation that impacts the sample and therefore the detector is high, this decreases the noise to signal ratio. The laser reference, Connes, advantage this is derived from the sampling method, where the time interval at which information is sampled is determined by utilising a laser with a fixed wavelength, typically 632.8 nm. This allows the averaging of scans to reduce the noise to signal ratio of the final spectrum.

A disadvantage of the FTIR system is that unwanted bands resulting from CO_2 or water vapour can appear in the spectrum unless subtraction of a spectrum of the sample compartment in the absence of a sample is carried out or the instrument is purged with a dry, infrared inactive gas such as nitrogen.

All samples characterised in this thesis are ≥0.5 mm thickness therefore transmission FTIR is unsuitable for characterisation as the IR beam will not be able to penetrate through the sample to the detector. Instead ATR-FTIR spectroscopy was utilised. ATR spectroscopy, also known as internal reflectance spectroscopy, IRS, is most commonly used to obtain the infrared spectra of solids or films (John and Loadman, 1998). This was originally described in detail by both Fahrenfort (1961) and Harrick (1963, 1965, and 1967). ATR can be achieved when the IR radiation traverses a prism so that it is internally reflected from the sample/surface interface, figure 2.4.

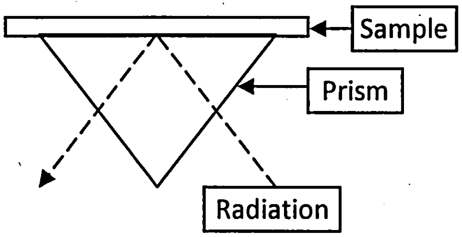

Figure 2.4: Optical diagram of the internal-reflection technique, single reflection from a prism.

Depending on the angle of incidence, θ_1, and the ratio of the indexes of refraction of the dense material, n_1, and rare material, n_2, three effects to the beam may be observed within the prism, figure 2.5.

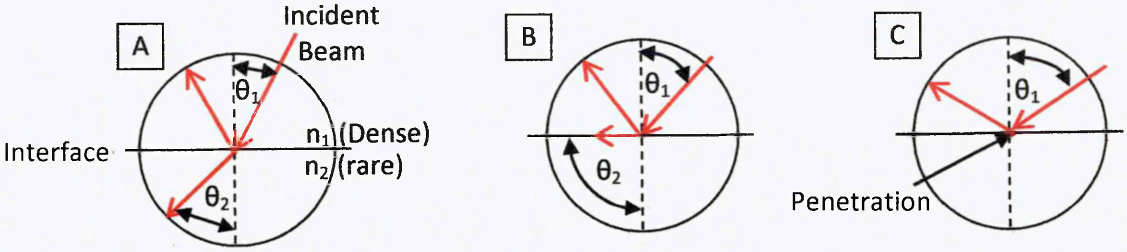

Figure 2.5: Optical diagram of the internal-reflection technique showing how reflections depend on the angle of incidence and the refraction medium. A) If $\sin\theta_1 < n_2/n_1$ some reflection will occur but the larger part of the beam will be refracted, the angle of refraction θ_2 being larger than θ_1. B) If $\sin\theta_1 = n_2/n_1$, then the angle of refraction, $\theta_2 = 90$ °, and the radiation will travel along the interface. In this case θ_1 is called the critical angle, θ_c. C) If $\sin\theta_1 > n_2/n_1$, then the angle of refraction θ_2 is imaginary and all the radiation is reflected back into the dense medium.

The condition required for total internal reflectance is displayed in figure 2.5 C. This indicates that the evanescent wave is capable of interacting with an absorbing medium just beyond the interface leading to a reduction, attenuation, of the total reflected radiation (Colthup et al., 1990).

2.1.2.2. ATR-FTIR Analysis

ATR-FTIR spectroscopy is a surface technique, unlike transmission, since the IR radiation does not penetrate through the whole sample. The sample is placed in contact with an ATR crystal, IR radiation is passed through the crystal which undergoes total reflection at the crystal/sample interface.

The evanescent wave is selectively absorbed at the surface of the sample in contact with the prism or plate providing a spectrum of a sample e.g. PU, figure 2.6. The ATR infrared intensities are equivalent to a penetration depth of a few microns e.g. 4 to 6 µm, into the substance. Due to this, sample preparation is fairly simple for many materials allowing efficient collection of spectra.

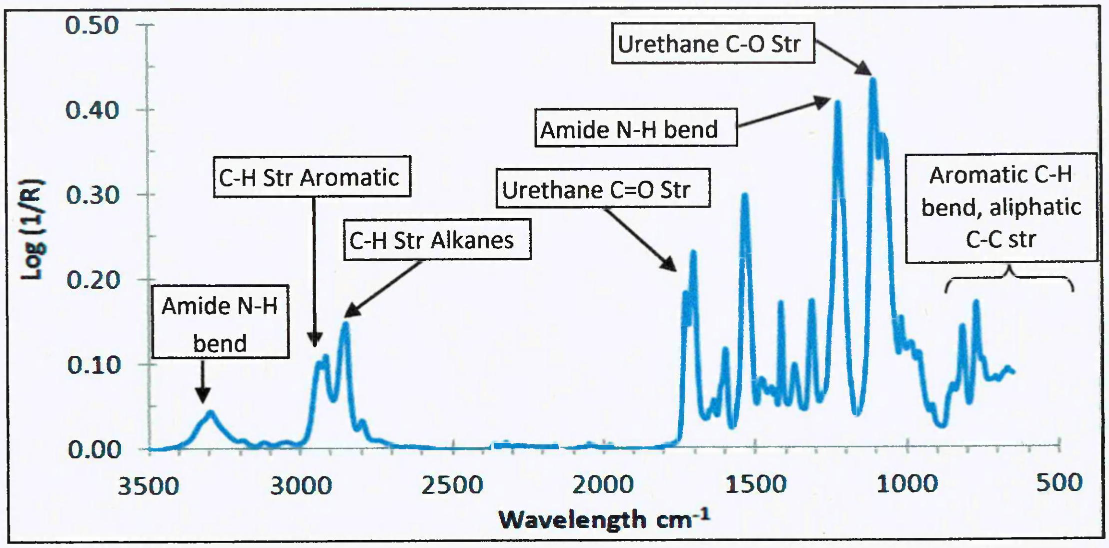

Figure 2.6: ATR-FTIR spectrum of a PU homopolymer including expected vibrational modes.

ATR-FTIR spectra are commonly presented so that the horizontal coordinate is either linear with λ or with $\bar{\nu}$. The wavenumber is often referred to as, frequency in cm^{-1}, which is understood to mean the frequency (in Hz) divided by the velocity of light (in cm/sec) or the reciprocal of the radiation wavelength (in cm) (Colthup et al., 1990).

2.1.3. Differential Scanning Calorimetry (DSC)

2.1.3.1. DSC Theory

Differential scanning calorimetry, DSC, is a technique based on monitoring the heat flux, or differential power, to the sample against time, in selected atmospheres and temperatures. Temperature is usually increased or decreased linearly or sometimes held isothermally for selected periods of time. The heat flux of a sample is typically measured by the difference in heat flux of a pan containing the sample and an empty pan. DSC is primarily used to measure the glass transition temperature, T_g, material melting temperature, T_m, crystallisation/re-crystallisation temperature, T_c, heat of fusion, ΔC_p, and heat capacity, H_C, as well as measuring reacting systems i.e. cure measurements, figure 2.7 (Hu, 2007).

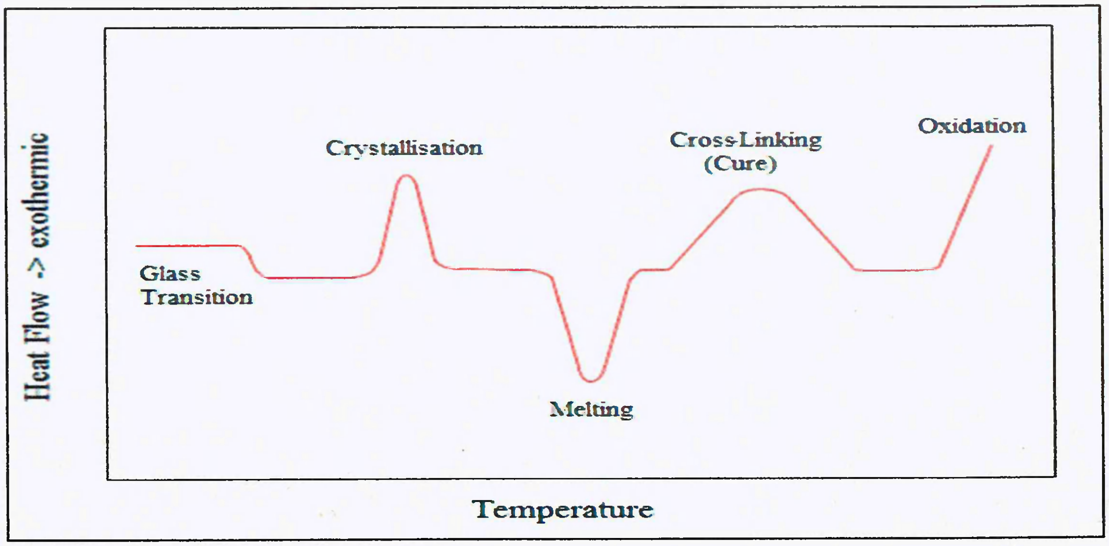

Figure 2.7: DSC thermogram depicting predicted T_g, T_c, T_m, cure measurements and oxidation/thermal stability endotherm and exotherm curves.

As all materials have a finite heating capacity, heating or cooling a sample results in a flow of heat in or out of the sample. The most common DSC measuring cells are the heat flux DSC and the power compensation approach, figure 2.8 (Shah, 1998).

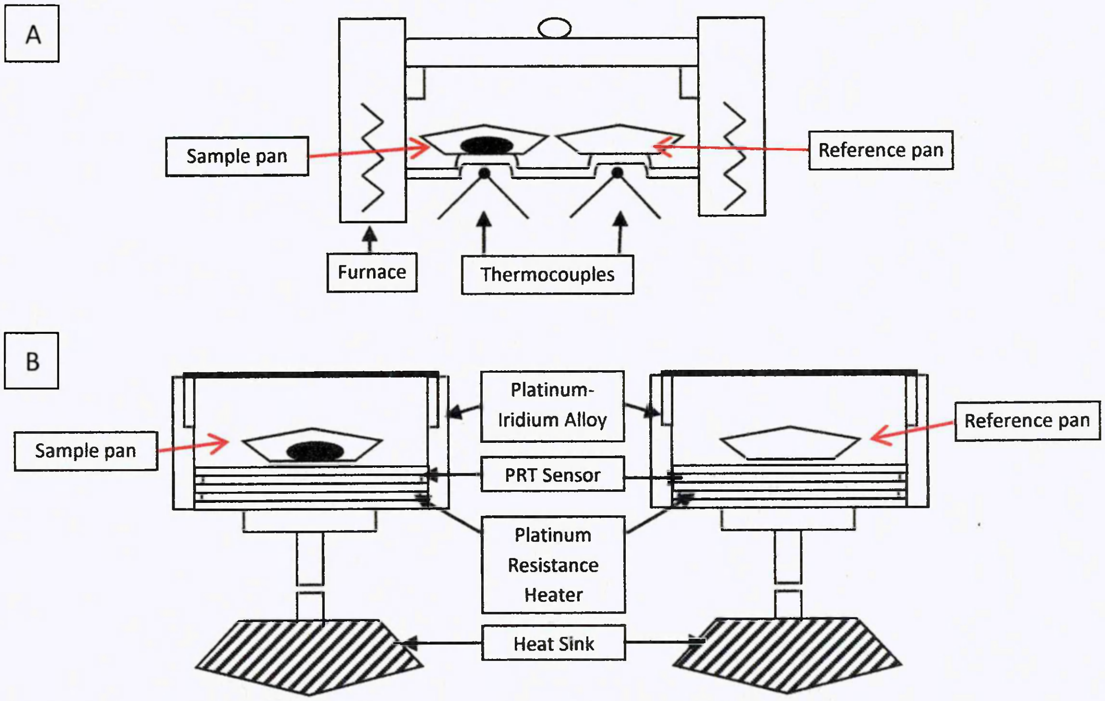
A
Sample pan
Reference pan
Furnace
Thermocouples
B
Platinum-
Iridium Alloy
Sample pan
Reference pan
PRT Sensor
Platinum
Resistance
Heater
Heat Sink

Figure 2.8: A) Heat-flux and B) power compensation DSC measuring cells.

The heat-flux DSC utilises a disk containing a sample pan and a reference pan, containing nothing, which are heated by a common furnace. Within the furnace the differential heat flow to the sample is proportional to the temperature difference that occurs between the junction of the thermocouples of both the sample and reference. The power compensation approach, used in this thesis, controls the temperature of an oven that the sample and the reference are contained in. Via amplified feedback from platinum resistance thermometers, PRT, it records the differential energy flow to maintain the sample on a specified temperature program. With both approaches the output is heat flow, normally expressed in milli-watts, watts/gram (normalised), or watts/gram-degree (specified heat units) (Nicula, 2002).

2.1.3.2. DSC Analysis

There are many experimental factors which influence the properties of interest on a DSC thermogram including whether the sample and reference pans are open or sealed, the heating rate and if dynamic or isothermal heating/cooling gradients are used, the atmosphere and flow rate, the sample holder, and the sample size and packing density. Whether the sample and reference pans are open or closed is very important when recording a DSC thermogram. If the pan is open, atmospheric interaction plays an important role in how a sample will react to heat. If the pan is sealed it improves thermal contact between the sample, pan and heating disc, reduces thermal gradients in the sample and minimalizes spillage. In this thesis the sample and reference pans were both sealed.

Depending on the type of experiment either a dynamic heating or an isothermal hold will be utilised. Dynamic heating allows the properties of a material to be discerned over a temperature range e.g. the T_g and T_m, however an isothermal experiment allows the observation of a thermal event over time e.g. sample curing at a set temperature. The heating rate affects the resolution and sensitivity of the DSC thermogram, a high heating rate causes an increase in sensitivity while a low heating rate improves resolution as there is more time to take readings between thermal events. In this thesis dynamic heating was used with a slow heating rate to ensure the difference between the actual and recorded sample temperatures are kept to a minimum.

The typical choice of purge gas used in DSC is either nitrogen or helium. The interaction of the sample and the gas involved is crucial. Nitrogen increases DSC sensitivity as it is a relatively poor thermal conductor, however helium increases DSC resolution as it is a good conductor of heat to and from the sample. In this thesis nitrogen was the sole purge gas used.

The sample holder in this thesis was made of aluminium; this was used to ensure the sample would not react with the sample container and because it would withstand the expected temperature ranges. Depth of the sample container, if open, can influence the degradation mechanism of a material. Deeper sample containers have poor purge flow over the sample therefore slowing degradation of materials. However this would not be relevant for a closed sample container, which was used in this thesis.

If large samples are used, poorly resolved thermal events may arise due to temperature gradients occurring within the sample and/or trapping of volatile materials. In order to avoid this all samples were typically cut into ca. 1x1 mm^2 squares. Packing density was maintained from sample to sample as much as possible to avoid variations in results.

2.1.4. Thermogravimetric Analysis (TGA)

2.1.4.1. TGA Theory

Thermogravimetric analysis, TGA, allows the continual recording and measurement of changes in mass of a material as a function of time at a determined temperature, or more typically over a temperature range e.g. 30 to 1000 °C, using a predetermined linear heating rate. This allows a material's thermal stability to be assessed, and also allows the volatility of a given material to be observed.

A TGA instrument, figure 2.9, is essentially a microbalance, where a sample, contained in a refractory crucible, is placed on a sample platform, which is linked to the microbalance, and then surrounded by a furnace. As the mass of a sample changes, either loss or gain caused by e.g. evaporation, decomposition, gas absorption, desorption and dehydration, it is recorded by a computer which plots the sample weight against a function of time, for isothermal studies, or as a function of temperature, for experiments using a linear heating rate (Ramachandran et al., 2002).

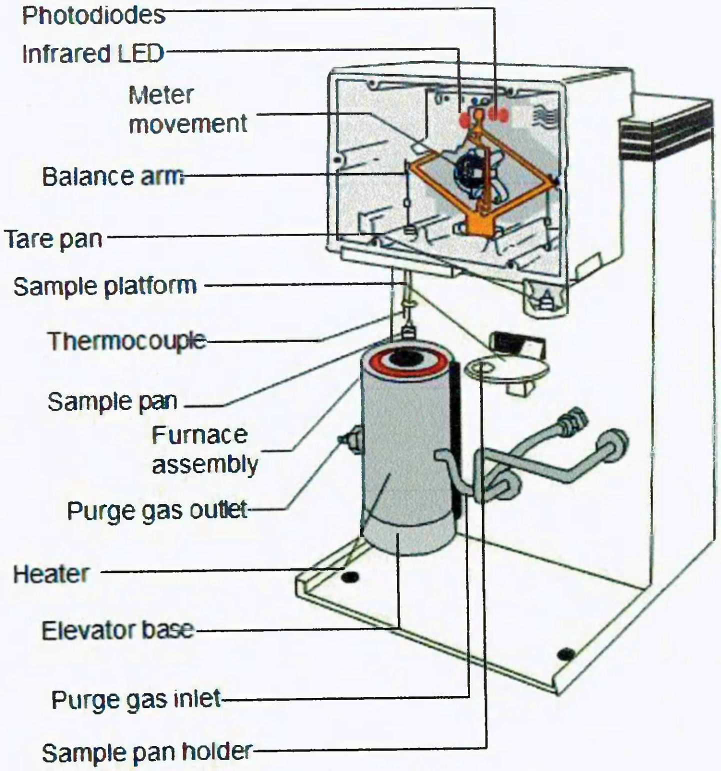
Photodiodes
Infrared LED
Meter movement
Balance arm
Tare pan
Sample platform
Thermocouple
Sample pan
Furnace assembly
Purge gas outlet
Heater
Elevator base
Purge gas inlet
Sample pan holder

Figure 2.9: Diagram of a TGA instrument (Mohomed, 2007).

TGA is very useful for determining the composition of materials and to predict their thermal stability at elevated temperatures e.g. 1000 °C. However, with certain experimental procedures, additional information about the kinetics of decomposition and in-use lifetime predictions can be obtained.

2.1.4.2. TGA Process

A weight loss a TGA thermogram or TG weight loss curve, figure 2.10 A, can be produced from a sample e.g. polyurethane, allowing the determination of a material's thermal stability e.g. degradation onset temperature, the temperature at which 5 wt% of the sample has been degraded, and 50% degradation temperature. As subtle weight changes in a TG curve are often hard to distinguish an alternative representation is regularly used, which denotes the negative 1st derivative of the TG weight loss curve i.e. the derivative thermogram, DTG, figure 2.10 B.

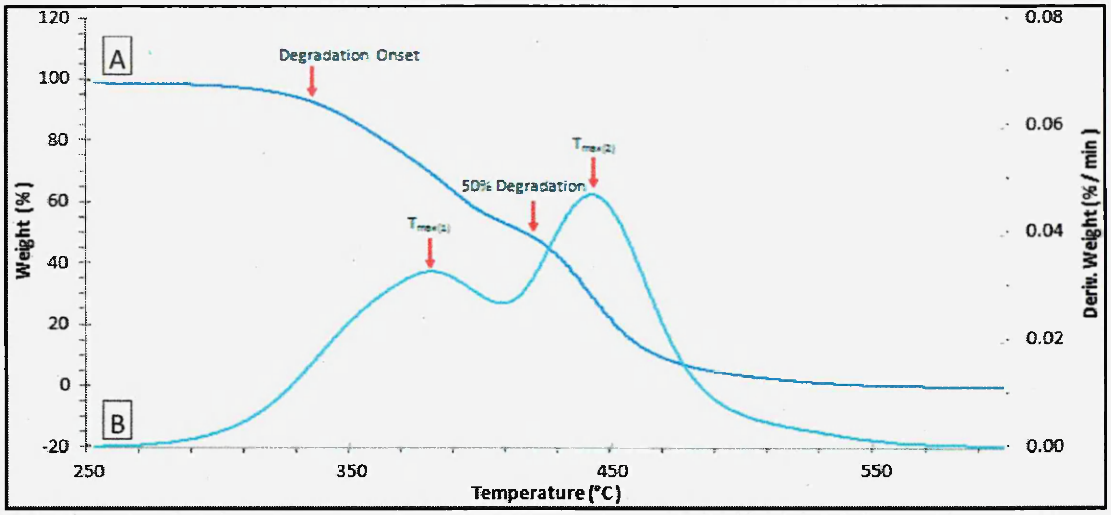

Figure 2.10: Typical decomposition of a thermoplastic PU using a linear heating rate of 5 °C per minute, from 250 °C to 600 °C. A) TG weight loss curve, displaying degradation onset temperature, the temperature at which 5 wt% of the sample has been degraded, and 50 % degradation temperature and B) DTG curve, displaying two decomposition stages, $T_{max(1)}$ and $T_{max(2)}$.

There are many experimental factors which influence the shape of the TG curve and therefore the DTG, these include the heating rate, the sample holder, the sample size and packing density and the atmosphere and flow rate.

The heating rate affects the resolution of the TG curve, a decrease in resolution is observed when the difference between the sample's actual and recorded temperature increases e.g. due to a thermal gradient developing within the sample. In this thesis a standard slow heating rate is used to ensure the difference between the actual and recorded sample temperatures are kept to a minimum.

The sample holder in this thesis was made of alumina, this was used to ensure the sample would not react with the sample container. Depth of the sample holder can influence the degradation mechanism. Deeper crucibles have poor purge flow over the sample therefore slowing degradation. The same crucible was used for each experiment; this ensured that depth of the sample holder had no effect.

As with DSC, large samples are used, poorly resolved thermal events may arise due to temperature gradients occurring within the sample and/or trapping of volatile materials. In order to avoid this all samples were typically cut into ca. 1x1 mm^2 squares. Sample packing density was maintained from sample to sample as much as possible to avoid variations in results.

The type of reaction a sample will undergo is very dependent on the choice of purge gas. In this thesis nitrogen was the sole purge gas used. The interaction of the sample with the gas involved is crucial. In an inert nitrogen atmosphere heating the sample will lead to a pyrolysis reaction whereas in an oxygen atmosphere (air) oxidation is more likely to occur. If the flow rate of the purge gas is low a rich atmosphere of decomposition products is likely to form over the sample, this may cause a delay for further decomposition of the sample as it is heated to higher temperatures. This is known as the Le Chatelier's principle, equation 2.5.

$$\mathbf{A}_{(solid)} \rightleftarrows \mathbf{B}_{(solid)} + \mathbf{C}_{(gas)}$$

Equation 2.5: Equilibrium of decomposition of a solid sample to a gas.

When there is an excess of C a decomposition rich atmosphere will exist, here the equilibrium will shift to the left, therefore reducing the decomposition of A to balance the equilibrium. Therefore having a fast flow rate is advantageous, removing the reaction products upon release therefore limits reducing the decomposition rate.

2.1.5. Dynamic Mechanical Analysis (DMA)

2.1.5.1. DMA Theory

Dynamic mechanical analysis, DMA, figure 2.11 A, is often utilised to assess how a material behaves in a specific application. The principles are based on applying an oscillating force to a sample and analysing the material's response to that force, figure 2.11 B. The sample is subjected to a controlled stress or strain. For a known stress the sample will deform a certain amount. In DMA the oscillating force applied is sinusoidal. The force motor generates an oscillating sinusoidal force which is transmitted to the sample via the drive shaft, the applied stress on the sample generates a sinusoidal strain curve. Measuring amplitude of the sine wave and the lag between the stress and strain sine waves of the material response, means that the modulus, viscosity and damping of a sample can be calculated, figure 2.11 B (Perkin-Elmer, 2008).

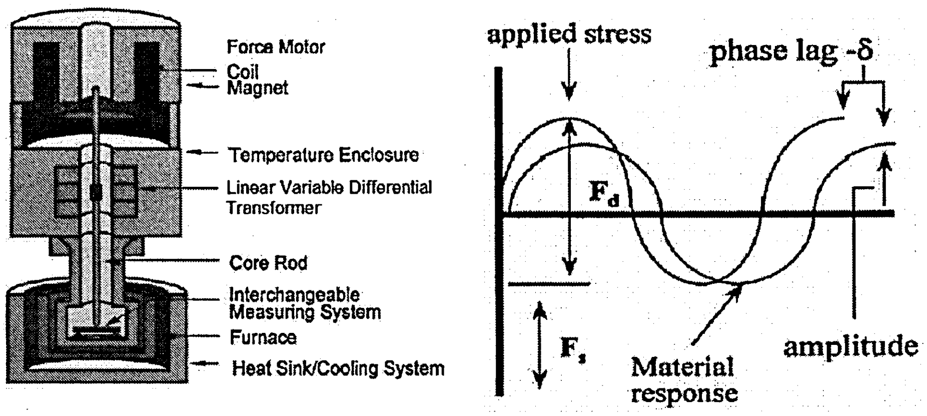
Force Motor
Coil
Magnet
Temperature Enclosure
Linear Variable Differential Transformer
Core Rod
Interchangeable Measuring System
Furnace
Heat Sink/Cooling System
applied stress
phase lag -δ
F_d
F_s
Material response
amplitude

Figure 2.11: A) Schematic of a typical DMA and B) example of a sinusoidal oscillatory force curve and the material response sine curve when a material is analysed with DMA. F_d = dynamic or oscillatory force, F_s = static or clamping force (Perkin-Elmer, 2008).

The modulus measured by DMA is separated into two distinct types, storage modulus and loss modulus. The storage modulus is a measure of the amount of energy stored in a material, representing the elasticity/stiffness. The loss modulus is a measure of how applied energy dissipates through heat which represents the viscous portion of the material.

DMA records modulus values for a material each time a sine wave is applied, this allows the modulus to be recorded over a selected temperature range e.g. -150 to 400 °C, at a linear heating rate or as isothermal holds. Selected frequency ranges e.g. 0.01 to 100 Hz range, can also be run, e.g. an experiment could be programmed to run at 1 Hz which would record a modulus result every 1 cycle/second over a varying temperature range with a heating rate of 10 °C/min, therefore the temperature change during each sine wave cycle is not significant (Menard, 1999).

Modulus measured during DMA is not the same as the typical Young's modulus which is purely a measure of a materials stiffness that can be calculated from a stress-strain curve in the initial linear region, figure 2.12.

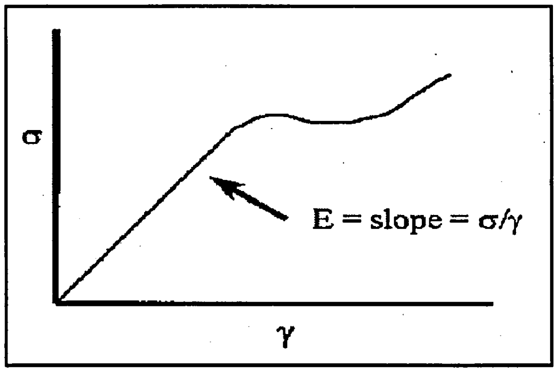

Figure 2.12: Example of standard stress-strain curve of a polymeric material. The initial part of the stress-strain curve is used to calculate Young's modulus. E = modulus.

The DMA modulus, rather than Young's modulus, provides better characterisation of a material's ability to store energy, E', to lose energy, E", and shows the ratio of these effects, tan δ, which allows the damping to be observed. Modulus values change with temperature and the transitions e.g. T_g and T_m, can be viewed as changes in the E' or tan delta curves. Other subtler changes can also be viewed if samples are analysed in the appropriate temperature region e.g. $T_g\delta$, $T_g\gamma$ and $T_g\beta$. An idealized scan of various DMA transitions is presented in figure 2.13 (Menard, 1999).

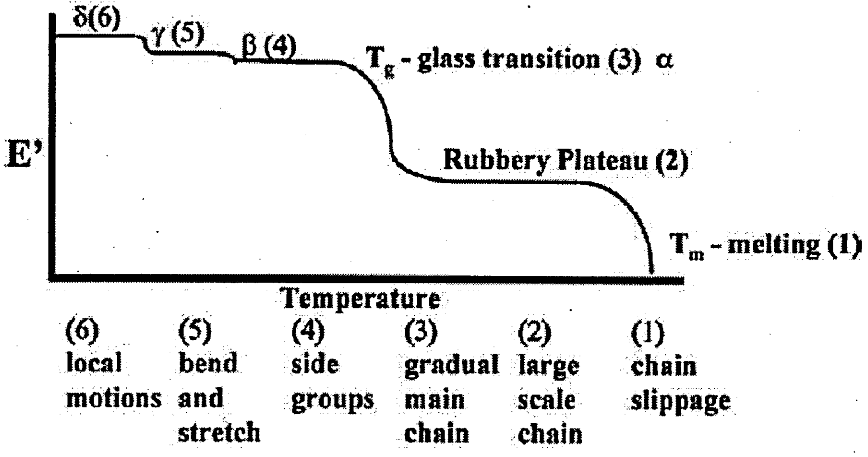

Figure 2.13: Idealized DMA scan depicting the effect of various molecular relaxations on the storage modulus, *E'*, curve (Perkin-Elmer, 2008).

With the information collected from the DMA, figure 2.13, a material's operating range can be determined e.g. for polyethylene terephthalate, PET, the range between $T_g\alpha$ and $T_g\beta$, the material possesses the stiffness to resist deformation, whereas above the $T_g\beta$ transition it has the flexibility not to shatter under strain.

2.1.5.2. DMA Process

In order to achieve good data collection there are several guidelines to follow. One of the most important is to properly calibrate the instrument; this involves calibrating both the temperature and applied force. The sample needs to be prepared suitably with reasonable aspect dimensions, e.g. the sample should have parallel sides with an even thickness throughout. Using the correct DMA geometry for the sample is also essential, this is primarily dictated by the information desired from the sample e.g. flexibility or tensile strength. Another important factor to consider is the samples physical state at the beginning of an experiment. The experiment that needs to be run and the difficulty of sample loading are also major factors. The major geometries that can typically be used in DMA include 3-point bending, single cantilever, dual cantilever, tension, compression and shear geometries, table 2.3.

Sample Modulus, Pa	Preferred Geometry	Sample Thickness, mm	Free Length, mm	Ideal Heating / Cooling rate, °C/min
10^{10} to 10^{6}	Tension	<0.02	2	5
10^{10} to 10^{6}	Tension	0.02 to 1	2 to 10	5
10^{10} to 10^{6}	Single cantilever	1 to 2	5 to 10	3
10^{10} to 10^{6}	Single cantilever	2 to 4	10 to 15	2
10^{10} to 10^{6}	Single cantilever	>4	15 to 20	1
10^{10} to 10^{6}	Dual cantilever	2 to 4	10 to 15	2
10^{12} to 10^{8}	3-point bending	1 to 3	10 to 20	3
10^{11} to 10^{7}	3-point bending	>4	15 to 20	2
10^{7} to 10^{2}	Simple shear	0.5 to 2	5 to 10	≤2
10^{7} to 10^{2}	Compression	0.5 to 10	5 to 10	≤2

Table 2.3: Preferred geometry for indicated sample sizes (Perkin-Elmer inc., 2008).

Other considerations, as indicated by table 2.3, are that reasonable strains and heating rates should be applied to the sample when performing DMA. In general, and assuming the correct geometry for the sample, a deformation or pre-strain of 50 μm and a heating rate of 2 to 3 °C per minute should ensure good data collection.

In this thesis DMA was carried out in tension mode using a Perkin-Elmer DMA8000, a schematic of which is shown in figure 2.14 A. The sample e.g. poly(tert-butyl acrylate), figure 2.14 B, was prepared, placed into the tension geometry, subjected to cooling and then heated in order to view its molecular relaxations.

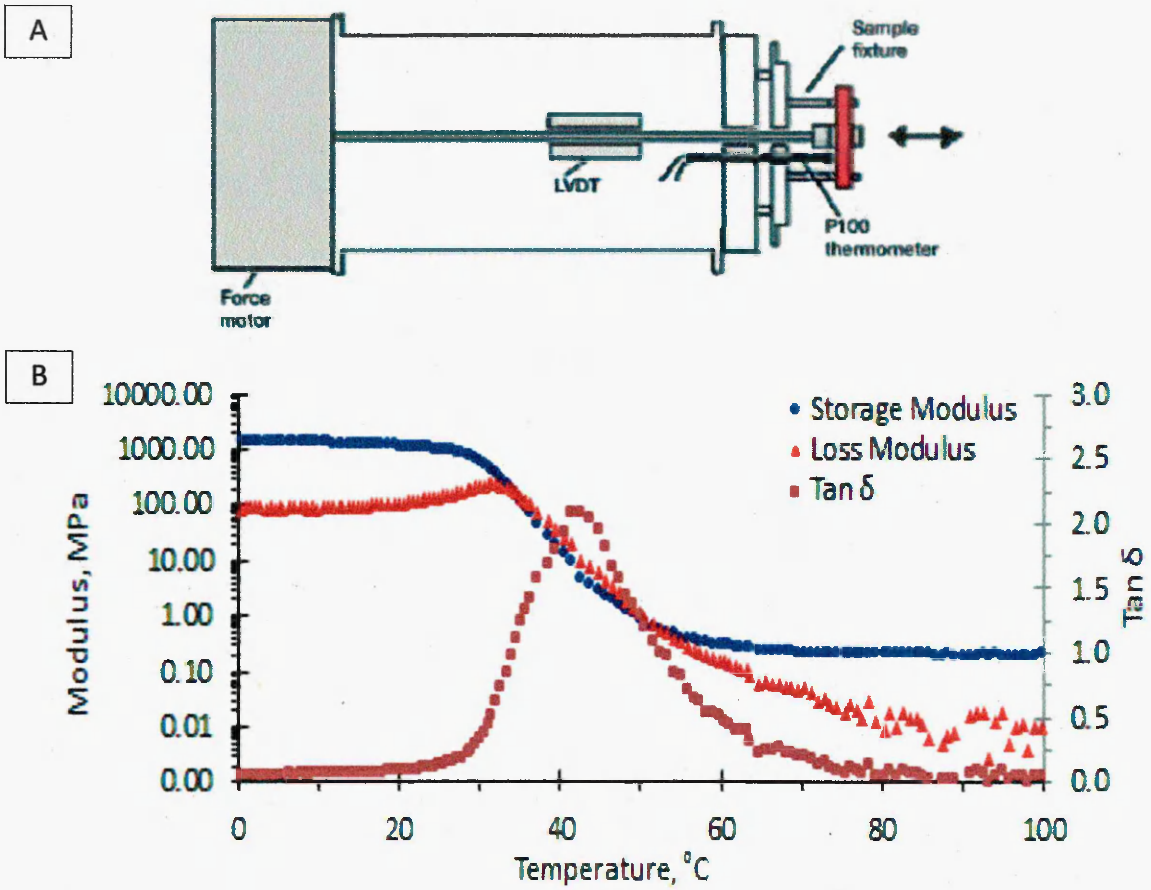

Figure 2.14: A) Schematic of the DMA8000 and B) an example a DMA scan, run in tension geometry, of poly(tert-butyl acrylate) showing storage and loss modulus with tan δ.

DMA is a very sensitive technique capable of detecting faint transitions, i.e. T_γ and T_β, these are often missed by other techniques such as DSC and thermomechanical analysers. Therefore this sensitivity allows the DMA to characterise materials to a greater extent, including highly cross-linked thermosets or thin polymer coatings (Menard, 1999).

2.1.6. Shape Memory Effect (SME)

2.1.6.1. Evaluation of the Unconstrained SME Theory

In order to characterise the macroscopic shape memory properties of a polymer, a set of parameters which can define the whole shape memory process are required including the shape fixity, R_f, shape recovery, R_r and shape recovery rate at a set temperature, $R_r(T)$, (section 1.4, equation 1.6).

In order to evaluate a polymer for shape memory ability the shape memory bending test, (section 1.4.2), is typically utilised as it requires no specialised equipment, figure 2.15.

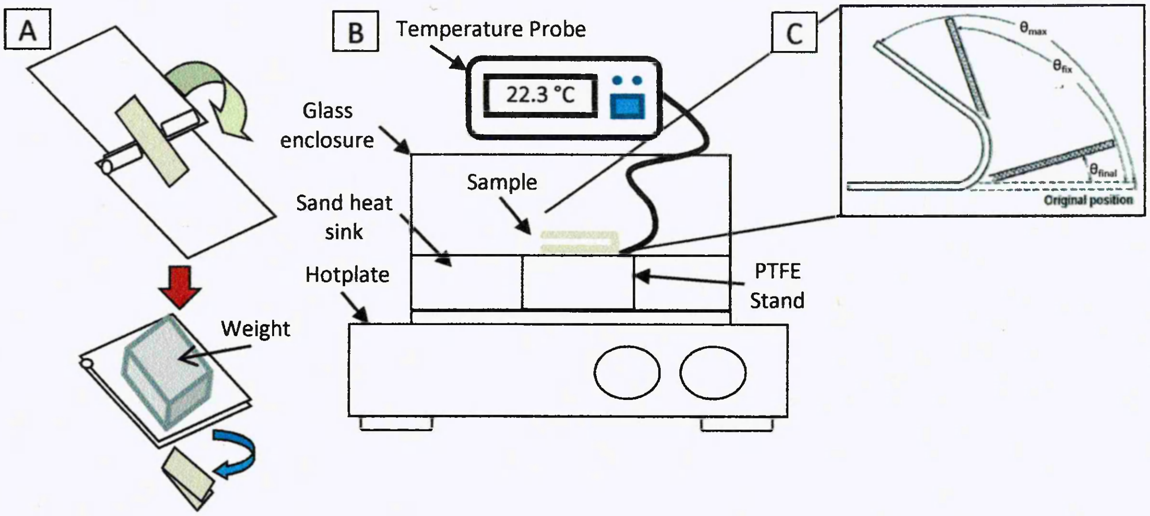
A
B
Temperature Probe
22.3 °C
C
Glass enclosure
Sample
Sand heat sink
Hotplate
Weight
PTFE Stand
θ_{max}
θ_{fix}
θ_{final}
Original position

Figure 2.15: A) Schematic of deformation device, B) schematic of a customised SME evaluation platform and C) SME of a SMP. 1) Sample is heated and deformed to a temporary shape using an external force, which applies a fixed compression stress. 2) The sample is fixed into temporary shape by rapid cooling in a fridge, 3±2 °C, while the external force is maintained. 3) The external force is removed and the sample is assessed for R_f, 4) the sample is placed in the SME chamber at a fixed temperature and $R_r(T)$ is recorded over time (Lin and Wu, 1992).

2.1.6.2. Evaluation of the Unconstrained SME Analysis

With the SME evaluation data a shape memory recovery graph can be plotted, figure 2.16, allowing a comparison of the SME with that of other SMP.

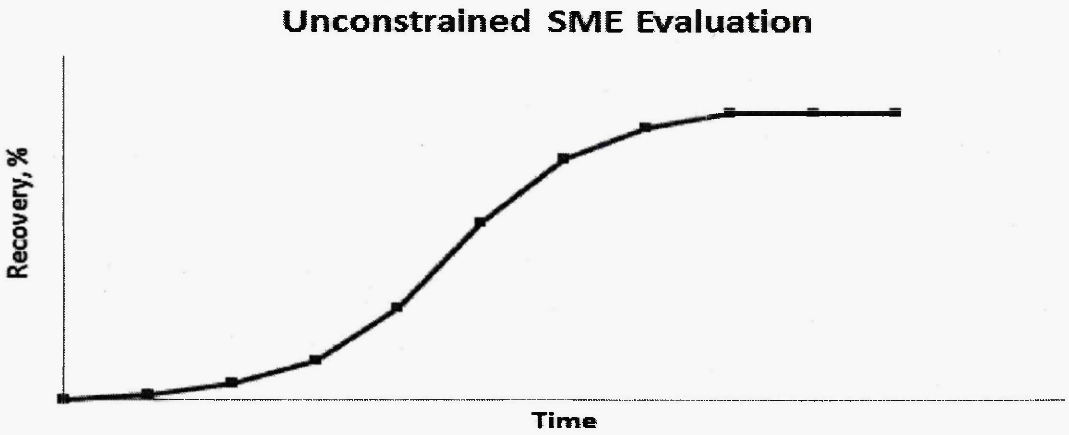

Figure 2.16: Typical unconstrained SME recovery graph. Recovery is measured in percentage, starting at 0 % and potentially finishing at 100% over the given time period.

In order to evaluate coated substrates, a variation on the standard bending test was introduced (Lin and Wu, 1992). The sample was cut to a specific shape, with slits in set positions, figure 2.17 A. A rod is inserted between the slits to exert the external force that deforms the sample to its temporary shape, this maintains a set amount of stretching stress, figure 2.17 B. After deformation the rod is removed and SME evaluation is carried out as above using a modified stand within the glass enclosure of the SME evaluation platform, figure 2.17 C.

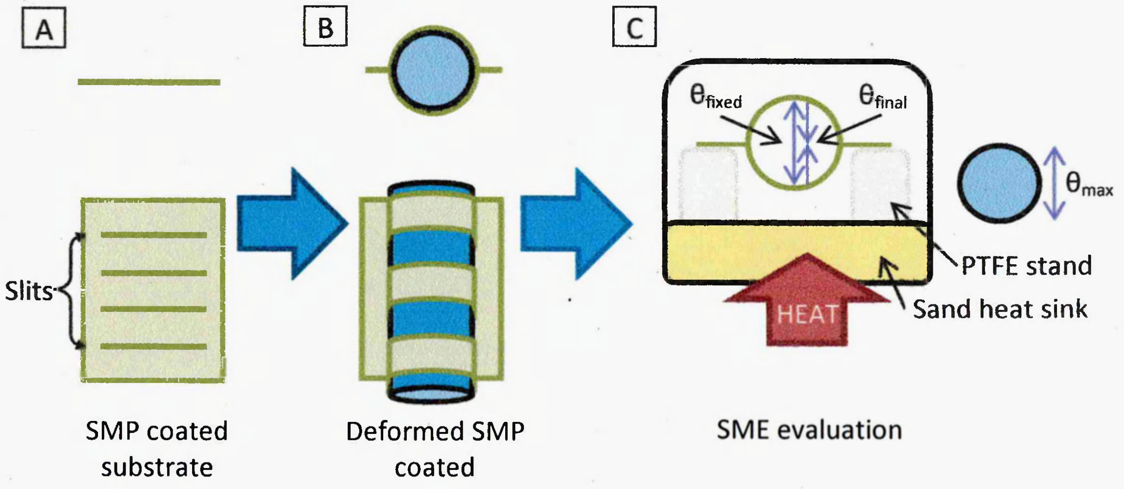
A
B
C
Slits
θ_{fixed}
θ_{final}
θ_{max}
PTFE stand
Sand heat sink
HEAT
SMP coated substrate
Deformed SMP coated
SME evaluation

Figure 2.17: Schematic of alternate deformation method from standard bending test.

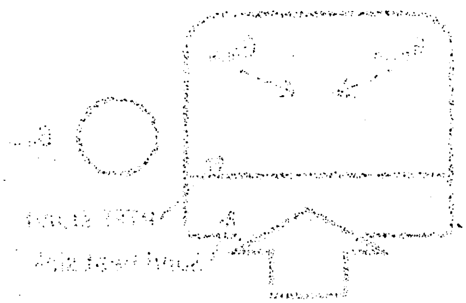

C

B

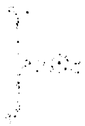

A

2.2. References

ASKELAND, D.R., FULAY, P.P., and WRIGHT, W.J., 2011. The Science and Engineering of Materials. 6th Ed., Canada: Global Engineering.

COLTHUP N.B., DALY L.H., and WIBERLEY S.E., 1990. Introduction to infrared and Raman spectroscopy. 3rd Ed., London: Academic Press Inc.

HU J.L., 2007. Shape memory polymers and textiles. Cambridge: Woodhead publishing limited.

JOHN, M., and LOADMAN, R., 1998. Analysis of rubber and rubber-like polymers. 4th Ed., Netherlands: Kluwer Academic Publishers.

LIN, H. C. and WU, S. K., 1992. Strengthening effect on shape recovery characteristic of the equiatomic tini alloy. Scripta metallurgica et materialia, 26 (1), 59-62.

MENARD, K.P., 1999. Dynamic Mechanical Analysis, A Practical Introduction. London: CRC Press.

MOHOMED K., 2007. Thermogravimetric Analysis, Theory, Operation, Calibration and Data Interpretation. New Castle, DE 19720: TA Instruments.

NICULA. R., 2002. Introduction to Differential Scanning Calorimetry. [online] Rostock University, Last accessed 09 January 2012: http://wwwswt.informatik.uni-rostock.de/englisch/projekte/Physik2000/ExperimentII/ta2web001.pdf

PERKIN-ELMER INC., 2008. Introduction to Dynamic Mechanical Analysis (DMA). Waltham: PerkinElmer Inc.

RAMACHANDRAN, V.S., PAROLI, R.M., BEAUDOIN, J.J., and DELGADO, A.H., 2002. Handbook of Thermal Analysis of Construction Materials. Norwich, NY: Noyes Publications/William Andrew Publishing.

SAUERBRUNN, S., and GILL, P., 2002. Decomposition Kinetics using TGA. New Castle, DE 19720. TA Instruments.

SHAH V., 1998. Handbook of Plastics Testing Technology book. 2nd ed. New York (NY): John Wiley & Sons, Inc.

FAHRENFORT, J., 1961. Attenuated total reflection - A new principal for the production of useful infra-red reflection spectra of organic compounds. Spectrochim. Acta 17, 698-709.

HARRICK, N. J., 1963. Total internal reflection and its application to surface studies. Annals of the New York Academy of Sciences, 101: 928–959.

HARRICK, N. J., 1965. Electric Field Strengths at Totally Reflecting Interfaces. J. Opt. Soc. Am. 55: 851-856.

HARRICK, N. J., 1967. Internal Reflection Spectroscopy, 327 pp. Wiley, New York.

X-RAY FLUORESCENCE ANALYSIS ROHS - terrachem analytical laboratory - X-ray diffraction analysis (XRD) [online]. Last accessed 14/04/2012 2012 at: http://www.terrachem.de/roentgenbeugungsanalyse.php?language=en.

Chapter 3: Evaluation of tert-Butyl Acrylate as Potential Packaging SMP

3. Introduction

As SME can occur in both physically cross-linked thermoplastic based polymers and in chemically cross-linked thermoset based polymers (Liu et al., 2007). An attractive SMP system would be thermoset based because these SMP are chemically cross-linked, and the bonds between individual polymer chains allow them to commonly achieve full shape recovery at high strains over all temperature ranges between the T_g and combustion. These are therefore favoured over thermoplastic SMP when an application requires complete shape memory recovery i.e. fully recoverable permanent shape at high strains (Voit et al., 2010). Some specific materials include epoxies (Gall et al., 2002) and acrylates (Yang et al., 2007)

Acrylate polymers represent an ideal system for a SMP packaging solution as they have highly tuneable thermomechanical properties and can be tailored specifically for recoverable strain capacity (Voit et al., 2010). This tuneable ability of acrylate properties comes from the cross-linked polymer chains. These crosslinks have been shown to greatly influence the physical and mechanical properties of polymers, demonstrating enhanced creep resistance, improved dimensional stability, increased thermal stability, increased mechanical strength, and increased resistance to solvent absorption compared with linear polymers without crosslinks (Ortega et al., 2008).

When copolymerizing different acrylate monomers, small compositional changes exert a large effect on mechanical properties, including elastic modulus, strain-to-failure, T_g, brittleness at ambient temperatures, and percentage deformation in the rubbery regime. Copolymerizing linear acrylates (mono-functional monomers) with cross-linking acrylates (multifunctional monomers) yields SMP with tuneable properties that can be optimized for very specific applications (Voit et al., 2010).

In order to form a chemically cross-linked SMP network the type of curing method has to be considered. For acrylate type polymers there are two common routes, thermal polymerisation, figure 3.1, and photopolymerisation, figure 3.2.

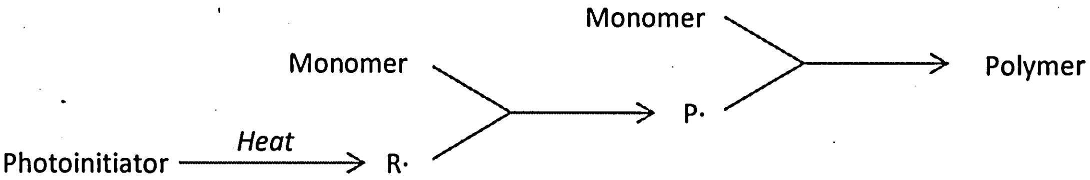

Figure 3.1: Schematic representation of thermal polymerisation, where R· = initiator radical and P· = polymer radical.

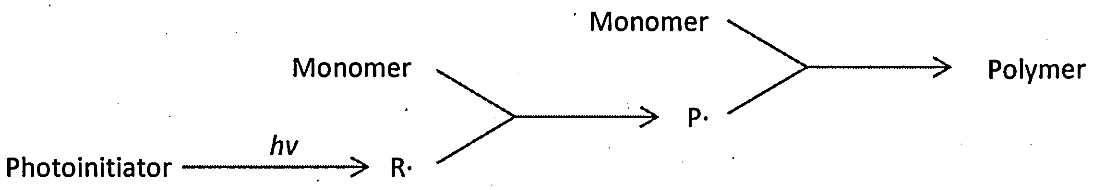

Figure 3.2: Schematic representation of photopolymerisation, where R· = initiator radical and P· = polymer radical.

Photopolymerisation of mono- and multifunctional monomers as a means to create network polymers is of increasing interest due to the many advantages over thermal polymerisation such as spatial and temporal control, reaction speed, and the possibility of ex-vivo or in-situ polymerization for biomedical applications (Ortega et al., 2008). Photopolymerisation has also been historically used in thin film coating applications potentially making it an ideal choice to fulfil the aim of this research e.g. producing a coherent SMP layer on top of thin board or paper for a packaging application (Ortega et al., 2008).

Thermoset SMP typically recover all of the applied strain stored in them, however they often have lower failure strains than thermoplastics. In terms of high-strain capacity, the ideal SMP material may exist at the boundary of a thermoset and thermoplastic based system, where the number of cross-links is small enough to facilitate large strain-to-failure, but high enough to achieve full recovery of the permanent shape (Voit et al., 2010).

In order to form a suitable SMP packaging solution an experimental investigation of the shape memory ability of tert-butyl acrylate, tBA, figure 3.3 A, and poly(ethylene glycol dimethacrylate), PEGDMA, figure 3.3 B, based polymers was carried out. Studies on tBA cross-linked with PEGDMA have been previously reported by Yang et al., (2007), Yakacki et al., (2007) and Ortega et al., (2008). It was found that tBA-co-PEGDMA fully polymerised networks have shape memory ability, are easily produced and the thermal and mechanical properties are readily tailored. The mono-acrylate and ethylene glycol based polymers also have a proven history in biomedical applications (Behl and Lendlein, 2007) which is attractive for food contact applications (Yang et al., 2007).

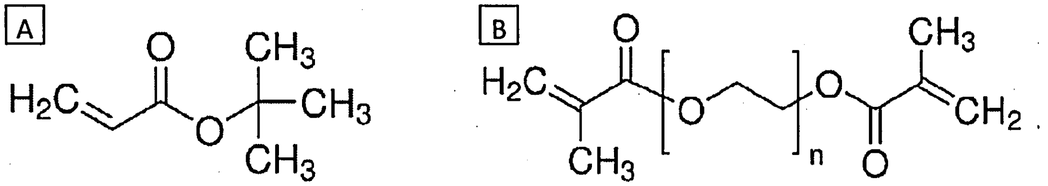

Figure 3.3: Chemical structure of A) tBA and B) PEGDMA

The thermo-mechanical properties of acrylates i.e. methacrylate networks, can be tailored (Yakacki et al., 2008). The T_g and rubbery modulus can be varied independently of each other by varying the cross-link density, where the T_g primarily controls the free strain recovery time and rubbery modulus primarily controls the recovery stress produced (Safranski et al., 2008). Therefore considering the way the cross-link density of the acrylate polymer network affects the properties, the objective in this section is to establish the most suitable composition ratio of tBA to PEGDMA for use as a thermally stable SMP packaging solution. A series of tBA-co-PEGDMA networks were produced in order to determine the most suitable ratio. The cross-linked polymer network properties including storage and loss modulus, tan δ, thermal stability, and SME were determined and analysed.

3.1. Experimental

All characterisation methods were carried out at the Materials and Engineering Research Institute, MERI, at Sheffield Hallam University.

3.1.1. Materials

The mono-functional acrylate tBA, the di-functional acrylate PEGDMA, with an average molecular weight of 750 g mol^{-1} for the poly(ethylene glycol) portion, the photoinitiator 2,2-dimethoxy-2-phenylacetophenone, DMPA, and ethyl-4-(dimethylamino) benzoate, EDB, were purchased from Sigma-Aldrich and used as received. The purity of tBA was 98%, while the purities of the other reagents were greater than or equal to 99%. The initial inhibitors from the tBA and PEGDMA were not removed in order to prevent any curing occurring during the mixing of the liquid monomers and the photoinitiators. The Cloisite 10A, C10A, a C10A montmorillonite in which Na$^+$ has been replaced by dimethyl, benzyl, hydrogenated tallow quaternary ammonium, was supplied from Rockwood Specialties Inc. (2009). The substrates 100 µm thick polyethylene terephthalate, PET, were supplied by HiFi films ltd (2010) and 60 µm thick Sulpak paper was supplied by Dr David Guemi, CTP.

3.1.2. C10A Clay Washing

C10A was washed prior to use in order to remove any residual contaminants. The clay was dispersed in water and heated to 80 °C while being stirred for 1 hr. The clay and water mixture was cooled to room temperature. The clay and water mixture was filtered using a Buchner funnel and washed with isopropanol. The clay was washed and filtered a further 7 times, and finally dried in an oven at 70 °C.

3.1.3. Sample Preparation

3.1.3.1. tBA-co-PEGDMA

For this study a series of polymer networks were formed by varying ratios of tBA and PEGDMA monomers, table 3.1. In order to effectively and uniformly blend tBA and PEGDMA to form comonomer solutions, the tBA, PEGDMA, DMPA and EDB were weighed out and added together in a glass vial. The vial was wrapped in foil and the comonomer solution was stirred using a polytetrafluoroethylene, PTFE, coated magnetic spin-bar on a stirrer plate with a moderate stir speed (lv 6) for 30 minutes at room temperature ca. 22 °C. After this the comonomer solution, still wrapped, was placed in an ultrasound bath and sonicated for an additional 30 minutes.

Sample Description	Short Description	tBA, wt%	PEGDMA, wt%	DMPA, wt%	EDB, wt%
tBA0/PEGDMA100	t0/P100	0	100	3.5	1.5
tBA15/PEGDMA85	t15/P85	15	85	3.5	1.5
tBA60/PEGDMA40	t60/P40	60	40	3.5	1.5
tBA70/PEGDMA30	t70/P30	70	30	3.5	1.5
tBA80/PEGDMA20	t80/P20	80	20	3.5	1.5
tBA90/PEGDMA10	t90/P10	90	10	3.5	1.5
tBA100/PEGDMA0	t100/P0	100	0	3.5	1.5

Table 3.1: Comonomer solution, tBA and PEGDMA compositions, for the production of cross-linked polymer networks

3.1.3.2. tBA-co-PEGDMA C10A

The t90/P10 polymer network was used as a host for varying amounts of C10A, table 3.2. In order to effectively and uniformly blend tBA, PEGDMA and clay to form clay/comonomer solutions, the tBA, PEGDMA, DMPA, EDB and C10A were weighed out and added together in a glass vial. The vial was wrapped in foil and the clay/comonomer solution was stirred using a PTFE-coated, magnetic, spin-bar on a hot plate stirrer with a moderate stir speed (lv 6) for 24 hours at room temperature ca. 22 °C. After 24 hours the clay/comonomer solution, still wrapped, was placed in an ultrasound bath and sonicated for an additional 30 minutes (Decker et al., 2005).

Sample Description	Short Description	tBA, wt%	PEGDMA, wt%	DMPA, wt%	EDB, wt%	C10A, wt%
tBA90/PEGDMA10/C10A 0	t/P/C10A 0	90	10	3.5	1.5	0
tBA90/PEGDMA10/C10A 1	t/P/C10A 1	90	10	3.5	1.5	1
tBA90/PEGDMA10/C10A 3	t/P/C10A 3	90	10	3.5	1.5	3
tBA90/PEGDMA10/C10A 5	t/P/C10A 5	90	10	3.5	1.5	5

Table 3.2: Clay/comonomer solutions, tBA, PEGDMA and C10A compositions, for the production of cross-linked polymer nanocomposite networks.

3.1.3.3. Coated Substrate Sample Preparation

The t/P/C10A 0 to 1 networks were used to coat PET and Sulpak paper, table 3.3. The samples were prepared as in section 3.1.3.1.

Sample Description	Substrate	tBA, wt%	PEGDMA, wt%	DMPA, wt%	EDB, wt%	C10A, wt%
t/P/C10A 0 P	PET	90	10	3.5	1.5	0
t/P/C10A 0 S	Sulpak	90	10	3.5	1.5	0
t/P/C10A 1 P	PET	90	10	3.5	1.5	1
t/P/C10A 1 S	Sulpak	90	10	3.5	1.5	1

Table 3.3: Clay/comonomer solution, tBA, PEGDMA and C10A compositions, for the production of cross-linked polymer nanocomposite networks coated on to PET and Sulpak substrates.

3.1.4. Photopolymerisation Methods

In order to photopolymerise tBA-co-PEGDMA and t90/P10 C10A networks a typical photopolymerisation technique was utilised. Two glass slides, 100 x 100 x 1.0 mm^3, of ultraviolet, UV, clear glass were coated on one side each with 3M spray glue and a UV clear layer of PET film, 12 x 12 x 0.1 mm^3 was attached. The PET film acts as a non-reacting, release surface for the comonomer solution. The tBA-co-PEGDMA or t90/P10 C10A network polymer solutions were injected between the two coated glass slides, which are separated by a, pre-determined thickness, PTFE spacer and secured together with binder clips. The entire configuration was then placed into a UV chamber (model CL-1000 ultraviolet cross-linker, λ = 254 nm, output energy = 200 mJ/cm^2). The entire mould was turned every 5 minutes for ca. 30 minutes to ensure an even cure. The UV cured films were removed from the mould, stored and analysed.

In order to polymerise the t/P/C10A network polymer solution onto the substrate, the glass slide technique would not be suitable. Therefore the polymer solution was first applied to the substrate, via a brush, leaving ca. a 20 to 30 μm thick film. The coated film was placed into a nitrogen filled chamber, equipped with a UV transparent window, and the entire configuration was placed into a UV chamber (model CL-1000 ultraviolet cross-linker, λ = 254 nm, output energy = 200 mJ/cm^2) for ca. 30 min. The UV cured coated substrate was removed from the nitrogen chamber, stored and analysed.

3.1.5. Techniques

3.1.5.1. Swelling Test

Swelling tests were performed to confirm that cross-linking had occurred during the polymerization process, and to determine the ability of polymers of different monomer ratios to swell.

tBA-co-PEGDMA network sheets were cut to produce ca. 10 mm^2 samples. These samples were weighed for their initial mass, W_i, and separated into vials where they were soaked in 20 ml of propan-2-ol, a tBA homopolymer solvent. The samples were removed from the solvent periodically, dried lightly and weighed until an equilibrium, swollen, weight, W_s, was reached. The equilibrium swelling ratio, q, was calculated from the relationship, equation 3.1.

$$q = \frac{W_s}{W_i}$$

Equation 3.1: Relationship between swelled weight and initial weight.

3.1.5.2. X-Ray Diffraction

XRD, was performed to determine the extent of the C10A dispersion within the t/P/C10A 1 to 5 wt% composites.

A Philips X'Pert XRD, Cu x-ray source (λ = 1.542 Å), with a Philips Miniprop detector was used for characterisation. The sample material was cast onto a glass slide, and measured ca. 20 x 40 x 0.1 ± 0.05 mm^3. This sample was mounted onto the sample stage using a clamp, a ¼ Inch divergence slit and a ½ inch anti-scatter slit were used along with a 10 cm fixed mask. The positions of the source and detector were reset to their starting positions. The trace was collected from 5 to 40 ° 2θ, lasting 40 minutes with approximately 10,000 counts in total. The diffraction traces of the samples were recorded and analysed.

3.1.5.3. ATR-FTIR Spectroscopy

ATR-FTIR, was used to observe the vibrational modes in the polymer networks. ATR-FTIR was performed on a Nicolet, Nexus FT-IR model at room temperature. ATR-FTIR was carried out on the sample, nine spectra were collected from the top surface and nine spectra were collected from the bottom surface, from top left to bottom right on each side of each sample. There were no significant differences between the spectra taken at each point so they were combined to obtain an average spectrum for each sample which was recorded and analysed.

3.1.5.4. Thermogravimetric Analysis

TGA, was performed to observe the thermal degradation of the polymers. TGA was carried out on a Mettler TG50, with a 15-25 ml min^{-1} N_2 purge. Alumina crucibles were filled with 15$\pm$0.5 mg of the polymer networks cut into small pieces measuring approximately 1 x 1 x 0.5 mm^3. The test had a 15 minute isothermal hold at 35 °C and then a 20 °C min^{-1} ramp to 600 °C. The mass loss profile of the sample during heating was recorded and analysed.

3.1.5.5. Dynamic Mechanical Analysis

DMA, was carried out to investigate the viscoelastic properties of the polymer networks. A PerkinElmer DMA8000 model was used in tension mode, no pre-load was applied, over a temperature range of -50 to 90 °C, at frequencies of 1 and 10 Hz. The polymer network samples, 25 x 5$\pm$0.1 x 0.5 mm^3, were equilibrated at -50 °C for 3 minutes then raised to 90 °C at a 3 °C min^{-1} ramp rate. The T_g was defined as the peak of the tan δ curve. The rubbery modulus was determined from the storage modulus, when it had reached a steady state above the T_g as indicated by the unchanging tan δ curve. The 1 Hz storage modulus, loss modulus, and tan δ plots were recorded and analysed.

3.1.5.6. Unconstrained Shape Memory Effect Evaluation

Unconstrained SME testing was performed to investigate the tBA-co-PEGDMA and t/P/C10A networks shape memory ability. Unconstrained SME testing was performed on a customised platform utilising a hotplate, a glass enclosure and a temperature probe, section 2.1.6, figure 2.15. The hotplate was pre-heated to a maximum temperature, T_g +10 °C (T_{high}) of the highest network T_g. The polymer network sample, 40 x 20 x 0.5 mm^3, was placed inside the enclosure for 10 minutes to equilibrate at temperature. The sample was deformed, θ_{max}, using a 250 g steel weight and maintained at T_{high} in the glass enclosure, for an additional 5 minutes while the samples were under strain. The sample was removed from the enclosure and cooled to 3±2 °C, T_{low}, in a fridge. At T_{low} the external force was removed and the fixed deformability, θ_{Fixed}°, was recorded. The sample was placed inside the heated glass enclosure, T_{high}, and the SME recovery angles, $\theta_i(T)$, were recorded. Once the sample had finished its SME, or recovered its original shape, θ_{Final}°, was recorded. The sample was removed from the enclosure and stored. The shape memory abilities of the polymer networks were recorded and analysed.

In order to determination the unconstrained SME of the coated substrates a variant of the unconstrained SME test was followed. The standard SME test platform was used and set up as in section 2.1.6, figure 2.17. The sample t/P/C10A coated substrates, 60 x 20 x 0.01 to 0.04 mm^3, were placed inside the enclosure for 10 minutes to equilibrate at temperature and deformed using an external force, figure 2.17 B. Standard unconstrained SME testing was then carried out with $\theta_i(T)$ being recorded every 30 seconds. Once the sample had finished its SME, or recovered its original shape, θ_{Final}° was recorded. The sample was removed from the enclosure and stored. The shape memory ability of the t/P/C10A coated substrates were recorded and analysed.

3.2. tBA-co-PEGDMA Results and Discussion

3.2.1. Polymer Network Structure

3.2.1.1. Swelling Test

The swelling test data for the tBA-co-PEGDMA composites, t100/P0 to tBA0/P100, was carried out in order to assess the extent of cross-linking in the network structure, figure 3.4, with all equilibrium swelling values recorded in table 3.4.

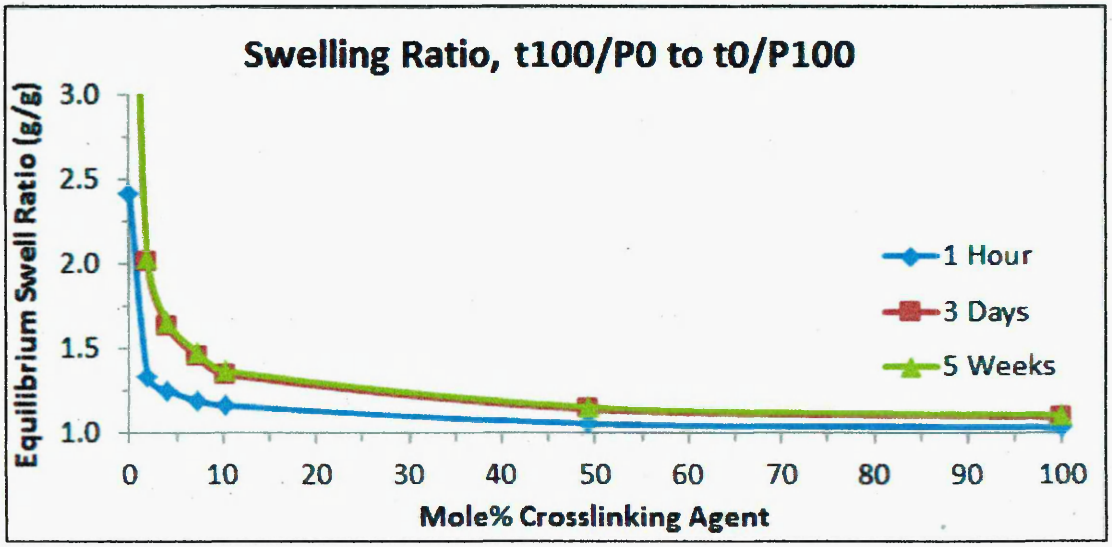

Figure 3.4: Equilibrium swelling ratios, q, of t0/P100 to t100/P0 at 1 hour, 3 days and 5 weeks

It has been established previously by Ortega et al., (2008), Smith et al., (2009) and Warren et al., (2010), that the extent to which a polymer swells in the presence of a solvent i.e. propan-2-ol, can be related to the degree of cross-linking in the network structure, with the level of the equilibrium swelling, q, decreasing with the increasing degree of cross-link density. The swelling test was used to establish the extent of cross-linking of the final polymer networks as a function of composition. It was found that the uncross-linked polymer, t100/P0, completely dissolved in propan-2-ol in a matter of hours confirming the absence of chemical cross-linking.

Sample Description	Mole % PEGDMA	q at 1 Hour	q at 3 Days	q at 5 Weeks
t100/P0	0.0	2.4	-	-
t90/P10	1.9	1.3	2.0	2.0
t80/P20	4.1	1.3	1.6	1.7
t70/P30	7.3	1.2	1.5	1.5
t60/P40	10.2	1.2	1.4	1.4
t15/P85	49.2	1.1	1.1	1.2
t0/P100	100.0	1.0	1.1	1.1

Table 3.4: Equilibrium swelling values of interest for the t100/P0 to t0/P100 networks

For networks, t90/P10 to t0/P100, the equilibrium swelling ratios, q, in propan-2-ol decrease as the amount of cross-linking agent increases. This is attributed to the cross-links not allowing the structure to swell as they act as physical restraints on the polymer network. Thus also stopping the tBA segment of the network from dissolving. However an alternative theory is that as PEGDMA becomes the dominant network constituent, it will not swell in propan-2-ol as it does not dissolve in that solvent, therefore it will not swell to a significant degree. Gall et al., (2005) also reported this trend, finding that as the amount of cross-linker increased the degree of swelling was reduced.

The q values as a function of time show that the majority of the swelling occurs quickly, as seen by the results at 1 hour where each network had begun to swell. Between 1 hour and 3 days of swelling a saturation point was reached, as seen by the overlapping results of 3 days and 5 weeks where there is very little difference in q compared to the large difference in time. The equilibrium swelling results overall suggest that all the polymer networks, except t100/P0, are cross-linked which agrees with the results of other research groups including Smith et al., (2009), Warren et al., (2010) and are very similar to the results of Ortega et al., (2008) who were also swelling tBA-co-PEGDMA networks.

3.2.1.2. ATR-FTIR Spectroscopy

ATR-FTIR spectra, 700 to 3500 cm^{-1}, of the t100/P0 to t0/P100 networks are presented in figure 3.5. This work was carried out to confirm that the polymer networks were fully polymerised and to study the effects of increasing PEGDMA, and therefore the cross-linking density on the polymer networks.

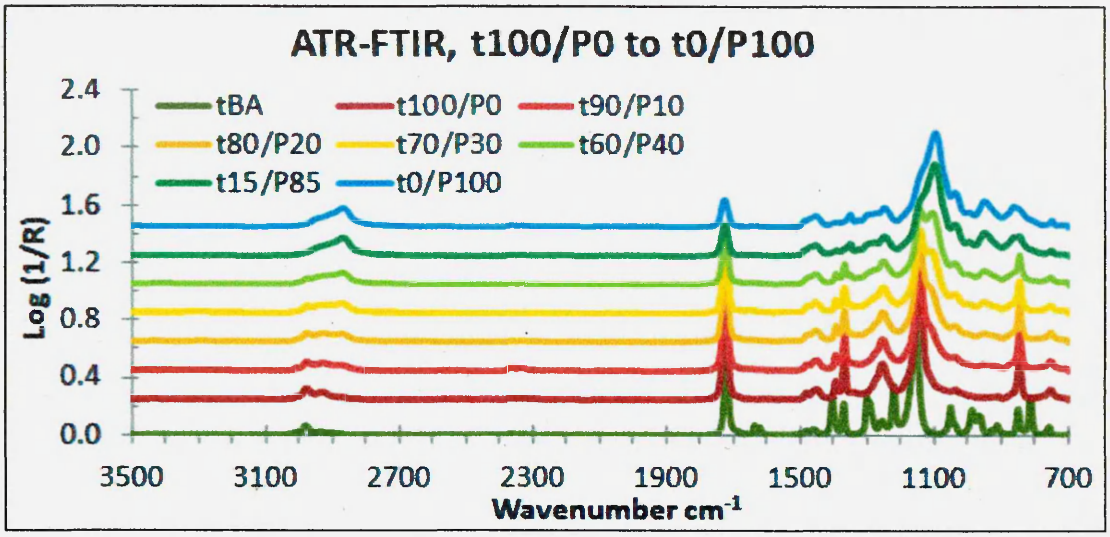

Figure 3.5: ATR-FTIR spectra of unreacted tBA and cured t100/P0 to t0/P100 networks.

For unreacted tBA the major peaks displayed in the high frequency region, ca. 3100 to 2700 cm^{-1}, that were observed arise from CH_3, CH_2 and CH stretches. At lower frequency, ca. 1800 to 1100 cm^{-1}, ester C=O stretch, C=C stretch, tert-butyl CH_3 deformations and an ester C-O stretch were observed. Finally at the lower frequencies, below 1000 cm^{-1}, IR bands due to $C=CH_2$ rock and wag, C=CH wag and $C=CH_2$ twist as well as CH_3 rock vibrations are observed (Colthup et al., 1990).

Cured samples of t100/P0 to t0/P100 displayed major peaks in the high frequency region, ca. 3100 to 2700 cm^{-1}, that arise from CH_3 and CH_2 stretches. At lower frequency, ca. 1800 to 1100 cm^{-1}, ester C=O stretch, tert butyl CH_3 deformations and an ester C-O stretch was observed. Finally at the lower frequencies, below 1000 cm^{-1}, IR bands due to CH_3 rock vibrations are observed (Colthup et al, 1990).

In order to assess whether the t100/P0 to t0/P100 polymer networks were crosslinked, ATR-FTIR was used to monitor the disappearence of peaks assigned to the acrylate functional group. As the monomer, tBA, and the cross-linker, PEGDMA, join together forming chains, they lose the active acrylate functional group, therefore the disappearence of those bands in the spectra would be expected, this approach was also used by Warren et al., (2010) to assess the completion of the reaction in a similar acrylate network. There are three peaks that illustrate the disappearence of the functional acrylate group. The C=C peaks, ca. 1636 and 1620 cm^{-1}, and the $C=CH_2$ twist, ca. 811 cm^{-1}, figure 3.6.

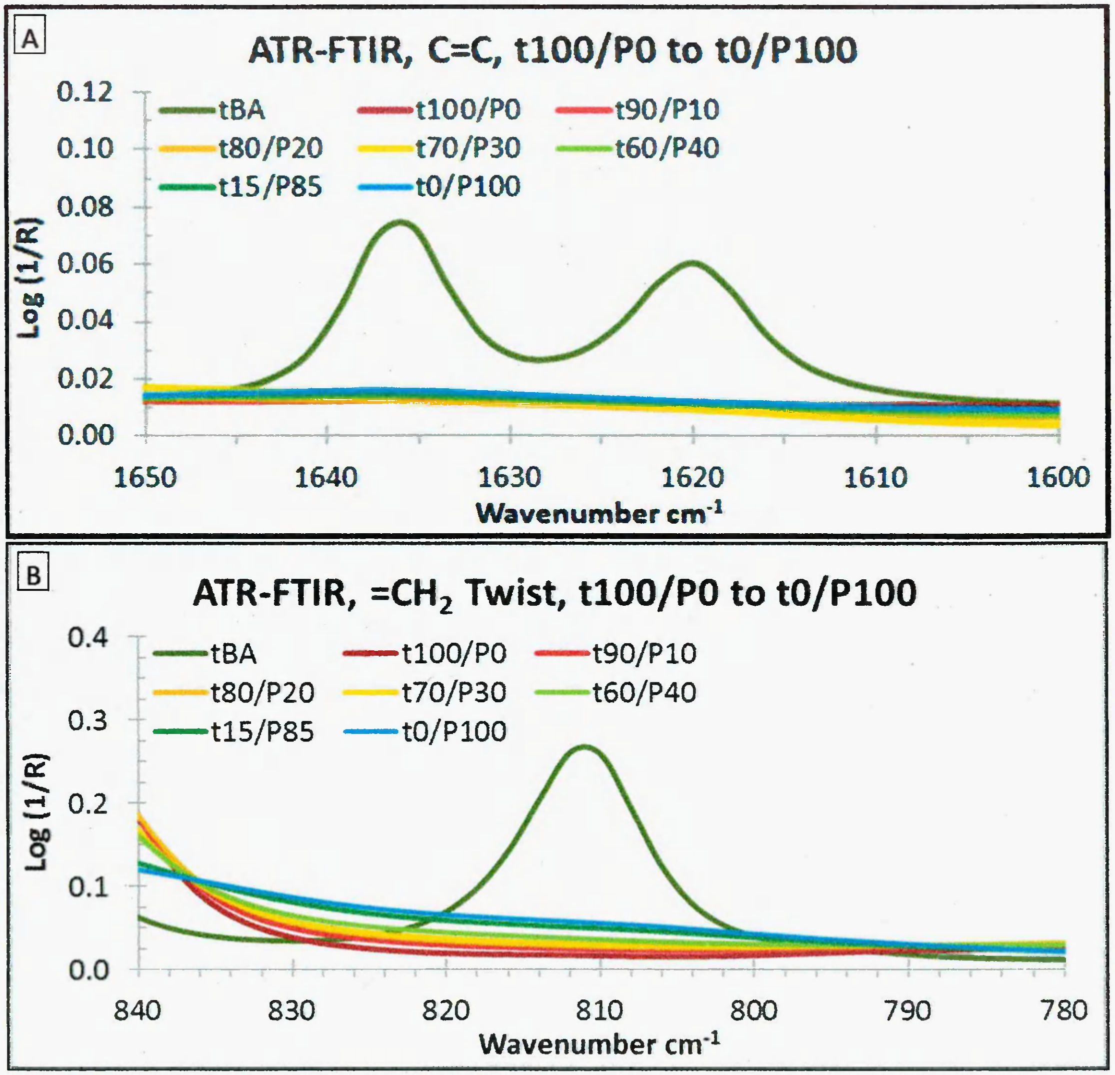

Figure 3.6: ATR-FTIR spectra of unreacted tBA and the cured t100/P0 to t0/P100 networks, A) comparison of peaks in the C=C region and B) comparison of peaks in the C=CH$_2$ twist region.

Figure 3.6 shows that, after curing of t100/P0 to t0/P100 networks, the C=C peaks and C=CH$_2$ peak disappear to unobservable levels. This indicates that after curing the polymer networks are fully polymerised, with no evidence for acrylate functional groups remaining. This supports the swelling experiment results which suggested that cross-linking had occurred within the tBA-co-PEGDMA networks. This result also suggests that even with increasing PEGDMA content, and therefore an increase in viscosity, there was no residual areas where acrylate bands are observed, confirming that an even cure occurred and that there are potentially no regions of uncured material present, which could have been due to being trapped during the curing

process. However as the ATR FTIR only penetrates to a depth of 4 to 6 μm in the sample, a full cure cannot be fully confirmed.

3.2.2. Thermal Results

3.2.2.1. Thermogravimetric Analysis

The TGA thermograms and their derivatives, obtained on heating the t100/P0 to t0/P100 networks prepared in this study are shown in figure 3.7 and the thermal events of interest are summarized in table 3.5.

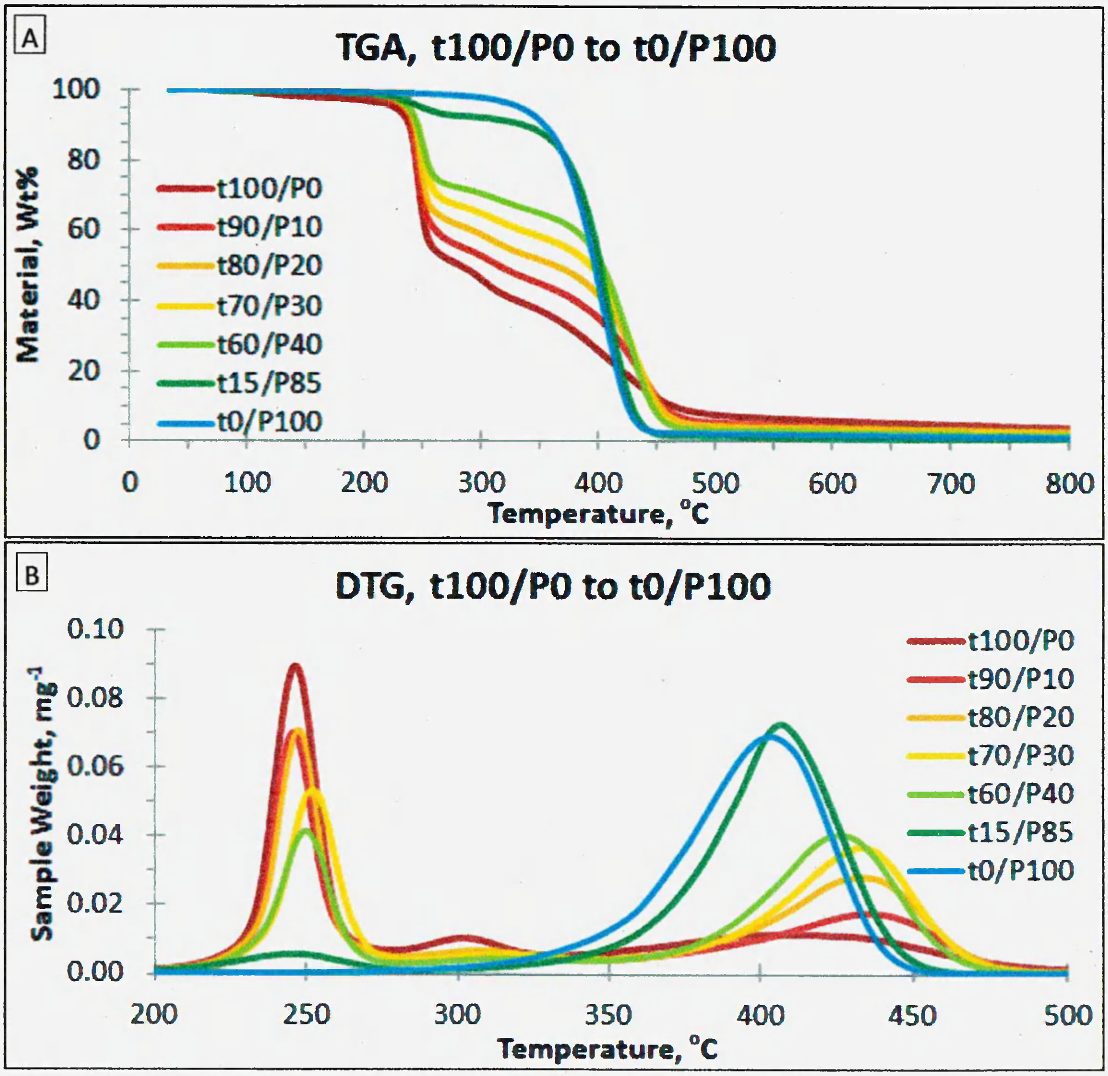

Figure 3.7: TGA A) thermograms and B) DTG of the t100/P0 to t0/P100 networks.

The TGA profiles for the t100/P0 to t0/P100 networks shows that there is no significant degradation below 200 °C. The t100/P0 network exhibits three distinct decomposition stages, a sharp weight loss with a peak in the derivative thermogram at ca. 244 °C,

$T_{max(1)}$, a second peak with a DTG maximum at ca. 301 °C, $T_{max(2)}$, and a broad third peak with a DTG maximum at ca. 411 °C, $T_{max(3)}$. After 500 °C the polymer is fully degraded with only some minor char residue remaining. The first and second degradation stages are attributed to the decomposition of the tert-butyloxygen moieties of the tBA chains while the third is attributed to the full decomposition of the remaining residual tBA polymer (Kong et al., 2004). The t0/P100 network exhibits a single broad but intense decomposition stage with a DTG maximum at ca. 402 °C, $T_{max(3)}$. After 450 °C the polymer is fully degraded with only some minor char residue remaining. The DTG maximum at 402 °C is attributed to the total decomposition of PEGDMA chain, and corresponds well with previously reported PEGDMA decomposition data (Li et al., 2009).

The t90/P10 to t15/P85 networks show a two stage decomposition behaviour in which the degradation stages occur at T_{max} values close to those of the pure polymer networks, tBA and PEGDMA. As the PEGDMA content increases the intensity of $T_{max(1)}$ diminishes and shifts slightly to higher temperatures up to the t70/P30 network. From the t60/P40 network the degradation peak continues to reduce in intensity but shifts back to lower temperatures until the t15/P85 network when the $T_{max(1)}$ is almost at the same temperature as the t90/P10 network.

Sample Description	$T_{5\%}$, °C	$T_{max(1)}$, °C	$T_{max(2)}$, °C	$T_{max(3)}$, °C
t100/P0	226	244	301	411
t90/P10	233	246	-	439
t80/P20	235	247	-	434
t70/P30	235	252	-	435
t60/P40	238	250	-	427
t15/P85	249	245	-	407
t0/P100	331	-	-	402

Table 3.5: TGA thermal properties of t100/P0 to t0/P100 networks, including the degradation onset temperature, $T_{5\%}$, defined as the temperature at which the sample weight decreases by 5 wt% and the temperature at which the maxima occur in the DTG trace, $T_{Max\,(1)}$ to $T_{Max\,(3)}$.

As the PEGDMA content increases the intensity under the $T_{max(2)}$ peak disappears. As the PEGDMA content increases from the t90/P10 to t70/P30 network $T_{max(3)}$ shifted to higher temperature and increases in intensity. However as the PEGDMA content continued to increase to the t15/P85 network $T_{max(3)}$ shifted to lower temperatures and increased in intensity. This indicates that there is a gain in initial thermal stability with increasing content of PEGDMA but as the PEGDMA content increases the degradation of the PEGDMA component dominates the thermal stability.

3.2.3. Mechanical Properties

3.2.3.1. Dynamic Mechanical Analysis

The dynamic mechanical properties, storage modulus, loss modulus and tan δ, of t100/P0 to t0/P100, are plotted in figure 3.8 as a function of temperature, -50 to 90 °C, while the dynamic mechanical properties are summarized in table 3.6.

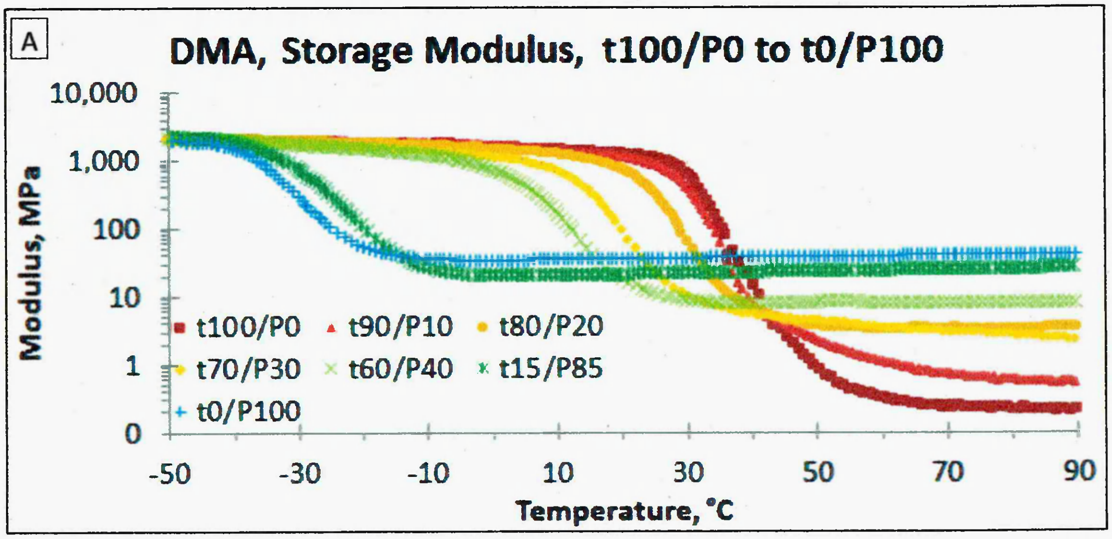

Figure 3.8: DMA data: temperature dependance of A) storage modulus, B) loss modulus and C) tan δ of the t100/P0 to t0/P100 networks over the temperature range -50 to 90 °C.

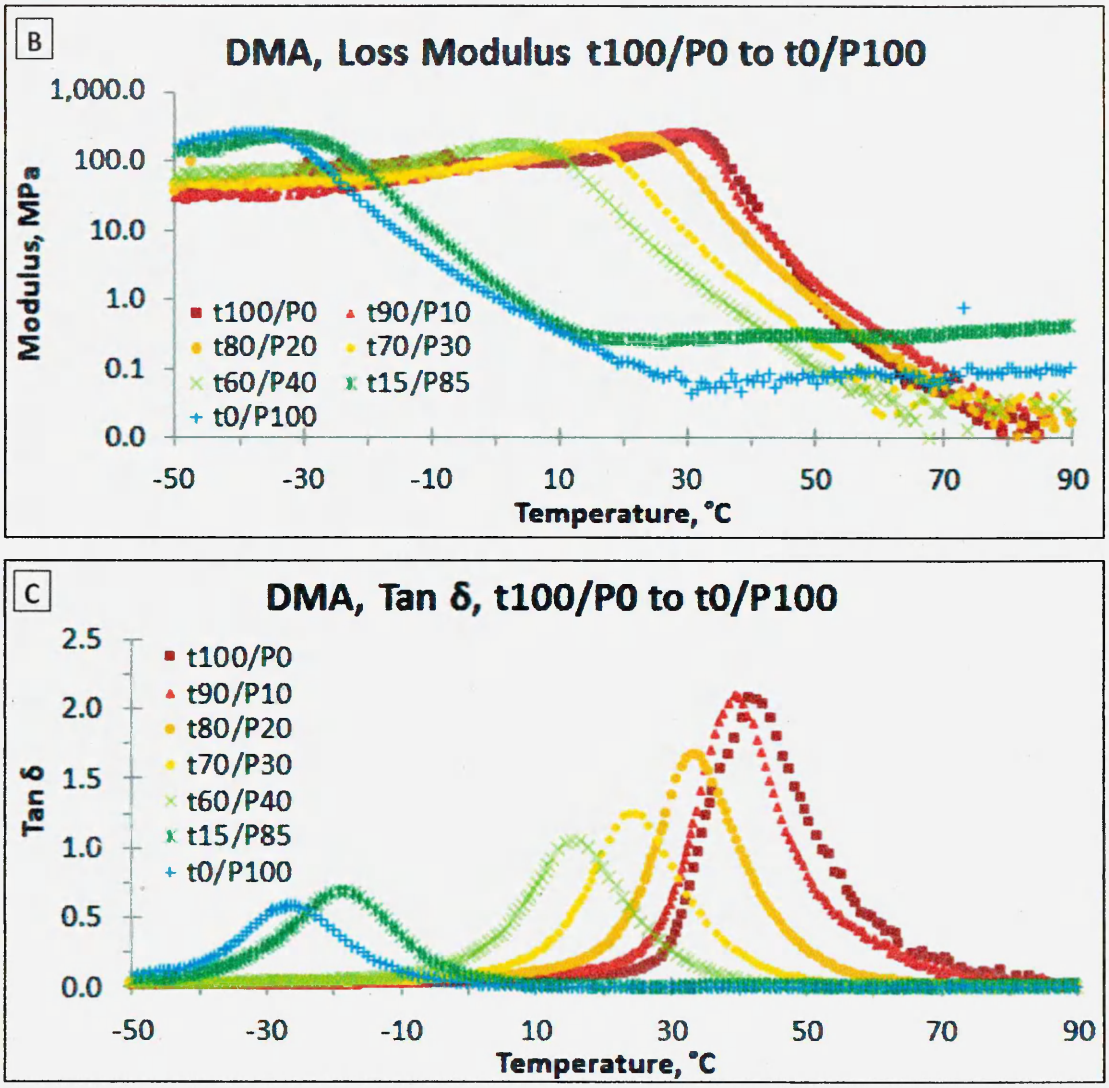

Figure 3.8: DMA data: temperature dependance of A) storage modulus, B) loss modulus and C) tan δ of the t100/P0 to t0/P100 networks over the temperature range -50 to 90 °C.

At -50 ˚C an initial storage modulus of ca. 2005 MPa was observed for the t100/P0 network, figure 3.8 A. The modulus drops steadily until ca. 22 °C, at this stage the modulus has dropped to ca. 1145 MPa, ca. 57 %. After this the modulus begins to steeply drop, this indicates the onset of the $T_{g\alpha}$ transition stage, figure 3.8 C, the stage where shape memory effect is predicted to begin. At the tan δ_{max}, 2.1 tan δ, the T_g of the polymer system is established, 41 °C. The high intensity tan δ_{max} result indicates that the SMP will behave more like an elastomer and experience large shape recovery when SME is carried out. Alternatively low intensity tan δ_{max} results indicate that smaller shape recovery will occur (Chun et al., 2002, Tsai et al., 2009).

At tan δ_{max} the modulus has dropped to ca. 22 MPa, this continues to drop steadily until the $T_{g\alpha}$ transition stage has finished, ending with a modulus of ca. 0.2 MPa. Tsai et al., (2008) suggested that a sharp, at least one order of magnitude, drop in storage modulus indicates that a polymer system will demonstrate SME (Du and Zhang, 2010). The t100/P0 network demonstrates ca. a four order magnitude drop in storage modulus, therefore a usable SME is indicated.

The t0/P100 network exhibited an initial storage modulus of 2129 MPa at - 50 °C which steadily decreased reaching a value of 1903 MPa at -47 °C; approximately 89 % of the initial storage modulus. A steep drop in the modulus marked the onset of the $T_{g\alpha}$ transition and established the starting point of the shape memory effect. For t0/P100 the T_g is -26 °C and the tan δ_{max} value is 0.6 tan δ. This latter value is just large enough to assume that this network will behave like an elastomer or exhibit some degree of useful shape memory properties. The t0/P100 network exhibits a drop in modulus of ca. a one and a half order of magnitude, from 2129 MPa at -50 °C to 34 MPa at the end of the $T_{g\alpha}$ transition. However as temperature increases, after the $T_{g\alpha}$ transition stage, the storage modulus also increased, up to 42 MPa, potentially due to thermally induced crystallisation, which could cause an increase in modulus (Smith et al., 2009). Overall, the t0/P100 network is predicted to exhibit some useful shape memory properties.

Sample Description	Storage Modulus, MPa								$T_{g\alpha}$, °C	Tan δ_{max}
	-50 °C	-30 °C	-10 °C	10 °C	30 °C	50 °C	70 °C	90 °C		
t100/P0	2005	1756	1605	1368	637	0.8	0.2	0.2	41	2.1
t90/P10	2108	1961	1782	1416	425	2	0.7	0.5	39	2.1
t80/P20	2035	1847	1597	1194	61	4	3	3	33	1.7
t70/P30	1923	1688	1342	659	10	4	3	2	24	1.3
t60/P40	2168	1719	1194	160	9	8	8	8	15	1.1
t15/P85	2249	759	27	21	22	24	25	27	-18	0.7
t0/P100	2129	292	36	35	37	39	41	42	-26	0.6

Table 3.6: Summary of the dynamic mechanical values for the t100/P0 to t0/P100 networks obtained from DMA over temperature range of -50 to 90 °C.

An initial storage modulus of ca. 2108, 2035, 1923, 2168 and 2249 MPa was recorded for the t90/P10 to t15/P85 networks, respectively, at -50 °C. The moduli drop steadily until ca. 10, 10, 2, -9 and -40 °C, respectively, at these temperatures the moduli has dropped to ca. 1406, 1194, 1051, 1138 and 1886 MPa, ca. 67, 59, 55, 52 and 84 % of the initial modulus. After this the moduli begin to steeply drop, indicating the onset of the $T_{g\alpha}$ transition. At the tan δ_{max}, 2.1, 1.7, 1.3, 1.1 and 0.7 tan δ, respectively, the T_g values for the polymer networks are 39, 33, 24, 15 and -18 °C, respectively. The higher intensity tan δ_{max} results i.e. t90/P0 to t60/P40 networks, indicate large shape recovery when SME is carried out whereas the lower intensity tan δ_{max} result i.e. t15/P85 network, indicate that a smaller shape recovery will occur (Chun et al., 2002, Tsai et al., 2009).

At tan δ_{max} the moduli have dropped to ca. 10, 23, 28, 41 and 70 MPa, respectively, and they continue to drop steadily until the $T_{g\alpha}$ transition stage has finished, ending with a modulus of ca. 0.5, 3, 3, 8 and 21 MPa, respectively. The t90/P10 to t15/P15 networks all demonstrate at least a two order magnitude drop in storage moduli, therefore SME is indicated (Tsai et al., 2008, Du and Zhang, 2010).

These results are as expected, with the drop in storage modulus magnitude and increase of rubbery modulus after the $T_{g\alpha}$ transition stage falling between the pure tBA and PEGDMA polymer networks, decreasing and increasing, respectively, as PEGDMA content increases (Kramer et al., 2010).

Overall the DMA results, storage modulus, loss modulus and tan δ results, suggest that addition of PEGDMA to tBA causes a controllable shift, to lower temperatures, of the $T_{g\alpha}$ transition phase and a reduction in the tan δ_{max} peak intensity.

There is no clear trend in initial starting modulus, however all networks were within ca. 250 MPa of the t100/P0 or t0/P100 networks.

The rubbery storage modulus of each polymer network increased as the PEGDMA content increase. These results correspond well to other research groups such as Gall et al., (2005), Ortega et al., (2008) and Kramer et al., (2010).

3.2.4. Shape Memory Effect Testing

3.2.4.1. Unconstrained Shape Memory Effect Evaluation

Unconstrained SME testing was carried out in order to assess whether every polymer network would demonstrate SME and to explore the effect of increasing PEGDMA content on SME, figure 3.9. Cross-linked tBA-co-PEGDMA polymer networks are characterised as a class I type SMP, with a $T_{trans} = T_g$ (Lui et al., 2007). Therefore an appropriate SME temperature range needs to be adopted to account for the different

T_g values for the various network compositions, as seen in the DMA, figure 3.8 C. As t100/P0 has the highest T_g, 41 °C, utilising a T_{high} at ca. 51 °C, which is 10 °C above the T_g, should ensure a full shape recovery. However the lowest network T_g occurs at -26 °C for t0/P100, this is much lower than the desired storage temperature of typical packaging material, therefore a T_{low} of 0 to 5 °C was adopted instead. In order to view only the effect of PEGDMA on the SME, each network was annealed at 70 °C for 15 minutes prior to being tested. Samples of t100/P0 to t0/P100 were deformed and their recovery determined as described in the section 2.1.6, figure 2.15. The SME properties of interest are summarized in table 3.7.

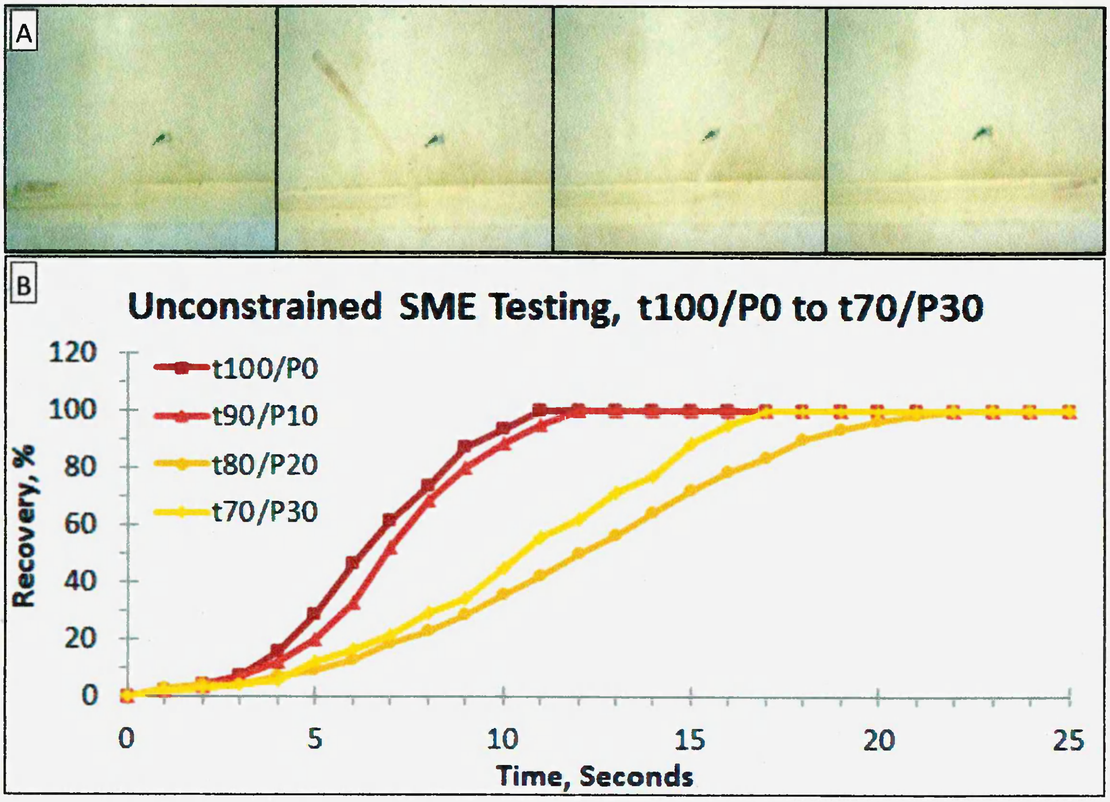

Figure 3.9: Unconstrained SME testing of tBA-co-PEGDMA networks, from temporary shape to permanent shape, A) still images of tBA/PEGDMA SMP at sequential intervals, B) plotted against time at a fixed temperature, ca. 51 °C.

The shape memory abilities of the t60/P40 and t15/P85 networks were not recorded due to increased brittleness of the networks caused by the higher PEGDMA content. Both samples were deformed to a θ_{Max} of 100 %, however when the constraint was removed each sample had fractured at the hinge region and was rendered unusable for unconstrained SME testing. This has previously been reported by Ortega et al., (2008) and indicated by Safranski and Gall, (2008), where increased cross-links caused

the stress-strain behaviour of the material to change from an elastomeric response to a stiff network with a pronounced brittle response.

The t100/P0 network exhibited a θ_{Max} of 100 %, demonstrating that it is elastic enough to accommodate a high level of deformation stress. After the deformation constraint was removed and the sample was kept at T_{low}, 0 to 5 °C, no recovery occurred, leading to a θ_{Fixed} of 100 %. This demonstrates that the t100/P0 can easily store the full load of imparted strain. It has previously been reported by Yang et al., (2007) that at low temperatures i.e. T_{low}, the entropy driven strain recovery forces are simply not enough to overcome the barrier for recovery. Therefore the deformation cannot recover while the sample is at T_{low} even when given sufficient time as the activation energy required to initiate recovery cannot be achieved.

Shape memory recovery was carried out at 50 °C and the recovery angle, $\theta_i(T)$, was recorded every 1 second until t100/P0 reached its θ_{Final}. The t100/P0 network demonstrated, by achieving a θ_{Final} of 100 %, that it can store the deformed strain at T_{low}, and return to its original shape. This result corresponds well to results predicted in the literature, Ortega et al., (2008), where it was expected that low, possibly negligible, cross-link density would produce a SME with large recoverable strain but low force generation.

In order to further assess the shape memory ability of the t100/P0 network, the $\theta_{1/2\ Final}$ and θ_{Final} time of recovery, ca. 6 and 11 seconds were recorded, respectively. These results indicate that the tBA100/P0 network recovers ca. 50 % of its permanent shape in ca. half of the full recovery time.

Sample Description	θ_{Max}, %	θ_{Fixed}, %	$\theta_{1/2Final}$, %	θ_{Final}, %	$\theta_{1/2Final}$ Time, Sec	θ_{Final} Time, Sec
t100/P0	100	100	50	100	6	11
t90/P10	100	100	50	100	7	13
t80/P20	100	100	50	100	12	22
t70/P30	100	100	50	100	10	17

Table 3.7: SME test results, θ_{Max}, θ_{Fixed}, $\theta_{1/2Final}$, θ_{Final}, $\theta_{1/2Final}$ Time, and θ_{Final} Time, from the t100/P0 to t70/P30 networks, temporary shape to permanent shape recovery, plotted against time at a fixed temperature, 50 °C.

The t90/P10 to t70/P30 networks displayed a θ_{Max} of 100 %, the same as the t100/P0 network, indicating that although the PEGDMA content, and therefore the number of cross-links, had increased there was no retardation of elasticity or ability to accommodate a high level of deformation strain. The θ_{Fixed} was recorded at 100 % for all networks, t90/P10 to t70/P30, which indicates that as the PEGDMA content increases to 30 wt% it does not diminish the network ability to retain its temporary shape at T_{low}.

Shape memory recovery was carried out at 50 °C and the $\theta_i(T)$ was recorded every 1 second until each network reached its θ_{Final}. The t90/P10 to t70/P30 networks demonstrated, by achieving a θ_{Final} of 100 %, that they can store the deformed strain at T_{low}, and return to their original shape when unconstrained SME evaluation is carried out. These networks also performed as predicted, based on the DMA results, figure 3.8, showing large recoverable strains (Ortega et al., 2008).

In order to further assess the shape memory ability of the t90/P10 to t70/P30 networks the $\theta_{1/2\ Final}$ time of recovery, ca. 7, 12 and 10 seconds and θ_{Final} time of recovery, ca. 13, 22 and 17 seconds, respectively, were recorded. These results indicate that t90/P10 to t70/P30 networks also recover 50 % of the permanent shape in ca. half the full recovery time.

Overall these results indicate that with increasing PEGDMA content there is an increase in $\theta_{1/2\ Final}$ and θ_{Final} time of recovery from the initial t100/P0 network. Interestingly the t70/P30 network demonstrated a faster $\theta_{1/2\ Final}$ and θ_{Final} time of recovery than the t80/P20 network. This may potentially be due to the increased number of cross-links which could have allowed it to store greater amounts of energy that provide a faster response. However not all the samples could be tested, therefore a true assessment of the SME of the t100/P0 to t0/P100 networks could not be obtained. However had SME evaluation been possible for the t15/P85 and t0/P100 networks it would have been anticipated that the shape recovery would be lower than the previous samples as highly cross-linked networks generally demonstrate low recoverable strain (Ortega et al., 2008).

These results correspond well to the DMA results which predicted that the tested networks would show SME and would have large recoverable strains.

3.3. tBA-co-PEGDMA Summary

The effect of cross-link content in an acrylate copolymer network, tBA-co-PEGDMA, was studied in order to assess its influence on the thermal and mechanical properties. The objective was to establish the most suitable composition ratio of tBA to PEGDMA in order to be able to produce a thermally stable SMP packaging solution for the pharmaceutical and commercial industries. A series of tBA-co-PEGDMA networks were produced and were characterised for homogeneity, thermal and mechanical properties, particularly for SME.

The tBA-co-PEGDMA networks proved to be fully polymerised, thermally stable, offering good mechanical properties with most providing a shape memory response. Not all the networks were equally good and some had fairly poor shape memory properties, being brittle and fracturing during large deformations. The network that demonstrated the most promise with regard to a thermally stable SMP packaging solution was the t90/P10 network. This was because it had a T_g in the correct temperature range for the proposed application, can be fully polymerised, offered good mechanical properties, with similar elasticity and SME as the t100/P0 network as well as having a modulus above its T_g that can maintain some mechanical loading. However this network still shows some of the classic shortcomings of SMP, especially when compared to SMAs i.e. low mechanical strength.

One of the immediate methods to reinforce the network is by using high modulus fillers i.e. clay. It was found, in previous studies (Wu et al., 2010, Ingram et al., 2008, Oral et al., 2009), that incorporation of clay into an acrylate network allowed the thermal and mechanical properties to be further tailored improving mechanical properties. Therefore an investigation into incorporation of clay into the tBA-co-PEGDMA networks was carried out.

3.4. t/P/C10A Results and Discussion

3.4.1. C10A Dispersal

3.4.1.1. X-Ray Diffraction

XRD traces in the region 2 to 40 °2θ for the t/P/C10A 0 to 5 networks were recorded in order to assess the state of dispersion of C10A in the t90/P10 host copolymer, figure 3.10.

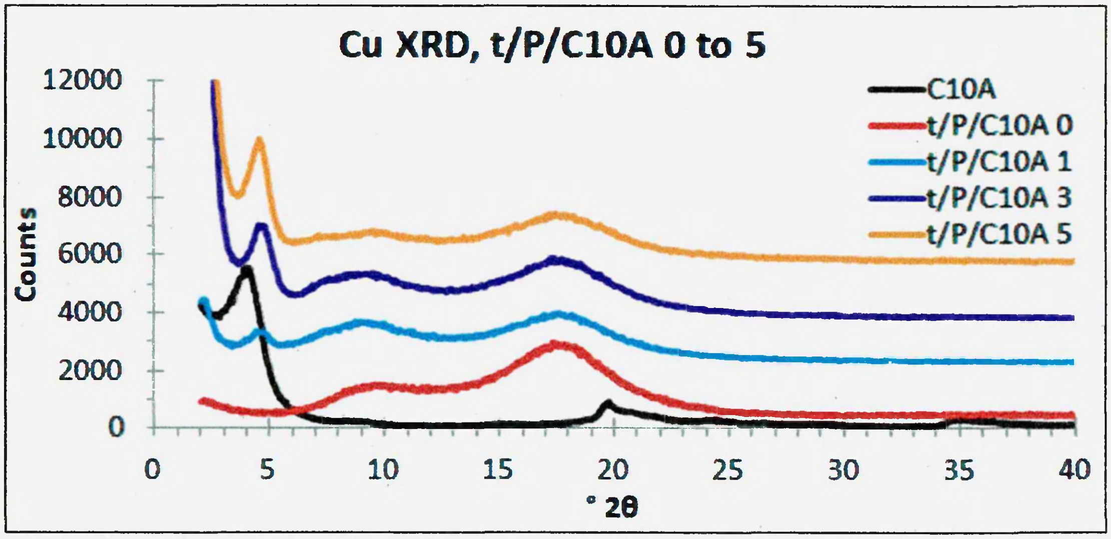

Figure 3.10: Cu XRD trace of C10A and t/P/C10A 0 to 5 networks.

The Cu XRD trace of C10A powder displayed peaks at, 4.2 °2θ (21.0 Å), 19.7 °2θ (4.5 Å) and 35.0 °2θ (2.6 Å), these peaks correspond to d001, and d(110,020) reflections, respectively (Rockwood Specialties Inc., 2009). The Cu XRD trace of the t/P/C10A 0 shows two broad peaks at 9.1 (9.7 Å) and 17.5 (5.1 Å) with no other observable peaks, these are polymer peaks. Cu XRD traces for the t/P/C10A 1 to 5 samples all exhibit a peak at 4.5 °2θ (19.6 Å) with no other peak from the C10A observed. The two host polymer peaks at 9.5 (9.7 Å) and 17.5 (5.1 Å) are observed in all samples and most likely obscures the 19.7 °2θ (4.5 Å) and 35.0 °2θ (2.6 Å) peaks of the C10A which are too weak to be seen.

Overall the C10A peak in the t/P/C10A 1 to 5 networks appears at higher angles than that of the C10A powder, suggesting that the polymerisation process reduces the interlayer content of C10A. Therefore it is difficult to ascertain whether the t/P/C10A 1 to 5 networks are intercalated nanocomposites or microcomposites.

Literature results where clay was incorporated into an acrylate polymer found that a benzoylbenzyl-N,N-dimethyl-N octadecylammonium bromide, BDOB, modified montmorillonite, MMT, dispersed in an epoxy acrylate network showed a peak at 2.8 °2θ (31.5 Å), when viewed by XRD (Wu et al., 2010). This indicated that the clay structures were in an intercalated state as an increase of the d-spacing, by 18.9 Å, was observed when compared to Na-MMT, 7.0 °2θ (12.6 Å). Oral et al., (2009) found that azide-functionalized C30B, azide-C30B, dispersed in MMA formed intercalated structures at 3 and 5 wt% azide-C30B content, with an XRD peak at ca. 3.0 °2θ (29.4 Å), and exfoliated structures at 1 wt% azide-C30B content, as no XRD d_{001} peak was observed. While Ingram et al., (2008) found that dimethyl dehydrogenated tallow quaternary ammonium modified Cloisite 20A, M-C20A, and Cloisite 15A, M-C15A, and bis-2-hydroxyethyl-methyl tallow quaternary ammonium chloride modified C30B, M-C30B, all formed exfoliated/intercalated nanocomposites in a MMA network. The MMA 1 and 2 wt% M-C30B networks displayed no peaks on an XRD trace, suggesting full exfoliation, whereas the 4 wt% M-30B displayed a peak at 2.1 °2θ (42.0 Å) suggesting intercalation. The 4 wt% M-C20A and M-C15A MMA composites showed no significant differences from the 4 wt% M-30B MMA composites suggesting intercalated nanocomposites were also formed.

3.4.1.2. ATR-FTIR Spectroscopy

ATR FTIR spectra, 700 to 3500 cm^{-1}, of the t/P/C10A 0 to 5 networks, vibrational modes are presented in figure 3.11. This was carried out to provide evidence that the polymer networks were fully cured and to view the effects of increasing C10A content on the t90/P10 network host copolymer.

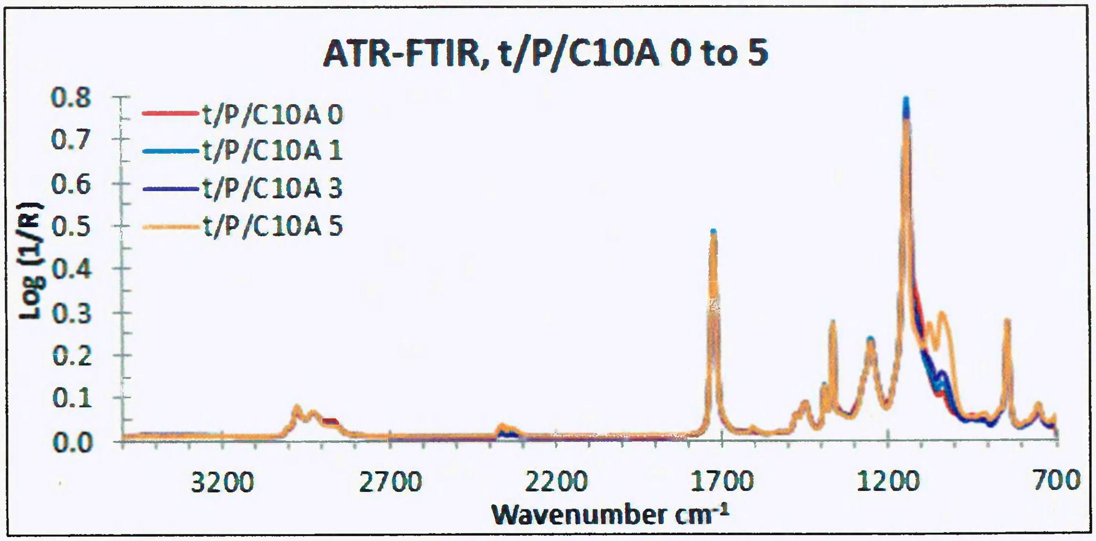

Figure 3.11: ATR-FTIR spectra of cured t/P/C10A 0 to 5 networks

The t/P/C10A 0 to 5 networks displayed major peaks in the high frequency region, ca. 3100 to 2700 cm^{-1}, that arise from CH_3 and CH_2 stretches. As the frequency becomes lower, ca. 1800 to 1100 cm^{-1}, ester C=O stretch, tert butyl CH_3 deformations and an ester C-O stretch was observed. At ca. 1000 cm^{-1} the t/P/C10A 1 to 5 networks all show the presence of Si-O bands, indicating the presence of C10A within the network that are not observed in the t/P/C10A 0 network. Finally at the lower frequencies, below 1000 cm^{-1}, IR bands due to CH_3 rock vibrations are observed (Colthup et al., 1990).

In order to assess whether the t/P/C10A 0 to 5 networks were crosslinked, ATR-FTIR was used to monitor the disapearence of peaks where the acrylate functional group was involved (Keller et al., 2004, Wu et al., 2010). The three peaks that display the dissapearence of the functional acrylate group the most clealy were the C=C peaks, ca. 1636 and 1620 cm^{-1}, and the C=CH_2 twist, ca. 811 cm^{-1}, figure 3.12.

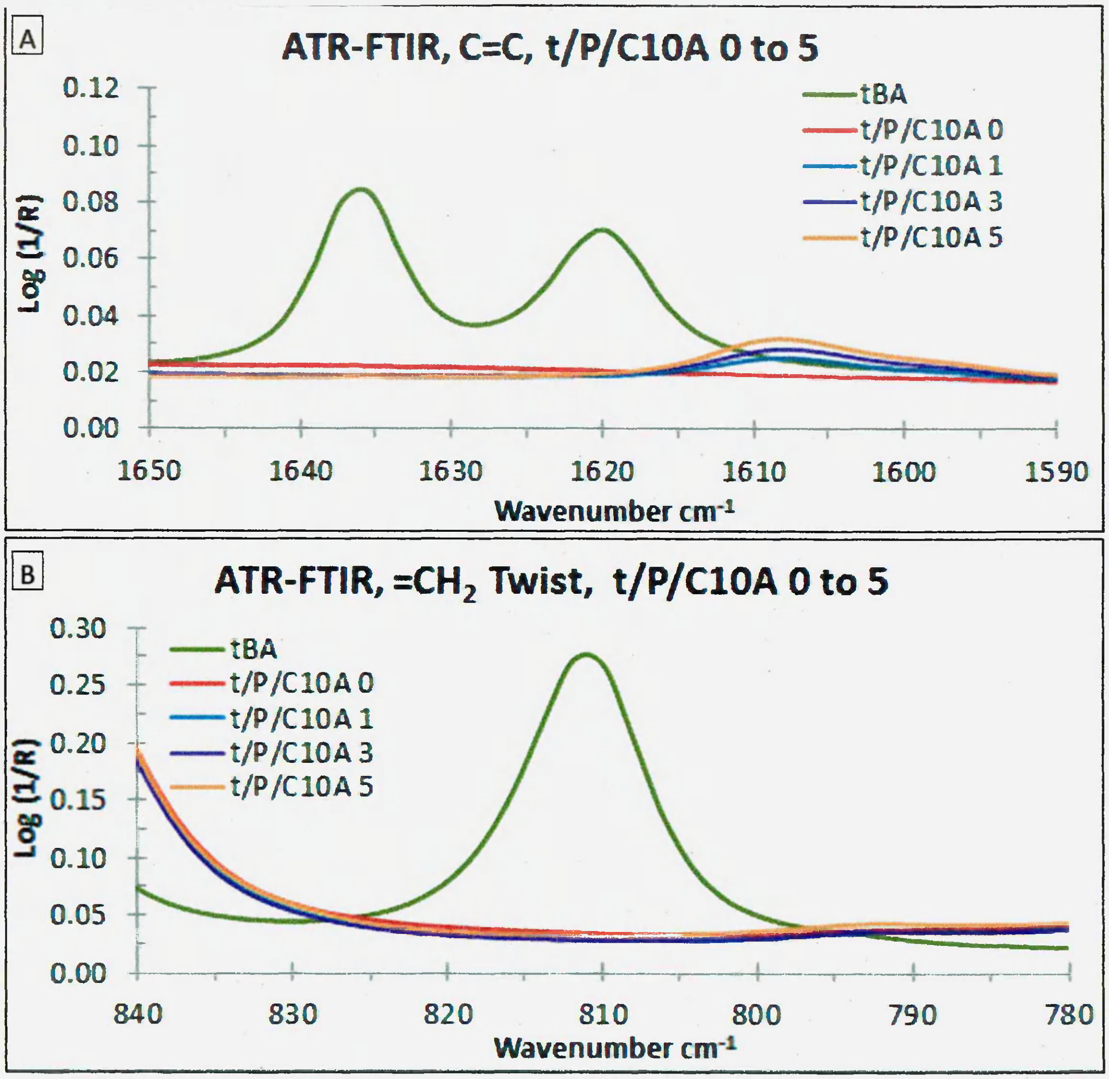

Figure 3.12: ATR-FTIR spectra of uncured tBA and post-cured t/P/C10A 0 to 5 networks, A) comparison of peaks in the C=C region and B) comparison of peaks in the $C=CH_2$ twist region.

As can be seen in figure 3.12, after curing the t/P/C10A 0 to 5 networks, the C=C peaks and $C=CH_2$ peak disappear to unobservable levels. This indicates that post cure the polymer networks are fully polymerised, with no apparent acrylate functional groups remaining. However although there appears to be no remaining C=C bonds, figure 3.12 A, a peak ca. 1607 cm^{-1} is observed that increases almost linearly as C10A content increases, this peak however is currently unidentified.

It is clear that C10A is present in the t/P/C10A 0 to 5 networks, however it appears that C10A does not alter the t/P/C10A 0 to 5 networks vibrational modes in a significant way, as no major effects to the total cure or major bond vibrations were observed. However it was found that as C10A content increased the peak at ca. 1115 cm^{-1},

attributed to the saturated ether groups of PEGDMA, decreased in intensity, figure 3.13.

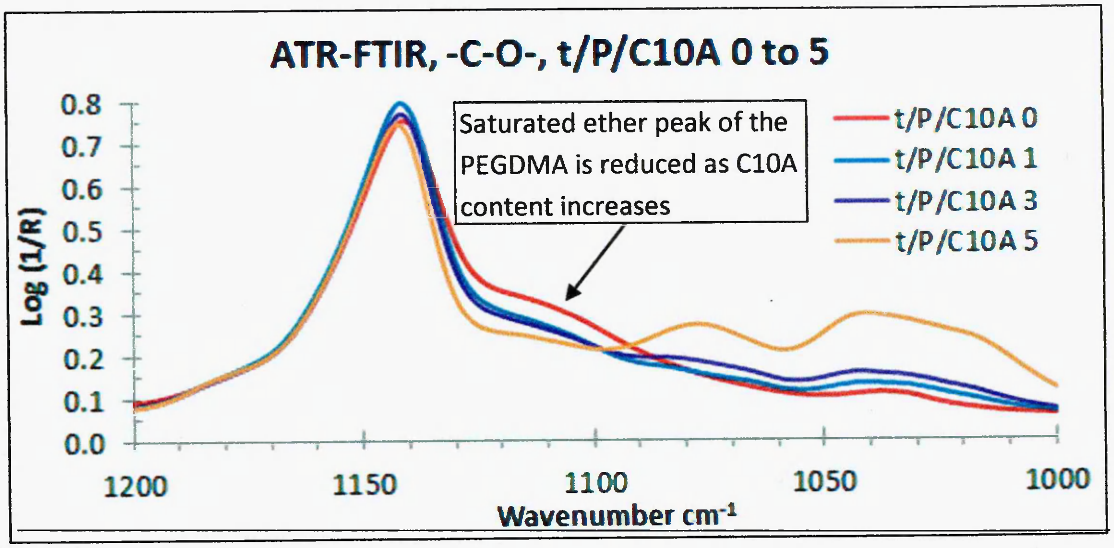

Figure 3.13: ATR-FTIR spectra of t/P/C10A 0 to 5 networks, effect of increasing C10A content on the PEGDMA saturated ether vibration.

The decrease in intensity of the PEGDMA peak at ca. 1115 cm^{-1} is possibly due to the effect of C10A on the migration of PEGDMA molecules to the surface of the t/P/C10A 0 to 5 networks. Pühringer (2012) suggested that with thick films, >0.5 mm, when the tBA-co-PEGDMA networks are initially cured, the PEGDMA molecules migrate towards the UV exposed surface causing an increased level of cross-linking in the surface of the polymer and a decreased amount of cross-linking in the bulk of the polymer. Therefore when stored the edges of the networks 'curl' due to differences in the cross-link densities throughout the network. As C10A content increases so does the viscosity of the liquid acrylate solution, retarding the ability of the PEGDMA to migrate due to physical blocking, possibly causing the 'labyrinth effect' associated with dispersed clay platelets (Keller et al., 2004). Therefore it would be expected that the PEGDMA peak at ca. 1115 cm^{-1} would decrease in intensity as PEGDMA migration to the surface is retarded during curing with increasing clay content. It is observed that in t/P/C10A 1 to 3 networks, the PEGDMA peak reduction was insignificant, especially compared to the reduction observed in the t/P/C10A 5 network. This is possibly due to a saturation point being achieved in the acrylate network at ca. 1 wt% C10A that is then not overcome until significantly more C10A is added.

Overall the ATR-FTIR spectra show that C10A is present in the networks, there is no residual, uncross-linked, acrylate remaining confirming fully polymerised networks and there is no significant effect on the overall vibrational mode of the t90/P10 network structure. However it was observed that with increasing C10A content there is an observable effect on the suggested migration of PEGDMA monomer during curing.

3.4.2. Mechanical Properties

3.4.2.1. Dynamic Mechanical Analysis

The dynamic mechanical properties, storage modulus, loss modulus and tan δ, of the t/P/C10A 0 to 5 networks, are plotted in figure 3.14 as a function of temperature, -50 to 150 °C, while the dynamic mechanical properties of interest are summarized in table 3.8.

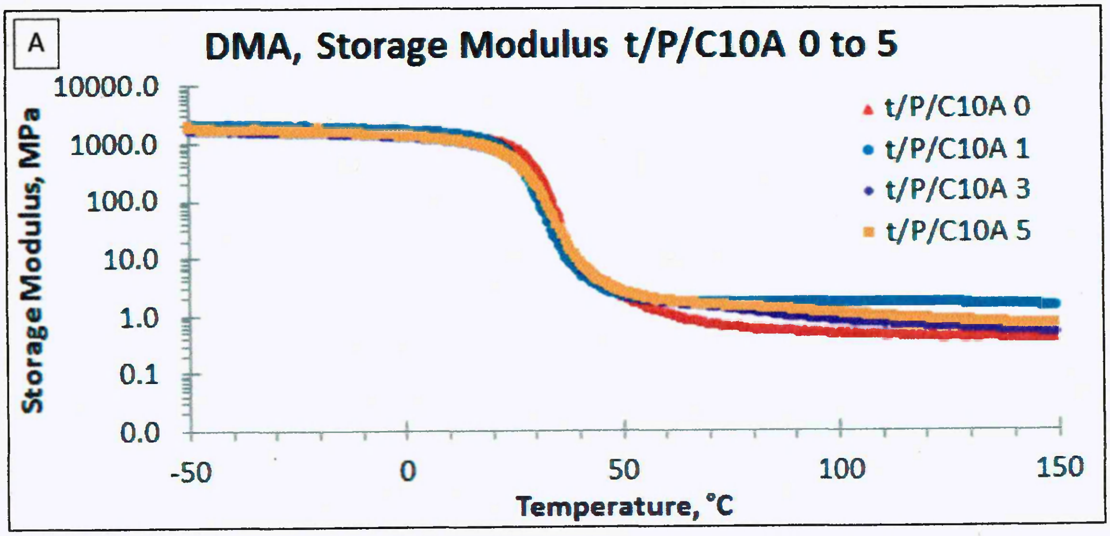

Figure 3.14: DMA data: temperature dependance of A) storage modulus, B) loss modulus and C) tan δ of the t/P/C10A 0 to 5 networks over the temperature range -50 to 150 °C.

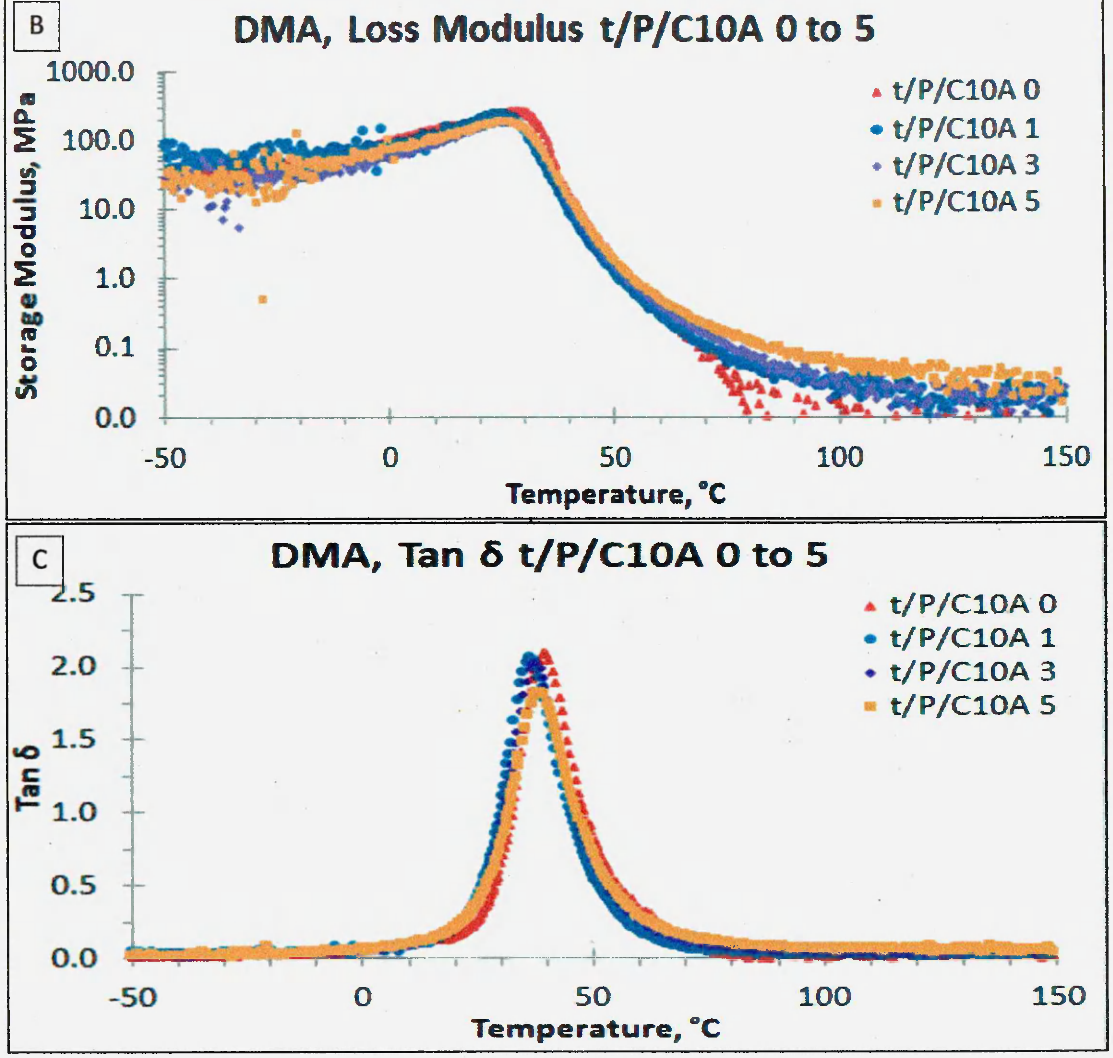

Figure 3.14: DMA data: temperature dependance of A) storage modulus, B) loss modulus and C) tan δ of the t/P/C10A 0 to 5 networks over the temperature range -50 to 150 °C.

At -50 ˚C an initial storage modulus of ca. 2107 MPa was recorded for the t/P/C10A 0 network (figure 3.14 A). The modulus drops steadily until ca. 10 °C, reaching ca. 1424 MPa, i.e. 68% of the initial value. After this the modulus begins to steeply drop, indicating the onset of the $T_{g\alpha}$ transition (figure 3.14 C) the point at which the shape memory effect is predicted to begin. At the tan δ_{max}, 2.1 tan δ, the T_g of the polymer system is established as 40 °C. The high intensity tan δ_{max} value indicates that the SMP will behave more like an elastomer and experience large shape recovery when SME is carried out (Chun et al., 2002, Tsai et al., 2009). The modulus continues to drop steadily until the $T_{g\alpha}$ transition has finished, ending with a modulus of ca. 0.4 MPa. Tsai et al., (2008) has suggested that a sharp, at least one order of magnitude, drop in

storage modulus means that a polymer system will demonstrate SME (Du and Zhang, 2010). The t/P/C10A 0 network demonstrates ca. a three and a half order magnitude drop in storage modulus, therefore SME should occur.

Sample Description	Storage Modulus, MPa							Tg, °C	Tan δ_{max}
	-50 °C	-25 °C	0 °C	25 °C	50 °C	100 °C	150 °C		
t/P/C10A 0	2107	1928	1629	876	2	0.5	0.4	40	2.1
t/P/C10A 1	1949	1808	1563	549	2	2.0	1.0	37	2.1
t/P/C10A 3	1629	1562	1276	459	2	0.8	0.5	37	2.0
t/P/C10A 5	1702	1564	1322	508	3	1.0	0.6	38	1.8

Table 3.8: Summary of the dynamic mechanical values obtained for the t/P/C10A 0 to 5 networks from DMA over temperature range of -50 to 150 °C.

The t/P/C10A 1 to 5 networks exhibited initial storage moduli of ca. 1949, 1629 and 1702 MPa, respectively, at - 50 °C which steadily decreased reaching a value of ca. 1417, 1040 and 1083 MPa at 13, 12 and 12 °C; approximately 73, 64 and 64 %, respectively, of the initial storage modulus. A steep drop in the moduli marked the onsets of the $T_{g\alpha}$ transition and established the starting point of the shape memory effect. For t/P/C10A 1 to 5 samples the T_g is 37, 37 and 38 °C, respectively, and the tan δ_{max} value is 2.1, 2.0 and 1.8 tan δ, respectively. These latter values are large enough to confidently predict that these networks will behave like elastomers and exhibit useful shape memory properties. However as these results are similar to the t90/P10 network host polymer no increase of shape memory abilities are expected.

The t/P/C10A 1 to 5 networks exhibit reductions in modulus of at least three and a half orders of magnitude, from 1949, 1629 and 1702 MPa at -50 °C to 1.0, 0.5 and 0.6 MPa, respectively, at the end of the $T_{g\alpha}$ transitions. Consequently, it is predicted that all networks will exhibit very useful shape memory properties.

The DMA results suggest that addition of C10A to t90/P10 networks causes no significant shift of the $T_{g\alpha}$ transition or any significant reduction in the tan δ_{max} peak intensity.

It was observed that the t/P/C10A 1 network has a much larger, greater than double, rubbery modulus compared to all the other networks, indicating it can maintain mechanical loading to a greater extent than the other networks when the temperature is above the T_g. This effect occurring at only 1 wt% C10A corresponds well with literature results observed by Benfarhi et al., (2004) and Okamoto et al., (2000) who found optimal modulus results at ca. 1 wt% clay loading although this was not in a SMP.

However as C10A content increases the initial modulus decreases from the initial storage modulus of the host polymer. These results correspond to literature reports where acrylate networks, PU-based acrylates and expoxy-based acrylates, show a drop in initial storage modulus with increasing clay content (Keller et al., 2004, Benfarhi et al., 2004). However it is more typical for an increase in initial storage modulus to occur as filler is added (Zang et al., 2009, Shemper et al., 2004) e.g. polyphenoxy-acrylate, poly(MMA) and poly(ethyl acrylate)-co-poly(MMA) acrylate networks when combined with clay have shown an increase in the initial storage modulus (Decker et al., 2005, Okamoto et al., 2001, Xu et al., 2006).

3.4.3. Shape Memory Effect Testing

3.4.3.1. Unconstrained Shape Memory Effect Evaluation

An unconstrained SME evaluation was carried out in order to assess whether the t/P/C10A 0 to 5 networks would demonstrate a SME and to explore the effect of increasing C10A content on the SME, figure 3.15. As previously described in section 3.2.4 an appropriate SME temperature range was adopted to account for the network composition T_g range, as seen in the DMA figure 3.14 C. The t/P/C10A 0 to 5 networks were deformed and their recovery determined as described in the section 2.1.6, figure 2.15. The SME properties of interest are summarized in table 3.9.

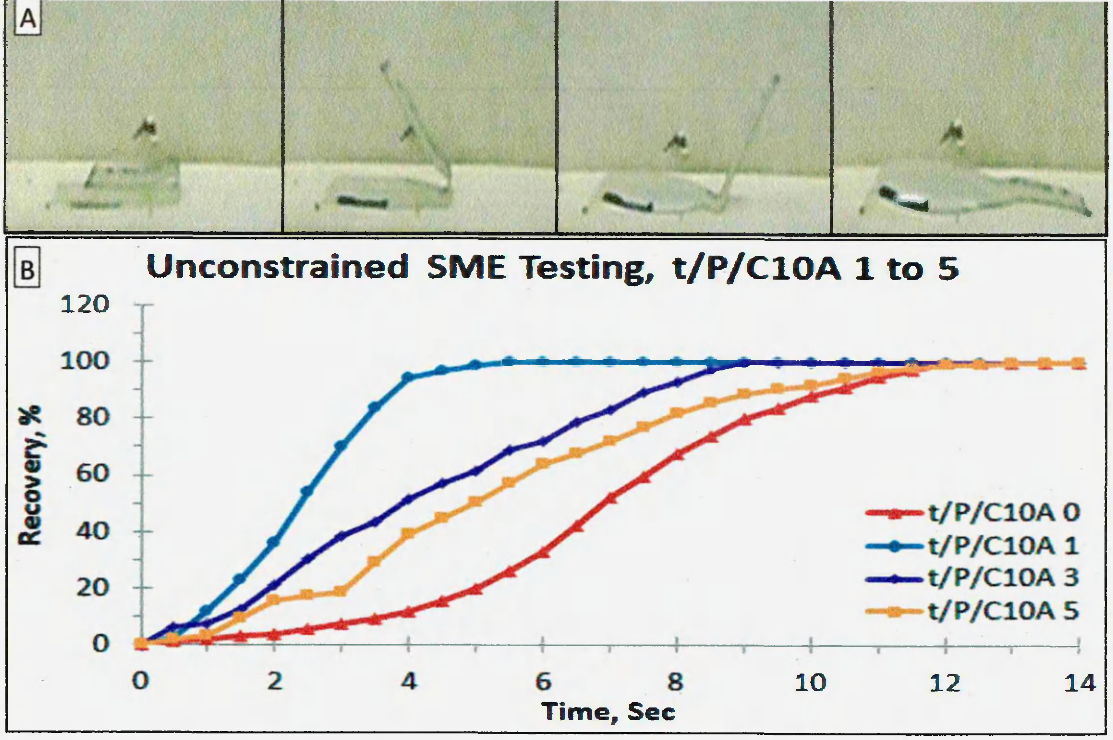

Figure 3.15: Unconstrained SME testing of t/P/C10A 0 to 5 networks, from temporary to permanent shape, A) still images of t/P/C10A SMP at sequential intervals, B) plotted against time at a fixed temperature, 50 °C.

The t/P/C10A 0 network exhibited a θ_{Max} of 100 %, demonstrating that it can accommodate a high level of deformation stress. After the deformation constraint was removed, the network was kept at T_{low}, 0 to 5 °C, no recovery occurred, leading to a θ_{Fixed} of 100 %. This demonstrates that the t/P/C10A 0 can easily store the full load of imparted strain within itself. Shape memory recovery was carried out at 50 °C and the $\theta_i(T)$ was recorded every 0.5 seconds until the t/P/C10A 0 network reached its θ_{Final}. The t/P/C10A 0 network demonstrated, by achieving a θ_{Final} of 100 %, that it can store the deformed strain at T_{low}, and return to its permanent shape. In order to further assess the shape memory ability of the t/P/C10A 0 network the $\theta_{1/2\ Final}$ and θ_{Final} time of recovery, ca. 7 and 12 seconds were recorded, respectively. These results indicate that the SME of the t/P/C10A 0 network recovers 50 % of the permanent shape in ca. half the full recovery time.

Sample Description	θ_{Max}, %	θ_{Fixed}, %	$\theta_{1/2Final}$, %	θ_{Final}, %	$\theta_{1/2Final}$ Time, Sec	θ_{Final} Time, Sec
t/P/C10A 0	100	100	50	100	7	12
t/P/C10A 1	100	100	50	100	2.5	5.5
t/P/C10A 3	100	100	50	100	4	9
t/P/C10A 5	100	100	50	100	5	13

Table 3.9: The t/P/C10A 0 to 5 networks SME test results, θ_{Max}, θ_{Fixed}, $\theta_{1/2Final}$, θ_{Final}, $\theta_{1/2Final}$ Time, and θ_{Final} Time, from temporary shape to permanent recovery, plotted against time at a fixed temperature, 50°C.

The t/P/C10A 1 to 5 networks displayed a θ_{Max} of 100 %, the same as the t/P/C10A 0 network, indicating that the C10A content causes no retardation of elasticity or ability to accommodate a high level of deformation strain. The θ_{Fixed} results were recorded at 100 % for all networks, t/P/C10A 1 to 5, also indicating that as C10A content increases it does not reduce the ability of the networks to retain their temporary shape at T_{low}.
The $\theta_i(T)$ was recorded every 0.5 seconds until each network reached its θ_{Final}. The t/P/C10A 1 to 5 networks demonstrated, by achieving a θ_{Final} of 100 %, that they can store the deformed strain at T_{low}, and return to their permanent shape.
The t/P/C10A 1 to 5 networks $\theta_{1/2\ Final}$ time of recovery, 2.5, 4.0 and 5.0 seconds, and θ_{Final} time of recovery, 5.5, 9.0 and 13.0 seconds, respectively, were recorded. These results indicate that the t/P/C10A 1 to 5 networks could also recover 50 % of the permanent shape in ca. half the full recovery time.
These results correspond well to the results predicted by DMA, however it was observed that a much faster shape memory recovery was achieved with addition of C10A, with the fastest recovery being achieved at 1 wt% C10A. Although the DMA predicted that each network, t/P/C10A 1 to 5, would demonstrate a fast shape memory recovery, it was unexpected that they would recover before the host polymer.

3.5. t/P/C10A Summary

The effect of C10A content in an acrylate copolymer network, t90/P10, was studied in order to assess the effects on the thermal and mechanical properties. The objective was to establish if addition of C10A would provide any significant enhancements to the shape memory ability of the t90/P10 network for the aim of creating a thermally stable SMP packaging solution. Three C10A loaded samples, t/P/C10A 1 to 5, were produced and compared to the host polymer, t/P/C10A 0, and were characterised for homogeneity, thermal and mechanical properties including shape memory ability.

The t/P/C10A 0 to 5 networks proved to be fully polymerised, thermally stable, offering good mechanical properties with all networks exhibiting shape memory abilities. All networks had good shape memory properties with no indications of increased brittleness or fracturing during large deformations with increasing C10A content. These results indicate that all the t/P/C10A 1 to 5 acrylate networks can potentially fulfil the requirements for creating a thermally stable SMP packaging solution, however the network that demonstrated the most promise was the t/P/C10A 1 network.

The t/P/C10A 1 network demonstrated enhanced mechanical and shape memory abilities compared to the host polymer while maintaining a T_g in the temperature range for the proposed application. Therefore it was decided to produce a shape memory coating, 20 to 30 µm, on selected packaging substrates; 100µm PET film and 60µm Sulpak paper, in order to confirm that this nanocomposite SMP system would be fully suitable for use in the packaging industry.

3.6. Coated Substrate Results and Discussion

3.6.1. C10A Dispersal

3.6.1.1. X-Ray Diffraction

XRD trace in the region 2 to 40 ° 2θ for t/P/C10A 1 PET or Sulpak, subsequently referred to as t/P/C10A 1 P or S, were carried out in order to assess the state of dispersion of C10A in the t90/P10 copolymer coating, figure 3.16.

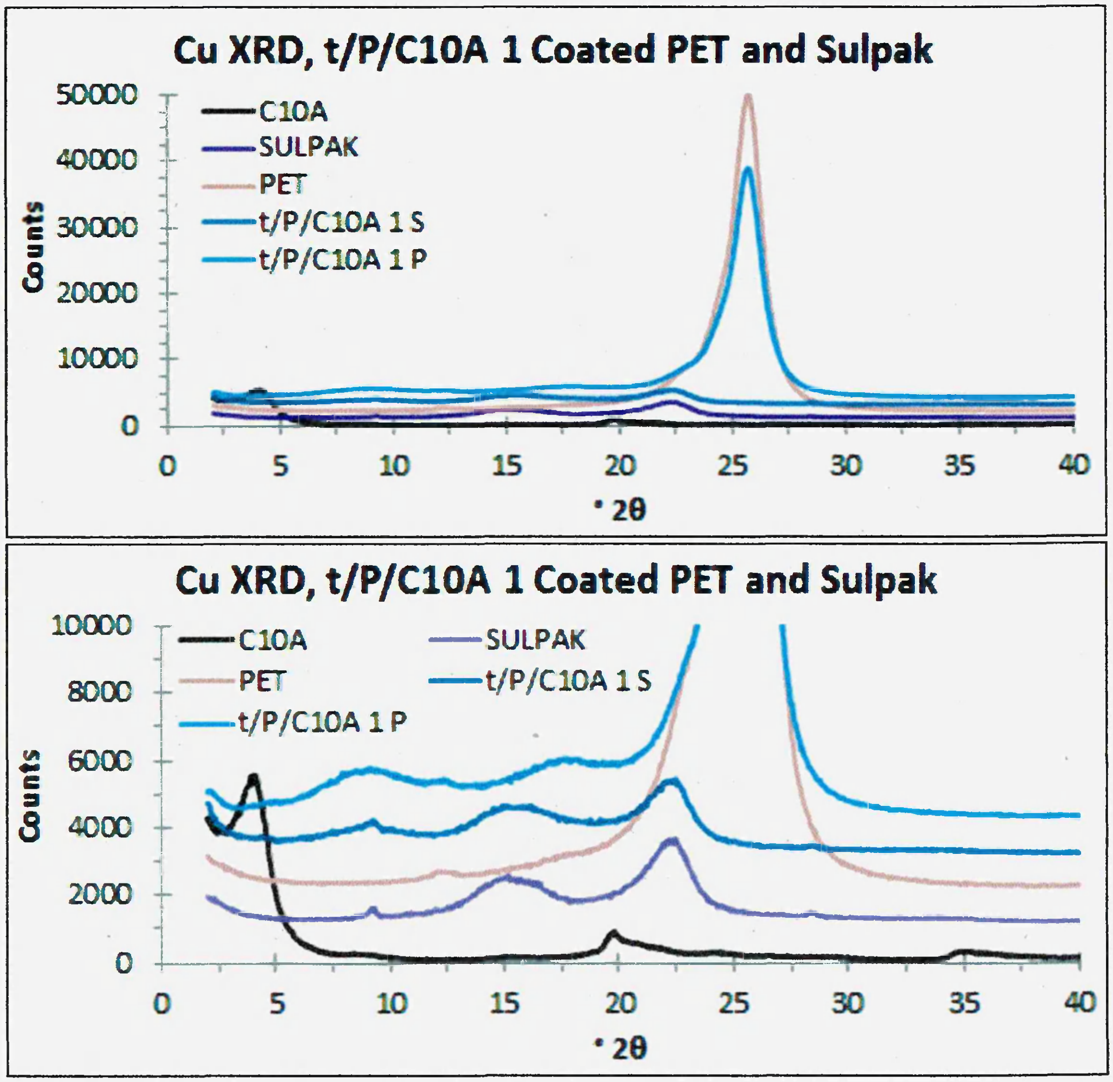

Figure 3.16: Cu XRD trace of C10A, PET, Sulpak and the t/P/C10A 1 S and P coated substrates.

The Cu XRD trace of C10A powder displayed peaks at, 4.0 °2θ (22.1 Å), 19.7 °2θ (4.5 Å) and 35.0 °2θ (2.6 Å), these peaks correspond to the d001, and (110, 020) reflections, respectively. This is what would be expected from an unorientated C10A (Rockwood Specialties Inc. 2009). The PET XRD trace displays an intense broad peak at 25.8 °2θ

(3.5 Å) while the Sulpak paper XRD trace displays a minor peak at 9.2 °2θ (9.6 Å), and two broad peaks at 15.2 °2θ (5.8 Å) and 22.4 °2θ (4.0 Å). The XRD trace of the t/P/C10A 1 P shows two broad peaks, observed at 9.1 (9.7 Å) and 17.5 (5.1 Å), both attributed to the acrylate host, while another broad intense peak at 25.8 °2θ (3.5 Å) is attributed to the PET. The XRD trace of the t/P/C10A 1 S shows three peaks, at 9.2 °2θ (9.6 Å), and two broad peaks at 15.2 °2θ (5.8 Å) and 22.4 °2θ (4.0 Å) which all appear to be attributed to the Sulpak with no other peaks observed.

Overall it appears that the C10A is either exfoliated or intercalated as no peaks were observed.

3.6.2. Shape Memory Effect Testing

3.6.2.1. Unconstrained Shape Memory Effect Evaluation

An unconstrained SME evaluation was carried out in order to assess whether the SMP coated substrates would demonstrate a SME and to explore the effect of C10A content on SME, figure 3.17. Each sample was annealed at 70 °C for 15 minutes prior to being tested. The t/P/C10A 0 to 1, P and S samples and non-coated Sulpak and PET sheets were deformed and their shape memory recoveries determined as described in section 2.1.6, figure 2.17. The SME properties of interest are summarized in table 3.10.

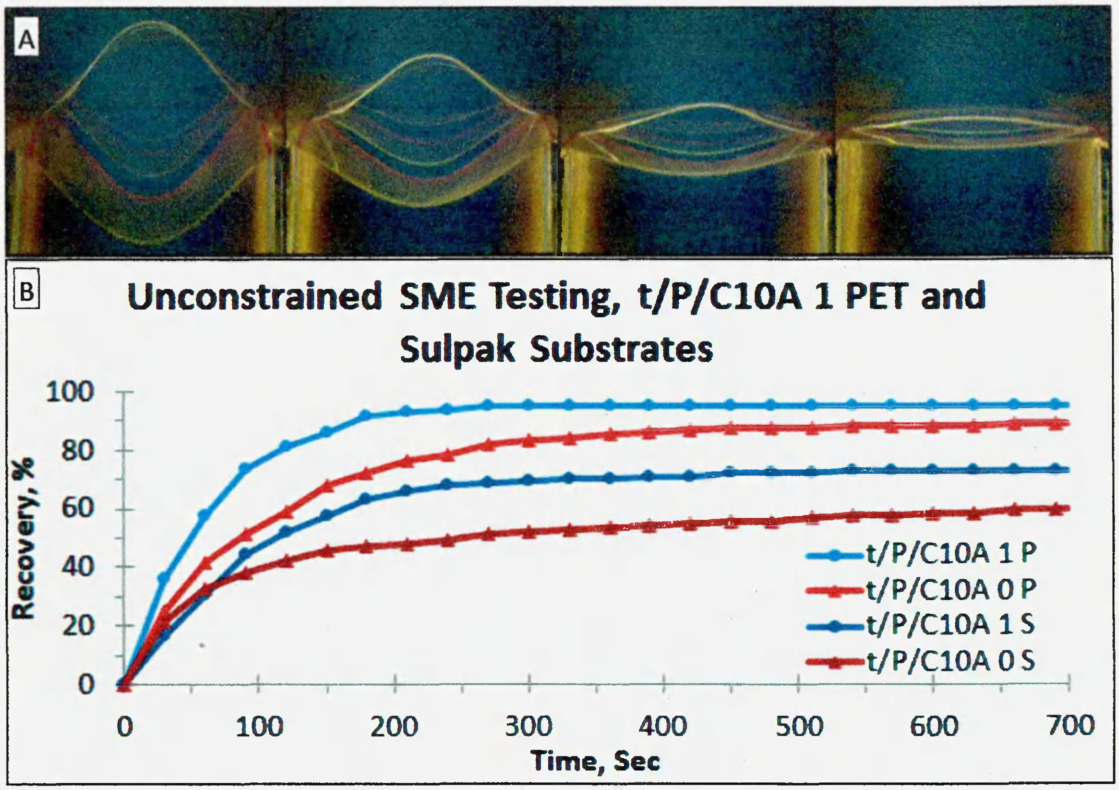

Figure 3.17: Unconstrained SME testing of t/P/C10A 0 to 1 P and S coated substrates, from temporary to permanent shape, A) still images of a t/P/C10A SMP coated PET at sequential intervals, B) plotted against time at a fixed temperature, 50 °C.

The non-coated Sulpak and PET samples were deformed to a θ_{Max} of 100 % and cooled to T_{low}, 0 to 5 °C. Upon removal of the deformation constraint each sample immediately collapsed, demonstrating θ_{Fixed} values of ca. 0%. There was some residual shape remaining in the Sulpak sample which was attributed to damaged cellulose chains that could not return to their original position.

The t/P/C10A 0 P and S coated substrates exhibited a θ_{Max} of 100 %, demonstrating that they can accommodate a high level of deformation stress. After the deformation constraint was removed, the samples were kept at T_{low}, 0 to 5 °C, with each coated substrate losing an amount of shape fixity, leading to θ_{Fixed} results of 92 and 93 %, respectively. This demonstrates that both t/P/C10A 0 P and S coated substrates can be deformed to a large degree and store the majority of the imposed strain, despite the tendency for the substrates themselves to collapse back to their permanent shapes.

Unconstrained SME evaluation was carried out with the recovered displacement being recorded every 30 seconds until the t/P/C10A 0 P and S coated substrates reached their θ_{Final}. The t/P/C10A 0 P and S coated substrates demonstrated, by achieving a

θ_{Final} of 90 and 63 %, respectively, that neither could fully recover the permanent shape and that the Sulpak substrate has a much lower recovery compared to the PET substrate.

In order to further assess the shape memory ability t/P/C10A 0 P and S coated substrates shape memory ability the $\theta_{1/2\ Final}$ time of recovery, ca. 52 and 33 seconds, and θ_{Final} time of recovery, ca. 450 and 660 seconds were recorded, respectively. These results indicate that the t/P/C10A 0 P and S coated substrates recovers 50 % of the θ_{Final} in a much shorter time compared to the final recovery time.

Sample Description	θ_{Max}, %	θ_{Fixed}, %	$\theta_{1/2Final}$, %	θ_{Final}, %	$\theta_{1/2Final}$ Time, Sec	θ_{Final} Time, Sec
t/P/C10A 0 S	100	93	28.0	63	33	660
t/P/C10A 1 S	100	83	28.0	73	24	510
t/P/C10A 0 P	100	93	41.5	90	52	450
t/P/C10A 1 P	100	80	38.0	96	18	270

Table 3.10: Unconstrained SME test results for t/P/C10A 0 to 1 P and S coated substrates, θ_{Max}, θ_{Fixed}, $\theta_{1/2Final}$, θ_{Final}, $\theta_{1/2Final}$ Time, and θ_{Final} Time, from temporary shape recovery, plotted against time at a fixed temperature, 50°C.

The t/P/C10A 1 P and S coated substrates exhibited a θ_{Max} of 100 %, demonstrating that it can accommodate a high level of deformation stress. After the deformation constraint was removed, the samples were kept at T_{low}, 0 to 5 °C, with each coated substrate losing an amount of shape fixity, leading to θ_{Fixed} results of 80 and 83 %, respectively. This demonstrates that both t/P/C10A 1 P and S coated substrates can be deformed to a large degree and store the majority, though less than a pure polymer film, of the imposed strain.

Unconstrained SME evaluation was carried out and the t/P/C10A 1 P and S coated substrates achieved a θ_{Final} of 96 and 73 %, respectively. This demonstrated that neither the t/P/C10A 1 P or S coated substrates can fully recover the permanent shape. The t/P/C10A 1 P and S coated substrates $\theta_{1/2\ Final}$ time of recovery, 18 and 24 seconds, and θ_{Final} time of recovery, 270 and 510 seconds, were recorded, respectively. These results indicate that the SME of the t/P/C10A 1 P and S coated substrates recovers 50 % of its θ_{Final} in a shorter time when compared to the t/P/C10A 0 P and S coated substrates.

These results demonstrate that addition of a small amount of C10A, 1 wt%, can drastically affect the SME on a SMP coated substrate. It was observed overall that addition of C10A causes a reduction in shape fixity but an increased and faster SME recovery.

3.7. Conclusion

It was decided to produce a shape memory coating, 20 to 30 µm, on selected packaging substrates, 100µm PET film and 60µm Sulpak paper, in order to ensure that the tBA-co-PEGDMA C10A SMP system would be fully suitable for use in the packaging industry. It was not fully clarified whether C10A formed intercalated or microcomposite networks when mixed with tBA-co-PEGDMA due to the lack of clear XRD results. However a significant difference was observed during SME evaluation between the SMP coated Sulpak and PET substrates and SMP nanocomposite coated Sulpak and PET substrates indicating that the clay was probably intercalated at 1 wt% loading.

The results observed via unconstrained SME testing revealed that depending on the substrate, the SME can be strong or weak. This is observed clearly in the coated PET and Sulpak paper, as there was a significant difference between the recovery rate and θ_{Final} recovery, with the coated PET film having a faster and greater recovery of the permanent shape compared to the coated Sulpak. However it was noted there was little difference in the initial θ_{Fixed} result or overall time of recovery. On addition of 1 wt% C10A the θ_{Fixed} result decreased in both coated substrates but a greater SME recovery rate and θ_{Final} result was observed. However neither system fully recovered even with addition of 1 wt% C10A.

It was decided to send the t90/P10 and t/P/C10A network samples to the sponsor company, Chesapeake, to attempt a sample run on their UV curing machine, a Superior Quartz UV curer, with each pass through the instrument providing a UV dose of ca. 150 mJ/cm^2.

It was found that the intensity of the UV curing machine caused the SMP system to combust during curing. This was attributed to tBA's low flash point, 18 °C.

It was therefore decided to find an alternative monomer, replacing tBA, to stop the combustion occuring during the UV curing process.

3.8. References

BEHL, M., and LENDLEIN, A., (2007). Shape-memory polymers. Materials Today, 10 (4), 20-28.

BENFARHI, S., et al. (2004). Synthesis of clay nanocomposite materials by light-induced crosslinking polymerization. European Polymer Journal, 40 (3), 493-501.

CHUN, B.C., et al. (2002). Enhanced dynamic mechanical and shape-memory properties of a poly(ethylene terephthalate)-poly(ethylene glycol) copolymer crosslinked by maleic anhydride. Journal of Applied Polymer Science, 83 (1), 27-37.

COLTHUP, N.B., DALY, L.H., and WIBERLEY, S.E., 1990. Introduction to infrared and raman spectroscopy. 3rd ed., USA ISBN 0-12-182554-X

DECKER, C., et al. (2005). Synthesis of nanocomposite polymers by UV-radiation curing. Polymer, 46 (17), 6640-6648.

DU, H.Y., and ZHANG, J.H., (2010). Shape memory polymer based on chemically cross-linked poly(vinyl alcohol) containing a small number of water molecules. Colloid and Polymer Science, 288 (1), 15-24.

GALL, K., et al. (2002). Shape memory polymer nanocomposites. Acta Materialia, 50 (20), 5115-5126.

GALL, K., et al. (2005). Thermomechanics of the shape memory effect in polymers for biomedical applications. Journal of Biomedical Materials Research Part A, 73A (3), 339-348.

HIFI INDUSTRIAL FILM LTD [online] (2010). Last accessed 1/23/2012 2012 at: http://www.hififilm.com/index.html.

INGRAM, S., et al. (2008). Influence of clay type on exfoliation, cure and physical properties of in situ polymerised poly(methyl methacrylate) nanocomposites. Polymer International, 57 (10), 1118-1127.

KELLER, L., et al. (2004). Synthesis of polymer nanocomposites by UV-curing of organoclay-acrylic resins. Polymer, 45 (22), 7437-7447.

KONG, H., GAO, C. and YAN, DY (2004). Constructing amphiphilic polymer brushes on the convex surfaces of multi-walled carbon nanotubes by in situ atom transfer radical polymerization. Journal of Materials Chemistry, 14 (9), 1401-1405.

KRAMER, N.J., et al. (2010). Shape memory polymer thin films deposited by initiated chemical vapor deposition. Macromolecules, 43 (20), 8344-8347.

LI, Q., et al. (2009). Synthesis and characterization of chitosan-based hydrogels. International Journal of Biological Macromolecules, 44 (2), 121-127.

LIU, C., QIN, H., and MATHER, P.T., (2007). Review of progress in shape-memory polymers. Journal of Materials Chemistry, 17 (16), 1543-1558.

OKAMOTO, M., et al. (2000). Synthesis and structure of smectic clay/poly(methyl methacrylate) and clay/polystyrene nanocomposites via in situ intercalative polymerization. Polymer, 41 (10), 3887-3890.

OKAMOTO, M., et al. (2001). Dispersed structure change of smectic clay/poly(methyl methacrylate) nanocomposites by copolymerization with polar comonomers. Polymer, 42 (3), 1201-1206.

OKAMOTO, M., et al. (2001). Dispersed structure change of smectic clay/poly(methyl methacrylate) nanocomposites by copolymerization with polar comonomers. Polymer, 42 (3), 1201-1206.

ORAL, A., et al. (2009). Poly(methyl methacrylate)/clay nanocomposites by photoinitiated free radical polymerization using intercalated monomer RID B-8338-2008. Polymer, 50 (16), 3905-3910.

ORTEGA, A.M., et al. (2008). Structure-property relationships in photopolymerizable polymer networks: Effect of composition on the crosslinked structure and resulting thermomechanical properties of a (meth)acrylate-based system. Journal of Applied Polymer Science, 110 (3), 1559-1572.

PÜHRINGER, F., (2012). Summer Placement Student, Montanuniversität Leoben. Conversation with the author, 19 January. Personal communication.

SAFRANSKI, D.L., and GALL, K., (2008). Effect of chemical structure and crosslinking density on the thermo-mechanical properties and toughness of (meth)acrylate shape memory polymer networks. Polymer, 49 (20), 4446-4455.

SAFRANSKI, D., and GALL, K., (2008). Effect of chemistry on thermo-mechanical shape-memory properties of acrylate networks. Advances in Heterogeneous Material Mechanics 2008, 637.

SHEMPER, B.S., et al. (2004). Synthetic clay nanocomposite-based coatings prepared by UV-cure photopolymerization. Journal of Applied Polymer Science, 93 (3), 1252-1263.

SMITH, K.E., et al. (2009). The effect of the glass transition temperature on the toughness of photopolymerizable (meth)acrylate networks under physiological conditions. Polymer, 50 (21), 5112-5123.

SMITH, K.E., TEMENOFF, J. S. and GALL, K. (2009). On the toughness of photopolymerizable (meth)acrylate networks for biomedical applications. Journal of Applied Polymer Science, 114 (5), 2711-2722.

SOUTHERN CLAY PRODUCTS, INC. / A subsidiary of Rockwood Specialties Inc., 2009. Product bulletin/Cloisite®. Gonzales: Southern Clay Products, Inc.

TSAI, T.Y., et al. (2009). Effect of clay with different cation exchange capacity on the morphology and properties of poly(methyl methacrylate)/clay nanocomposites. Polymer Composites, 30 (11), 1552-1561.

TSAI, Y., et al. (2008). Shape memory effects of poly(ethylene terephthalate-co-ethylene succinate) random copolymers. European Polymer Journal, 44 (2), 550-554.

VOIT, W., et al. (2010). High-strain shape-memory polymers. Advanced Functional Materials, 20 (1), 162-171.

WARREN, P.D., MCGRATH, D.V., and GEEST, J.P.V., (2010). Effect of crosslinker length and composition on the hydrophobicity and thermomechanical response of acrylate-based shape-memory polymers. Macromolecular Materials and Engineering, 295 (4), 386-396.

WU, G.L., et al. (2010). Preparation and characteration of UV-cured EA/MMT nanocomposites via in-situ polymerization. Journal of Macromolecular Science Part A-Pure and Applied Chemistry, 47 (7), 647-654.

XU, Y.J., et al. (2006). Improving the physical properties of PEA/PMMA blends by the uniform dispersion of clay platelets. Polymer, 47 , 4564-4570.

YAKACKI, C.M., et al. (2011). Impact of shape-memory programming on mechanically-driven recovery in polymers. Polymer, 52 (21), 4947-4954.

YANG, F., et al. (2007). Nanoscale indent formation in shape memory polymers using a heated probe tip. Nanotechnology, 18 (28), 285302.

ZANG, Y.L., et al. (2009). Preparation of ultraviolet-cured bisphenol A epoxy Diacrylate/Montmorillonite nanocomposites with a bifunctional, reactive, organically modified montmorillonite as the only initiator via in situ polymerization. Journal of Applied Polymer Science, 111 (2), 813-818.

Chapter 4: Evaluation of Isobornyl Acrylate, Isobonyl Methacrylate and tert-Butyl Methacrylate as Potential Packaging SMP

4. Introduction

Previously tBA was copolymerised with PEGDMA using DMPA as a photoinitiator, it was found that SMP films could be cast or coated onto a packaging substrate e.g. Sulpak paper. As the sample properties were promising the tBA-co-PEGDMA solutions were sent for UV curing at the Chesapeake factory in Bradford. Unfortunately when the polymer solution was coated onto a substrate and UV cured, on a Superior Quartz UV curer, the high intensity of the UV light and the subsequent heat produced, caused the tBA monomer to combust.

This combustion made the tBA monomer unsuitable for main line production using a UV curing method, therefore a replacement was required. In order to source a replacement monomer for tBA a number of factors needed to be considered including, SME, T_g, flash point, boiling point and viscosity, table 4.1.

Monomer	T_g, °C	Flash Point, °C	Boiling Point, °C	Viscosity, mPa.s at 25 °C	SME
tert-butyl acrylate, tBA (Gall and Safranski, 2009)	41	18	120	1.3	YES
Methyl acrylate, MA (Yakacki et al., 2008)	8	-3	80	0.5	YES
Cyclohexyl acrylate	15	68	-	2.5	NO
Lauryl acrylate	15	110	120	4	NO
Stearyl acrylate, StA (Kagami et al., 1996)	35	191	153	11	YES
Stearyl methacrylate, StMA (Agarwal et al., 1997)	-100	198	270	8.2	YES
Isobutyl methacrylate	48	45	155	0.9	NO
Isobornyl acrylate, IBoA (Voit et al., 2008)	62	109	104	2.6	YES
Methyl methacrylate, MMA (Yakacki et al., 2008)	105	11	101	0.6	YES
tert-butyl methacrylate, tBMA (Gall and Safranski, 2009)	107	30	67	0.9	YES
Isobornyl methacrylate, IBoMA (Tong, 2007, 2011)	>111 to 155	117	120	7.4 to 13	YES

Table 4.1: Properties of interest for potential replacement monomers of tBA in order to produce a SMP capable of undergoing an intense UV cure process.

There are several choices available to replace the tBA monomer, table 4.1, however not all possible replacements are suitable. The monomers cyclohexyl acrylate, lauryl acrylate and isobutyl methacrylate are examples of potential monomers which have several desirable properties i.e. T_g, flash point, boiling point and viscosity, however, to our knowledge, no reports of SME have been published therefore they are not considered replacements of tBA.

Agarwal et al., (1997) and Kagami et al., (1996) have reported the potential of stearyl methacrylate, StMA, copolymerised with poly(MMA) and stearyl acrylate, StA copolymerised with StMA cross-linked by N,N'-methylenebisacrylamide, respectively, to show SME (Lendlein and Kelch, 2002). Kagami et al., prepared the StA-co-StMA SMP via a radical polymerisation, using α,α'-azobis(isobutyronitrile) as a thermal radical initiator, and found that the T_{trans} of the resulting SMP network was the T_m. It was also found that with a StA content of 25 mol% a T_m of ca. 35 °C could be achieved with good shape fixity, no shape return at storage temperature when stretched by 150 %, and that the permanent shape could be fully recovered when it was re-heated to the T_{trans}, T_m. The StA-co-StMA SMP demonstrates a good SME with desirable properties, flash point, boiling point and viscosity, from both StA and StMA.

Another report of StA based SMP was presented by Lin et al., (2010) where a SMP poly(StA-co-acrylamide) network was formed. The poly(StA-co-AM) SMP has a T_{trans} = T_m, at ca. 34 °C with an optimal network shape recovery of 97 %. However the material is not very stiff above or below its T_m, with a storage modulus ranging from ca. 11 MPa at 0 °C to < 1 MPa at 50 °C. This makes these polymer systems undesirable for a SMP packaging device as it is unlikely that they will be able to generate enough force in order to show SME whilst coated onto a substrate.

A photopolymerised SMP blend of MMA copolymerised with PEGDMA using DMPA as an initiator has been reported by Yakacki et al., (2008). It was found that the T_{trans} (= T_g) could be tailored between 56 to 92 °C, and that the rubbery modulus could be tailored between 9.3 and 23.0 MPa. Each SMP sample was heated to its T_{trans}, compressed by 30 %, and fixed at ca. 0 °C. Each SMP showed good shape fixity, displaying no early onset of recovery at the storage temperature, and full shape recovery when undergoing free strain recovery vs temperature. This demonstrates that MMA is an impressive SMP when cross-linked with PEGDMA, however it has a lower flash point than tBA making it unsuitable for a high intensity UV photopolymerisation cure, therefore it is an unsuitable replacement for tBA.

Gall and Safranski (2009) reported that tert-butyl methacrylate, tBMA, can be potentially used as a SMP when cross-linked with PEGDMA. Although no specific results pertaining to SME of tBMA were reported, it was commented that with the addition of methyl side groups or large ringed structures close to the functional group an increase in the T_g temperature was anticipated. This suggests that tBMA could be a suitable replacement for tBA as it has a higher T_g, flash point, boiling point and a lower viscosity, table 1.

Photopolymerised isobornyl acrylate, IBoA, copolymerised with methyl acrylate and cross-linked with bisphenol A ethoxylate di(meth)acrylate has been reported as a SMP (Voit et al., 2010). It was found that the MMA-co-IBoA T_g could be readily adjusted between 28 and 55 °C by varying the weight ratios of the monomers. The copolymer with a T_g of 28 °C displayed recoverable strains of up to ca. 800 %, a copolymer with a T_g of 37 °C displayed a full recoverable strain of up to ca. 660 % and a copolymer with a T_g of 55 °C demonstrated a full recoverable strain of up to ca. 550 %. This indicates that although methyl acrylate has a much lower T_g, flash and boiling point compared to tBA it can be combined with IBoA and show impressive SME properties.

It has also been reported by Tong (2007, 2011) that IBoA and isobornyl methacrylate, IBoMA, can potentially be used to form SMP. The monomer, IBoA or IBoMA, is initially copolymerised using a small amount of a silane cross-linker forming alkylsiloxyl groups in the acrylate polymer. The polymer is then dissolved in a solvent to form a polymer solution. The polymer is then dried at room temperature, the alkylsiloxyl groups are converted into silanol groups, via hydrolysis, forming a SMP network structure by polycondensation. Althought the exact shape memory abilities were not reported both IBoA and IBoMA have desirable T_g, flash points, boiling points and viscosities in the correct range to replace tBA.

From the potential replacements of tBA, table 4.1, the most suitable monomers are the IBoA, tBMA and IBoMA, figure 4.0, as they have the most desirable and potentially beneficial properties. Therefore in order to establish which of these is the most suitable for UV initiated large scale production each will need to be characterised for cure in UV, mechanical properties and shape memory abilities.

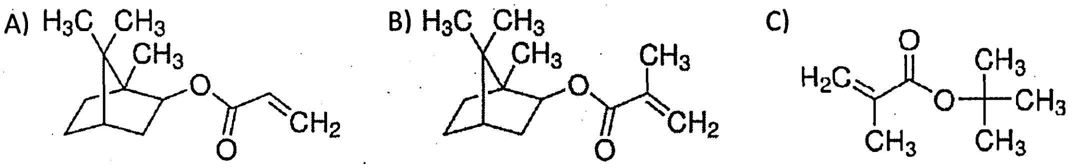
A)
H3C
CH3
CH3
O
O
CH2
B)
H3C
CH3
CH3
CH3
O
O
CH2
C)
O
H2C
O
CH3
CH3
CH3
CH3

Figure 4.0: Chemical structure of A) IBoA, B) IBoMA and C) tBMA.

4.1. Experimental

All characterisation methods were carried out in MERI at Sheffield Hallam University.

4.1.1. Materials

The mono-functional acrylates IBoA, IBoMA, tBMA, di-functional acrylate PEGDMA, with an average molecular weight of 750 g mol^{-1} for the PEG portion, photoinitiator DMPA, isopropylthioxanthone, ITX, EDB, and ethanolamines, triethanolamine, TEA, and methyl diethanolamine, DEA, were purchased from Sigma-Aldrich and used as received. The initial inhibitor was not removed from the IBoA, IBoMA, tBMA and PEGDMA in order to prevent any curing occurring during the mixing of the liquid polymers and the photoinitiators.

The photoinitiator ethyl (2,4,6-trimethylbenzoyl)-phenyl phosphinate, TPO-L, and oxygen scavenger, 2-Ethylhexyl 4-(dimethylamino)benzoate, EHA were both supplied by Chesapeake, Bradford.

The 100 µm thick PET substrates were supplied by HiFi films ltd (2010) and 60 µm thick Sulpak paper was supplied by Dr David Guerin, CTP.

4.1.2. IBoA, IBoMA and tBMA Network Sample Preparation

SMP networks were formed by using selected ratios of IBoA, IBoMA or tBMA and PEGDMA monomers, table 4.2. These were uniformly blended using method reported in section 3.1.3.1.

Sample Description	Short Description	Acrylate wt%	PEGDMA wt%	DMPA wt%	EDB wt%
IBoA15/PEGDMA85	I15/P85	15	85	3.5	1.5
IBoA60/PEGDMA40	I60/P40	60	40	3.5	1.5
IBoA70/PEGDMA30	I70/P30	70	30	3.5	1.5
IBoA80/PEGDMA20	I80/P20	80	20	3.5	1.5
IBoA90/PEGDMA10	I90/P10	90	10	3.5	1.5
IBoA100/PEGDMA0	I100/P0	100	0	3.5	1.5
IBoMA15/PEGDMA85	IM15/P85	15	85	3.5	1.5
IBoMA60/PEGDMA40	IM60/P40	60	40	3.5	1.5
IBoMA70/PEGDMA30	IM70/P30	70	30	3.5	1.5
IBoMA80/PEGDMA20	IM80/P20	80	20	3.5	1.5
IBoMA90/PEGDMA10	IM90/P10	90	10	3.5	1.5
IBoMA100/PEGDMA0	IM100/P0	100	0	3.5	1.5
tBMA15/PEGDMA85	tM15/P85	15	85	3.5	1.5
tBMA60/PEGDMA40	tM60/P40	60	40	3.5	1.5
tBMA70/PEGDMA30	tM70/P30	70	30	3.5	1.5
tBMA80/PEGDMA20	tM80/P20	80	20	3.5	1.5
tBMA90/PEGDMA10	tM90/P10	90	10	3.5	1.5
tBMA100/PEGDMA0	tM100/P0	100	0	3.5	1.5

Table 4.2: Comonomer solutions containing IBoA, IBoMA or tBMA and PEGDMA compositions, for the production of cross-linked polymer networks.

4.1.3. Coated Substrate Sample Preparation

IBoA networks, I90/P10, with varying initiators and oxygen inhibitors were prepared in order to coat Sulpak paper substrates, table 4.3. Previously reported in section 3.1.3.1.

Sample Description:	Photoinitiator wt%			Oxygen Inhibitors wt%			
	TPO-L	DMPA	ITX	EDB	EHA	TEA	DEA
C00	-	3.50	-	1.50	-	-	-
C01	-	3.50	-	1.50	-	5.00	-
C02	-	3.50	-	1.50	-	-	5.00
C03	-	3.50	-	3.00	-	-	5.00
C04	-	4.50	-	1.50	-	-	5.00
C05	-	5.50	-	1.50	-	-	5.00
C06	1.75	-	1.75	-	1.50	-	-
C07	1.75	-	1.75	-	1.50	5.00	-
C08	1.75	-	1.75	-	1.50	5.00	-
C09	3.50	-	1.75	-	1.50	5.00	-
C10	1.75	-	3.50	-	1.50	5.00	-
C11	1.75	-	1.75	-	3.00	5.00	-
C12	1.75	-	1.75	-	4.50	5.00	-
C13	1.75	1.75	-	1.50	-	-	5.00
C14	1.75	1.75	-	-	1.50	-	5.00
C15	3.50	-	-	1.50	-	-	5.00
C16	3.50	-	-	-	1.50	-	5.00
C17	-	0.35	-	4.50	-	-	5.00

Table 4.3: Comonomer solutions of I90/P10 compositions, for the production of cross-linked polymer networks. Designed to evaluate different initiator and oxygen inhibitors.

4.1.4. IBoA, IBoMA and tBMA Network Photopolymerisation Method

Previously reported in section 3.1.4.

4.1.5. Coated Substrate Photopolymerisation Method

In order to polymerise the comonomer solution onto the substrate, the typical glass slide technique, section 4.1.4, was not suitable as the substrate creases within the mould and does not achieve a smooth coating. Therefore the polymer solution first had to be applied to the substrate, via a meter bar, leaving ca. a 30 μm thick film. The coated film was placed onto the UV conveyer belt (Superior Quartz UV curer), and a UV dose of 150 mJ/cm^2 per pass was applied. The coated substrate was removed at the end of the conveyer belt and tested for cure; if not fully cured the process was repeated until a full cure was achieved. After full cure the sample was stored.

4.1.6. Techniques

4.1.6.1. ATR-FTIR Spectroscopy

ATR-FTIR was used to observe the vibrational modes in the IBoA, IBoMA and tBMA -co-PEGDMA750 networks. ATR-FTIR is reported on previously in section 3.1.5.3.

4.1.6.2. Coated Substrate Cure Assessment

IBoA, IBoMA and tBMA-co-PEGDMA networks were produced and coated onto substrates. The coated substrates were mounted onto stiff card, and passed through the UV curer. Cure was assessed after each pass through the UV curer by the 'educated' thumb test, a simplistic technique used to continuously judge the progress of curing (Dent, 2010). The thumb test is achieved by applying pressure through the thumb onto the cured film, twisting the thumb 90 ° and assessing the state of the film. If curing was not fully complete the action of the thumb caused damage to the film and the coated substrate would require further curing.

4.1.6.3. Dynamic Mechanical Analysis

DMA was carried out to investigate the SMP samples viscoelastic properties. DMA is reported on previously in section 3.1.5.5.

4.1.6.4. Unconstrained Shape Memory Effect Evaluation

Unconstrained recovery of the SMP coated substrates was performed to investigate shape memory ability in the absence of strain. SME is reported on previously in section 3.1.5.6.

4.2. IBoA, IBoMA and tBMA Network; Results and Discussion

4.2.1. Network Structure

4.2.1.1. ATR-FTIR spectroscopy

ATR-FTIR spectra, 700 to 3500 cm^{-1}, of the I100/P0 to I0/P100 networks are presented in figure 4.1, IM100/P0 to IM0/P100 networks, figure 4.3 and tM100/P0 to tM0/P100 networks, figure 4.5, respectively. This work was carried out to confirm that the polymer networks were fully polymerised and to study the effects of increasing PEGDMA, and therefore the cross-linking density, on the IBoA, tBMA and IBoMA polymer networks.

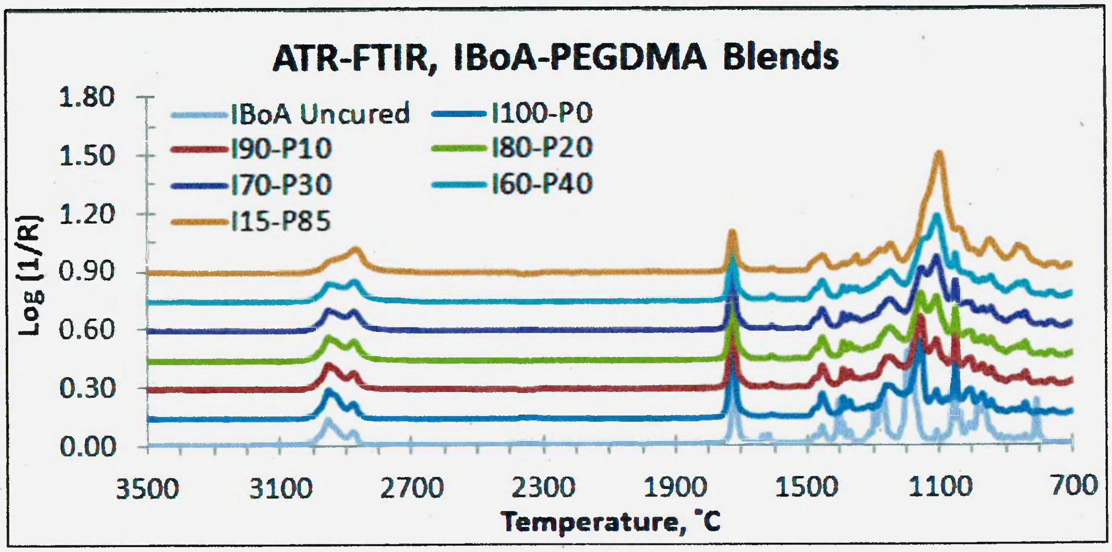

Figure 4.1: ATR-FTIR spectra of unreacted IBoA and cured I100/P0 to I15/P85 samples

For unreacted IBoA the major peaks displayed in the high frequency region, ca. 3100 to 2700 cm^{-1}, that were observed arise from CH_3, CH_2 and CH stretches. At lower frequency, ca. 1800 to 1100 cm^{-1}, ester C=O stretch, C=C double bond stretch and an ester C-O stretch were observed. Finally at the lower frequencies, below 1000 cm^{-1}, IR bands due to $C=CH_2$ rocking and wag, C=CH wag and $C=CH_2$ twist as well as CH_3 rocking vibrations are observed (Colthupet al., 1990).

Cured samples of I100/P0 to I15/P85 displayed major peaks in the high frequency region, ca. 3100 to 2700 cm^{-1}, that arise from CH_3, CH_2 and CH stretches. At lower frequency, ca. 1800 to 1100 cm^{-1}, ester C=O stretch, and ester C-O stretch was observed. Finally at the lower frequencies, below 1000 cm^{-1}, IR bands due to CH_2, CH_3

and CH vibrations are observed (Colthup et al., 1990). The IR bands relating to the C=C double bond previously observed were no longer present.

In order to assess whether the I100/P0 to I15/P85 polymer networks were crosslinked, ATR-FTIR was used to establish the disappearence of peaks assigned to the acrylate functional group, the C=C double bond (Warren et al., 2010). The three peaks that illustrate the disappearence of the functional acrylate group most clearly were the C=C peaks, ca. 1638 and 1615 cm^{-1}, and the C=CH$_2$ twist, ca. 809 cm^{-1}, figure 4.2.

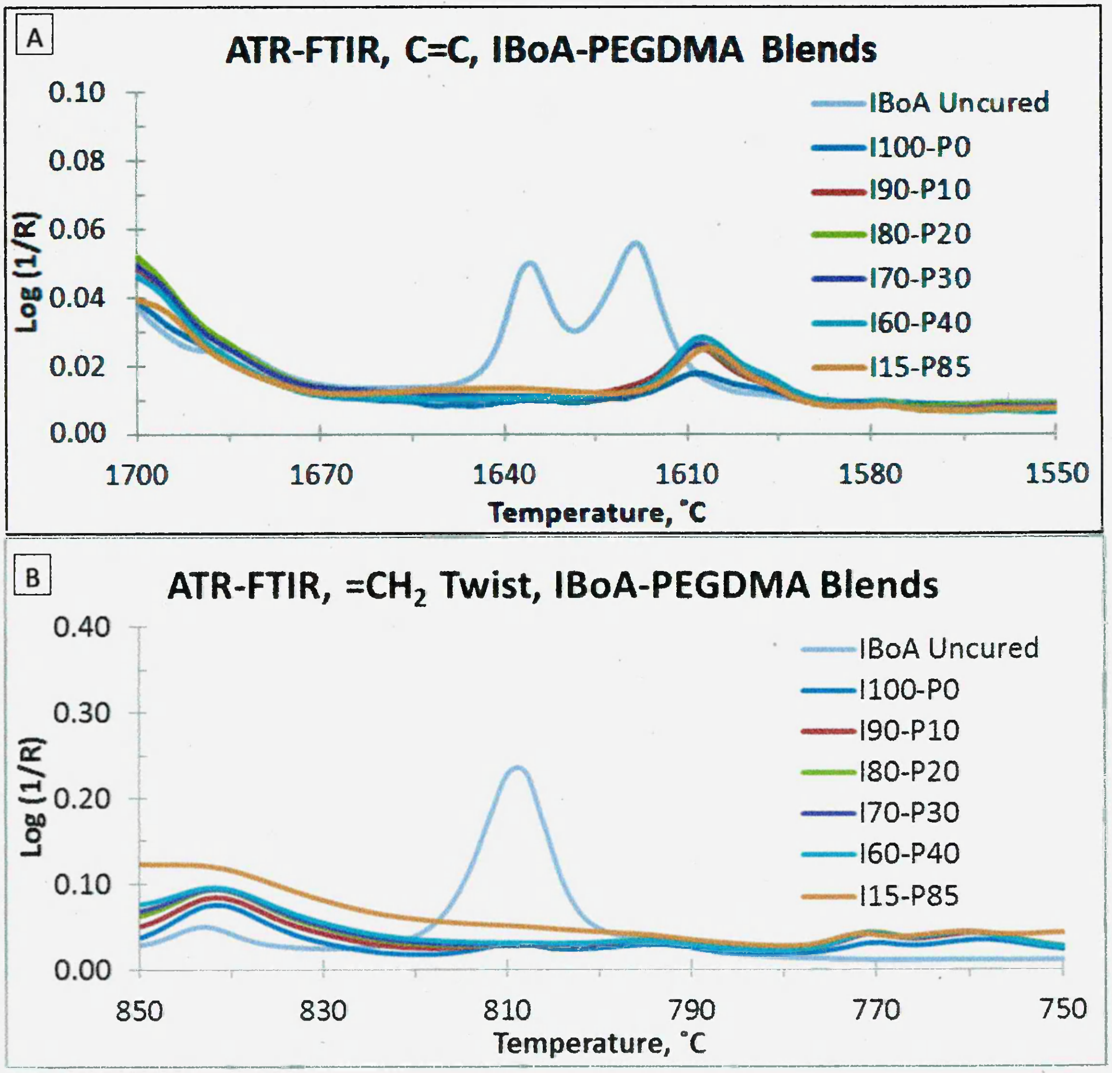

Figure 4.2: ATR-FTIR spectra of unreacted IBoA and cured I100/P0 to I15/P85 samples, A) comparison of peaks in the C=C region and B) comparison of peaks in the C=CH$_2$ twist region.

Figure 4.2 shows that after curing of I100/P0 to I15/P85 samples, the C=C peaks and C=CH$_2$ peak reduce to unobservable levels. This indicates that the cured polymer

networks are fully polymerised, with no evidence for acrylate functional groups remaining. This result also suggests that, with increasing PEGDMA content and therefore an increase in viscosity, there was no apparent residual areas on the surface where acrylate bands are observed indicating a total surface cure.

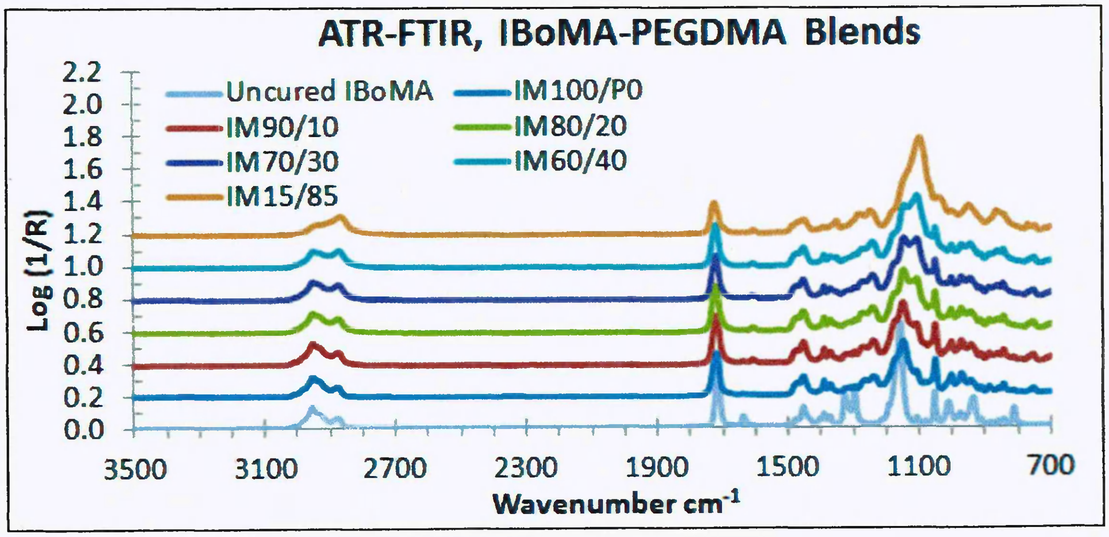

Figure 4.3: ATR-FTIR spectra of unreacted IBoMA and cured IM100/P0 to IM15/P85 samples.

For unreacted IBoMA the major peaks present are similar to those of IBoA, except there is no CH stretching. When the spectrm of the unreacted IBoMA was compared to those for the cured networks it was observed that the C=C double bonds were no longer present.

Once again, ATR-FTIR was used to evaluate the extent of cross-linking by comparing the spectrum for unreacted IBoMA to those for the cured networks. Two peaks demonstate this clearly, the single C=C peak, ca. 1637 cm^{-1}, and the $C=CH_2$ twist, ca. 812 cm^{-1}, figure 4.4.

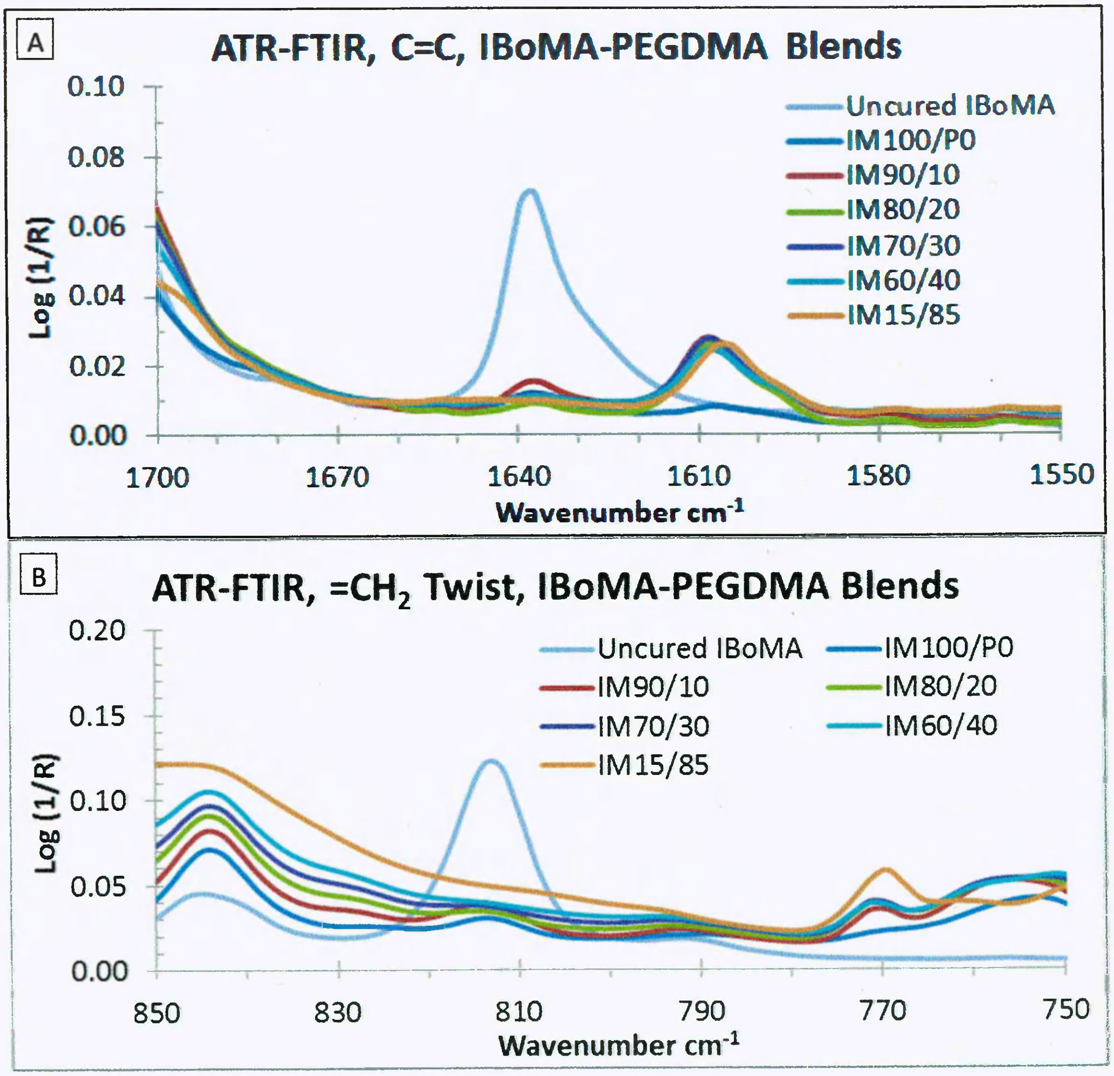

Figure 4.4: ATR-FTIR spectra of unreacted IBoMA and cured IM100/P0 to IM15/P85 samples, A) comparison of peaks in the C=C region and B) comparison of peaks in the $C=CH_2$ twist region.

Figure 4.4 shows that after curing the IM100/P0 to IM15/P85 samples, both the single C=C peak and $C=CH_2$ peak reduced to unobservable levels. This indicates, once again, that after curing the polymer networks are fully polymerised on the surface, with no evidence for acrylate functional groups remaining.

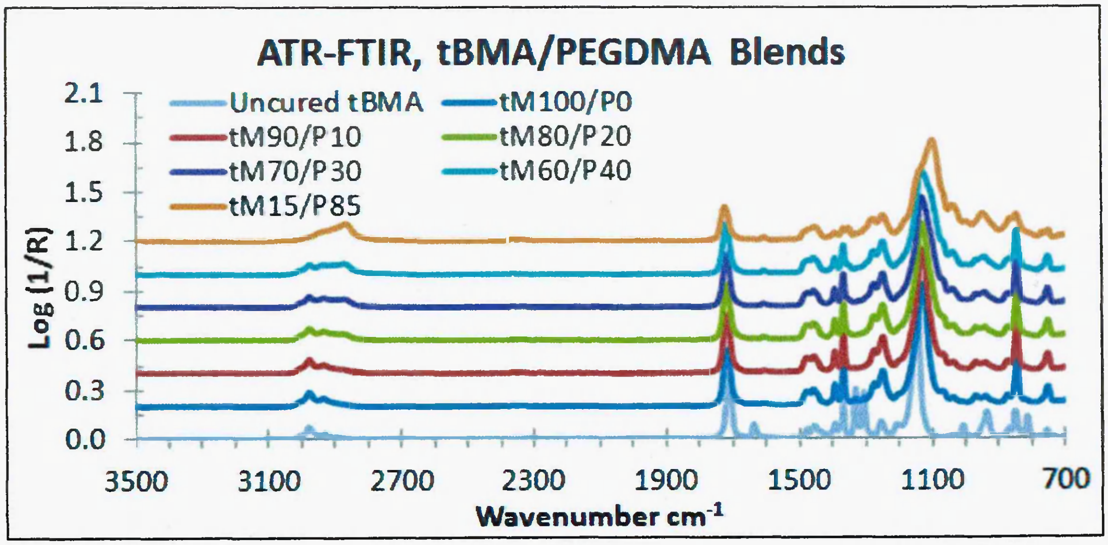

Figure 4.5: ATR-FTIR spectra of unreacted tBMA and cured tM100/P0 to tM15/P85 samples

For unreacted tBMA the major IR peaks present are similar to those of IBoA, with the exception of the CH stretching and tert-butyl CH_3 deformations at ca. 1350 cm^{-1} which are not present. When the spectrum for the unreacted tBMA was compared to those for the cured networks it was observed that the C=C double bonds were no longer present. ATR-FTIR was again used to categorise the extent of cross-linking by comparing unreacted tBMA to the cured networks. Two peaks demonstate this clearly, the single C=C peak, ca. 1638 cm^{-1}, and the $C=CH_2$ twist, ca. 812 cm^{-1}, figure 4.6.

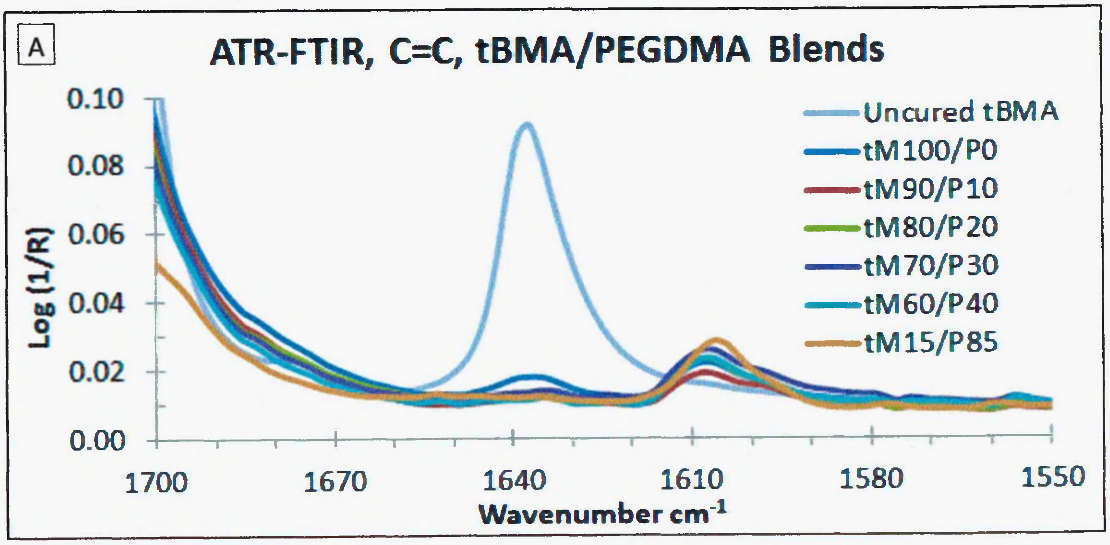

Figure 4.6: ATR-FTIR spectra of unreacted tBMA and cured tM100/P0 to tM0/P100 samples, A) comparison of peaks in the C=C region and B) comparison of peaks in the $C=CH_2$ twist region

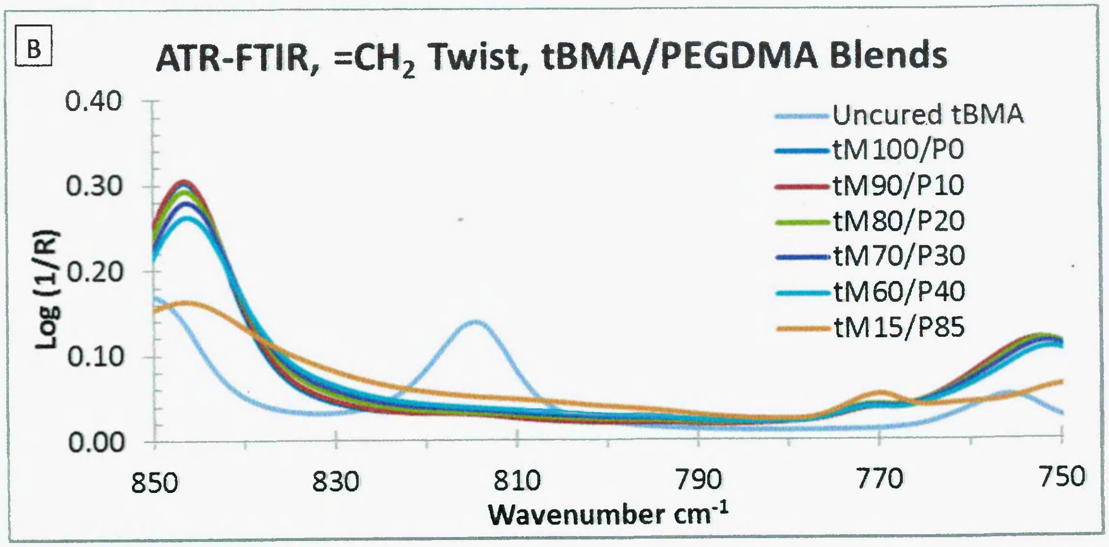

Figure 4.6: ATR-FTIR spectra of unreacted tBMA and cured tM100/P0 to tM0/P100 samples, A) comparison of peaks in the C=C region and B) comparison of peaks in the C=CH$_2$ twist region.

Figure 4.6 shows that after curing of tM100/P0 to tM15/P85 samples, the single C=C peak and C=CH$_2$ peak were essentially absent. This once again confirms that the cured polymer networks are fully polymerised on the surface.

Overall the ATR-FTIR spectra of the IBoA, IBoMA and tBMA networks indicate that they are all fully cured which was identical to the tBA networks. However as the ATR FTIR only penetrates to a depth of 4 to 6 µm in the sample a full cure within the sample bulk cannot be fully confirmed.

4.2.2. Mechanical Properties

4.2.2.1. Dynamic Mechanical Analysis

The dynamic mechanical properties, storage modulus, loss modulus and tan δ, of t90/P10, I100/P0 to I0/P100, IM100/P0 to IM0/P100 and tM100/P0 to tM0/P100 are plotted in figures 4.7, 4.8 and 4.9, respectively, as a function of temperature, -40 to 140 °C. The corresponding dynamic mechanical properties are summarized in tables 4.4, 4.5 and 4.6, respectively. The t90/P10 network is included for a direct comparison of the original selected network.

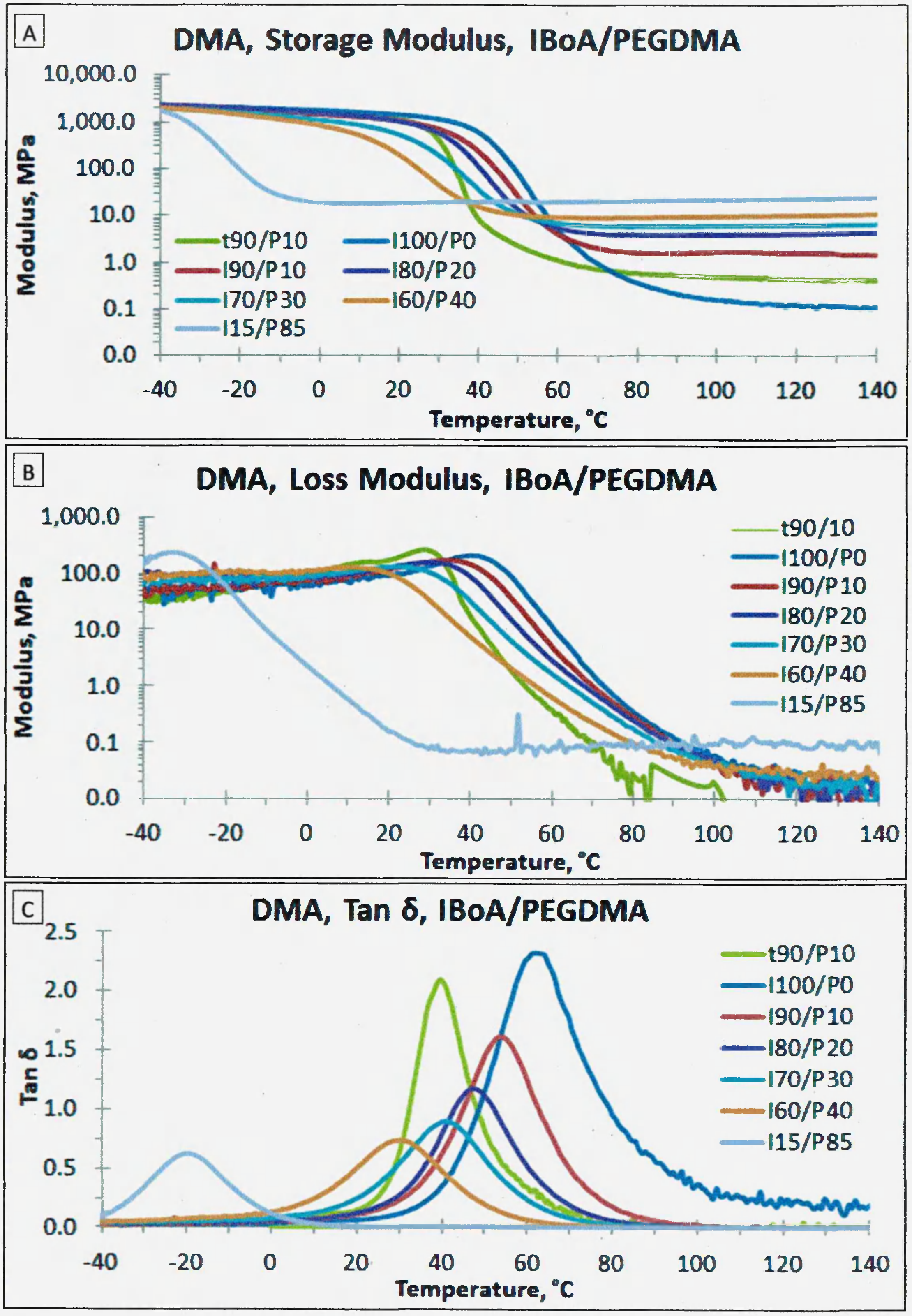

Figure 4.7: DMA data: temperature dependance of A) storage modulus, B) loss modulus and C) tan δ of t90/P10 and I100/P0 to I15/P85 over the temperature range -40 to 140 °C.

At -40 °C an initial storage modulus of ca. 2264 MPa was recorded for the I100/P0 network, figure 4.7 A. The modulus drops steadily until ca. 28 °C reaching ca. 1211 MPa, i.e. ca. 53 % of the initial value. After this the modulus begins to drop steeply, indicating the onset of the $T_{g\alpha}$ transition, figure 4.7 A, the point at which the shape memory effect is predicted to begin. At the tan δ_{max}, 2.3 tan δ, the T_g of the polymer system is established as 62 °C, figure 4.7 C. The high intensity tan δ_{max} value indicates that the SMP will behave more like an elastomer and experience a large amount of shape recovery when SME is carried out. Alternatively a low intensity tan δ_{max} value indicates that a smaller amount of shape recovery will occur (Chun et al., 2002, Tsai et al., 2009).

At tan δ_{max} the modulus has dropped to 3.4 MPa and continues to drop steadily until the $T_{g\alpha}$ transition has finished, ending with a modulus of ca. 0.2 MPa. Tsai et al., (2008) has suggested that a sharp, at least one order of magnitude, drop in storage modulus means that a polymer system will demonstrate SME (Du and Zhang, 2010). The I100/P0 network demonstrates ca. a four order magnitude drop in storage modulus therefore SME should occur. The I0/P100 i.e. pure PEGDMA, network has been described previously, section 3.2.3.

Sample Description	Storage Modulus, MPa							$T_{g\alpha}$ °C	Tan δ_{max}
	-40 °C	-20 °C	10 °C	40 °C	70 °C	100 °C	140 °C		
t90/P10	2043	1888	1406	8	0.7	0.5	0.4	39	2.1
I100/P0	2264	2032	1602	583	1.0	0.2	0.1	62	2.3
I90/P10	1938	1743	1272	222	2	2	1.0	53	1.6
I80/P20	2338	1970	1317	113	4	4	4	47	1.2
I70/P30	1920	1550	857	41	6	6	7	41	0.9
I60/P40	1993	1447	507	15	9	10	11	31	0.7
I15/P85	1794	93	18	20	20	22	25	-20	0.6

Table 4.4: Summary of dynamic mechanical values for t90/P10 and I100/P0 to I15/P85 obtained from DMA over the temperature range of -40 to 140 °C.

At -40 °C an initial storage modulus of ca. 1938, 2338, 1920, 1993 and 1794 MPa was recorded for the I90/P10 to I15/P85 networks, respectively. The moduli drop steadily until ca. 18, 16, 6, -6 and -39 °C, respectively, reaching values of ca. 1112, 1145, 970, 1014 and 1627 MPa i.e. ca. 57, 49, 51, 51 and 91 %, respectively, of the initial values. After this the moduli begin to steeply drop, indicating the onset of the $T_{g\alpha}$ transition. At the tan δ_{max}, 1.6, 1.2, 0.9, 0.7 and 0.6 tan δ, respectively, the T_g of the polymer networks are 53, 47, 41, 31 and -20 °C, respectively. The higher intensity tan δ_{max} results i.e. I90/P0 to I70/P30 networks, suggests a large amount of shape recovery will occur when SME is carried out whereas the lower intensity tan δ_{max} results i.e. the I60/P40 and I15/P85 networks, indicate that less shape recovery will occur (Chun et al., 2002, Tsai et al., 2009).

At tan δ_{max} the moduli have dropped to ca. 12, 21, 28, 38 and 85 MPa, respectively, and continue to drop steadily until each $T_{g\alpha}$ transition has finished, ending with moduli values of ca. 2, 4, 6, 9 and 20 MPa, respectively. The I90/P10 to I15/P15 networks all demonstrate at least a two order magnitude drop in storage modulus therefore useful SME is predicted (Tsai et al., 2008, Du and Zhang, 2010).

These results are as expected, with the drop in storage modulus magnitude and increase of rubbery modulus after the $T_{g\alpha}$ transition falling between the pure IBoA and PEGDMA polymer networks, decreasing and increasing, respectively, as the PEGDMA content increases.

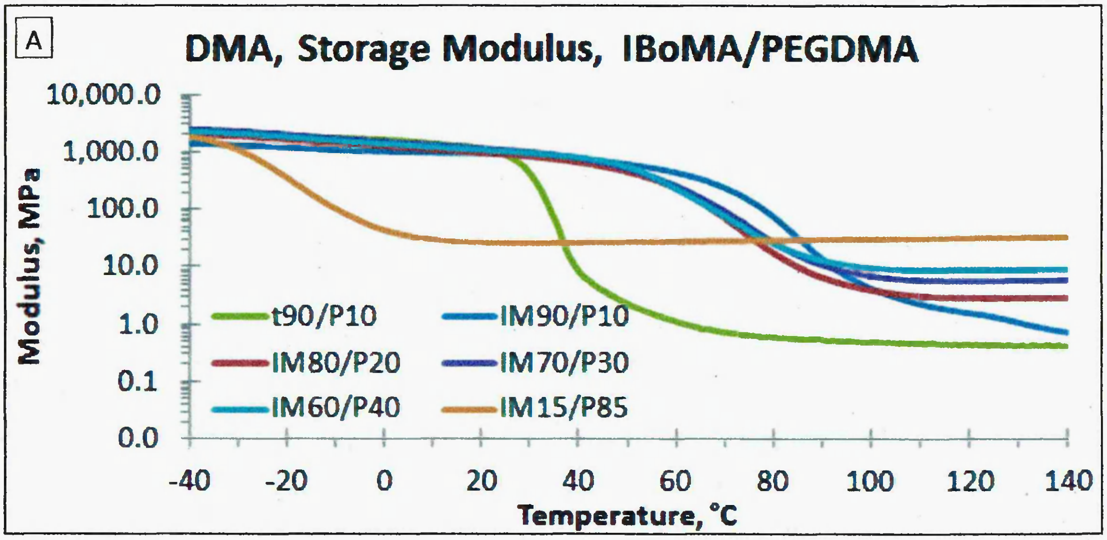

Figure 4.8: DMA data: temperature dependance of A) storage modulus, B) loss modulus and C) tan δ of t90/P10 and IM90/P10 to IM15/P85 over the temperature range -40 to 140 °C.

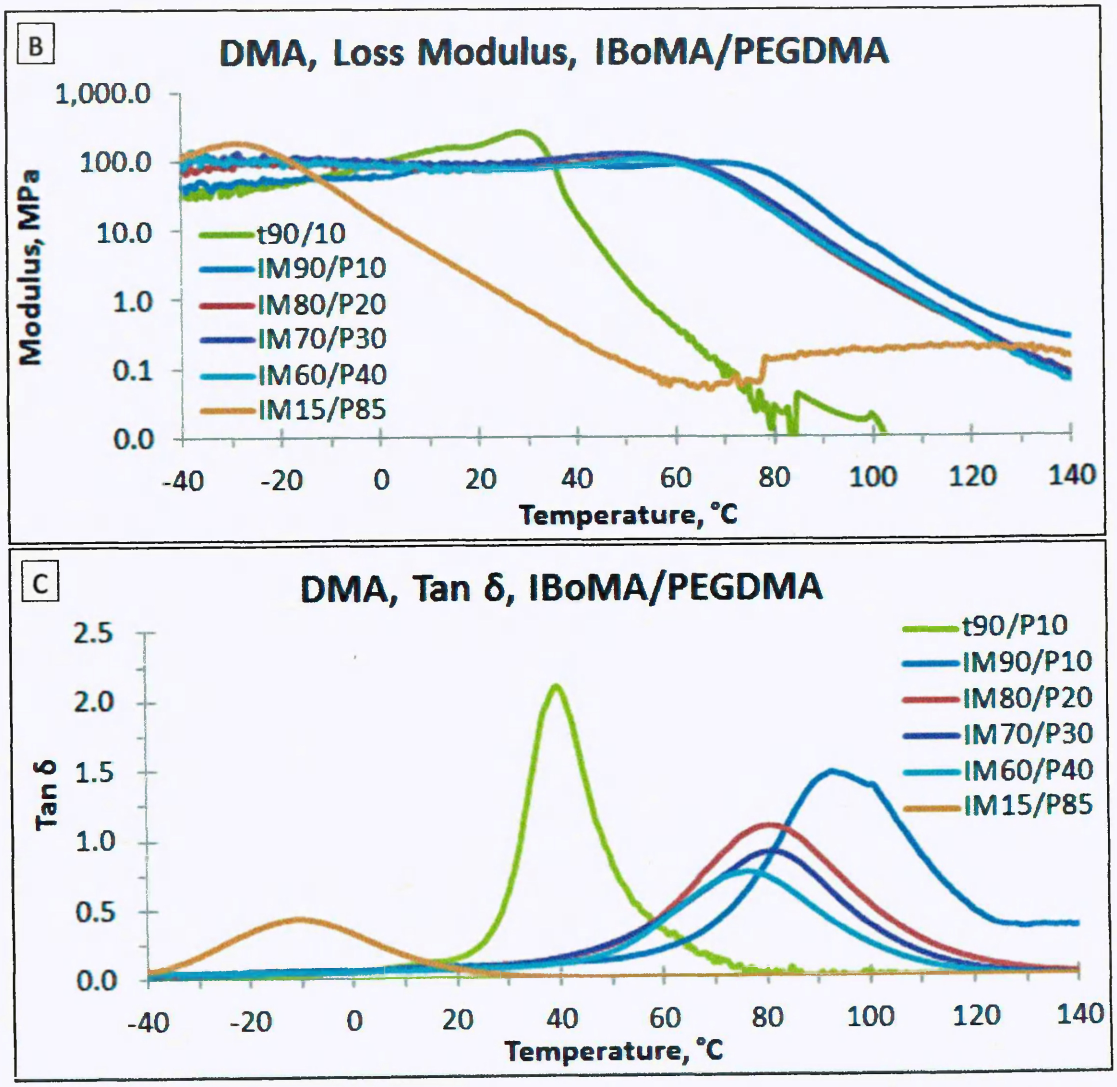

Figure 4.8: DMA data: temperature dependance of A) storage modulus, B) loss modulus and C) tan δ of t90/P10 and IM90/P10 to IM15/P85 over the temperature range -40 to 140 °C.

The IM100/P0 network was found to be brittle at lower temperatures which resulted in slippage from the clamps at higher temperatures before a tan δ peak could be recorded; therefore no DMA data is available.

An initial storage modulus of ca. 1420 MPa was recorded for the IM90/P10 network at - 40 °C, figure 4.8 A. After a steady decrease the modulus reaches 893 MPa at ca. 29 °C, i.e. 63% of its value at - 40 °C. The onset of the $T_{g\alpha}$ transition, identified by a steep drop in the modulus, was then observed indicating the point at which the shape memory effect begins. The T_g of the polymer system was established as 93 °C, figure 4.8 C; i.e. the point at which the tan δ curve reached a maximum, tan δ_{max}. The numerical value of tan δ_{max}, 1.5 tan δ, is large enough to indicate that the SMP will behave like an elastomer and exhibit a large shape recovery during shape memory evaluation (Chun et al., 2002, Tsai et al., 2009).

The modulus at tan δ_{max} was 9 MPa and this continued to decrease until the $T_{g\alpha}$ transition ended at which the value of the modulus was 0.5 MPa. Thus, the IM90/P10 exhibits a drop in modulus from 1420 to 0.5 MPa; i.e. over three orders of magnitude, well beyond Tsai et al.'s prerequisite that a decrease of one order of magnitude will result in a shape memory effect, particularly if the tan δ peak is sharp (Tsai et al., 2008, Du and Zhang, 2010).

Sample Description	Storage Modulus, MPa						$T_{g\alpha}$ °C	Tan δ_{max}
	-40 °C	-10 °C	30 °C	70 °C	100 °C	140 °C		
t90/P10	2043	1782	381	0.7	0.5	0.4	39	2.1
IM90/P10	1420	1085	888	243	4	0.4	93	1.5
IM80/P20	2069	1430	831	73	4	3	81	1.1
IM70/P30	2491	1756	996	95	7	6.	81	0.9
IM60/P40	2317	1599	951	79	10	9	77	0.8
IM15/P85	1863	103	26	28	30	34	-11	0.4

Table 4.5: Summary of dynamic mechanical values for the t90/P10 and IM90/P10 to IM15/P85 networks obtained from DMA over the temperature range of -40 to 140 °C.

Initial storage moduli of ca. 2069, 2491, 2317 and 1863 MPa were recorded for the IM80/P20 to IM15/P85 networks, respectively, at -40 °C. After a steady decrease the moduli reach ca. 806, 976, 846 and 1541 MPa at ca. 31, 31, 37 and -35 °C, i.e. ca. 40, 39, 37 and 83 %, respectively, of the value at -40 °C. The onsets of the $T_{g\alpha}$ transitions were then observed for each network, indicating the point at which the shape memory effect begins. The T_g of the polymer networks were established as 81, 81, 77 and -11 °C, respectively. The numerical value of the tan δ_{max}, 1.1 tan δ for the IM80/P20 network, is large enough to indicate that the SMP will behave like an elastomer and exhibit a large shape recovery during shape memory evaluation. However the numerical values of tan δ_{max} peaks, 0.9, 0.8 and 0.4 tan δ i.e. the IM70/P30 to IM15/P85 networks, respectively, indicates that the SMP will exhibit a lesser shape recovery during shape memory evaluation (Chun et al., 2002, Tsai et al., 2009).

The modulus at tan δ_{max} was 16, 25, 35 and 110 MPa, respectively, which continued to decrease until the $T_{g\alpha}$ transition for each network ended, at which point the moduli values were ca. 3, 6, 9 and 26 MPa, respectively. Thus, the IM80/P20 to IM15/P85 networks exhibits a drop in modulus from ca. 2069, 2491, 2317 and 1863 to 3, 6, 9 and

26 MPa, respectively; i.e. at least two orders of magnitude each, well beyond Tsai et al.'s prerequisite (Tsai et al., 2008, Du and Zhang, 2010).

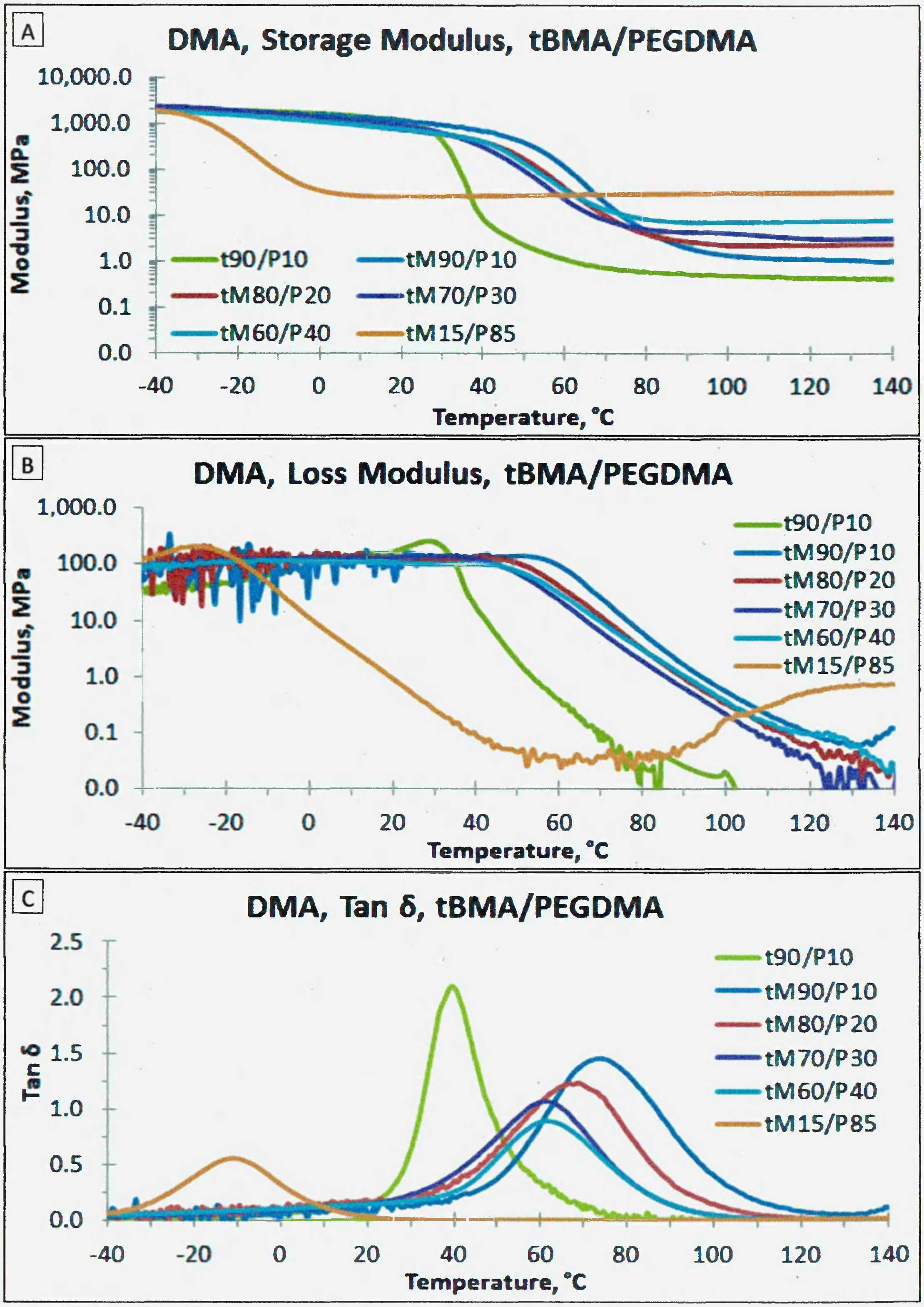

Figure 4.9: DMA data: temperature dependance of A) storage modulus, B) loss modulus and C) tan δ of t90/P10 and tM90/P10 to tM15/P90 over the temperature range -40 to 140 °C.

The tM90/P10 network, like the IM100/P0 sample, was found to be brittle at lower temperatures causing slippage from the clamps at higher temperatures before a tan δ peak could be formed, therefore no DMA data is available.

The tM90/P10 network exhibited an initial storage modulus of 1891 MPa at -40 °C , figure 4.9 A, which steadily decreased reaching a value of 1078 MPa at 23 °C; approximately 57 % of the initial storage modulus. A steep drop in the modulus marked the onset of the $T_{g\alpha}$ transition and established the starting point of the shape memory effect. For tM90/P10 the T_g is 74 °C and the tan δ_{max} value is 1.5 tan δ, figure 4.9 C. This latter value is large enough to be confident that this network will act like an elastomer and exhibit useful shape memory properties (Tsai et al., 2008, Du and Zhang, 2010). The tM90/P10 network exhibits a drop in modulus of ca. three orders of magnitude, from 1891 MPa at -40 °C to 1.1 MPa at the end of the $T_{g\alpha}$ transition. Consequently, it is expected to exhibit very useful shape memory properties. The tM0/P100 i.e. pure PEGDMA, network was reported earlier, section 3.2.3.

Sample Description	Storage Modulus, MPa						$T_{g\alpha}$ °C	Tan δ_{max}
	-40 °C	-10 °C	30 °C	70 °C	100 °C	140 °C		
t90/P10	2043	1782	381	0.7	0.5	0.4	39	2.1
tM90/P10	1891	1550	921	20	1	0.3	74	1.5
tM80/P20	2116	1426	569	11	2	2	68	1.2
tM70/P30	2355	1632	605	8	4	3	61	1.1
tM60/P40	1818	1286	578	14	7	8	61	0.9
tM15/P85	1920	89	26	28	30	32	-11	0.6

Table 4.6: Summary of dynamic mechanical values for the t90/P10 and tM90/P10 to tM15/P85 networks obtained from DMA over the temperature range of -40 to 140 °C.

The tM80/P20 to tM15/P85 networks exhibited initial storage moduli of ca. 2116, 2355, 1818 and 1920 MPa, respectively, at -40 °C with each steadily decreasing reaching a value of ca. 1269, 1322, 1232 and 1618 MPa at ca. -5, 1, -8 and -35 °C, approximately 60, 56, 68 and 84 %, respectively, of the initial storage moduli. A steep drop in the moduli marked the onset of the $T_{g\alpha}$ transitions and established the starting points of the shape memory effect. For tM80/P20 to tM15/P85 the T_g is 68, 61, 61 and -11 °C, respectively, and the tan δ_{max} values are 1.2, 1.1, 0.9 and 0.6 tan δ, respectively.

The higher intensity tan δ_{max} values for the tM80/P20 and tM70/P30 networks are large enough to be confident that these networks will behave like elastomers and display useful shape memory properties. However the lower intensity tan δ_{max} values for the tM60/P40 and tM15/P85 networks indicate that the networks will have less useful shape memory properties (Tsai et al., 2008, Du and Zhang, 2010). The moduli for the tM80/P20 to tM15/P85 networks exhibit drops of at least two orders of magnitude, from ca. 2116, 2355, 1818 and 1920 MPa at -40 °C to ca. 12, 18, 30 and 95 MPa, respectively, at the end of the $T_{g\alpha}$ transitions. Consequently all networks are predicted to exhibit very useful shape memory properties. The tM0/P100 i.e. pure PEGDMA, network was presented earlier, section 3.2.3.

From the DMA storage modulus, loss modulus and tan δ results, it is observed that addition of PEGDMA to IBoA, IBoMA and tBMA causes controllable shifts, to lower temperatures, of the $T_{g\alpha}$ transition phase. It causes a reduction of tan δ_{max} peak intensity as well as providing a higher rubbery storage modulus for each polymer network as the PEGDMA content increases. These results correspond well to those of other research groups including Gall et al., (2005), Ortega et al., (2008) and Kramer et al., (2010). Compared to the t90/P10 network, the I90/P10 has a larger initial modulus, 1938 MPa, whereas the IM90/P10 and tM90/P10 networks both have a lower initial modulus, 1420 and 1891 MPa, respectively. All the I90/P10, IM90/P10 and tM90/P10 networks have similar or larger storage moduli at tan δ_{max} and completion of the $T_{g\alpha}$ transition phase, with moduli of 12, 9 and 10 MPa and 2, 0.5 and 1 MPa, respectively. The tan δ_{max} for I90/P10, IM90/P10 and tM90/P10 was recorded as 1.6, 1.5 and 1.5 tan δ, with the $T_{g\alpha}$ observed at 53, 93 and 74 °C, respectively, compared to the t90/P10 network values of tan δ_{max}, 2.1 tan δ, and $T_{g\alpha}$, 39 °C. Overall it appears that from the samples evaluated that the I90/P10 network has the most useful properties to replace the t90/P10 network as it possesses greater initial and final storage modulus, an intense tan δ_{max} peak and a T_g onset temperature in the required range for a SMP packaging solution, when compared to the other networks.

4.2.3. Shape memory properties

4.2.3.1. Unconstrained Shape Memory Effect Evaluation

Unconstrained SME testing was carried out in order to assess whether the polymer networks based on IBoA, IBoMA and tBMA would demonstrate SME and to explore the effect of increasing PEGDMA content on the SME, figure 4.10, 4.11 and 4.12, respectively. As previously described in section 3.2.4, cross-linked tBA-co-PEGDMA polymer networks are a class I type SMP (Lui et al, 2007), this is also true of the IBoA-co-PEGDMA, IBoMA-co-PEGDMA and tBMA-co-PEGDMA networks. Therefore an appropriate SME temperature range needs to be identified for each acrylate network to account for the T_g values of the different network compositions, derived from the tan δ traces, figure 4.7 C, 4.8 C and 4.9 C. As the highest network T_g for each system was, 62, 93 and 74 °C, respectively, establishing the T_{high} at ca. 72, 103 and 84 °C, respectively, which is ca. 10 °C above each maximum T_g should ensure a full SME from each network.

However the lowest network T_g values occur at -20, -11 and -11 °C, respectively, which is much lower than the storage temperature of typical packaging materials, therefore a T_{low} of 0 to 5 °C was adopted instead as it is a more suitable storage temperature. In order to view only the PEGDMA effect on the SME, each sample was annealed at 100 °C for 15 minutes, then cooled to room temperature prior to being tested. Each sample network was deformed and their recovery determined, section 2.1.6, figure 2.15. The SME properties of interest are summarized in tables 4.7, 4.8 and 4.9, respectively.

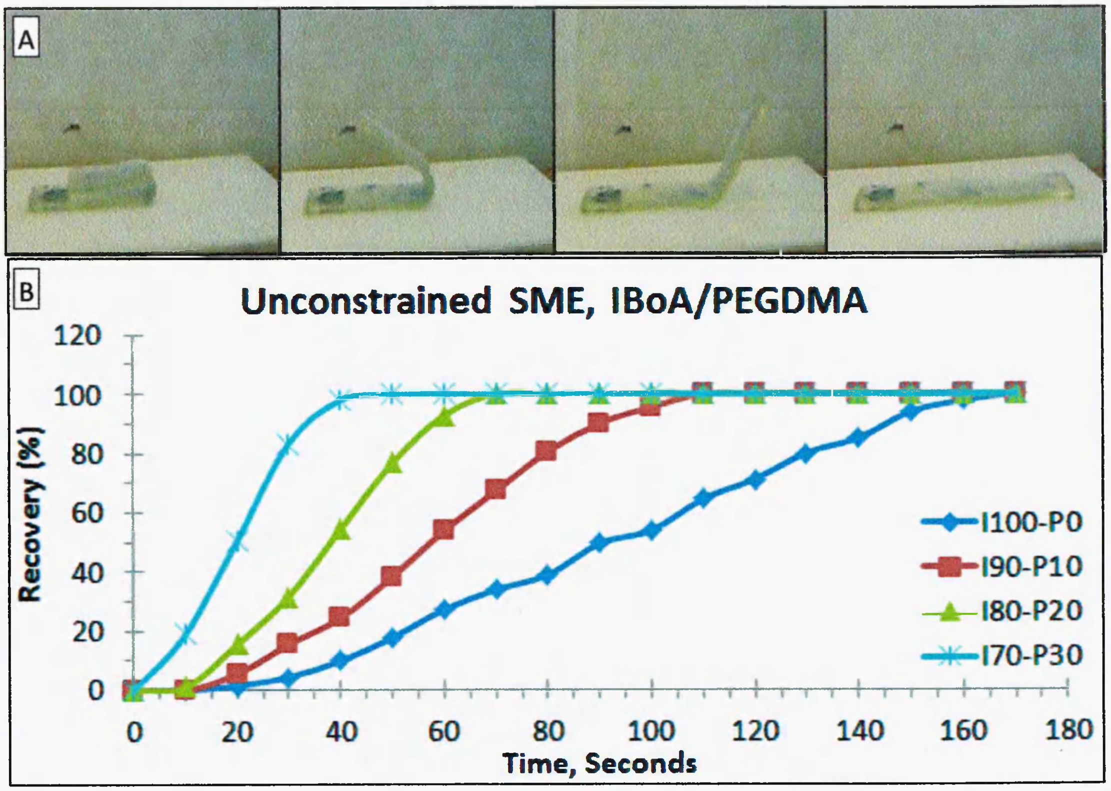

Figure 4.10: Unconstrained shape memory effect testing of IBoA-co-PEGDMA networks, from temporary to permanent shape, A) still images of IBoA-co-PEGDMA SMP at sequential intervals, B) plotted against time at a fixed temperature, 72 °C.

The I60/P40 and I15/P85 networks shape memory abilities were not recorded due to increased brittleness caused by the higher PEGDMA content. Both samples were deformed to a θ_{Max} of 100 %, but when the constraint was removed they each fractured at the hinge region and were rendered unusable for unconstrained SME testing. This has previously been reported by Ortega et al., (2008) and indicated by Safranski and Gall, (2008), where increased cross-links caused the stress-strain behaviour of the material to alter from an elastomeric response to a stiff network with a pronounced brittle response.

The I100/P0 network exhibited a θ_{Max} of 180 °, 100 %, demonstrating that it can accommodate a high level of deformation strain. After the deformation constraint was removed, the sample was left at T_{low}, 0 to 5 °C, and no shape recovery occurred, leading to a θ_{Fixed} of 180 °, 100%. This demonstrated that the I100/P0 network can store 100 % of the strain conferred by deformation. This was as expected due to a previous report by Yang et al. (2007) who demonstrated that at low temperatures the entropy driven strain recovery forces for class I SMP are simply not enough to overcome the fixed glassy chain interactions. Therefore the temporary shape would not be expected to demonstrate any shape memory recovery over time as the activation energy required to initiate recovery cannot be reached.

Shape memory recovery was carried out at 72 °C and the angle was recorded every 10 seconds until I100/P0 reached its θ_{Final}, 100 %. The I100/P0 network demonstrated that it can store 100 % of the deformed strain at T_{low}, and return to its original shape when unconstrained SME testing is carried out. This result corresponds well to predicted literature results including Ortega et al., (2008), where it was expected that low, possibly negligible, cross-link density would produce a SMP with large recoverable strain.

In order to further assess the shape memory ability of the I100/P0 network the $\theta_{1/2\,Final}$ time of recovery and θ_{Final} time of recovery, ca. 92 and 170 seconds, respectively, were recorded. These results indicate 50 % recovery of its permanent shape is achieved in ca. half the time of the 100 % recovery.

Polymer Identifier	θ_{Max}, %	θ_{Fixed}, %	$\theta_{1/2Final}$, %	θ_{Final}, %	$\theta_{1/2Final}$ Time, Sec	θ_{Final} Time, Sec
I100/P0	100	100	50	100	92	170
I90/P10	100	100	50	100	57	110
I80/P20	100	100	50	100	39	70
I70/P30	100	100	50	100	20	40

Table 4.7: Unconstrained SME test results, θ_{Max}, θ_{Fixed}, $\theta_{1/2Final}$, θ_{Final}, $\theta_{1/2Final}$ Time, and θ_{Final} Time, from I100/P0 to I70/P30 temporary shape recovery, plotted against time at a fixed temperature, 72 °C.

The I90/P10 to I70/P30 networks displayed a θ_{Max} of 100 % indicating that although the PEGDMA content, and therefore the number of cross-links, had increased there was no discernible retardation of elasticity or ability to accommodate the deformation strain. The θ_{Fixed} result were recorded at 100 % for all networks, I90/P10 to I70/P30, indicating that as the PEGDMA content increases it does not diminish the network's ability to retain its temporary shape at T_{low}.

Unconstrained shape memory recovery was carried out at 72 °C and the recovery angle was recorded every 10 seconds until each network reached its θ_{Final}. The I90/P10 to I70/P30 networks demonstrated, by achieving a 100 % recovery, that they can store the deformed strain at T_{low}, and return to their original shape. These networks performed as expected, showing large recoverable strains (Ortega et al., 2008).

In order to further assess the I90/P10 to I70/P30 networks shape memory ability the $\theta_{1/2\ Final}$° time of recovery, ca. 57, 39 and 20 seconds, respectively, and θ_{Final}° time of recovery, ca. 110, 70 and 40 seconds, respectively, were recorded. These results indicate that the I90/P10 to I70/P30 networks also recover 50 % of the original shape in ca. half the full recovery time.

These results indicate that with increasing PEGDMA content there is a decrease in $\theta_{1/2\ Final}$ and θ_{Final} time of recovery from the initial I100/P0 network. However not all the samples could be tested, therefore a true assessment of the unconstrained SME testing of the I100/P0 to I0/P100 networks could not be obtained. However it would be expected that the I60/P40 and I15/P85 networks shape recovery would be less than the other networks because shape recovery of greater cross-linked networks typically demonstrates lower recoverable strain (Ortega et al., 2008).

These results correspond well to the DMA results which predicted, due to high storage modulus and steep, intense tan δ peaks, that the tested networks would demonstrate shape memory ability and would have a large amount of shape memory recovery.

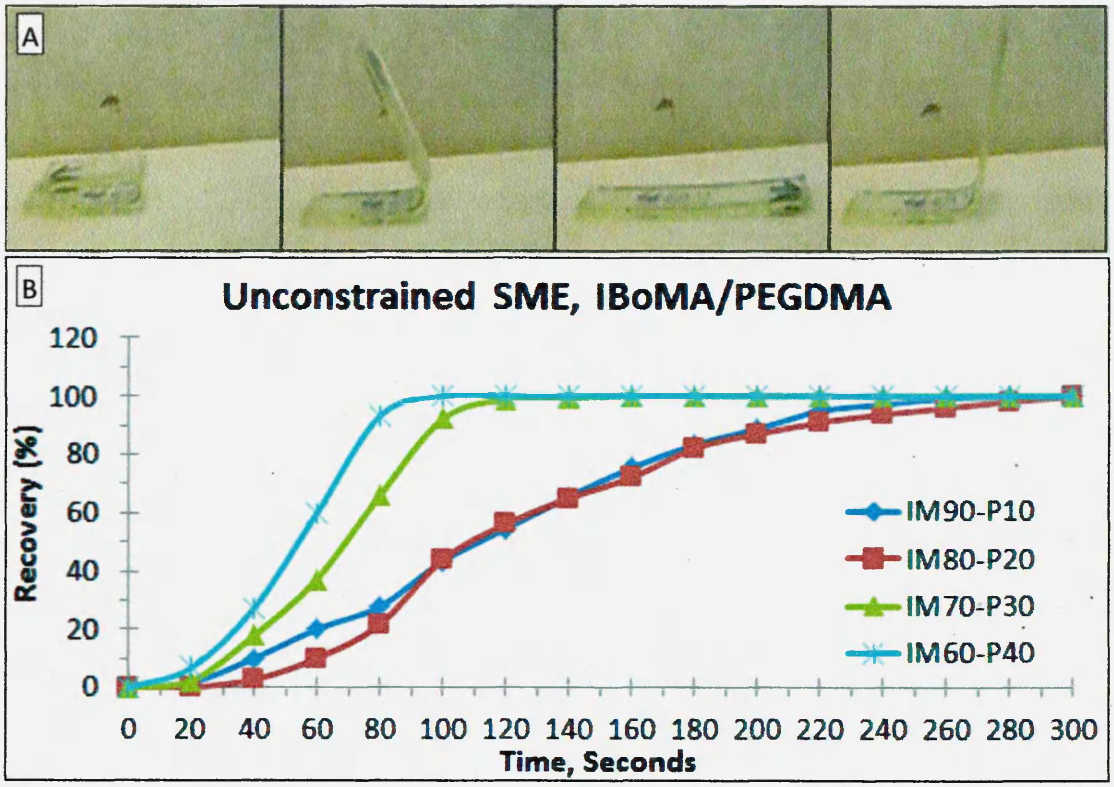

Figure 4.11: Unconstrained shape memory effect testing of IBoMA-co-PEGDMA networks, from temporary to permanent shape, A) still images of IBoMA-co-PEGDMA SMP at sequential intervals, B) plotted against time at a fixed temperature, 103 °C.

The shape memory abilities of the IM100/P0 and IM15/P85 networks were not recorded due to the IM100/P0 breaking during the casting processes, leaving no suitable sample to evaluate unconstrained SME testing. The IM15/P85 network, due to high cross-link content, fractured during the deformation process. This effect was previously reported by Ortega et al., (2008) and indicated by Safranski and Gall, (2008). A high level of deformation strain was exhibited by the IM90/P10 network, θ_{Max} of 100 %. Once the deformation constraint was removed no recovery occurred while the sample was kept at T_{low}, 0 to 5 °C, leading to a θ_{Fixed} of 100 %. This demonstrates that the IM90/P10 can accommodate the full load of imparted strain.

Unconstrained SME testing was carried out at 103 °C and the recovery angle was recorded every 20 seconds until the IM90/P10 network reached θ_{Final}. The IM90/P10 network demonstrated, by achieving a θ_{Final} of 100 %, that it can store 100 % of the deformed strain at T_{low}, and return to its original shape. This result corresponds well to literature results where it was expected that low cross-link density would produce a

SMP with large recoverable strain but low mechanical stress generation (Ortega et al., 2008).

In order to further assess the shape memory ability of the IM90/P10 the $\theta_{1/2\,Final}$ time of recovery and θ_{Final} time of recovery, ca. 112 and 280 seconds, respectively, were recorded. These results indicate that the IM90/P10 network recovers 50 % of the original shape in ca. ⅖ of the full recovery time.

Polymer Blend Identifier	θ_{Max}, %	θ_{Fixed}, %	$\theta_{1/2Final}$, %	θ_{Final}, %	$\theta_{1/2Final}$ Time, Sec	θ_{Final} Time, Sec
IM90/P10	100	100	50	100	112	280
IM80/P20	100	100	50	97	108	280
IM70/P30	100	100	50	100	69	140
IM60/P40	100	100	50	100	54	100

Table 4.8: Unconstrained SME test results, θ_{Max}, θ_{Fixed}, $\theta_{1/2Final}$, θ_{Final}, $\theta_{1/2Final}$ Time, and θ_{Final} Time, from IM90/P10 to IM60/P40 temporary shape recovery, plotted against time at a fixed temperature, 103°C.

The IM80/P20 to IM60/P40 networks displayed a θ_{Max} of 100 %, the same as the IM90/P10 network. The θ_{Fixed} results were recorded as 100 % for all networks.

Shape memory recovery was carried out at 103 °C and the recovery was recorded every 20 seconds until each network reached its θ_{Final}. The IM80/P20 network did not fully recover when heated, achieving a θ_{Final} of 97 %, the IM70/P30 and IM60/P40 networks achieved a θ_{Final} of 100 %. This demonstrates that the IBoMA networks can store all of the deformed strain at T_{low}, and almost fully return to their original shape. These networks performed as expected, showing large recoverable strains (Ortega et al., 2008).

The IM80/P20 to IM60/P40 networks $\theta_{1/2\,Final}$ time of recovery, ca. 108, 69 and 54 seconds and θ_{Final} time of recovery, ca. 280, 140 and 100 seconds, respectively, were recorded. These results indicate that the IM80/P20 network recovers 50 % of the permanent shape in ca. ⅖ of the full recovery time while the IM70/P30 and IM60/P40 networks recover in ca. half the full recovery time. These results suggest that as PEGDMA increases the 50 % recovery of the permanent shape time increases from ⅖ to ½ of the full time of recovery. As previously commented, section 4.2.2.1, Tsai et al., (2009) and Du and Zhang (2010) suggested that a sharp drop in modulus will produce a

SME, implying that the sharper the tan δ peak, the greater the SME. It was observed that as the PEGDMA content increased the tan δ peak becomes sharper, although not as intense, which potentially caused the increase of the 50 % recovery of the permanent shape of the IM70/P30 and IM60/P40 networks. It is also observed that the θ_{Final} time of recovery of the IBoMA-co-PEGDMA networks is ca. twice as long as the IBoA-co-PEGDMA networks, this is potentially caused by the methyl group attached to the C=C double bond in IBoMA, figure 4.0. When cured the methyl groups in the IBoMA chains possibly act as 'hooks', partially linking the chains together more tightly, retarding the ability of the chains to slip past one another during deformation and shape recovery.

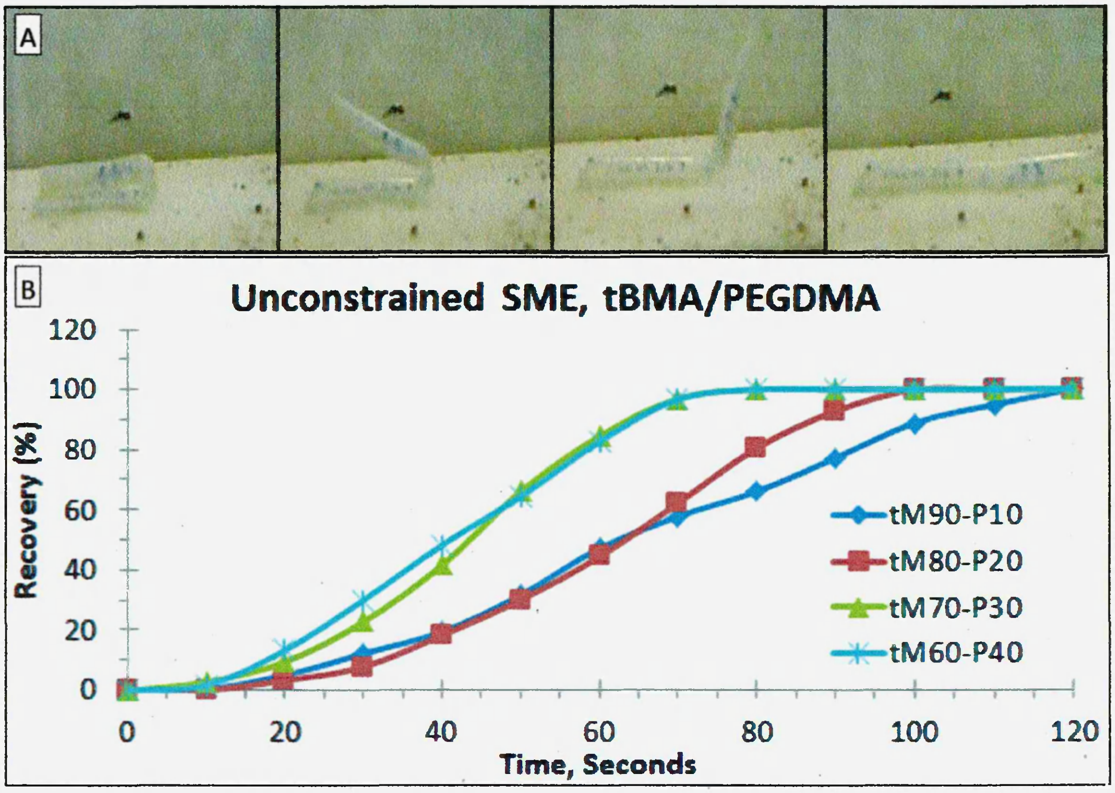

Figure 4.12: Unconstrained shape memory effect testing of tBMA-co-PEGDMA networks, from temporary to permanent shape, A) still images of tBMA-co-PEGDMA SMP at sequential intervals, B) plotted against time at a fixed temperature, 84 °C.

The tM100/P0 and tM15/P85 networks shape memory abilities were not recorded due to the tM100/P0 network breaking during the casting processes with no suitable sample to evaluate unconstrained SME testing. The tM15/P85 fractured during the deformation process.

The tM90/P10 network exhibited a θ_{Max} of 100 % with no recovery occurring after the deformation constraint was removed, leading to a θ_{Fixed} of 100 %.

Shape memory recovery was carried out at 84 °C and the recovery was recorded every 10 seconds until tM90/P10 reached its θ_{Final}. The tM90/P10 network achieved a θ_{Final} result of 100 %. In order to further assess tM90/P10 shape memory ability the $\theta_{1/2\,Final}$ and θ_{Final} time of recovery, ca. 62 and 120 seconds, respectively, were recorded. These results indicate that the unconstrained SME of tM90/P10 recovers 50 % of the permanent shape in ca. half the full recovery time.

Polymer Blend Identifier	θ_{Max}, %	θ_{Fixed}, %	$\theta_{1/2Final}$, %	θ_{Final}, %	$\theta_{1/2Final}$ Time, Sec	θ_{Final} Time, Sec
tM90/P10	100	100	50	100	62	120
tM80/P20	100	100	50	100	64	105
tM70/P30	100	100	50	100	44	80
tM60/P40	100	100	50	100	41	70

Table 4.9: Unconstrained SME test results, θ_{Max}, θ_{Fixed}, $\theta_{1/2Final}$, θ_{Final}, $\theta_{1/2Final}$ Time, and θ_{Final} Time, from tM100/P0 to tM70/P30 temporary shape recovery, plotted against time at a fixed temperature, 84 °C.

The tM80/P20 to tM60/P40 networks displayed a θ_{Max} of 100 %, the same as the tM90/P10 network, with the θ_{Fixed} results being recorded at 100 % for all networks. The tM80/P20 to tM60/P40 networks achieved a θ_{Final} of 100 % after undergoing SME evaluation.

The $\theta_{1/2\,Final}$ time of recovery, ca. 64, 44 and 41 seconds and θ_{Final} time of recovery, ca. 105, 80 and 70 seconds, respectively, were recorded. These results indicate that the tM80/P20 to tM60/P40 networks also recover 50 % of the permanent shape in ca. half the full recovery time.

Overall unconstrained SME testing revealed the majority of the IBoA, IBoMA and tBMA networks have shape memory ability and are able to fix a temporary shape and return to the permanent shape upon triggering with an external stimulus. When compared to the unconstrained SME testing of tBA networks, a longer time is required for full shape recovery, possibly due to the tBA networks being 0.5 mm in thickness compared to the IBoA, IBoMA and tBMA networks 1.0 mm thickness. Due to the significant difference in thickness, a longer time to conduct heat to the entire network is required, as the outer surface will reach the T_{trans} before the inner core, therefore a slower SME is to be expected.

The shape of the unconstrained SME curve, of all networks, are very similar, as is the trend of the polymer networks to return 50 % of the permanent shape in ca. half the full recovery time. However there are differences in the order of return, the tBA network tends to return faster with less cross-link density, however the IBoA, IBoMA and tBMA networks all tend to return faster with greater cross-link density. This is possibly due to entanglement effects of the differing networks. The tBA network has the least branched polymer chains compared to the IBoA, IBoMA and tBMA polymer chains. As the cross-link density increases in the tBA-co-PEGDMA network the polymer chains become constricted and cannot move as easily this could then cause a reduced SME when returning to the permanent shape. However as the IBoA, IBoMA and tBMA networks have bulkier side groups, the polymer chains hook/catch onto each other due to the proximity to one another. As cross-link density increases the space between the polymer chains would potentially increase, caused by the bridging effects of the cross-links, this would then allow them to slide past each other easier causing an increased SME. However as the cross-links increase further a reduction would most likely be observed in the SME as the cross-links begin to hinder the movement of the polymer networks.

4.3. IBoA, IBoMA and tBMA Network Summary

The effect of cross-link content in an acrylate copolymer network, tBA-co-PEGDMA, was discussed in chapter 3 in order establish the most suitable ratio of tBA to PEGDMA for use in a thermally stable SMP packaging solution. However the low flash point of tBA made it unsuitable for industrial scale production, therefore a series of acrylate monomers were studied to find a suitable replacement for tBA. Networks of IBoA, IBoMA and tBMA were produced and characterised with emphasis on mechanical properties and shape memory abilities.

Overall the results indicated that IBoA was the most likely substitute for tBA, because it has a greater flash point, boiling point and similar tan δ_{max} values to tBA, appearing to fully cure, and display useful unconstrained SME for the I100/P0 to I70/P30 networks. IBoA also has a higher storage modulus after the $T_{g\alpha}$ transition phase and a higher T_g than tBA. Therefore it was decided to send the I90/P10 and I80/P20 sample solutions for evaluation on the UV curing machine at Chesapeake.

When the I90/P10 and I80/P20 networks were exposed to the intense UV curing at Chesapeake they did not combust.

Both the I90/P10 and I80/P20 networks were coated, 76 µm thick, onto substrates and required seven passes through the UV curing machine conveyer at full power (UV dose of 150 mJ/cm^2 per pass). For a commercially viable coating process 2 passes is the maximum.

To reduce the time required to cure the IBoA-co-PEGDMA network, I90/P10, a series of experiments were carried out where additional photoinitiators and oxygen inhibitors were introduced to form a photoinitiator 'cocktail' with the aim to produce a full cure in two passes on the UV cure instrument.

A multi-photoinitiated free radical mechanism is used quite routinely in industry in order to achieve the desired properties of a photo-curable material. The aim is to use photoinitiators that absorb at different wavelengths in the UV spectrum which allows more radicals to be produced causing a faster rate of polymerisation. Alternatively utilising both type I i.e. TPO-L and type II i.e. DMPA and ITX, photoinitiators to achieve a fast full cure is possible as type I photoinitiators are typically used to provide high rates of initiation while type II photoinitiators are used for applications requiring superior optical absorption properties in the near-UV spectroscopic region (Aydin et al., 2003).

An additional issue in creating a fast curing photoinitiator cocktail is the effect of oxygen inhibition during curing which represents a significant problem with most UV curable acrylate networks (Studer et al., 2003).

In previous cast samples oxygen inhibition has not occurred because all samples have either been prepared in a closed mould system or under a nitrogen atmosphere, however when attempting to cure on an industrial scale these methods are not practical or cost effective. Oxygen inhibits UV curing during polymerisation via rapidly scavenging the free radicals generated during photolyses and creating peroxyl radicals (Gruber, 1992).

The peroxyl radical species are not reactive towards the acrylate double bond and therefore do not initiate or participate in polymerisation leading to premature termination. The peroxyl radicals also abstract hydrogen atoms from the polymer backbone to form hydroperoxides, figure 4.13.

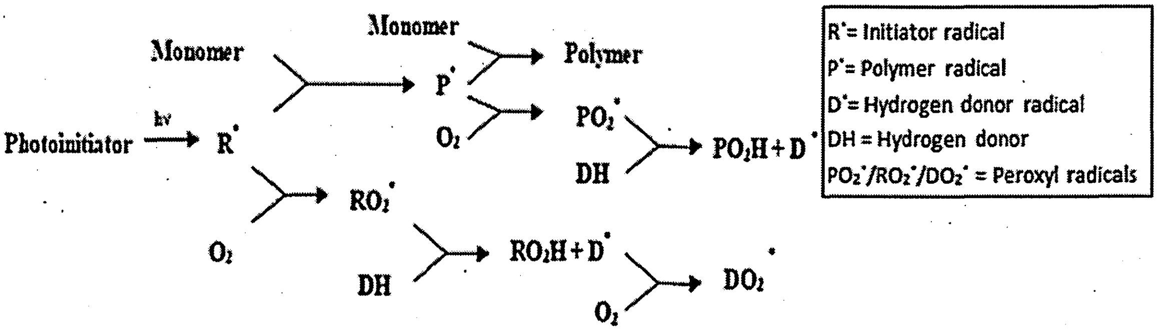

Figure 4.13: Schematic of oxygen inhibition in radical-induced photopolymerisation (Studer et al., 2003).

Premature termination of polymer chains and the presence of peroxyl groups or hydroperoxides alter the mechanical properties of networks formed compared to those prepared in an oxygen free atmosphere.

To overcome oxygen inhibition effects in acrylate polymer networks chemical and physical methods can be used. Chemical methods include increasing photoinitiator quantities and/or UV intensities (Awokola et al., 2002, Studer et al., 2003), addition of amine synergists (Studer et al., 2003, Santobianco et al., 2008) and conversion of dissolved oxygen into its excited singlet state to be scavenged by benzofuran derivatives (Belon et al., 2010). Physical methods include blocking/removing the atmospheric oxygen via UV initiation under water (Selli and Bellobono, 1993), with a protective coating e.g. wax (Bolon and Webb, 1978) or a protective layer i.e. polypropylene film (Decker et al., 2004), and utilising inert atmospheres (Gruber, 1992, Lee et al., 2004).

Awokola et al., (2002) found that increasing the length of time and UV intensity applied to a sample in oxygen atmospheres of a given content increased the cure of an acrylate system. While Studer et al., (2003) has reported that an increase in photoinitiator concentration also causes an increase of cure in the presence of oxygen.

In a UV cured photopolymerisation amines can be added to act as both a co-initiator, with a type II photoinitiator, and an oxygen scavenger. Struder et al., (2003) and Santobianco et al., (2008) both reported that low molecular weight amines are typically incorporated as a co-initiator for type II photoinitiators to enhance the hydrogen abstraction process to produce free radicals as well as scavenge for dissolved oxygen. Amines reduce oxygen inhibition via readily undergoing chain peroxidation reactions causing dissolved oxygen to be consumed.

Belon et al., (2010) reported that conversion of oxygen into its excited singlet state can be achieved via red light irradiation, in the presence of a dye sensitizer, which is rapidly scavenged by 1,3-diphenylisobenzofuran. The reaction generated 1,2-dibenzoylbenzene which proceeded to function as an additional photoinitiator. However due to unwanted discoloration of polymer networks this method was not widely used in further applications.

Carrying out UV photopolymerisation under water or with protective coating/layers forms a physical barrier to oxygen, thus there is minimal to no oxygen inhibition. However carrying out a UV cure under water or by applying a protective coating/film causes varying surface effects (Selli and Bellobono, 1993, Bolon and Webb, 1978, Decker et al., 2004).

Another method of photopolymerisation is curing in an inert atmosphere. Gruber (1992) and Lee et al., (2004) utilised nitrogen atmospheres while Studer et al., (2003) utilised a carbon dioxide atmosphere to prevent oxygen inhibition.

From a commercial perspective the chemical methods of preventing oxygen inhibition would be most suitable for the I90/P10 network. This is primarily due to the cost involved and need for extra equipment to utilise the other techniques i.e. inert atmospheres, converting dissolved oxygen into its excited singlet state, curing under water or using protective barriers.

As mentioned previously (Studer et al., 2003) increasing the amount(s) of photoinitiator(s) is required to overcome oxygen inhibition. Masson et al., (2004) reported that TPO-L was an effective type I photoinitiator that demonstrates almost complete photopolymerisation, ca. 90 %, at 5 wt% in air. It has also been reported by Gruber (1992) that mixtures of a type I and type II photoinitiator reduce the effects of oxygen inhibition.

A type II photoinitiator ITX was reported by Wang et al., (2009) to be widely used in industrial photocurable compositions. In order to produce free radicals efficiently ITX is commonly used in conjunction with an amine co-initiator. A synergistic amine, EHA, which works well when combined with ITX was recommended by Lambson Limited.

In order to keep oxygen inhibition to a minimum free-amines such as, DEA and TEA were also considered. Santobianco et al., (2008) reported that the free amines provide good thorough cure, contribute reducing oxygen inhibition and are compatible with photopolymerisation systems employing type I and type II photoinitiators.

Therefore TPO-L, ITX, EHA, DEA and TEA would be considered as additions to the photoinitiator cocktail for curing the I90/P10 network.

4.4. C00 to C17 I90/P10 network; Results and discussion

4.4.1. Network Polymerisation

4.4.1.1. Photopolymerisation in Air

Each I90/P10 network sample with varying photoinitiator formulations, C00 to C17, was coated onto a substrate, placed onto the UV conveyer belt and passed through the UV source. The sample was passed through the UV curer until the 'educated' thumb test established a full cure. The number of passes for each sample, C00 to C17, are summarised in table 4.10. After full cure was accomplished, each sample was stored separately for 1 day before analysis.

Sample Name:	Photoinitiator wt%			Oxygen Inhibitors wt%				UV Passes
	TPO-L	DMPA	ITX	EDB	EHA	TEA	DEA	
C00	-	3.50	-	1.50	-	-	-	6
C01	-	3.50	-	1.50	-	5.00	-	4
C02	-	3.50	-	1.50	-	-	5.00	6
C03	-	3.50	-	3.00	-	-	5.00	6
C04	-	4.50	-	1.50	-	-	5.00	4 to 5
C05	-	5.50	-	1.50	-	-	5.00	4
C06	1.75	-	1.75	-	1.50	-	-	6
C07	1.75	-	1.75	-	1.50	5.00	-	4
C08	1.75	-	1.75	-	1.50	5.00	-	3
C09	3.50	-	1.75	-	1.50	5.00	-	2
C10	1.75	-	3.50	-	1.50	5.00	-	3
C11	1.75	-	1.75	-	3.00	5.00	-	3
C12	1.75	-	1.75	-	4.50	5.00	-	3
C13	1.75	1.75	-	1.50	-	-	5.00	6
C14	1.75	1.75	-	-	1.50	-	5.00	6
C15	3.50	-	-	1.50	-	-	5.00	6
C16	3.50	-	-	-	1.50	-	5.00	6
C17	-	0.3 to 5	-	4.50	-	-	5.00	7 to 8

Table 4.10: UV cure passes of samples C00 to C17 at UV dose of 150 mJ/cm^2 per pass.

C00 is the original I90/P10 photoinitiator formulation and acts as the control result for comparison of C01 to C17. C00 achieved a full cure, as determined by the 'educated' thumb test, after 6 passes, producing a consistent film with a good surface shine. After storage for one day, minor surface tack and slight delamination from the substrate were observed.

C01 and C02 were formulated to identify whether TEA or DEA would enhance the curing time of the original photoinitiator formulation. It was found that incorporation of 5 wt% TEA caused a full cure with 4 passes, an improvement of 2 passes, whereas DEA showed no improvement in the cure. After one day's storage some minor delamination and surface tack was observed from the C01 sample.

As C02 showed no improvement, C03 to C05 were produced to identify if the full cure speed could be improved by increasing either DMPA or EDB. No improvements were observed after increasing EDB, but improvements were achieved by increasing the amounts of DMPA. Increasing DMPA from 3.5 to 4.5 wt% caused a full cure in 4 to 5 passes, and an increase to 5.5 wt% caused a full cure in 4 passes. All samples produced had consistent film surfaces with a good shine. After one day's storage some minor delamination was observed in all samples.

The C06 to C12 photoinitiator formulations were produced in order to establish if a combination of TPO-L and ITX would be a better photoinitiator combination. It was found that using a combination of 1:1 TPO-L:ITX at 1.5 wt% along with 1.5 wt% EDB was comparable to the standard DMPA and EDB formulation, C00, which cured in 6 passes. Also the addition of 5wt% TEA, C07, provided a full cure in 4 passes. However when combined with 2 wt% fumed silica, C08, it cured in 3 passes. This may have been a result of increased viscosity possibly reducing the penetration of oxygen molecules into the pre-cured film. The C09 to C12 formulations were used to determine if increasing TPO-L, ITX or EHA would achieve a faster full cure. Doubling TPO-L content, C09, resulted in a full cure in 2 passes, doubling ITX content, C10, or increasing the EHA content, C11 and C12, did not improve the speed of full cure which occurred in 3 passes for C10, C11 and C12. All photoinitiator formulations, C06 to C12, produced consistent film surfaces with good surface shine, except for C08 which produced a matt finish with a rougher than normal surface, due to presence of fumed silica. It was also noted that the C10 formulation had developed small white spots spread unevenly over the surface, potentially indicating that the increase in ITX may have caused differing cure levels in localised areas. After storage for one day, some slight delamination of sample C12 was observed.

The C13 and C14 photoinitiator formulations are a mixture of TPO-L, DMPA and DEA combined with EDB or EHA in order to improve the speed to full cure. It was discovered that neither combination improved the cure speed resulting in formulations C15 and C16 in which TPO-L and DEA were combined with either EDB or EHA in order to improve the speed to full cure. However neither C15 nor C16 improved the speed to full cure. It was observed that all four samples, C13 to C16, produced consistent film surfaces with good surface shine but after one day of storage they displayed minor residual tack and slight delamination.

As previously shown with samples C04, C05, C09 and C10, increasing the photoinitiator concentration rather than the oxygen inhibitor, as in samples C03, C11 and C12, appears to increase the speed of full cure. In order to prove that increases in the photoinitiator content were responsible for the increases in the speed to full cure, C17 was formulated using a low photoinitiator to oxygen inhibitor ratio; This resulted in a decrease in the speed to full cure compared to systems containing larger amounts of photoinitiator.

These results indicate that the combination of TPO-L, ITX, EHA and TEA together in formulation C09 should produce a I90/P10 network that can be cured in 2 passes, on an industrial level. It was also shown that formulation C17 cured the slowest requiring 7 to 8 passes, showing that having a low photoinitiator and high oxygen inhibitor content reduces the curing speed.

4.4.2. Mechanical Properties

4.4.2.1. Dynamic Mechanical Analysis

In order to assess the dynamic mechanical properties of the C09 formulation, a solid polymer network, 1.0 mm thick, was prepared. The dynamic mechanical properties, storage modulus, loss modulus and tan δ, of the C09 I90/P10 were compared to the DMA properties of the original C00 I90/P10 network as a function of temperature, -65 to 115 °C, figure 4.14. The dynamic mechanical properties of interest are summarized in table 4.11.

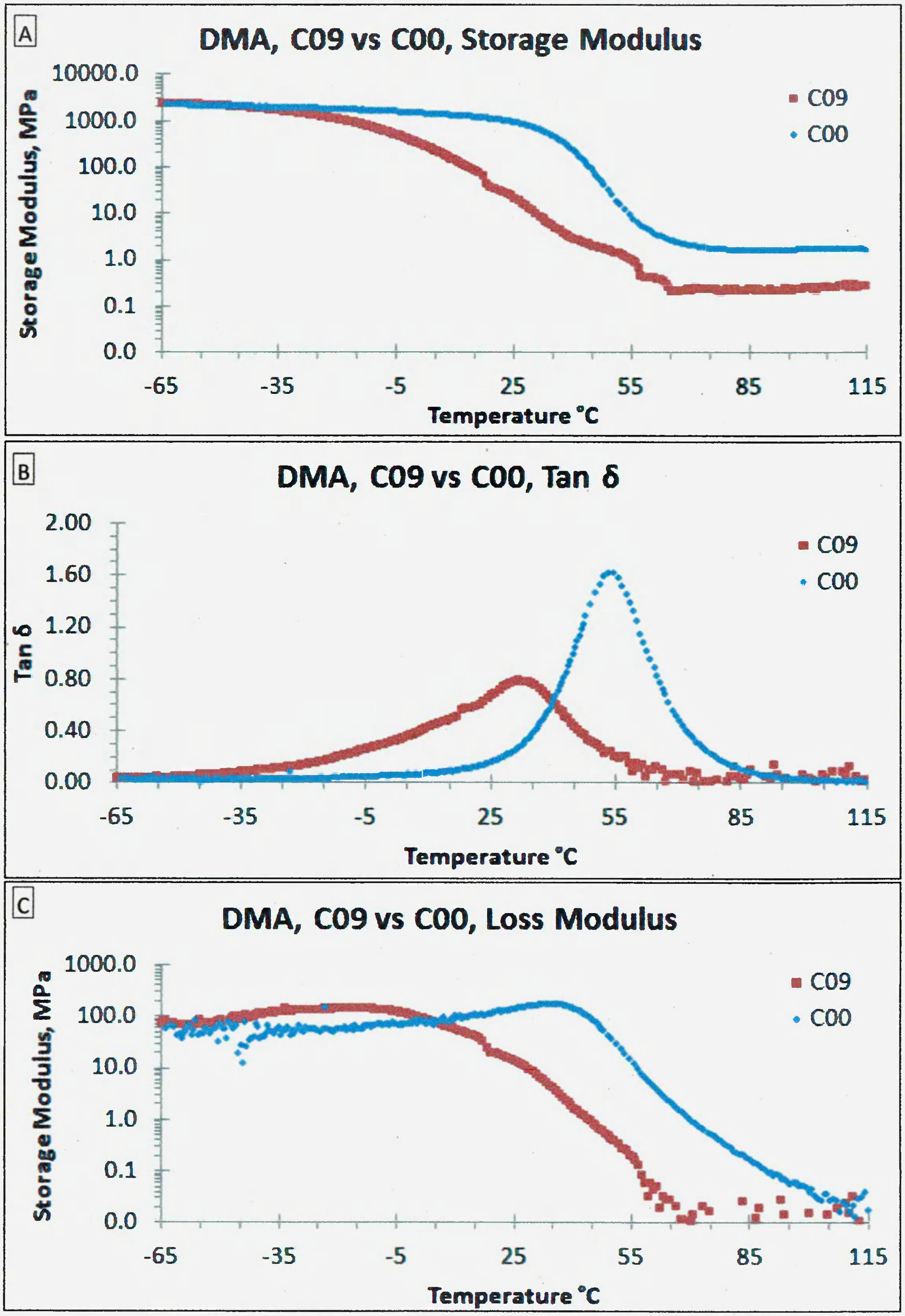

Figure 4.14: DMA data; temperature dependance of A) storage modulus, B) loss modulus and C) tan δ of C09 and C00 over the temperature range -65 to 115 °C.

At -65 ˚C an initial storage modulus of ca. 2132 MPa was recorded for the C00 I90/P10 network, figure 4.14 A. The modulus drops steadily until ca. 18 °C, reaching ca. 1112

MPa, i.e. ca. 52% of the initial value. After this the modulus begins to steeply drop, which indicates the onset of the $T_{g\alpha}$ transition, figure 4.14 C, i.e. the stage where the SME is predicted to begin. At the tan δ_{max}, 1.6 tan δ, the T_g of the polymer system is established at 53 °C. This indicates that the SMP will behave like an elastomer (Chun et al., 2002, Tsai et al., 2009). At tan δ_{max} the modulus had dropped to ca. 12 MPa, and continued to drop steadily until the $T_{g\alpha}$ transition stage had finished, ending with a modulus of ca. 1.7 MPa. The C00 I90/P10 network demonstrates ca. a four order magnitude drop in storage modulus, therefore SME should occur.

The C09 I90/P10 network exhibited an initial storage modulus of ca. 2224 MPa at -65 °C which steadily decreased reaching a value of 1282 MPa at -27 °C; approximately 58 % of the initial storage modulus. At -27 °C a marked drop in the modulus indicated the onset of the $T_{g\alpha}$ transition and established the predicted starting point of the shape memory effect. The T_g was recorded as 32 °C and had a tan δ_{max} value of 0.8 tan δ. This latter value is not large enough to confidently predict that this network will exhibit useful shape memory properties. Tsai et al., (2008) have suggested that a sharp, at least one order of magnitude drop in storage modulus provides a very good indication that a polymer system will demonstrate useful SME. However although the C09 I90/P10 network modulus has dropped by ca. four orders of magnitude, from 2224 MPa at -65 °C to 0.2 MPa, the $T_{g\alpha}$ transition stage is not sharp but very broad (Du and Zhang, 2010).

Sample Description	Storage Modulus, MPa							$T_{g\alpha}$ °C	Tan δ_{max}
	-65 °C	-35 °C	-5 °C	25 °C	55 °C	85 °C	115 °C		
C00	2132	1909	1526	902	10	2	2	53	1.6
C09	2225	1575	465	20	1	0.2	0.3	32	0.8

Table 4.11: Summary of, dynamic mechanical values obtained from DMA for C09 and C00 over temperature range -65 to 115 °C.

When the C09 network is compared to the C00 network there is a large difference between the mechanical properties. In terms of the tan δ results, figure 4.14 C, it is observed that the C09 tan δ_{max} decreases in intensity by ca. 50 % and shifts to a lower temperature, by ca. 32 °C, with the overall $T_{g\alpha}$ transition peak base i.e. from the onset to the end of the $T_{g\alpha}$ transition phase, broadening by ca. 25 °C.

The shift of the $T_{g\alpha}$ and peak base broadening indicate that the new formulation of initiators will result in a much earlier onset of the SME at ca. -35 °C compared to C00 SME onset at ca. 18 °C. This is much lower than the temperatures to which the polymer could be cooled, without specialised equipment, therefore it is probable that a temporary shape will be impossible to routinely fix, therefore no shape memory will be achieved. Due to the combination of the tan δ broadening and reducing in intensity, it is also expected, that even if a temporary shape could be fixed, the shape memory recovery would be very long and slow.

4.4.3. Shape Memory Properties

4.4.3.1. Unconstrained Shape Memory Effect Evaluation

An evaluation of the SME was carried out in order to assess whether the C09 polymer network would demonstrate SME and to explore the effect of the new photoinitiator formulation on SME. The SME testing was previously described in section 2.1.6, figure 2.17.

As the DMA results predicted, neither the coated substrate nor the polymer network displayed shape memory ability when tested.

4.5. C00 to C17 I90/P10 Network Summary

As the new photoinitiator formulation caused unwanted effects on the mechanical and shape memory properties of the original C00 I90/P10 network, it was decided to determine what the cause was. Therefore a series of new polymer films, D00 to D06 I90/P10, were prepared using selected amounts of ITX, EHA and TEA, table 4.12.

Sample Description:	Photoinitiator		Oxygen Inhibitor	
	TPO-L, wt%	ITX, wt%	EHA, wt%	TEA, wt%
D00	0.350	0.000	0.150	5.0
D01	0.350	0.100	0.150	5.0
D02	0.350	0.175	0.150	0.0
D03	0.350	0.175	0.000	5.0
D04	0.350	0.175	0.075	5.0
D05	0.125	0.175	0.150	5.0
D06	0.250	0.175	0.150	5.0

Table 4.12: Formulations D00 to D06 prepared using selected amounts of photoinitiator and oxygen inhibitors.

Each component of the C09 photoinitiator cocktail was varied or removed individually while keeping the others constant. This was to elucidate the effects of each component on the mechanical properties of the network and to optimise the formulation so it was comparable to the original C00 mechanical and shape memory properties.

Each sample was produced as described in section 4.1.5. The samples were stored for 24 hours prior to testing.

4.6. D00 to D06 I90/P10 Network; Results and Discussion

4.6.1. Mechanical Properties

4.6.1.1. Dynamic Mechanical Analysis

In order to assess the dynamic mechanical properties of the D series formulations, a solid polymer network, 1.0 mm thick, was formed. The dynamic mechanical properties, storage modulus, loss modulus and tan δ, of the I90/P10, D00 to D02, figure 4.15, and D03 to D06, figure 4.16, was compared to the DMA properties of the C00 and C09 network as a function of temperature, -65 to 115 °C. The dynamic mechanical properties of interest are summarized in table 4.13.

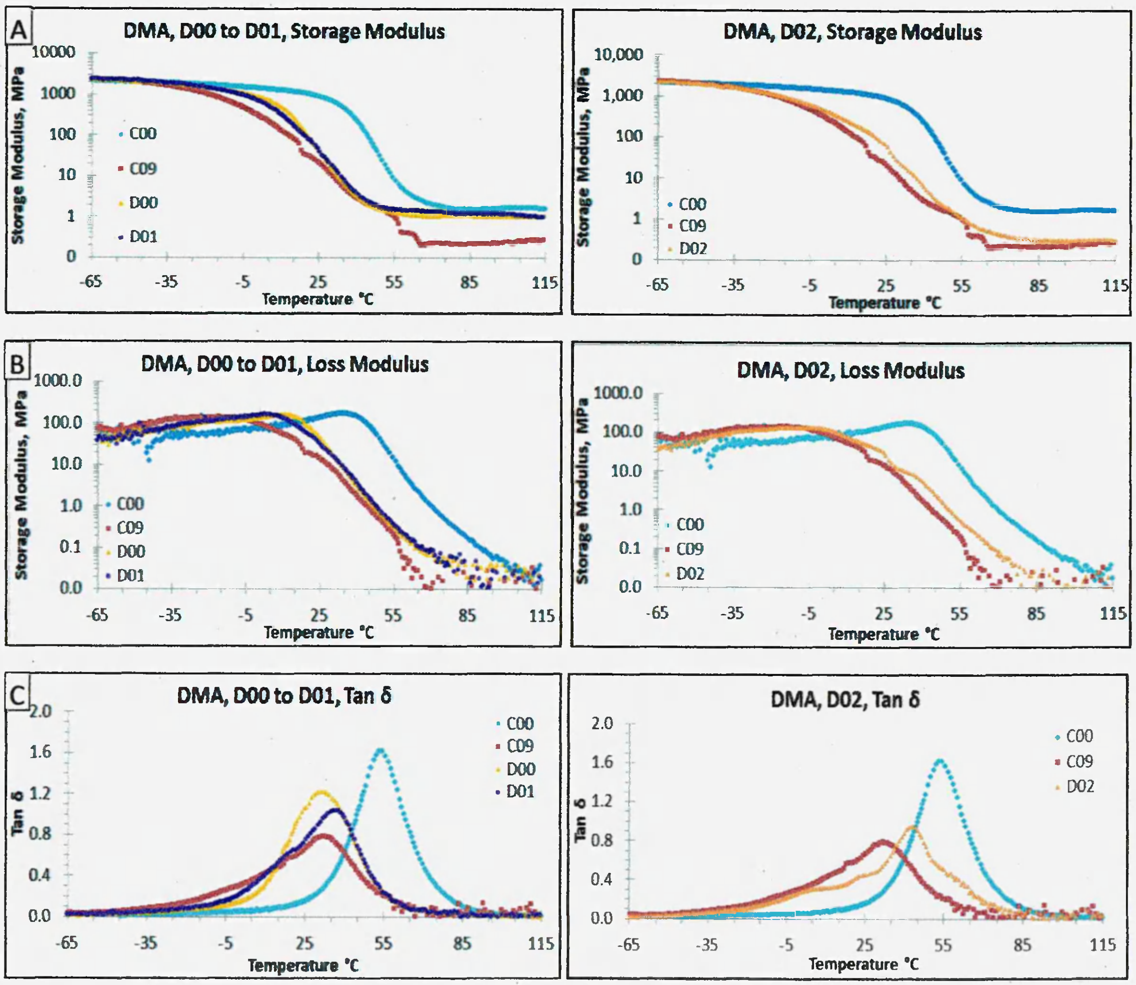

Figure 4.15: DMA data: temperature dependance of D00 to D02 A) storage modulus, B) loss modulus and C) tan δ over the temperature range -65 to 115 °C.

Initial storage moduli of ca. 2292, 2293 and 2252 MPa were recorded for the D00, D01 and D02 networks, respectively, at -65 °C, figure 4.15 A. After a steady decrease the moduli reached ca. 1152, 1227 and 1194 MPa at ca. -8, -13 and -21 °C, i.e. 50, 54 and

53 %, respectively, of the initial values at -65 °C. The onset of the $T_{g\alpha}$ transition, identified by a steep drop in the modulus, was then observed indicating the predicted point at which the shape memory effect begins, figure 4.15 C. The T_g of the polymer systems was established as 31, 37 and 44 °C, respectively; i.e. the point at which the tan δ curve reached a maximum, tan δ_{max}. The numerical values of tan δ_{max}, 1.2, 1.0 and 1.0 tan δ, respectively, are all large enough to indicate that the SMP will behave like elastomers and exhibit large shape recovery during shape memory evaluation (Chun et al., 2002, Tsai et al., 2009).

The moduli at tan δ_{max} were 14, 6 and 4 MPa, respectively, and continued to decrease until the $T_{g\alpha}$ transitions ended, at which the value of the moduli was ca. 1.2, 1.1 and 0.4 MPa, respectively. Thus, the D00 to D02 networks exhibit drops in moduli from ca. 2292, 2293 and 2252 to 1.2, 1.1 and 0.4 MPa; i.e. over three and a half orders of magnitude, well beyond Tsai et al.'s prerequisite (Tsai et al., 2008, Du and Zhang, 2010).

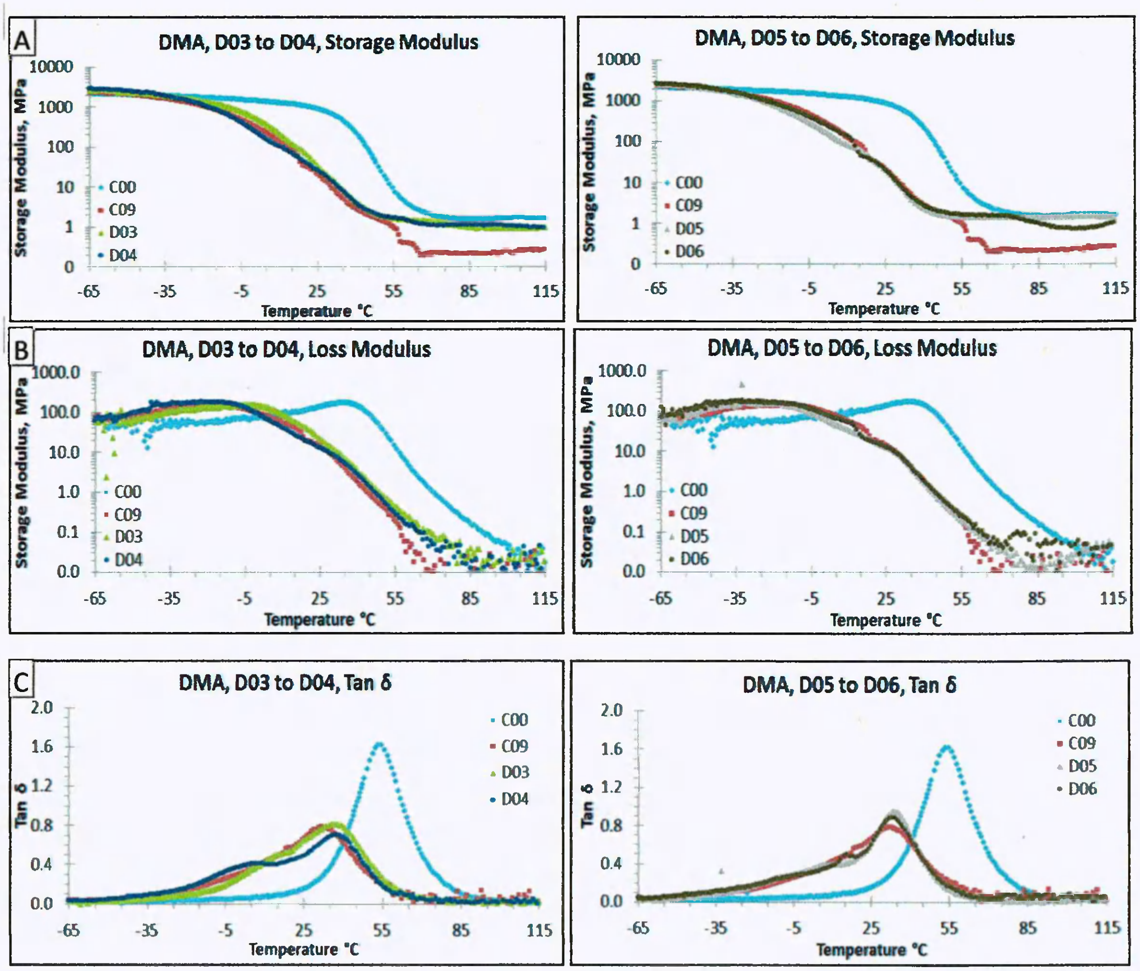

Figure 4.16: DMA data: temperature dependance of D03 to D06 A) storage modulus, B) loss modulus and C) tan δ over the temperature range -65 to 115 °C.

At -65 °C an initial storage modulus of 2529, 2819, 2706 and 2597 MPa was observed for the D03 to D06 networks, respectively, figure 4.16 A. The moduli drops steadily until ca. -18, -31, -33 and -36 °C reaching 1302, 1648, 1574 and 1692 MPa, ca. 51, 58, 57 and 65 % of the initial values, respectively. After this the moduli begin to steeply drop, indicating the onset of the $T_{g\alpha}$ transition, figure 4.16 C. At the tan δ_{max}, 0.8, 0.7, 1.0 and 0.9 tan δ, the T_g is 36, 36, 34 and 34 °C, respectively. At tan δ_{max} the modulus has dropped to ca. 7, 6, 5 and 6 MPa, respectively, continuing to drop steadily until the $T_{g\alpha}$ transitions have finished, ending with moduli of ca. 1.4, 1.1, 1.4 and 1.6 MPa, respectively.

Sample Description	Storage Modulus, MPa							$T_{g\alpha}$ °C	Tan δ_{max}
	-65 °C	-35 °C	-5 °C	25 °C	55 °C	85 °C	115 °C		
C00	2132	1909	1526	902	10	2.0	2.0	53	1.6
C09	2225	1575	465	20	1.0	0.2	0.3	32	0.8
D00	2292	1861	1094	44	1.2	1.1	1.0	31	1.2
D01	2293	1836	534	46	0.7	1.2	1.0	37	1.0
D02	2252	1637	635	69	1.7	0.4	0.4	44	1.0
D03	2529	1924	785	36	1.7	1.0	1.0	36	0.8
D04	2819	1852	413	27	1.5	1.1	1.0	36	0.7
D05	2706	1586	322	20	1.6	1.5	1.0	34	1.0
D06	2597	1629	432	21	1.9	1.0	1.0	34	0.9

Table 4.13: Summary of D00 to D06, dynamic mechanical values obtained from DMA over temperature range of -65 to 115 °C.

When the C09 I90/P10 network is compared to the D00 to D06 I90/P10 networks, figures 4.15 and 4.16, there are large differences between the mechanical properties. In terms of storage modulus, figures 4.15 A and 4.16 A, it is observed that the D00 to D03 I90/P10 networks show very little variation in initial storage modulus compared to C09 I90/P10, while the D04 and D05 I90/P10 networks show increases of >200 MPa. This indicates that reducing the ITX and TEA content has little effect on the initial modulus. Reducing, but not eliminating, the EHA and TPO-L content improves the initial storage modulus a little. The modulus recorded at tan δ_{max} for samples D00 to D06 show that there is not much variation except for the D00 which displayed a higher storage modulus compared to the other networks. This demonstrates that with increasing ITX content there is an observable decrease in storage modulus at tan δ_{max}. After the $T_{g\alpha}$ transition phase the storage moduli for all samples was recorded as above 1 MPa, except for the D02 I90/P10 network although this is not significant.

In terms of the tan δ results, figures 4.15 C and 4.16 C, it is observed that the tan δ $T_{g\alpha}$ transition for the D00 to D06 samples varies from the C09 network result and significantly depends on the photoinitiator and oxygen inhibitor content. The results for D00 and D01 indicate that reducing the amounts of ITX causes an increase in the $T_{g\alpha}$ transition onset, from -27 to -8 and -13 °C, respectively. The D02 I90/P10 network, which contains no TEA, has a $T_{g\alpha}$ transition onset of -21 °C demonstrating an improvement. The D03 and D04 I90/P10 network sample, containing reduced EHA, showed a $T_{g\alpha}$ transition onset of -18 and -31 °C, this indicates that with no EHA there is an improvement in onset temperature but with reduced EHA there is no significant difference. However D05 and D06 showed $T_{g\alpha}$ transition onsets at -33 and -36 °C, indicating that when the amounts TPO-L are reduced the $T_{g\alpha}$ transition onset temperature does not significantly shift.

Overall the $T_{g\alpha}$ peak results for the D00 to D06 I90/P10 networks indicate that with decreased ITX i.e. sample D01, the $T_{g\alpha}$ peak shifts from 32 to 37 °C. When no TEA is present i.e. sample D02, the $T_{g\alpha}$ peak shifts to 44 °C. With decreased EHA i.e. samples D03 and D04, the $T_{g\alpha}$ peak only shifts to 36 °C. No significant changes occurred with decreased TPO-L content i.e. samples D05 and D06, signifying that it has no effect on the composition with regard to $T_{g\alpha}$ peak.

It was observed that there was little change in the overall $T_{g\alpha}$ transition peak base width except for samples D00 and D01 which were reduced compared to C00.

As with the position of the $T_{g\alpha}$ transition peak, the tan δ_{max} intensities also change as the photoinitiator and oxygen inhibitor formulations are altered. It was found that with decreased ITX, D00 and D01, an increased tan δ_{max} occurs, 1.2 and 1.0 tan δ, respectively. When no TEA content is present, D02, the tan δ_{max} also increases. With decreased EHA, D03 and D04, there is no significant change in the tan δ_{max}, 0.8 and 0.7 tan δ, respectively. However a decreased TPO-L content, D05 and D06 resulted in small increases, 1.0 and 0.9 tan δ, respectively, compared to D03 and D04.

4.7. D00 to D06 I90/P10 Networks Summary

Overall there is no clear indicator about which or what amounts of photoinitiator or oxygen inhibitors are causing the undesired effects on the I90/P10 network.

From the variations previously formulated, the D00 to D06, it was decided that no one chemical was responsible for the undesired effects. Therefore a formulation was developed, D07 I90/P10 network, containing all the previous chemicals but in diminished quantities, except for TPO-L, table 4.14.

Sample Description:	Photoinitiator		Oxygen Inhibitor	
	TPO-L, wt%	ITX, wt%	EHA, wt%	TEA, wt%
D07	0.350	0.05	0.05	0.05

Table 4.14: Formulations D07 I90/P10 network with vary amounts of photoinitiator and oxygen inhibitors.

The TPO-L was kept at 3.5 wt% as it appeared to not affect the mechanical properties of the produced polymer network, however as all other photoinitiators and oxygen inhibitors caused a reduction to the SME onset temperature and were all reduced to 0.5 wt%. Using this initiator cocktail should lead to reduced retardation of the mechanical properties while still providing a large retardation against oxygen inhibition therefore maintaining the curing speed.

4.8. D07 I90/P10 Network; Results and discussion

4.8.1. Mechanical Properties

4.8.1.1. Dynamic Mechanical Analysis

In order to assess the dynamic mechanical properties of the D07 formulations, solid polymer networks, 1.0 mm thick, were formed. The dynamic mechanical properties, storage modulus, loss modulus and tan δ was compared to the DMA properties of the C00 and C09 I90/P10 networks as a function of temperature, -65 to 115 °C, figure 4.17. The dynamic mechanical properties of interest are summarized in table 4.15.

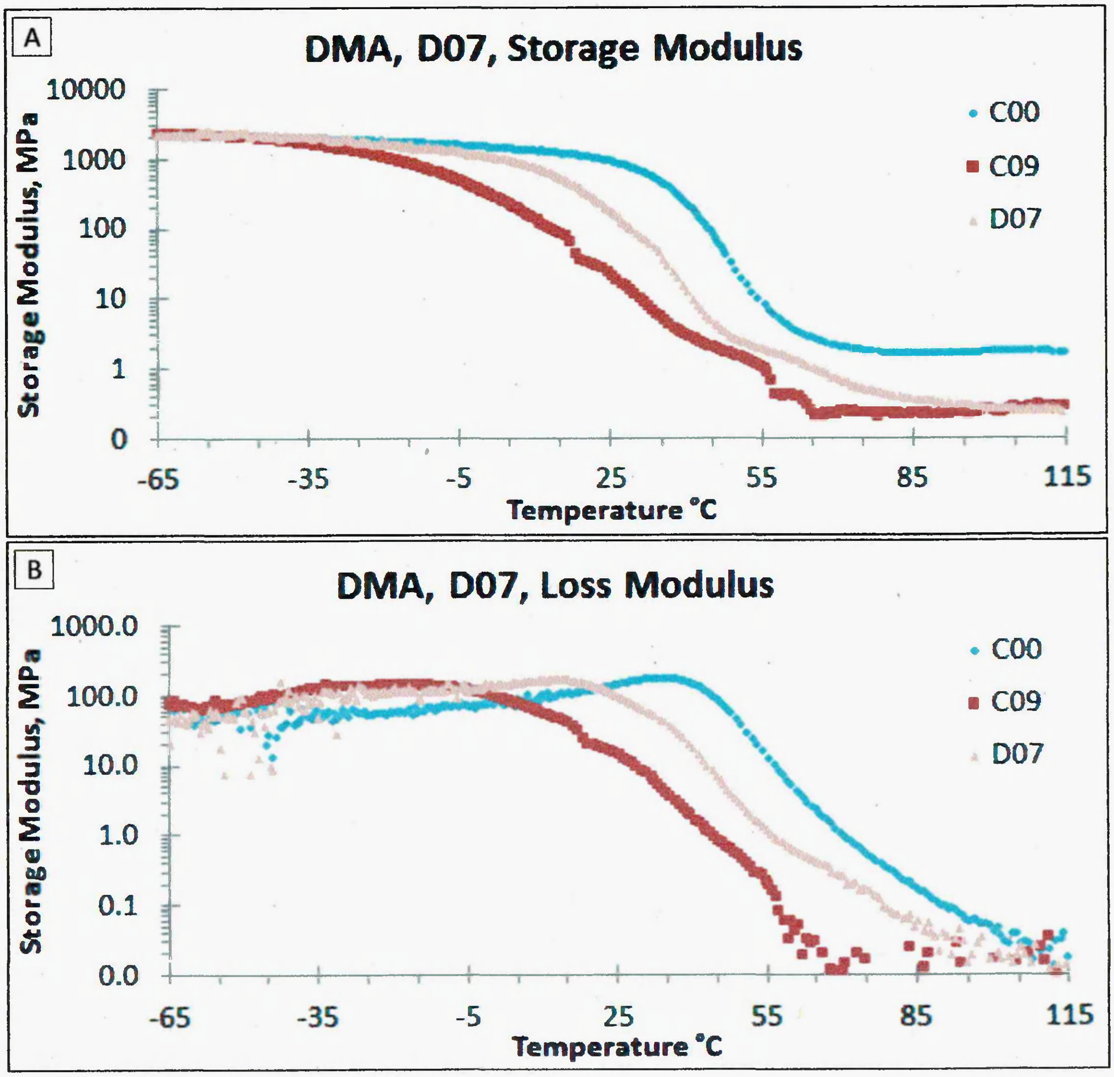

Figure 4.17: DMA data: temperature dependance of the D07 I90/P10 network A) storage modulus, B) loss modulus and C) tan δ over the temperature range -65 to 115 °C.

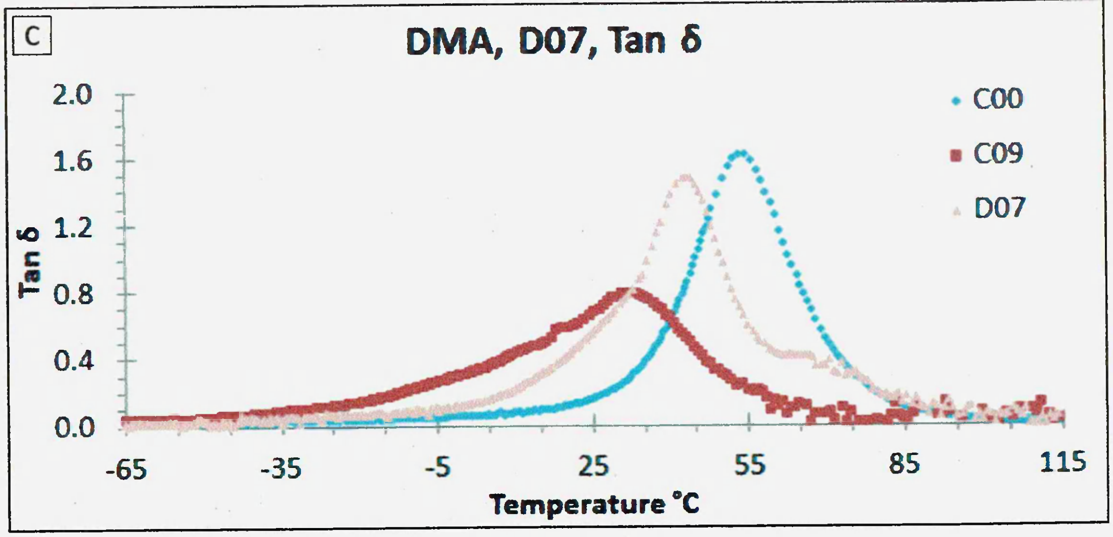

Figure 4.17: DMA data: temperature dependance of the D07 I90/P10 network A) storage modulus, B) loss modulus and C) tan δ over the temperature range -65 to 115 °C.

The D07 I90/P10 network exhibited an initial storage modulus of 2255 MPa at - 65 °C, figure 4.17 A, which steadily decreased reaching a value of 1319 MPa at -6 °C; approximately 58 % of the initial storage modulus. A steep drop in the modulus marked the onset of the $T_{g\alpha}$ transition and established the predicted starting point of the shape memory effect. For D07 I90/P10 the T_g is 43 °C and the tan δ_{max} value is 1.5 tan δ. This latter value is large enough to indicate that this network will behave like an elastomer and exhibit useful shape memory properties. The D07 I90/P10 network exhibits a drop in modulus of ca. three and a half orders of magnitude, from 2255 MPa at -65 °C to 0.4 MPa at the end of the $T_{g\alpha}$ transition. Consequently, it is predicted to exhibit very useful shape memory properties.

Sample Description	Storage Modulus, MPa							$T_{g\alpha}$ °C	Tan δ_{max}
	-65 °C	-35 °C	-5 °C	25 °C	55 °C	85 °C	115 °C		
C00	2132	1909	1526	902	10	2.0	2.0	53	1.6
C09	2225	1575	465	20	1.0	0.2	0.3	32	0.8
D07	2255	2009	1308	109	1.5	0.4	0.3	43	1.5

Table 4.15: Summary of the dynamic mechanical values for the D07 I90/P10 network, obtained from DMA over temperature range of -65 to 115 °C.

When the D07 I90/P10 network is compared to the C00 and C09 I90/P10 networks there are observable differences between the mechanical properties. Comparing the storage modulus, figure 4.17 A, there is no significant difference between the initial starting moduli, however as temperature increases there are clear differences, with C00 showing the sharpest drop, followed by D07 and C09. At the $T_{g\alpha}$ transition peak, the moduli of the C00, C09 and D07 I90/P10 networks were 12, 8 and 7 MPa, respectively, indicating that the D07 is still not fully comparable with the original C00 material. This trend of descending modulus is also similar during the rubbery modulus phase with moduli of 1.7, 0.2 and 0.4 MPa being recorded, respectively.

In terms of the tan δ results, figure 4.17 C, it is observed that the tan δ_{max} intensity for C09 decreases by ca. 50 %, compared to C00 and shifts to a lower temperature, ca. 32 °C, with the overall $T_{g\alpha}$ transition base broadening significantly by ca. 25 °C. Compared to the C00 demonstrates no significant loss of tan δ_{max} for D07 but the maximum shifts to lower temperatures, ca. 10 °C, with the overall $T_{g\alpha}$ transition base broadening significantly by ca. 24 °C, similar to C09.

The shift of the $T_{g\alpha}$ and broadening of the tan δ baseline indicates that the initiators used for D07 will still cause a much earlier onset of the SME, ca. 0 °C. This is lower than the polymer would be normally cooled, therefore it is probable that a temporary shape will be difficult to fix. As the tan δ_{max} did not diminish significantly the shape memory recovery is expected to be comparable to the original C00 I90/P10 network.

4.8.2. Shape Memory Properties

4.8.2.1. Unconstrained Shape Memory Effect Evaluation

The unconstrained SME testing was not carried out due to the onset temperature of the D07 I90/P10 network being much earlier, greatly outside desired onset temperature range, 18 to 22 °C, when compared to the original C00 I90/P10 network.

4.9. D07 I90/P10 Network Summary

As the fastest curing photoinitiator formulation was found to be that used in the C09 formulation, polymer films were produced and analysed. It was found that the mechanical properties were significantly different from the original C00 sample. Due to this further photoinitiator formulations, D00 to D06, were prepared and polymer films made and analysed. It was found that no individual photoinitiator or oxygen inhibitor component was the cause of the differing mechanical properties. Therefore a photoinitiator cocktail was formed containing reduced amounts of nearly all photoinitiator components, D07. It was found that it contained similar mechanical properties to the original C00 I90/P10 network but with a lowered shape memory onset temperature. Due to the earlier onset of shape memory, the D07 I90/P10 network is no longer in the desired shape memory onset temperature range, ca. 18 to 22 °C, for its intended purpose, SMP packaging. Therefore it was decided in order to create a fast curing SMP packaging solution a higher T_g polymer, with a higher SME onset, was required i.e. IBoMA.

Previously the IM80/P20 and IM70/P30 networks were found to have the desired storage modulus, T_g, and SME abilities, figures 4.8 and 4.11. SMP films, 0.5 mm thick, were formed from the IM80/P20 and IM70/P30 networks using the D07 photoinitiator formulation in order to carry out DMA and unconstrained SME testing.

4.10. D07 IM80/P20 to IM70/P30 Networks Results and Discussion

4.10.1. Networks Mechanical Properties

4.10.1.1. Dynamic Mechanical Analysis

In order to assess the dynamic mechanical properties of IM80/P20 and IM70/P30 networks when cured using the D07 initiator cocktail, solid polymer networks, 1.0 mm thick, were formed. The dynamic mechanical properties, storage modulus, loss modulus and tan δ were compared to the DMA properties of the C00, C09 and D07 I90/P10 networks as a function of temperature, -30 to 130 °C, figure 4.18. The dynamic mechanical properties of interest are summarized in table 4.16.

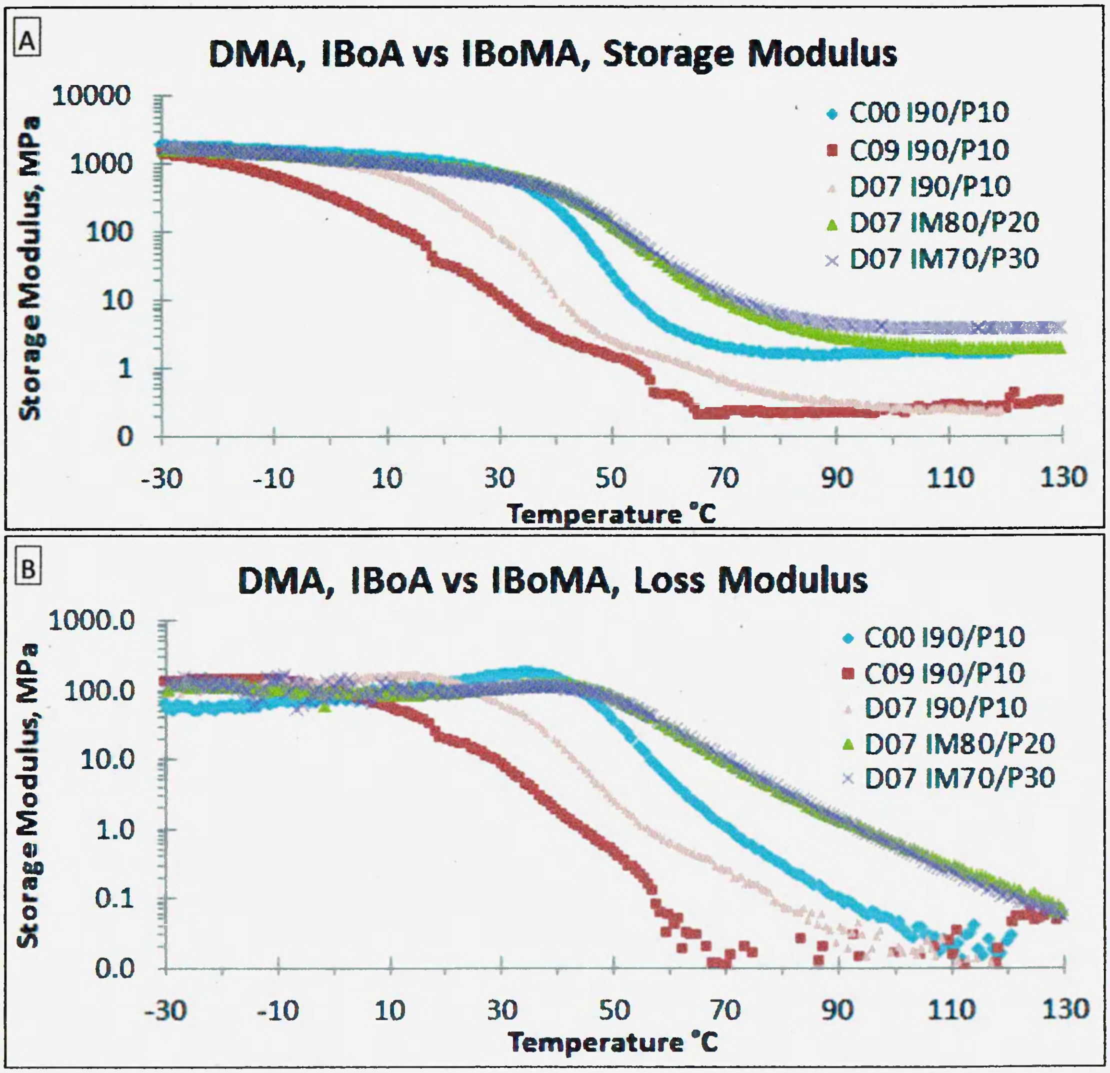

Figure 4.18: DMA data: temperature dependance of D07 IM80/P20 to D07 IM70/P30 networks A) storage modulus, B) loss modulus and C) tan δ over the temperature range -30 to 130 °C.

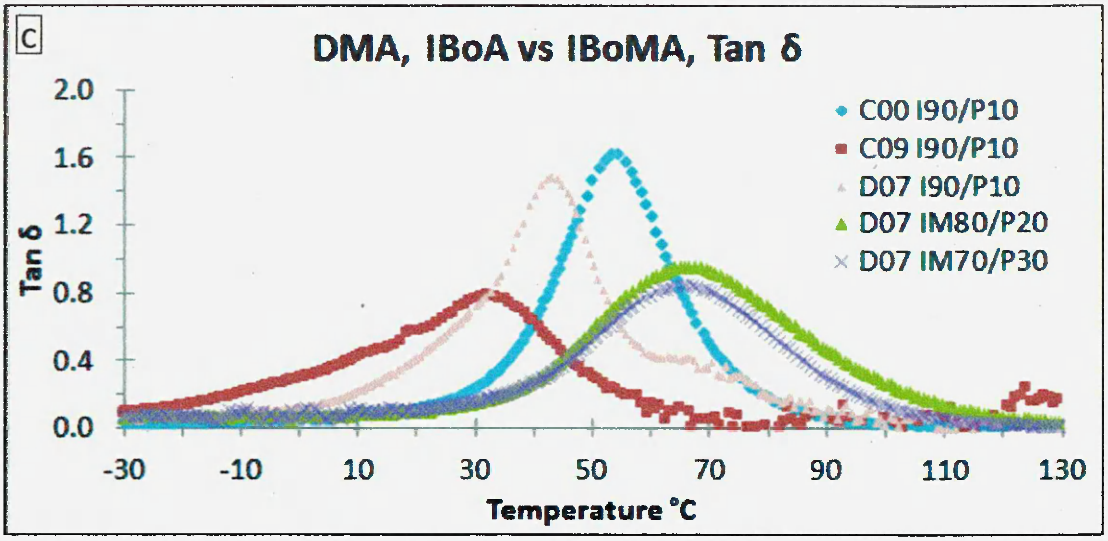

Figure 4.18: DMA data: temperature dependance of D07 IM80/P20 to D07 IM70/P30 networks A) storage modulus, B) loss modulus and C) tan δ over the temperature range -30 to 130 °C.

At -30 °C an initial storage modulus of 1634 and 1786 MPa was observed for the D07 IM80/P20 and IM70/P30 networks, respectively, figure 4.18 A. The modulus drops steadily until ca. 20 and 12 °C, respectively, reaching ca. 904 and 1014 MPa; ca. 55 and 58 %, respectively of the initial modulus values. After this the modulus begins to steeply drop, this indicates the onset of the $T_{g\alpha}$ transition stage, figure 4.18 C. At the tan δ_{max}, 1.0 and 0.8 tan δ, respectively, the T_g of the polymer networks are established, 66 and 65 °C, respectively. At tan δ_{max} the modulus has dropped to 16 and 20 MPa, respectively, these continue to drop steadily until the $T_{g\alpha}$ transition stage has finished, ending with a modulus of ca. 2 and 4 MPa, respectively. Both networks demonstrate ca. a two and a half order magnitude drop in storage modulus, therefore SME should occur.

Sample Description	Storage Modulus, MPa								$T_{g\alpha}$ °C	Tan δ_{max}
	-30°C	-10 °C	10 °C	30 °C	50 °C	70 °C	90 °C	130 °C		
C00 I90/P10	1857	1588	1272	686	24	2	1.6	1.6	53	1.6
C09 I90/P10	1418	660	133	11	1.4	0.2	0.2	0.3	32	0.8
D07 I90/P10	1810	1345	765	84	3	0.7	0.3	0.2	43	1.5
D07 IM80/P20	1634	1462	1078	699	130	10	3	2	66	1.0
D07 IM70/P30	1786	1444	1054	655	136	12	5	4	65	0.8

Table 4.16: Summary of dynamic mechanical values for the D07 IM80/P20 to D07 IM70/P30 networks, obtained from DMA over temperature range of -30 to 130 °C.

The D07 IM80/P20 and IM70/P30 networks compared to the original C00 I90/P10 network formulation show that there is an overall reduction in initial storage modulus up to ca. 30 °C, where it is observed that all the storage moduli are similar. At 50 °C both the D07 IM80/P20 and IM70/P30 networks have a greater storage modulus than the C00 I90/P10 network, this continues up to end of the $T_{g\alpha}$ transition stage, where again both the D07 IM80/P20 and IM70/P30 networks have a greater storage modulus, above T_g, than the C00 I90/P10 network.

In terms of tan δ, the D07 IM70/P30 network has a lower onset temperature for the $T_{g\alpha}$ transition by ca. 6 °C, while the D07 IM80/P20 network has a slightly higher onset by ca. 2 °C compared with C00. It is also observed that both D07 IM80/P20 and IM70/P30 networks, although having greater tan δ_{max} modulus by ca. 4 and 8 MPa, and higher T_g by ca. 13 and 12 °C, both have lower tan δ_{max} intensity of ca. 0.6 and 0.8 tan δ, respectively. Another observation is the broadening of the tan δ baseline, increasing by ca. 25 and 15 °C at higher temperatures, towards the end of the $T_{g\alpha}$ transition stage. Overall these results demonstrate that the D07 initiator formulation can produce an IBoMA network, D07 IM80/P20 network, with a similar T_g onset temperature and higher storage modulus. The predicted SME behaviour will be slower, due to a decrease in the tan δ_{max} intensities.

4.10.2. Shape Memory Properties

4.10.2.1. Unconstrained Shape Memory Effect Evaluation

Unconstrained SME testing was carried out in order to assess whether the D07 IM80/P20 to IM70/P30 networks would demonstrate SME and to explore the effect of the new photoinitiator formulation on SME, figure 4.19. The SME testing was previously described in section 2.1.6, figure 2.15. The SME properties of interest are summarized in tables 4.17.

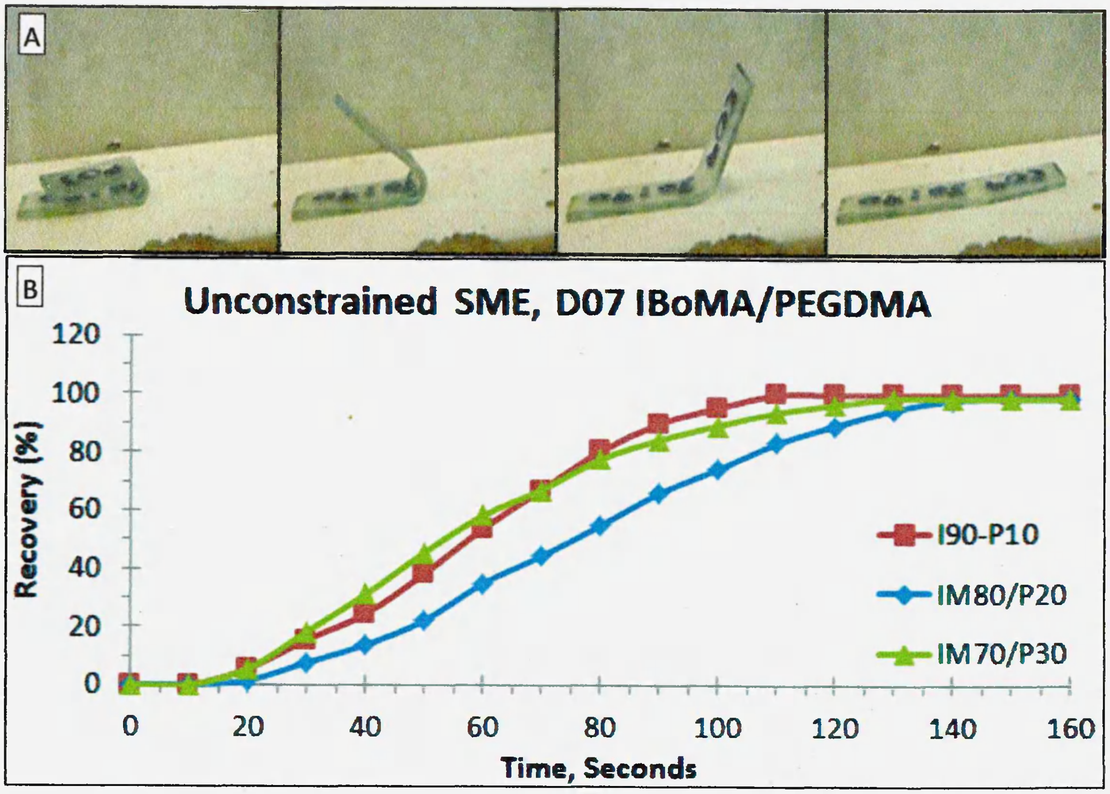

Figure 4.19: Unconstrained SME testing of I90/P10 and D07 IM80/P20 to IM70/P30 networks, from temporary to permanent shape, A) still images of IM70/P30 SMP at sequential intervals, B) plotted against time at a fixed temperature, ca. 72 and 76 °C, respectively.

The D07 IM80/P20 to IM70/P30 networks both exhibited θ_{Max} results of 100 %, 180 °, demonstrating that both can accommodate a high level of deformation strain. After the deformation constraint was removed, both networks were left at T_{low}, 0 to 5 °C, no recovery occurred, leading to θ_{Fixed} of 100%, 180 °. This demonstrated that the D07 IM80/P20 to IM70/P30 networks can store 100 % of the strain conferred by deformation. This was as expected due to a previous report by Yang et al. (2007) who demonstrated that at low temperatures i.e. T_{low}, in class I SMP the entropy driven strain recovery forces are simply not enough to overcome the fixed glassy chain interactions.

Sample Description	θ_{Max}, %	θ_{Fixed}, %	$\theta_{1/2Final}$, %	θ_{Final}, %	$\theta_{1/2Final}$ Time ,Sec	θ_{Final} Time ,Sec
C00 I90/P10	100	100	50	100	57	110
C00 IM80/P20	100	100	50	97	108	280
C00 IM70/P30	100	100	50	100	69	140
D07 IM80/P20	100	100	50	98	75	150
D07 IM70/P30	100	100	50	98	53	130

Table 4.17: SME test results, θ_{Max}, θ_{Fixed}, $\theta_{1/2Final}$, θ_{Final}, $\theta_{1/2Final}$ Time, and θ_{Final} Time, from C00 I90/P10 and D07 IM80/P20 to IM70/P30 networks temporary shape recovery, plotted against time at a fixed temperature, ca. 72 and 76 °C, respectively.

Shape memory recovery was carried out at 76 °C and the recovery was recorded every 10 seconds until D07 IM80/P20 to IM70/P30 networks reached the θ_{Final}. The D07 IM80/P20 to IM70/P30 networks demonstrated that it can store ca. 100 % of the deformed strain at T_{low}, and almost fully, 98 %, return to its original shape when unconstrained SME testing is carried out.

In order to further assess the D07 IM80/P20 to IM70/P30 networks shape memory ability the $\theta_{1/2\ Final}$ time of recovery and θ_{Final} time of recovery, ca. 75 and 53 seconds, respectively, were recorded. These results indicate 50 % recovery is achieved in ca. half the time of the full recovery time.

These results are similar to previous unconstrained SME testing carried out on C00 IM80/P20 to IM70/P30 networks, with the IM70/P30 network having a faster shape memory ability compared to the IM80/P20 network, 140 and 280 sec, respectively, and both able to achieve 50 % recovery in ca. half the time of the full recovery time. However it was observed that the D07 IM80/P20 network had a markedly decreased $\theta_{1/2Final}$ and θ_{Final} time when compared to the C00 IM80/P20 network while the D00 IM70/P30 showed minor improvements to the $\theta_{1/2Final}$ and θ_{Final} time when compared to C00 IM70/P30. This indicates that the new initiator cocktail has improved the SME time, allowing a faster full recovery compared to the original C00 formulation.

4.11. D07 IM80/P20 to IM70/P30 Networks Summary

Previously the D07 photoinitiator cocktail was formed which produced similar mechanical properties as the C00 photoinitiator cocktail in IBoA networks. However D07 caused a shift of the IBoA T_g to lower temperatures producing an earlier onset of shape memory. Therefore a polymer with a higher T_g, therefore a higher SME onset, was required i.e. IBoMA. It was established that the D07 IM80/P20 and IM70/P30 networks had the desired storage modulus, T_g, and SME abilities, figures 4.18 and 4.19 for a shape memory packaging solution. However it was found that when the D07 IM80/P20 and IM70/P30 networks were coated, 12 μm, onto a Sulpak substrate, a full cure could not be achieved in >10 passes. The lack of cure for the D07 IM80/P20 and IM70/P30 networks was potentially caused by the methacrylate double bond being less reactive than the acrylate double bond. Due to the slower cure the methacrylate networks became more susceptible to oxygen inhibition, which caused the production of oxygen peroxides, figure 4.13. The retarded polymer cure then allowed further oxygen to diffuse into the polymer, preventing a full cure from occurring. Therefore in order to assess the SME abilities of the D07 IM80/P20 and IM70/P30 networks a nitrogen atmosphere was utilised to form 40, 24 and 12 μm thick D07 IM80/P20 and IM70/P30 network coatings on Sulpak substrates.

4.12. Coated Substrate Results and Discussion

4.12.1. Shape Memory Properties

4.12.1.1. Unconstrained Shape Memory Effect Evaluation

Unconstrained SME testing was carried out in order to assess whether the D07 IM80/P20 and IM70/P30 networks would demonstrate SME when coated onto Sulpak, figure 4.20. The SME testing was previously described in section 2.1.6, figure 2.17. The SME properties of interest are summarized in tables 4.18.

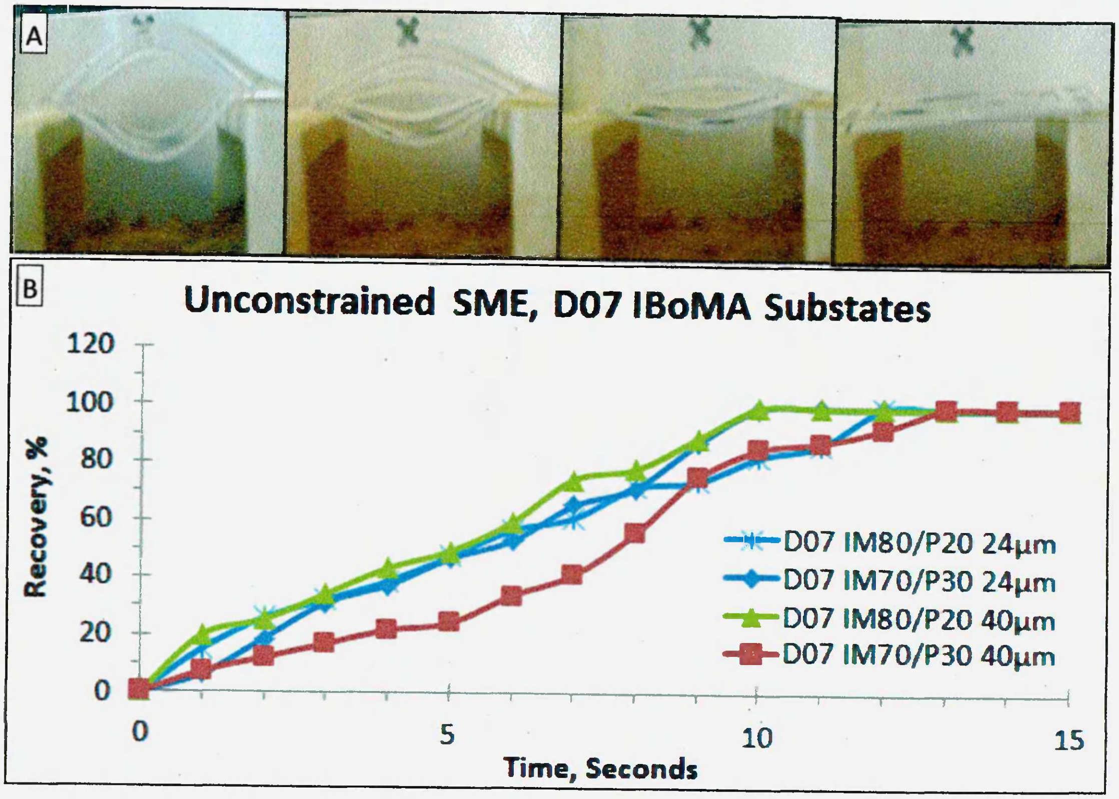

Figure 4.20: Unconstrained SME testing of D07 IM80/P20 and IM70/P30 24 and 40 µm networks coated on Sulpak, from temporary to permanent shape, A) still images of IM70/P30 40 µm SMP coated on Sulpak at sequential intervals, B) plotted against time at a fixed temperature, ca. 50 °C.

The D07 IM80/P20 to IM70/P30, 24 and 40 µm, networks coated on Sulpak all exhibited θ_{Max} results of 100 % demonstrating that all can accommodate a high level of deformation strain without breaking. After the deformation constraint was removed, all networks were left at T_{low}, 0 to 5 °C, some shape recovery occurred, leading to θ_{Fixed} results of 53, 61, 63 and 78 %, respectively. This was not fully expected as a previous report by Yang et al. (2007) demonstrated that at low temperatures i.e. T_{low}, the

entropy driven strain recovery forces of class I SMP are simply not enough to overcome the fixed glassy chain interactions. However when the SMP is coated onto a substrate, an additional strain is exerted from the substrate onto the polymer. This potentially causes an amount of forced shape loss to occur if the SMP is not mechanically strong enough to restrain the substrate in the temporary shape, as the substrate cannot maintain a temporary shape itself and will collapse without support.

Sample Description	θ_{Max}, %	θ_{Fixed}, %	$\theta_{1/2Final}$, %	θ_{Final}, %	$\theta_{1/2Final}$ Time ,Sec	θ_{Final} Time ,Sec
D07 IM80/P20 24 µm	100	53	50	100	5.0	12
D07 IM70/P30 24 µm	100	61	50	100	5.5	10
D07 IM80/P20 40 µm	100	63	50	100	5.0	10
D07 IM70/P30 40 µm	100	78	50	100	7.5	13

Table 4.18: SME test results, θ_{Max}, θ_{Fixed}, $\theta_{1/2Final}$, θ_{Final}, $\theta_{1/2Final}$ Time, and θ_{Final} Time, D07 IM80/P20 and IM70/P30 24 and 40 µm networks coated on Sulpak temporary shape recovery, plotted against time at a fixed temperature, ca. 50 °C.

Shape memory recovery of the IM80/P20 and IM70/P30 coated substrates was carried out at ca. 50 °C rather than 72 and 76 °C, respectively, section 4.10.2.1, in order to reduce the speed of the SME so that a more thorough evaluation could be made.

The recovery was recorded every 1 second until all networks reached θ_{Final}. All networks demonstrated full shape recovery, 100 %, to its original shape when unconstrained SME testing is carried out.

In order to further assess the D07 IM80/P20 to IM70/P30, 24 and 40 µm, network coated Sulpak shape memory ability the $\theta_{1/2\ Final}$ and θ_{Final} time of recovery, ca. 5.0, 5.5, 5.0 and 7.5 seconds, respectively, were recorded. These results indicate 50 % recovery is achieved in ca. half the time of the full recovery time, which corresponds well with the pure polymer networks, figure 4.19. However there is a marked difference in the $\theta_{1/2\ Final}$ and θ_{Final} time of recoveries between the pure polymers and coated substrates. This difference is due to sample thickness, the coated substrates polymer layer is only a fraction of the pure polymers thickness, and the non-shape memory character of the substrate forcing itself onto the SMP, both causing a faster shape recovery once the polymer undergoes the transition from a glassy solid state to a rubbery state.

These results show that if the methacrylates could be cured in oxygen they would be able to demonstrate large shape memory abilities at both 24 and 40 μm thicknesses when coated onto Sulpak paper. When comparing two different sample thicknesses it is observed that there is no significant difference between the two methacrylate networks at 24 μm thickness when coated onto a substrate. However an obvious difference arises between the 40 μm thickness samples with the IM70/P30 network displaying a greater shape fixity but also a slower shape return when compared to the IM80/P20 sample. Overall both IM80/P20 and IM70/P30 networks are good candidates for a SMP packaging solution provided the oxygen inhibition can be eradicated.

4.13. Conclusion

tBA was found to be unsuitable for mainline production using a UV curing method and a replacement monomer was required. Three substitute monomers, IBoA, IBoMA and tBMA, were chosen and investigated by ATR-FTIR, DMA and SME evaluation. Overall IBoA was found to be the most suitable replacement for tBA due to its higher flashpoint, boiling point and similar mechanical and curing properties. Although the IBoMA and tBMA also had higher flash points and boiling points than tBA the glass transition temperatures were significantly outside the typical working range of a potential SMP packaging solution. I90/P10 and I80/P20 network sample solutions were prepared and sent to Chesapeake for evaluation on the UV curing machine, with both samples being successfully cast onto substrates. Due to Chesapeake's requirements, curing in two passes on the UV curing machine, optimisation of the photoinitiator cocktail was required. In order to reduce the cure time of the IBoA-co-PEGDMA network, I90/P10, a series of experiments were carried out where additional photoinitiators and oxygen inhibitors are introduced to form a photoinitiator 'cocktail' with the aim to produce a full cure in two passes on the UV curer.

This goal was achieved with the C09 formulation; however the photoinitiator cocktail caused some unwanted effects on the mechanical properties and shape memory abilities of the polymer network. This caused reduced storage modulus below and above T_g, a broader and less intense $T_{g\alpha}$ transition stage with a lower T_g and a much earlier predicted SME onset temperature. Unconstrained SME testing was carried out but found no shape memory ability in the desired temperature range, therefore an alternative photoinitiator cocktail was formulated. The D07 formulation was found to have the least detrimental effects on the mechanical and shape memory properties of the I90/P10 network. The initial modulus above and below T_g were similar to the C00 I90/P10 network, the $T_{g\alpha}$ transition stage was broadened and reduced in intensity but not to the same extreme as the C09 I90/P10 network. However a lower T_g was observed with a much lower predicted SME onset temperature which was outside the desired temperature range for SMP packaging, therefore no SME testing was carried out.

Due to the diminishing effects on the mechanical and shape memory properties of the D07 photoinitiator cocktail IBoA was substituted for IBoMA which when photopolymerised with D07 produced polymer networks, IM80/P20 and IM70/P30. It was found that these networks had similar mechanical properties as the original C00 I90/P10 network with a greater storage modulus above T_g, indicating that greater mechanical stress would be generated when undergoing shape memory recovery. It was found that both D07 IM80/P20 and IM70/P30 networks still had a broadened $T_{g\alpha}$ transition stage with lower intensities than the C00 I90/P10 network. However the broadening primarily occurs at the end of the $T_{g\alpha}$ transition stage while the reduction in intensity simply indicates a slower SME transformation. With the combination of the unconstrained SME testing results, it was observed that the IM70/P30 network, which demonstrated superior shape memory ability compared to the D07 IM80/P20 network, would be the best candidate for a shape memory packaging solution. However it was discovered that neither the D07 IM80/P20 or IM70/P30 networks would cure in air, this was possibly due to oxygen inhibition and a lower reactivity of the methacrylate double bond. In order to establish the shape memory abilities of the networks however each was coated onto a substrate at 24 and 40 µm thickness and cured in a nitrogen atmosphere. All networks at both thicknesses were found to show shape memory ability as well as demonstrate relatively good shape fixity and original shape recovery. Overall if the methacrylate networks can be cured in air they would make a suitable SMP to use for packaging applications.

4.14. References

AGARWAL, S., CHOUDHARY, V., and VARMA, I.K., (1997). Structure-properties correlation in copolymers of methyl methacrylate & alkyl methacrylates. Defence Science Journal, 47 (3), 401-409.

AWOKOLA, M., et al. (2002). UV crosslinking of acryloyl functional polymers in the presence of oxygen. Progress in Organic Coatings, 44 (3), 211-216.

AYDIN, M., ARSU, N., and YAGCI, Y., (2003). One-component bimolecular photoinitiating systems, 2 - thioxanthone acetic acid derivatives as photoinitiators for free radical polymerization. Macromolecular Rapid Communications, 24 (12), 718-723.

BELON, C., et al. (2010). Overcoming the oxygen inhibition in the photopolymerization of acrylates: A study of the beneficial effect of triphenylphosphine. Journal of Polymer Science Part A: Polymer Chemistry, 48 (11), 2462-2469.

BOLON, D.A., WEBB, K.K., (1978) J. Appl. Polym. Sci. 22 (9) 2543.

CHUN, B.C., et al. (2002). Enhanced dynamic mechanical and shape-memory properties of a poly(ethylene terephthalate)-poly(ethylene glycol) copolymer crosslinked by maleic anhydride. Journal of Applied Polymer Science, 83 (1), 27-37.

COLTHUP, N.B., DALY, L.H., and WIBERLEY, S.E., 1990. Introduction to infrared and Raman spectroscopy. 3rd ed., USA ISBN 0-12-182554-X

DECKER, C., BIANCHI, C., and JONSSON, S., (2004). Light-induced crosslinking polymerization of a novel N-substituted bis-maleimide monomer. Polymer, 45 (17), 5803-5811.

DENT R.W., (2010). Preparation, Characterisation and Application of Electro-Conductive Assemblies. PhD, University of Leeds

GALL K.A., and SAFRANSKI D.L., (2009). Shape memory polymer materials with controlled toughness and methods of formulating same. US Patent 0149617 A1. Patent from Google Patents last accessed 16 February 2012 at: http://www.google.com/patents

GALL, K., et al. (2005). Thermomechanics of the shape memory effect in polymers for biomedical applications. Journal of Biomedical Materials Research Part a, 73A (3), 339-348.

GRUBER, H.F., (1992). Photoinitiators for free-radical polymerization. Progress in Polymer Science, 17 (6), 953-1044.

HIFI INDUSTRIAL FILM LTD [online]. Last accessed 1/23/2012 2012 at: http://www.hififilm.com/index.html.

KAGAMI, Y., GONG, J.P., and OSADA, Y., (1996). Shape memory behaviors of crosslinked copolymers containing stearyl acrylate. Macromolecular rapid communications, 17 (8), 539-543.

KRAMER, N.J., et al. (2010). Shape memory polymer thin films deposited by initiated chemical vapor deposition. Macromolecules, 43 (20), 8344-8347.

LEE, T. Y., et al. (2004). The effect of monomer structure on oxygen inhibition of (meth)acrylates photopolymerization. Polymer, 45 (18), 6155-6162.

LENDLEIN, A., and KELCH, S., (2002). Shape-memory polymers. Angewandte Chemie-International Edition, 41 (12), 2034-2057.

LIU, C., QIN, H., and MATHER, P.T., (2007). Review of progress in shape-memory polymers. Journal of Materials Chemistry, 17 (16), 1543-1558.

MASSON, F., et al. (2004). UV-curable formulations for UV-transparent optical fiber coatings I. acrylic resins. Progress in Organic Coatings, 49 (1), 1-12.

ORTEGA, A.M., et al. (2008). Structure-property relationships in photopolymerizable polymer networks: Effect of composition on the crosslinked structure and resulting thermomechanical properties of a (meth)acrylate-based system. Journal of Applied Polymer Science, 110 (3), 1559-1572.

SAFRANSKI, D.L., and GALL, K., (2008). Effect of chemical structure and crosslinking density on the thermo-mechanical properties and toughness of (meth)acrylate shape memory polymer networks. Polymer, 49 (20), 4446-4455.

SAFRANSKI, D.L., and GALL, K., (2008). Effect of chemistry on thermo-mechanical shape-memory properties of acrylate networks. Lancaster; 439 Duke Street, Lancaster, PA 17602-4967 USA, Destech Publications, Inc.

SELLI E., AND BELLOBONO I.R., (1993), Photopolymerization of multifunctional monomers: kinetic aspects, in: J.P. Fouassier, J.F. Rabek (Eds.), Radiation Curing in Polymer Science and Technology: Polymerisation Mechanisms, Vol. III, Elsevier Applied Science, London, p. 1.

STUDER, K., et al. (2003). Overcoming oxygen inhibition in UV-curing of acrylate coatings by carbon dioxide inerting, part I. Progress in Organic Coatings, 48 (1), 92-100.

STUDER, K., et al. (2003). Overcoming oxygen inhibition in UV-curing of acrylate coatings by carbon dioxide inerting: Part II. Progress in Organic Coatings, 48 (1), 101-111.

TONG T.H., (2007). Maleimide based high temperature shape memory polymers. US Patent 7276195 B1. Patent from Google Patents last accessed 16 February 2012 at: http://www.google.com/patents

TONG T.H., (2011). Shape memory polymers formed by self crosslinking of copolymers. US Patent 0282022 A1. Patent from Google Patents last accessed 16 February 2012 at: http://www.google.com/patents

TSAI, T.Y., et al. (2009). Effect of clay with different cation exchange capacity on the morphology and properties of poly(methyl methacrylate)/Clay nanocomposites. Polymer Composites, 30 (11), 1552-1561.

TSAI, Y., et al. (2008). Shape memory effects of poly(ethylene terephthalate-co-ethylene succinate) random copolymers. European Polymer Journal, 44 (2), 550-554.

VOIT, W., et al. (2010). High-strain shape-memory polymers. Advanced Functional Materials, 20 (1), 162-171.

WANG, Y.L., et al. (2009). Synthesis and characterization of a novel biodegradable thermoplastic shape memory polymer. Materials Letters, 63 (3-4), 347-349.

WARREN, P.D., MCGRATH, D.V., and GEEST, J.P.V., (2010). Effect of crosslinker length and composition on the hydrophobicity and thermomechanical response of acrylate-based shape-memory polymers. Macromolecular Materials and Engineering, 295 (4), 386-396.

XIAN K.L., LI C., YI P.Z., and ZHI Z.D., (2010). Synthesis and characterization of thermoresponsive shape-memory poly(stearyl acrylate-co-acrylamide) hydrogels. Journal of Materials Science, 45 (10), 2703.

YAKACKI, C.M., et al. (2008). Strong, tailored, biocompatible shape-memory polymer networks. Advanced Functional Materials, 18 (16), 2428-2435.

YANG, F., et al. (2007). Nanoscale indent formation in shape memory polymers using a heated probe tip. Nanotechnology, 18 (28), 285302.

Chapter 5: Evaluation of Polyurethane Composites as SMP

5. Introduction

Polyurethane, PU, is a thermoplastic polymer, with a repeating chain joined together by urethane linkages. It is formed by the polyaddition reaction of a diisocyanate and a long chain diol in the presence of a catalyst, figure 5.1. PU is one of the most used and most versatile products with elastic properties available in engineering thermoplastics and is in the top five most used thermoplastics in the world. Typically PU is characterised by a microphase-separated morphology, in which a soft domain, soft segment, SS, normally a linear long-chain diol, typically a polyester or polyether diol (Clemitson, 2008), is reinforced by condensation with a hard domain, hard segment, HS, consisting of a diisocyanate, figure 5.2.

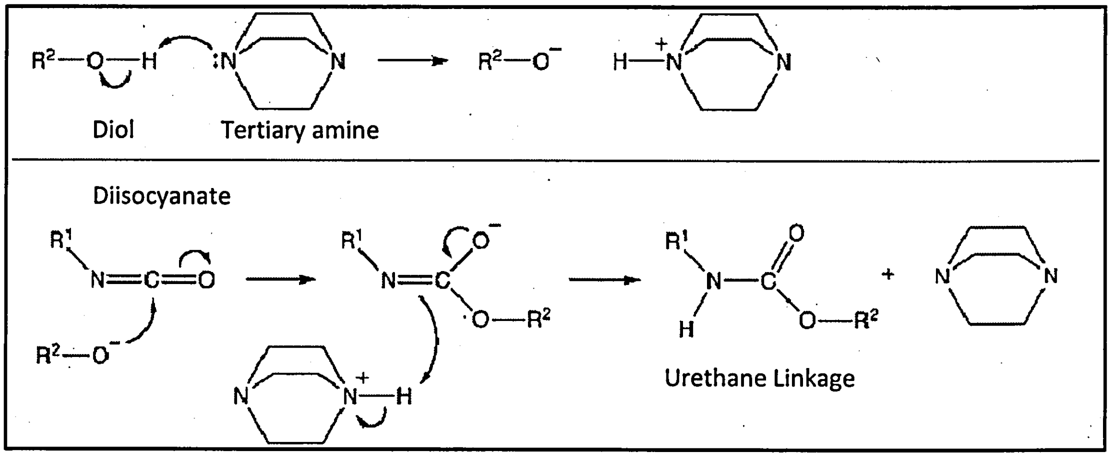

Figure 5.1: Polyaddition reaction of a diisocyanate and a diol in the presence of a tertiary amine forming a urethane linkage.

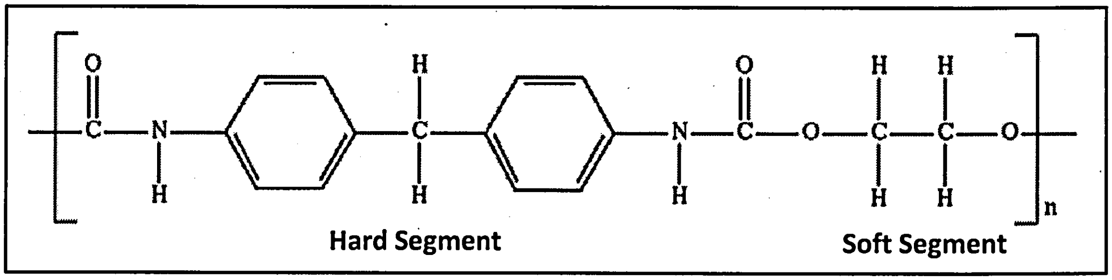

Figure 5.2: Standard PU repeat unit with an aromatic diisocyanate HS with a polyether SS.

The SS, which are quite mobile and are normally present in a coiled formation, alternate with stiff oligo-urethane HS and due to thermodynamic incompatibility of the HS and SS the polymer system forms a two-phase morphology in which hydrogen-bonded, glassy or semicrystalline hard micro-domains of HS aggregate amid the rubbery soft domains. Finnigan et al., (2004) and Yeh et al., (2003) found that depending on the ratio and interaction between the SS and HS, the hard microdomains can form either fibrillar, globular or lamellar structures in the SS matrix and even form an interconnected HS hard-domain network when the HS ratio is high, figure 5.3. Kim et al., (1996) and Lin and Chen (1998) found that as the PU HS have a high T_m and the SS have a low T_g the hard and soft domains are in a crystalline and rubbery state, respectively, at room temperature. Therefore by varying the amounts of HS and SS, the stiffness, or modulus, E, and strength, tensile stress at break, σ_{max}, of the PU increases with HS content. The extensibility, strain at failure, ε_{max}, increases with SS content. Varying the HS and SS content also allows the thermal transition temperatures and thermomechanical properties to be tailored, although it is difficult synthetically to increase the PU elastic modulus without reducing its high extensibility and vice-versa (Liff et al., 2007).

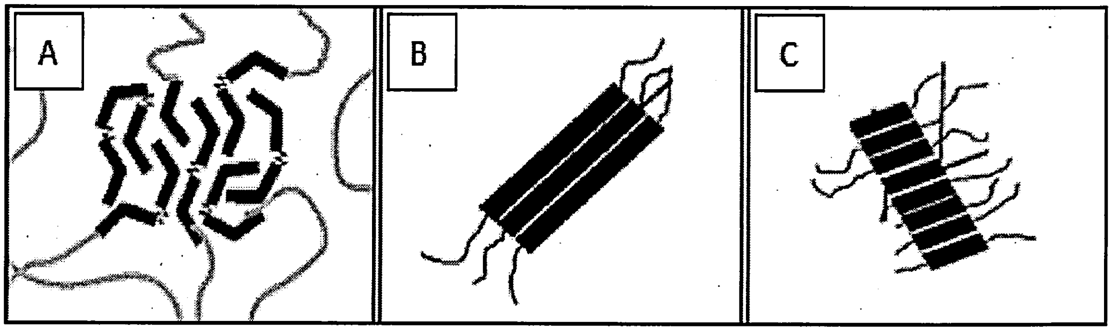

Figure 5.3: Two-phase morphology of PU, displaying possible semi-crystalline HS micro-domains dispersed in the SS, A) Globular, B) Fibrillar and C) Lamellar HS microdomain structures. (Finnigan et al., 2004, Yeh et al., 2003)

Generally PU polymers have high abrasion resistance, a higher tensile modulus compared to rubber, and resistance to oil, grease and many other solvents (Ha et al., 1998). However there are differences between the polyester and polyether based PU leading to different purposes depending on the composition, table 5.1. PU is used in a variety of fields including medical, construction, packaging, and electronics (PURRC, 2005). Some notable products are pace makers, lumbar spinal discs (Ward, 2008), insulation and packaging foams, simulated woods, and synthetic fibres (Hu, 2007).

Property	Polyester-based PU	Polyether-based PU
Abrasion resistance	very good	acceptable
Mechanical properties	very good	good
Low temperature flexibility	acceptable	very good
Heat ageing	good	poor
Resistance to hydrolysis	very poor	very good
Chemical resistance	very good	poor
Microbial resistance	very poor	good
Adhesion strength	good	poor
Injectability	very good	acceptable

Table 5.1: Major differences between polyester and polyether based PU.

As PU shows a two-phase morphology it can potentially be classified as a smart material, specifically a SMP. The SS rich phase potentially can act as a thermally reversible phase while the HS rich phase serves as the permanent phase (Hu et al., 2005). Lee et al., (2001) have reported that the HS to SS ratio plays a significant role in determining whether a PU will show a shape memory effect, SME. It was determined that in order for PU to show shape memory properties the HS content needed to be between 30 to 45 wt%, with higher or lower amounts causing a loss of SME.

Typically shape memory PUs are thermally-responsive, the SS acting as a thermally reversible phase maintaining the transient shape where the HS memorizes the original shape. The thermally reversible phase, SS, is designed to have a large drop in elastic modulus on heating above the transition temperature, T_{trans}.

Typical PU, not chemically cross-linked, can fit into two different classes of SMP, class III, physically cross-linked amorphous thermoplastics and class IV, physically cross-linked semicrystalline block copolymers, depending on their composition and structure. Class III PU have a T_{trans} caused by the SS T_g, while the permanent shape is retained by physical cross-linking of the HS through molecular interactions such as van der Waals, dipole-dipole interactions or hydrogen bonding. The Class IV PUs have a T_{trans} caused by the SS T_m, while their permanent shape is retained by physical cross-linking between HS through molecular interactions in the crystalline regions (Rousseau, 2008).

Therefore the T_g or T_m of the PU SS can be used as T_{trans}. Consequently when the SMP is deformed at the rubbery plateau just above the T_{trans}, and subsequently cooled below T_{trans} under constant strain, the deformed shape is fixed due to the micro-Brownian movement being frozen. Then as the PU SMP is reheated above T_g/T_m SS, the original shape is recovered by the elastic force generated and stored in the SS during the deformation (Jeong et al., 2001).

SMP, including SMP PU, when compared to other shape memory materials e.g. SMA, section 1.3 table 1.4, have some challenges to overcome including low mechanical strength, low shape recovery stress and onset of hysteresis after repeated deformation-recovery cycles (Rousseau, 2008). In order to overcome these disadvantages research groups such as those of McKinley et al., (Liff et al., 2007) Pan et al., (2008) Gunes et al., (2008) and recently He et al., (2011) have reinforced SMP via the incorporation of organic and inorganic fillers. McKinley et al., although not specifically targeting SME, found that the addition of a synthetic hectorite, Laponite RD©, into a polyether PU reinforces the HS, stiffening and toughening it, leading to significant thermomechanical enhancement. This result suggested that an improvement to shape memory performance may occur, due to enhanced rubbery modulus and thus enhanced restoring force, all without changing the glass-transition temperature (Liff et al., 2007). Pan et al., investigated the influence of heat-treated attapulgite on the T_g of the PU SMP, MM3520. In addition to confirming the strong influence of moisture, it was revealed that non-treated attapulgite, ca. 30 wt%, significantly reduces T_g of the composite, from 41 °C to 9 °C, while the influence of treated attapulgite on T_g was limited. It was concluded that the mechanical properties of the SMP composites containing heat-treated attapulgite were enhanced whereas in comparison SMP composites with non-treated attapulgite showed a decrease in both T_g and strength (Pan et al., 2008). Gunes et al., incorporated C30B, carbon nano-fibres, CNF, CB and SiC, into a SMP polyester PU at levels up to 5 wt%. It was found that CNF and SiC significantly reduced SS crystallinity, almost eliminating it at 5 wt% whilst CB and C30B only altered it slightly. As filler content increased it was seen that the tensile modulus increased with addition of C30B and CB whilst it dropped after 1 wt% of CNF and 3 wt% of SiC. Due to the CNF and SiC reducing SS crystallinity the composites experienced considerable reductions in shape memory recovery and fixed strain compared to the CB and C30B composites. It was also noted that the composite containing 5 wt% CB showed no shape memory ability (Gunes et al., 2008). He et al., utilising carbon nanotubes, CNTs, and Fe_3O_4 created a multicomposite SMP featuring remote and selective triggering of the recovery of multiple temporary shapes. The principle of the SMP composite system is based on the incorporation of Fe_3O_4 nanoparticles and CNTs that can selectively induce heat at two different radiofrequency ranges (296 kHz and 13.56 MHz frequency) thus when the two nanofillers were embedded into different regions of a PU SMP, it enabled independent heating (thus recovery) of each region when exposed to the two radiofrequency fields. It was found that Fe_3O_4 nanoparticles aggregated to form multi-particulate clusters, whereas CNT was homogeneously dispersed, this did not compromise the SME but did cause a reduction in the T_g, particularly in the case of Fe_3O_4 (He et al., 2011).

As the research carried out by previous groups indicate, the most suitable kind of filler to improve a pristine SMP PU would be clay (Gunes et al., 2008). Clays have previously proved to improve stiffness and toughness, as well as thermomechanical properties suggesting that it may also enhance shape memory properties (Liff et al., 2007). The objective of this work is to create a mechanically and thermally stable SMP packaging material. In order to achieve this aim, expanding on the research carried out by McKinley et al. is a good starting point. Laponite RD, figure 5.4, will be incorporated into an existing commercially available SMP system, Elasthane 80A©, a class III SMP, figure 5.5, in order to form SMP nanocomposites. The effects of varying Laponite wt% on Elasthane will be assessed, especially regarding the effects on the SME.

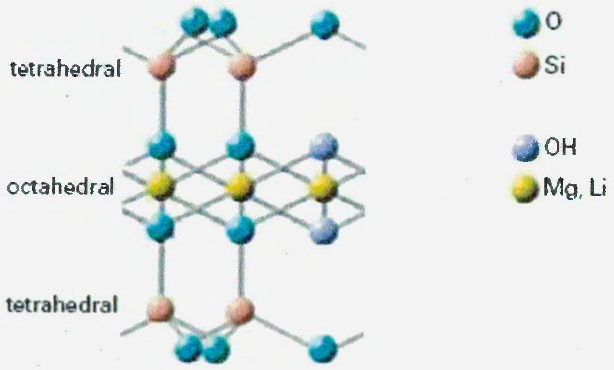

Figure 5.4: Structure of Laponite, a trioctahedral smectite, a synthetic layered silicate containing 59.5% SiO_2, 27.5% MgO, 2.8% Na_2O, and 0.8% Li_2O with an empirical formula $Na_{0.7}(Si_8Mg_{5.5}Li_{0.3})O_{20}(OH)_4 \cdot H_2O$. Each silicate is crystalline and comprised of

30,000-40,000 unit cells that create discotic platelets which are ca. 25 nm in diameter and 0.92 nm in thickness (Rockwood Specialties Inc., 2009).

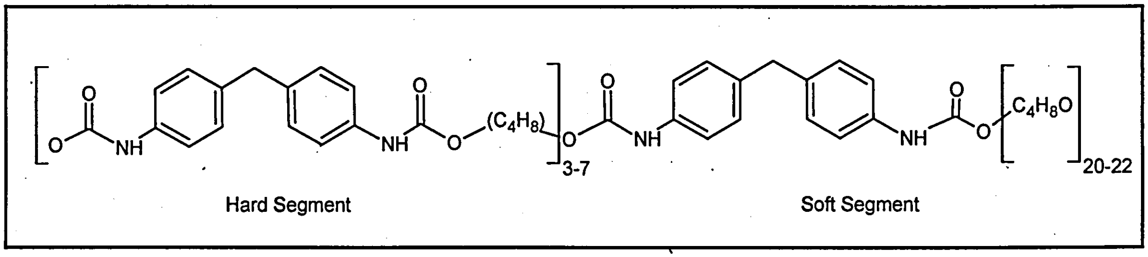
O
NH
NH
O
(C_4H_8)
3-7
O
NH
NH
O
C_4H_8O
20-22
Hard Segment
Soft Segment

Figure 5.5: Elasthane repeat unit with a HS of 4,4`-methylene bisphenyl diisocyanate, MDI, extended with 1,4-butanediol, BDO, linked with a polyether SS, polytetramethylene oxide, PTMO (Liff et al., 2007).

5.1. Experimental

5.1.1. Materials

The PU, Elasthane 80A©, composed of MDI, with a chain extender of BDO and a SS of PTMO (ca. 1,000 g mol^{-1}), was used as received from Polymer Technology Group (Berkeley, California). Elasthane hard-to-soft segment ratio is 40:60 wt%, molar mass 290,000 g mol^{-1}, and density 1.12 g cm^{-3} (Liff et al., 2007). Laponite RD©, a synthetic hectorite clay with a density of 2.65 g cm^{-3} was obtained from Rockwood Specialties Inc. (2009). N,N-dimethylacetamide, DMAc, (boiling point 165 °C) was used as received from Sigma-Aldrich.

5.1.2. Sample Preparation

In order to effectively and uniformly disperse Laponite in Elasthane a novel solvent-exchange method was used (Liff et al., 2007).

5.1.2.1. Clay Delamination Procedure

The Laponite was dispersed into the Elasthane via a delamination procedure, developed by McKinley et al., to fully disperse Laponite layers within an organic solvent, figure 5.6. (Liff et al., 2007).

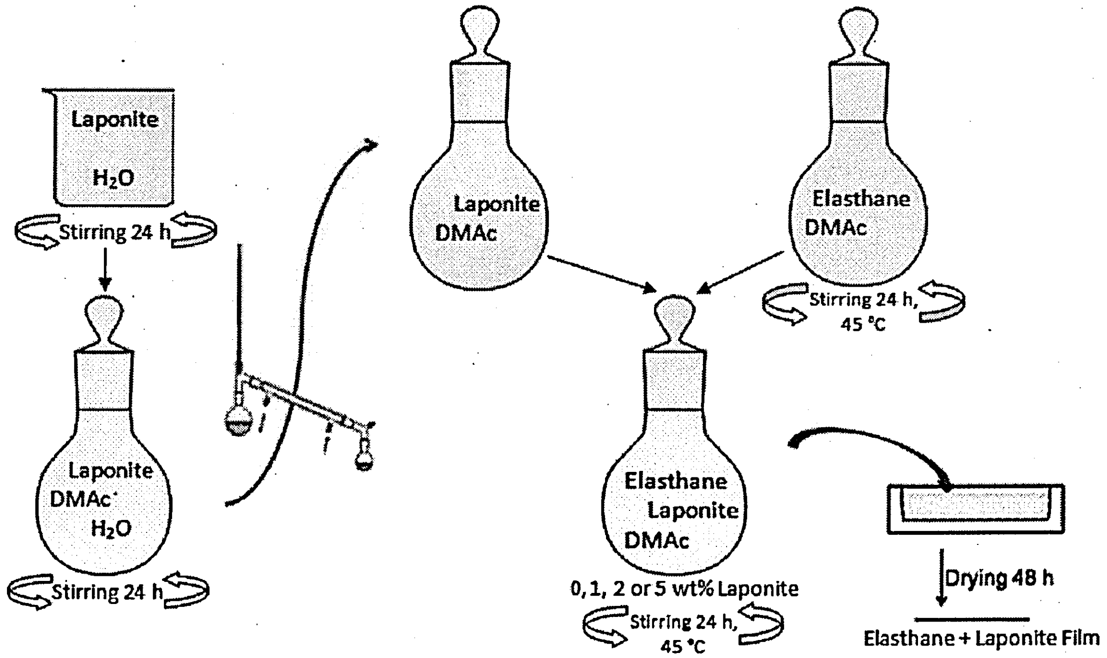
Laponite
H₂O
Stirring 24 h
Laponite
DMAc
H₂O
Stirring 24 h
Laponite
DMAc
Elasthane
DMAc
Stirring 24 h, 45 °C
Elasthane
Laponite
DMAc
0, 1, 2 or 5 wt% Laponite
Stirring 24 h, 45 °C
Drying 48 h
Elasthane + Laponite Film

Figure 5.6: The delamination of Laponite and its subsequent dispersal into the Elasthane host to produce Elasthane composites containing 1 to 5 wt% Laponite.

When using Elasthane and Laponite, it had been previously found by McKinley et al., that the optimal solvent pair was deionised water and DMAc. 1 g of Laponite was mixed with 100 g of deionised water. The solution was stirred using a PTFE-coated, magnetic, spin-bar on a hot plate stirrer with a moderate stir speed (lv 6) for 24 hours. 200 g DMAc was added to the solution and stirred at the same speed for 48 hours. The liquid-vapour phase equilibrium of the binary solvent system was utilized in order to evaporate off all the water from the solution. Water evaporates at 100 °C while DMAc evaporates at 165 °C, a distillation setup was used to remove the water. The flask containing the Laponite-H_2O-DMAc solution with the spin-bar (acting as a nucleation point) was attached to the distillation equipment and lowered into a pre-heated oil bath. The temperature was increased from 60 °C to 140 °C over a three hour period. The evaporation was not considered complete until the mass removed from the flask through evaporation was slightly greater than or equal to the mass of water added initially.

5.1.2.2. Solution Casting

Elasthane/Laponite composite films were prepared by a solution casting process. Elasthane was dissolved, for 24 hours, in DMAc. The Elasthane/DMAc solution was infused with pre-weighed amounts of Laponite dispersed in DMAc. The Elasthane-Laponite-DMAc polymer solutions, table 5.3, were cast in a pre-heated PTFE mould, 40 x 60 x 18 mm, and the solvent was removed by controlled evaporation in an oven for 48 hours at 70 °C. After this controlled evaporation the PULap composite film, 0.55±0.05 mm thick, which had formed was removed. The PULap composites were analysed using XRD, ATR-FTIR, TGA, DSC, DMA and SME testing.

Sample Description	Short Description	Elasthane, g	Laponite/DMAc suspension, g	DMAc, g
Elasthane 0 wt% Laponite	PULap 0	3.00	0.00	30.00
Elasthane 1 wt% Laponite	PULap 1	2.97	5.27	24.73
Elasthane 2 wt% Laponite	PULap 2	2.94	10.54	19.45
Elasthane 5 wt% Laponite	PULap 5	2.85	26.36	3.64

Table 5.3: PULap 0 to 5 composite formulations for solution casting to create thin films.

5.1.3. Characterisation Methods

All characterisation methods were carried out in MERI at Sheffield Hallam University.

5.1.3.1. X-Ray Diffraction

XRD was performed to determine the extent of the Laponite dispersal within the PULap 1 to 5 composites.

A Philips X'Pert XRD, Cu x-ray source (λ = 1.542 Å), with a Philips Miniprop detector was used. Sample material was cast onto a glass slide, sample measured ca. 20 x 40 x 0.1 ± 0.05 mm^3. The sample was mounted onto the sample stage using a clamp, the standard masks for the x-ray beam, ¼ Inch divergence slit and ½ inch anti-scatter slit along with a 10 cm fixed mask, were set into place. The positions of the source and detector were reset to their starting positions. The trace was collected from 5 to 90 ° 2θ, lasting 40 minutes with approximately 10,000 counts in total. The diffraction trace of the sample was recorded and analysed.

5.1.3.2. ATR-FTIR Spectroscopy

ATR-FTIR was carried out to observe the degree of dispersal of Laponite within the Elasthane host. ATR-FTIR was also used to observe the presence and location of bonding interactions between Elasthane and Laponite.

ATR-FTIR was performed on a Nicolet, Nexus FT-IR model at room temperature, ca. 22 °C. ATR-FTIR was carried out on each sample, nine spectra were collected from the top surface and nine spectra were collected from the bottom surface, from top left to bottom right on each side of each sample. There were no significant differences between the spectra taken for each sample so they were combined to obtain an average spectrum for each sample which was recorded and analysed.

5.1.3.3. Thermogravimetric Analysis

TGA was performed to verify that the PULap 0 to 5 samples contained the specified Laponite loading and to elucidate the effect of Laponite concentration on the thermal degradation of the samples.

TGA was carried out on a Mettler TG50, with a 15-25 ml min^{-1} N_2 purge. Alumina crucibles were filled with 15 ± 0.5 mg of PULap 0 to 5 samples, cut into small pieces measuring ca. 1 x 1 x 0.55 ± 0.05 mm^3. A 15 minute isothermal hold at 35 °C was utilised before the 20 °C min^{-1} ramp to 800 °C was started. The mass loss profile of the sample during heating was recorded and analysed.

5.1.3.4. Differential Scanning Calorimetry

DSC was performed to determine the effect of Laponite content on the glass, melting, and crystallisation transitions of the Elasthane.

DSC was performed on a Mettler DSC25 with a 65-75 ml min^{-1} N_2 purge. Aluminium pans were filled with 10 ± 0.5 mg of PULap 0 to 5 samples were cut into small pieces measuring approximately 1 x 1 x 0.55 ± 0.05 mm^3. The pan was left on the scales until no signs of weight fluctuation were observed (due to the pan swinging or air flow). The pan was removed from the scales and a lid was crimped on top. The sealed pan was placed in the DSC sample holder and the test was carried out. The test included a 15 minute isothermal hold at 35 °C and then from 55°C a 10°C min^{-1} ramp was used to achieve a maximum temperature of 255°C, the sample was then cooled at 10°C min^{-1} back to 55°C and the cycle was started a second time. The differential power profile of the sample during heating and cooling was recorded and analysed.

5.1.3.5. Dynamic Mechanical Analysis

DMA was carried out to investigate the effect of Laponite content on the viscoelastic properties of Elasthane.

DMA, was performed on a PerkinElmer DMA8000 model in tension mode, no pre-load was applied, over a temperature range of -50 to 150 °C, at frequencies of 1 and 10 Hz. The PULap 0 to 5 samples, size 25x 5 ± 0.1 x 0.55 ± 0.05 mm, were equilibrated at -100 °C for 3 minutes then raised to 150 °C at a 3 °C min^{-1} ramp rate. The T_g was defined as the peak of the tan δ curve. The rubbery modulus was determined from the storage modulus, when it had reached a steady state above the T_g as indicated by the unchanging tan δ curve. The storage modulus, loss modulus, and tan δ plots were recorded and analysed.

5.1.3.6. Unconstrained Shape Memory Effect Evaluation

Unconstrained SME evaluation was performed to investigate PULap 0 to 5 samples shape memory ability in the absence of strain, to elucidate the effects of Laponite content on the SME of Elasthane. SME was performed on a customised platform utilising a hotplate, a glass enclosure and a temperature probe, section 2.1.6, figure 2.15. The hotplate was pre-heated to a maximum temperature, 90±2 °C (T_{high}), the PULap composites, 40 x 20 x 0.55±0.5 mm, were placed inside the enclosure for 10 minutes to equilibrate at temperature. The sample was deformed using an external force, 250 g steel weight, section 2.1.6, figure 2.15 A, and the heated glass enclosure was maintained at T_{high} for an additional 10 minutes while the samples was under strain. The sample was, while still under strain, cooled to 0 to 5 °C (T_{low}). At T_{low} the external force was removed, the sample was allowed to warm to room temperature (22±2 °C) and the fixed deformability, θ_{Fixed} °, was recorded. The sample was placed inside the T_{high} heated glass enclosure and the SME recovery angle was recorded every 30 seconds. Once the sample had finished its SME, or recovered its original shape, θ_{Final} °, was recorded. The sample was removed from the enclosure and stored. The SME of the PULap 0 to 5 samples were recorded and analysed.

5.2. Results and Discussion

5.2.1. Homogeneity

5.2.1.1. X-Ray Diffraction

The XRD traces in the region 2 to 45 °2θ for Laponite powder and PULap 0 to 5 samples, were collected to assess the state of dispersion of Laponite in the Elasthane host polymer matrix, figure 5.7.

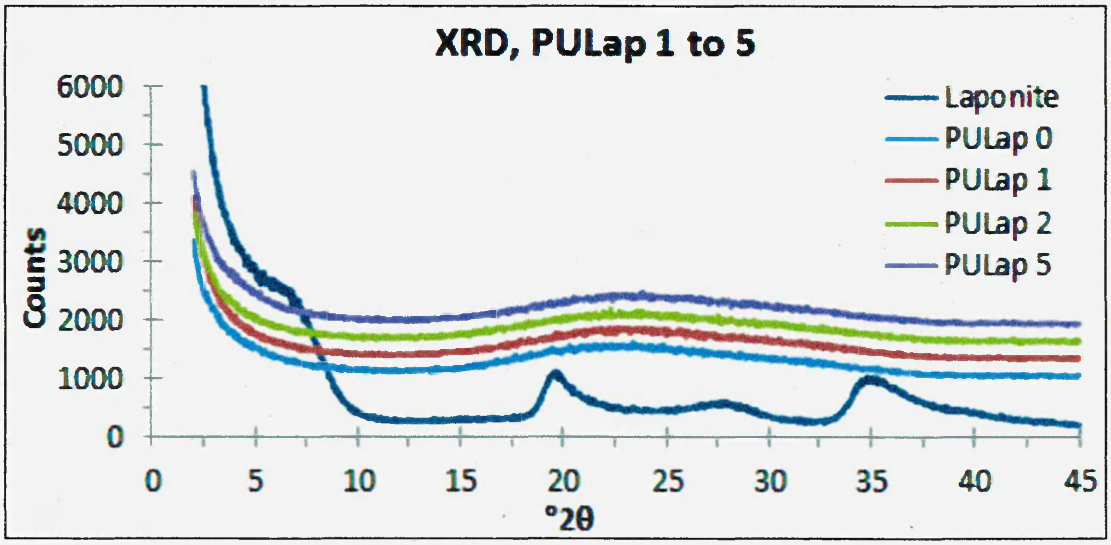

Figure 5.7: XRD trace of Laponite powder and PULap 0 to 5 samples.

The XRD trace of Laponite powder displayed peaks near, 6 °2θ (14.7 Å), 19 °2θ (4.7 Å), 27 °2θ (3.3 Å) and at 35 °2θ (2.6 Å). These peaks correspond to the d001, 110, 101, and 130 reflections, respectively. This is what would be expected from an unorientated Laponite (Mishra et al., 2008, Vicente, 2010). The XRD trace showed the PULap 0 sample had a broad peak, observed from 15 (5.9 Å) to 37 °2θ (2.4 Å) with no other observable peaks. This broad peak is indicative of the amorphous or quasi crystalline nature of PU. XRD traces for the PULap 1 to 5 samples exhibit practically XRD-silent traces. As Laponite's size is small, ca. 25 nm, and low quantities were used it has weak reflections due to imperfect platelet registration causing the 110, 101 and 130 peaks to be hidden in the broad diffraction halo of the PU. The XRD analysis showed only a slight d001 shoulder at 3 °2θ (29.4 Å) on the PULap 5 sample, corresponding to similar work carried out by Mishra et al., (2008) where a minor d001 peak, 5.3 °2θ (16.7 Å), occurred in a polyether based PU loaded with 5 wt% amine modified Laponite. The d001 shoulder in the PULap 5 sample is most likely caused by its higher Laponite content increasing the particle-particle interactions possibly causing the clay platelets to start re-aggregating. The aggregation of the Laponite may form an intercalated state of dispersal in the matrix rather than an exfoliated state, thus producing a weak d001 peak. Overall, with the exception of the small shoulder in the PULap 5 sample, the XRD traces suggest that the Laponite is extremely well dispersed within the Elasthane matrix.

5.2.1.2. ATR-FTIR Spectroscopy

Although XRD has suggested that the Laponite in the PULap 0 to 5 samples is well dispersed, the XRD can occasionally fail to detect agglomerated clay particles, giving the impression that full delamination/exfoliation has occurred when in fact it has not. This is due to the inability of XRD to distinguish between large and small clay tactoids as the signal strength is very dependent on the factors such as clay loading, number of layers in a stack and layer orientation.

Typically XRD results are confirmed via transmission electron microscopy, TEM. However this method is very time-consuming and requires special sample preparation. Therefore in order to support the XRD results ATR-FTIR was used. Here the mid-range wavelength region, 500 to 3500 cm^{-1}, was utilised, figure 5.8.

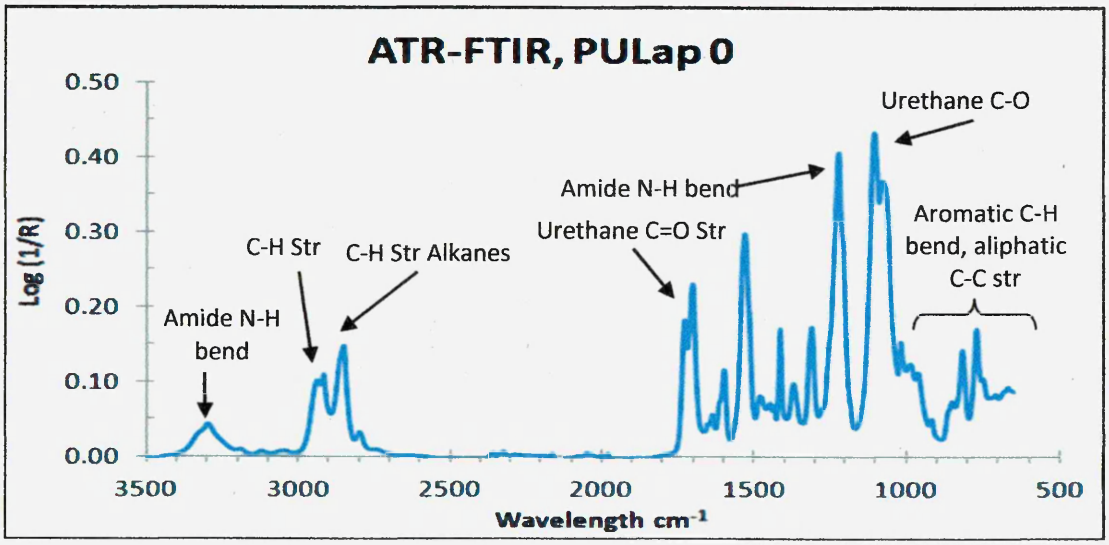

Figure 5.8: ATR-FTIR spectrum of the PULap 0 sample, wavelength 500 to 3500 cm^{-1}, displaying the key vibrational modes.

In the high frequency region, ca. 3400 to 2700 cm^{-1}, vibrations were observed that arise from amide N-H bending modes and the stretching of aliphatic and aromatic CH bonds. As the frequency becomes lower, ca. 1800 to 1000 cm^{-1}, the urethane C=O and C-O stretches were observed. Finally at the lower frequencies, 900 to 600 cm^{-1}, IR bands due to aromatic C-H bend and minor aliphatic C-C vibrations are observed. To confirm the presence and dispersal of Laponite the PULap 0 to 5 samples were analysed, figure 5.9.

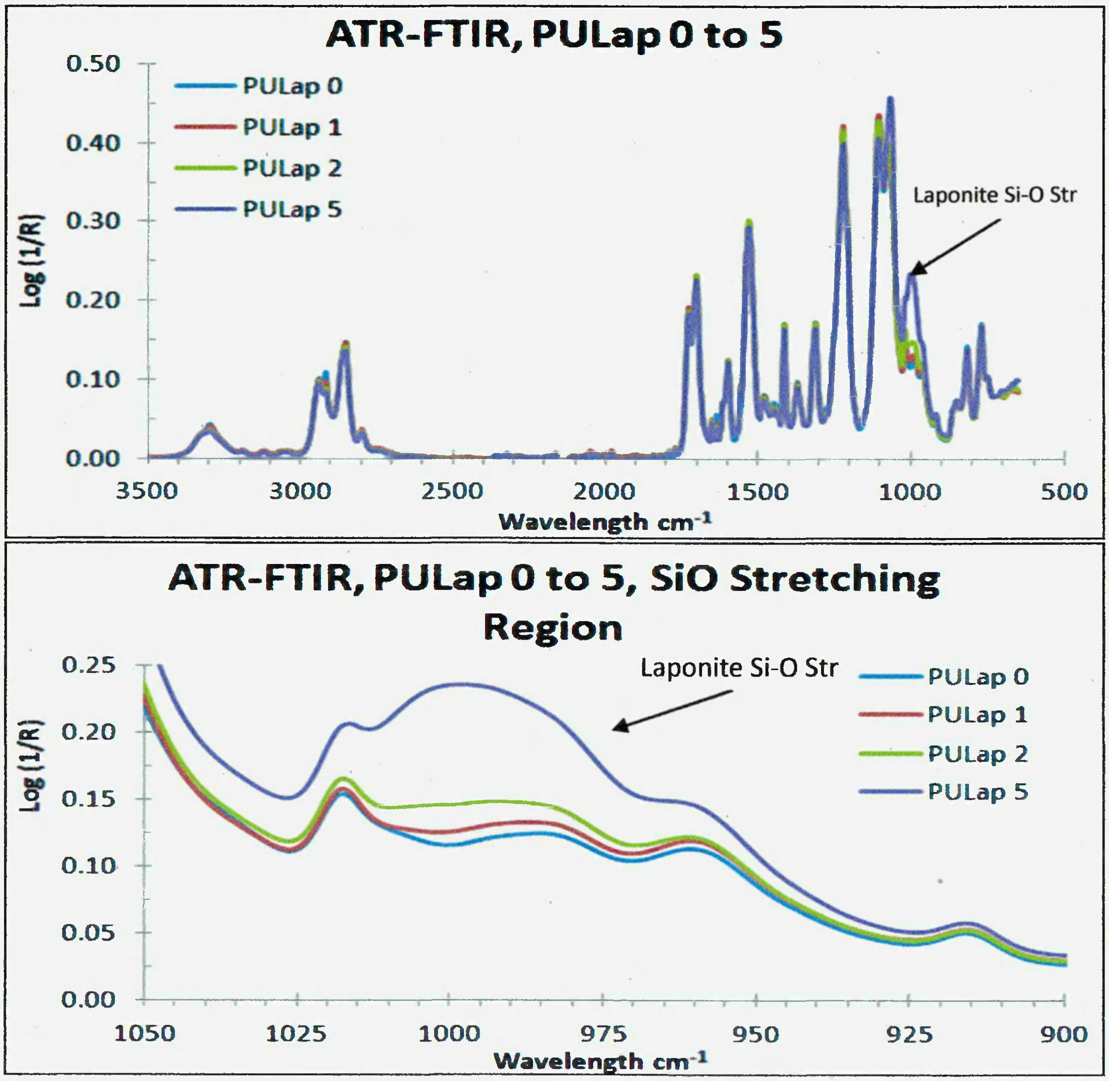

Figure 5.10: ATR-FTIR spectra for the PULap 0 to 5 samples, 900 to 1050 cm^{-1}.

The presence of Laponite in the PULap 1 to 5 samples, was confirmed via the observation of the Si-O stretching band at ca. 1000 cm^{-1}, this becomes more intense as the Laponite content increases from 0 to 5 wt%, figure 5.10.

In the region 3500 to 3000cm^{-1} the major NH absorption peaks from the Elasthane HS are observed. Two peaks are observed, both related to NH stretch vibrations, a major peak at 3310 cm^{-1}, related to the hydrogen-bonded NH, with a small shoulder on the higher wavelength site, at 3330 cm^{-1}, related to the free NH, figure 5.11 A. These results show that although the hydrogen-bonded NH decreases with increasing Laponite content, the majority of the NH groups are still hydrogen-bonded, while the amount of free NH remains constant with increasing Laponite content. In the 1780 to 1640 cm^{-1}, the carbonyl stretch region, there are two well separated peaks of similar intensity observed at ca. 1730 and 1700 cm^{-1} both from the Elasthane HS, figure 5.11 B. These peaks can be attributed to the free and hydrogen bonded carbonyl groups, respectively. In Elasthane the peak for the bonded carbonyls, 1700 cm^{-1}, is of greater intensity than that for the free carbonyls, 1730 cm^{-1}, however as the Laponite content increases no significant changes in intensity occur.

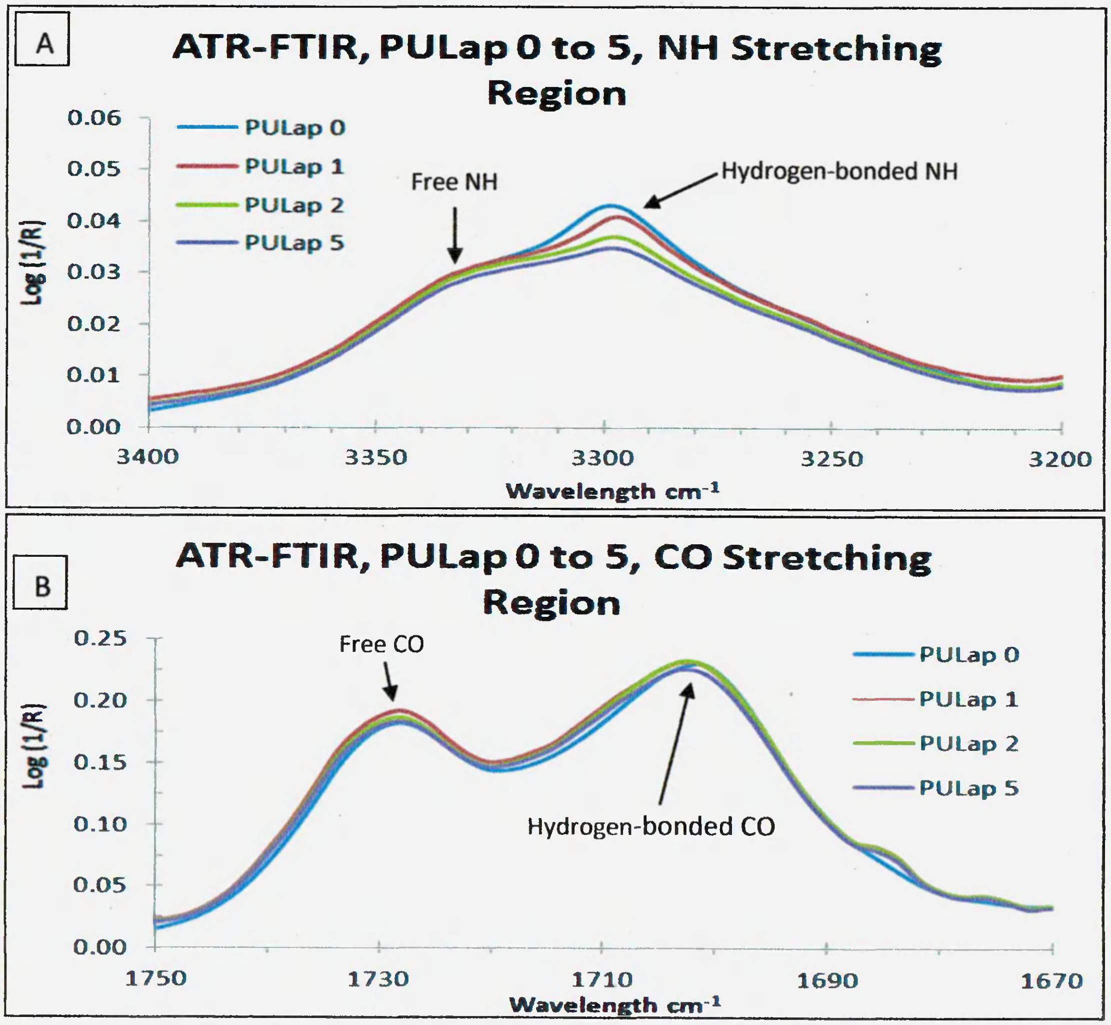

Figure 5.11: ATR-FTIR spectra of the PULap 0 to 5 samples vibrations of the A) NH bend, 3200 to 3400 cm^{-1} and B) CO stretch, 1670 to 1750 cm^{-1}.

These spectral changes are most likely caused by Elasthane-Laponite interactions altering the ability of the HS to form hydrogen bonds within the Elasthane matrix, as well as the presence of randomly orientated clay platelets. These results demonstrate that as the Laponite content increases there is a decrease of hydrogen bonded NH caused by reduced hydrogen bonding within the semi-crystalline HS region, causing a reduction in HS crystallinity. These results correspond to studies carried out by Tien and Wei (2001) and Pattanayak and Jana (2005), who used modified Na^+ MMT, and Na^+ Cloisite and C30B, respectively, to form nanocomposites in similar PU systems, both observed that clay platelets hindered the HS ability to form hydrogen bonds.

In order to verify the delamination of the Laponite in the PULap 1 to 5 samples, an ATR-FTIR technique developed by Ijdo et al., (2006) was adopted. The technique utilises infrared absorption to assess the degree of clay dispersion. Normally when hectorite clay i.e. Laponite, is dispersed in water and the layered stacks delaminate, two absorption bands are resolved for the Si-O bonds, assigned to the in-plane and out-of-plane bands, ca. 1000 cm^{-1} and ca. 1080 cm^{-1}, respectively, in the clay structure. As reported by Ijdo et al., stacking or agglomeration of clay layers causes broadening of the Si-O vibrations forming an overlap of the in-plane and out-of-plane Si-O bands, generating a single broad peak at ca. 1000 cm^{-1}. As shown in figure 5.8 and 5.9, only a single Laponite Si-O peak, ca. 1000 cm^{-1} is observed; this is due to masking by the Elasthane matrix. In order to reveal the state of Laponite delamination, a subtraction of the PULap 0 sample spectrum from the PULap 1 to 5 sample spectra was necessary, figure 5.12.

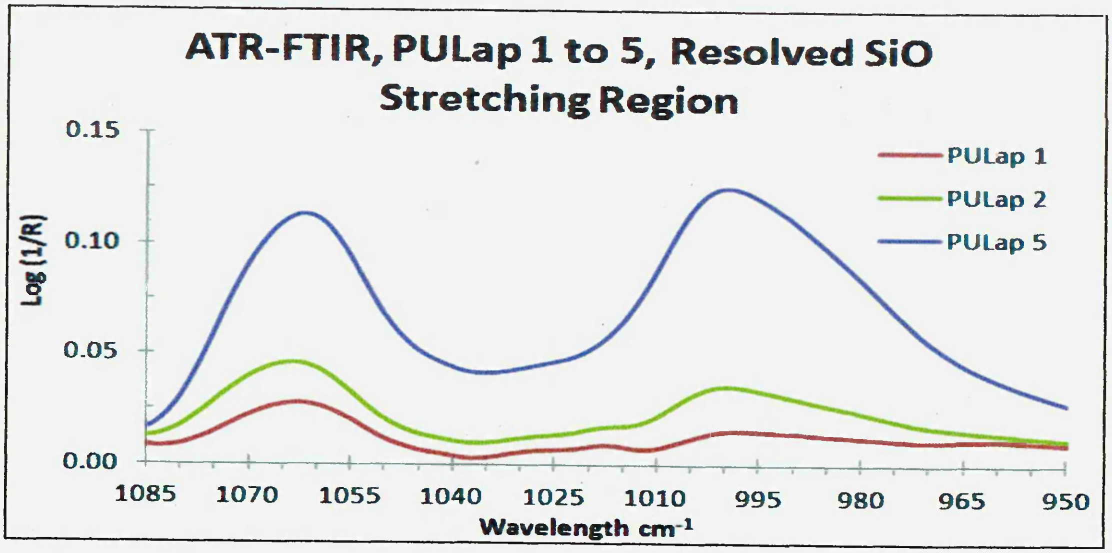

Figure 5.12: PULap 0 sample spectrum was subtracted from the PULap 1 to 5 sample spectra revealing the Laponite Si-O in-plane, 1000 cm^{-1} and out-of-plane 1080 cm^{-1} stretch peaks.

The subtracted spectra, figure 5.12, revealed two individual Si-O stretching peaks, in-plane and out-of-plane, ca. 1000 cm^{-1} and ca. 1063 cm^{-1} respectively, rather than a single broad peak. Ijdo et al., observed that for hectorite clay layers to be fully delaminated the distance at the full width at half maximum, FWHM, for the in-plane Si-O peak should be ca. 28 to 29 cm^{-1} (Ijdo et al., 2006). The FWHM for PULap 1 to 5 was 28.5, 31.0 and 36.0 cm^{-1}, respectively, which corresponds to ca. 95, 65, and 37 % clay delamination. These results indicate that as Laponite content increases the delamination decreases, however Ijdo et al., also reports the IR technique is more sensitive at low levels of delamination. These results suggest that the PULap 1 sample is a fully exfoliated nanocomposite, the PULap 2 sample is a partially exfoliated nanocomposite and that the PULap 5 sample is an intercalated composite (Ijdo et al., 2006). These results correlate well with the XRD results.

5.2.2. Thermoanalytical Results

5.2.2.1. Thermogravimetric Analysis

To study the effects of thermal degradation on Laponite and PULap 0 to 5 samples TGA was carried out, figure 5.13 and figure 5.14.

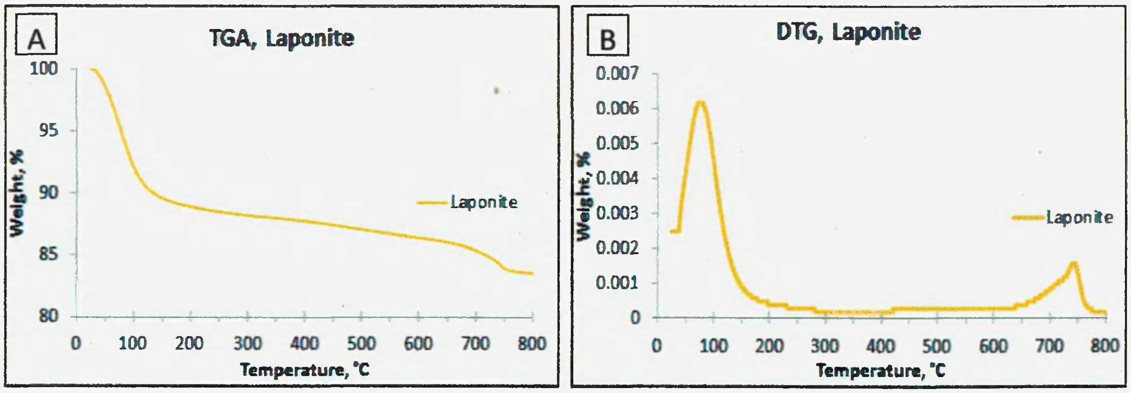

Figure 5.13: Laponite powder, 35 to 800 °C, A) TGA trace and B) DTG trace.

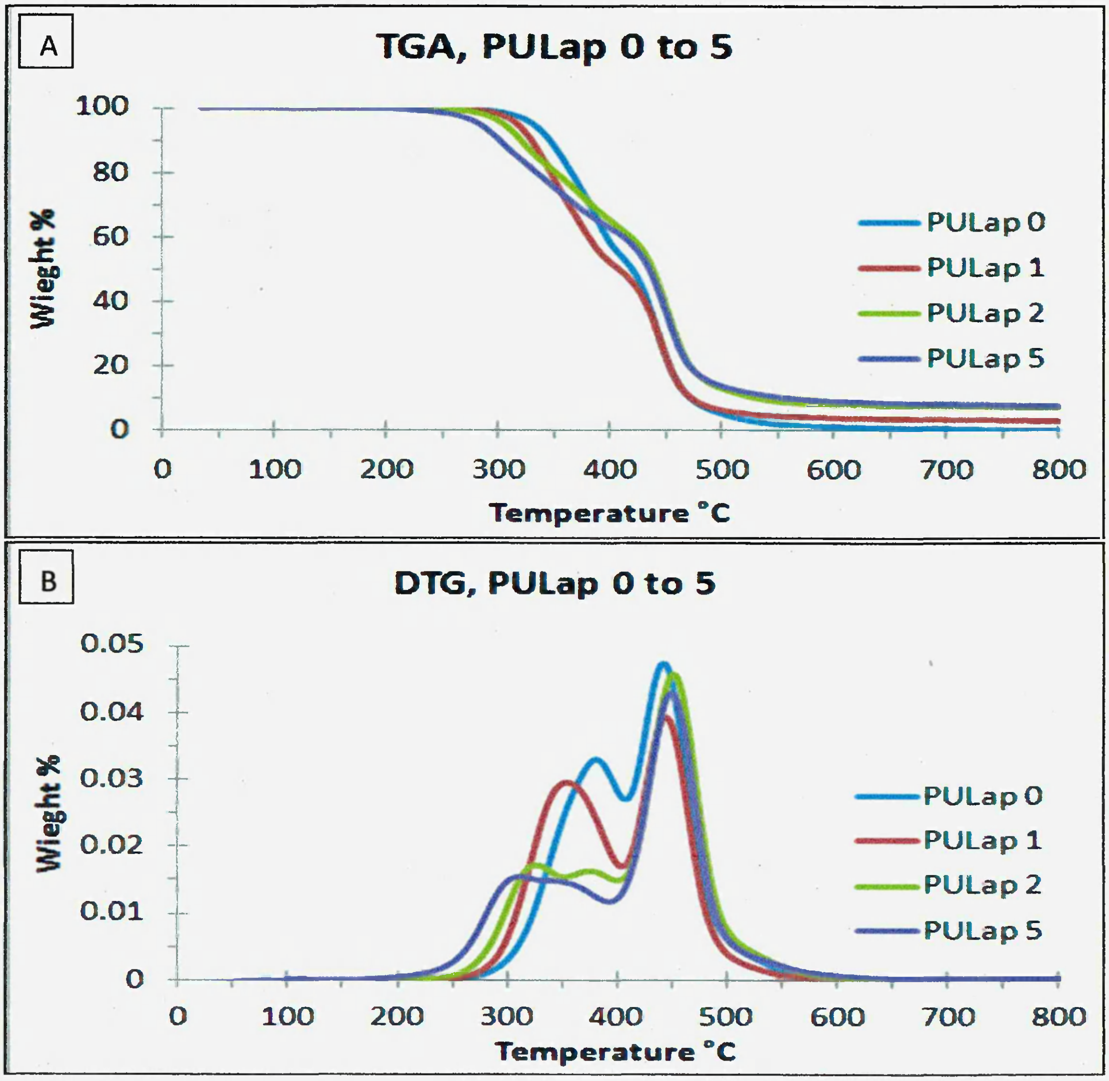

Figure 5.14: PULap 0 to 5 samples, 35 to 800 °C, A) TGA and B) DTG traces.

The Laponite DTG shows two peaks, figure 5.13 B, the first at ca. 77 °C, $T_{max(1)}$, relating to the evolution of water from within the Laponite and the second at ca. 742 °C, $T_{max(3)}$, that is associated with dehydroxylation of Laponite (Liff et al., 2007).

The PULap 0 sample, figure 5.14 A, exhibits two distinct decomposition stages, a steep weight loss, maximising at ca. 381 °C, $T_{max(1)}$, and a second degradation at ca. 444 °C, $T_{max(3)}$. Above 600 °C the polymer is fully degraded with only minor char residue remaining. The first degradation stage arises from the initial degradation of the Elasthane HS while the second degradation stage is caused by the complete decomposition of the SS (Ferguson and Petrovic, 1976, Shieh et al., 1999).

The PULap 1 to 5 samples show the same two distinct decomposition stages as the PULap 0 sample but as the Laponite content increases to 2 and 5 wt% another thermal event is observed in-between the two Elasthane peaks at 375 and 352 °C, respectively. As the Laponite content increases from 1 to 5 wt%, a decrease in degradation onset temperature, defined as the temperature at which the sample weight decreases by 5 wt%, occurs followed by a shift of $T_{max(1)}$ to lower temperatures, 354, 322 and 312 °C, respectively. The decrease in degradation onset temperature corresponds to a study by Seydibeyoglu et al., (2010), who utilising dispersed unmodified natural hectorite and Laponite, observed that as clay content increased, an earlier onset of PU degradation occurs. As the Laponite content increases to 2 and 5 wt% the $T_{max(2)}$ peak, like the $T_{max(1)}$, also decreases in temperature from 375 to 352 °C. The $T_{max(2)}$ peak possibly corresponds to HS decomposition in the PULap 2 and 5 samples where there is little interaction with clay, this would correspond to the ATR-FTIR results as there is only 60 and 37 % clay delamination, respectively. Therefore it is reasonable to expect that not all the PULap 2 and 5 samples HS domains have as many single clay platelets dispersed within them, so with fewer fully delaminated platelets these HS do not experience the same degree of early onset degradation as others containing many delaminated Laponite clay platelets, therefore leading to another individual thermal event, $T_{max(2)}$. For the PULap 1 sample the $T_{max(3)}$ remains practically the same as the PULap 0 sample, 443 °C, but for the PULap 2 and 5 samples there is a slight increase to 449 and 451 °C, respectively, table 5.4.

Sample Description	$T_{5\%}$, °C	$T_{Max (1)}$, °C	$T_{Max (2)}$, °C	$T_{Max (3)}$, °C
Laponite	78	77	-	742
PULap 0	331	381	-	444
PULap 1	317	354	-	443
PULap 2	305	322	375	449
PULap 5	283	312	352	451

Table 5.4: Laponite and PULap 0 to 5 samples TGA and DTG summary data including the degradation onset temperature, $T_{5\%}$, and the $T_{max\,(1)}$ to $_{(3)}$ values.

The TGA results indicate that the HS degradation temperature, $T_{max(1)}$, is decreasing with increasing Laponite content, this suggests that the intermolecular cohesive bonding of the HS is weakened, causing a reduction in thermal stability. For the PULap 1 sample there is no change in the degradation temperature of the SS, $T_{max(3)}$, but a 27 °C decrease to $T_{max(1)}$, possibly indicating preferential Laponite loading into the HS, whereas for the PULap 2 and 5 samples the decrease of $T_{max(1)}$ and increase of the $T_{max(3)}$ suggests that the Laponite is both interfering with the HS cohesive bonding while also making the SS structure more thermally stable. This is potentially caused by an earlier release of urea and amine groups from the HS, which have been found to have a stabilizing effect on polyether PU during degradation (Ferguson and Petrovic, 1976). A study by Liff et al., (2007), also observed that the intermolecular cohesive bonding of PU HS was weakened and SS degradation temperature increased with introduction of Laponite. However it appears that neither Liff et al., or Seydibeyoglu et al., observed a middle degradation stage in their PU composites as was seen in figure 5.14 B, $T_{max(2)}$. Overall these results correspond with the ATR-FTIR observation that there is a reduction in the amount of hydrogen-bonded NH with increasing Laponite content, thus supporting the interpretation that the Elasthane-Laponite interactions are altering the ability of the HS to form hydrogen bonds within the Elasthane matrix, reducing the HS thermal stability.

5.2.2.2. Differential Scanning Calorimetry

DSC was carried out to investigate the crystallinity of the PULap 0 to 5 samples over the range of 55 to 255 °C. In this temperature range it is not possible to observe the T_g of the SS. Instead the effects of Laponite on the crystallinity, SS T_m, HS T_g and HS T_m

was investigated, figure 5.15. The DSC thermal properties of interest are summarized in table 5.5.

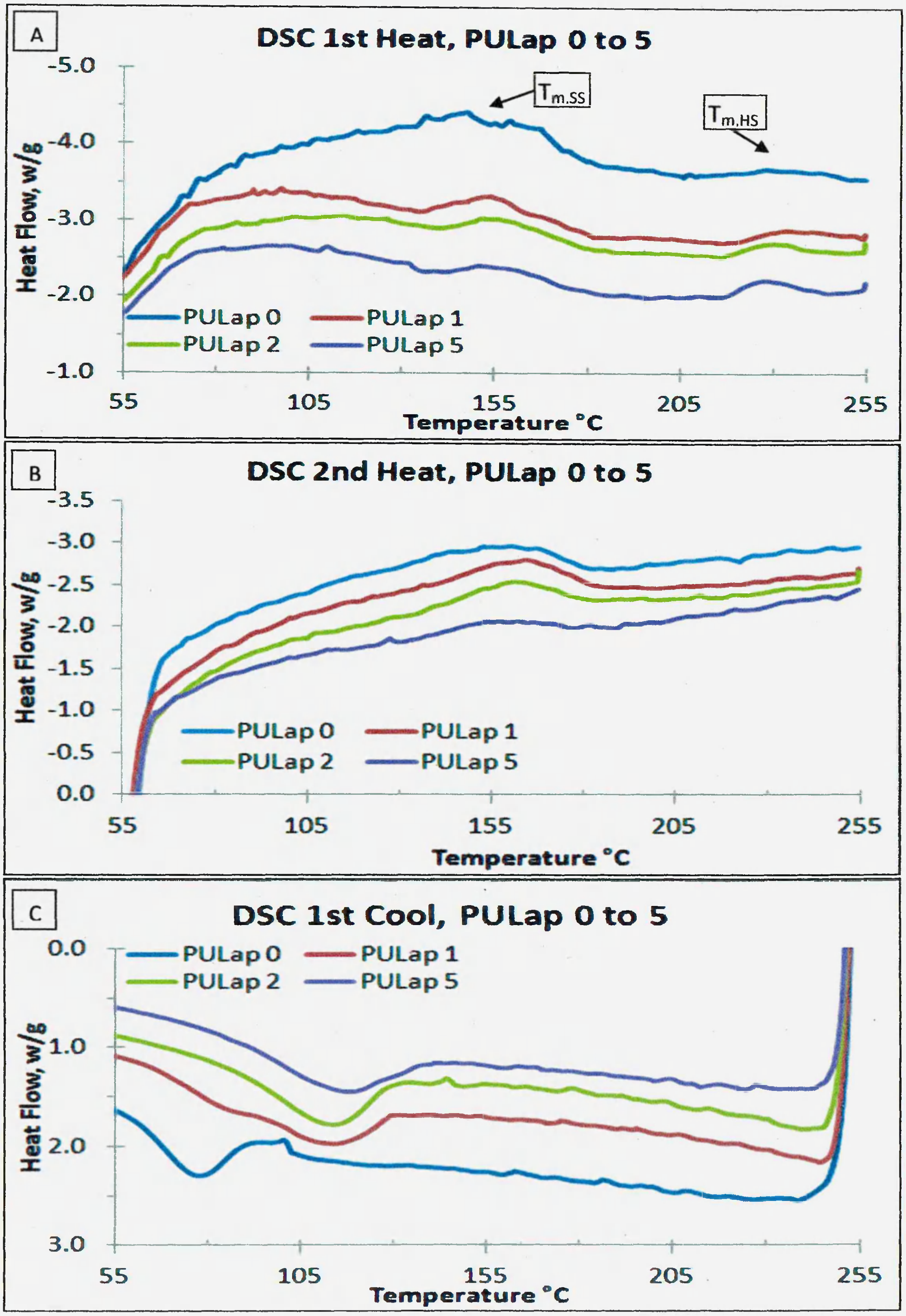

Figure 5.15: DSC A) first and B) second heating and C) first and D) second cooling of the PULap 0 to 5 samples.

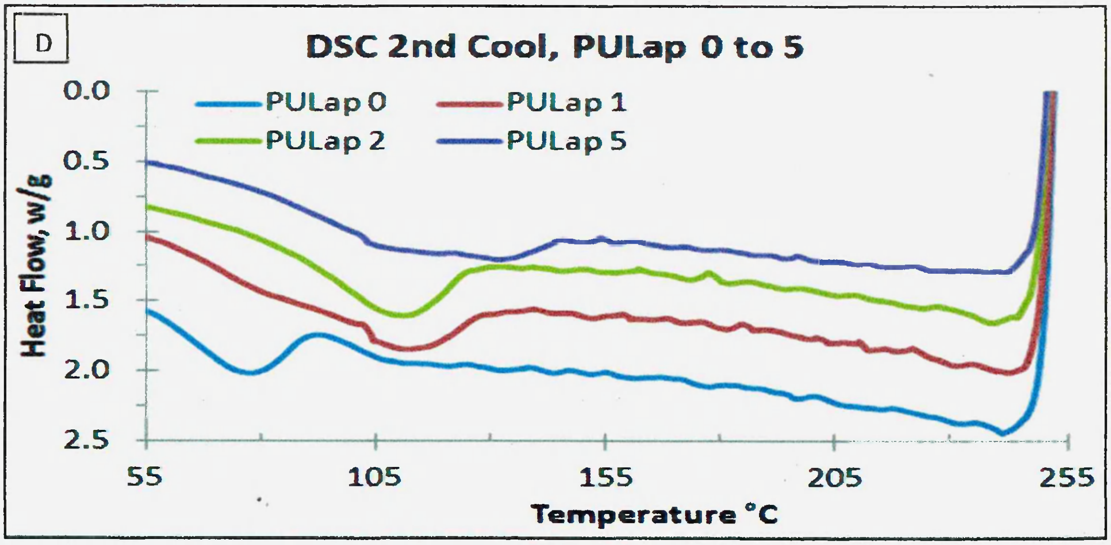

Figure 5.15: DSC A) first and B) second heating and C) first and D) second cooling of the PULap 0 to 5 samples.

The first heat results for the PULap 0 samples show that the PULap 0 sample has a SS melting endotherm, $T_{m,SS}$, at 155 °C. As the temperature rises further an endothermic melting peak is observed for the HS, $T_{m,HS}$, at ca. 230 °C. During the first cooling an exothermic peak is observed at 77 °C, this is associated with the re-crystallisation of the SS, $T_{c,SS}$. Upon second heating the $T_{m,SS}$ has shifted to a higher temperature ca. 167 °C. As the temperature increases there are no other peaks observed indicating that the $T_{m,HS}$ is non-reversible (Liff et al. 2007). During the second cooling phase the $T_{c,SS}$ is observed in the same position as the first cool, 77 °C. Overall during the DSC heating and cooling no evidence of a $T_{g,HS}$ was found, this is presumably due to it being hidden by the more prominent SS thermal transitions (Martin et al., 1999). However Lin and Chen (1998) reported that the $T_{g,HS}$ of an MDI-BDO polymer would be expected at ca. 90 to 100 °C.

The PULap 1 to 5 samples show a similar thermal profile to the PULap 0 sample, during the first heat, the $T_{m,SS}$ is observed in a very similar position as the PULap 0 sample at ca. 155 °C, with no significant decrease in intensity as the Laponite content increases. The $T_{m,HS}$, for samples PULap 1 to 5 appears to have shifted to lower temperature and intensity with increasing Laponite content from ca. 240 °C to ca. 238, 233 and 228 °C, respectively. During the first cooling only the $T_{c,SS}$ was observed, however as Laponite content increases it shifts the $T_{c,SS}$ to higher temperatures from ca. 77 °C to ca. 112 and

115 °C, respectively, and at 5 wt% causes a broadening and decreased intensity of the peak, 125 °C. Upon second heating the PULap 1 to 5 samples again have a thermal profile similar to the PULap 0 sample, the $T_{m,SS}$ is still present however it has shifted to a higher temperature compared with the first heating, as with the PULap 0 sample. However as the Laponite content increased the intensity decreased and the $T_{m,SS}$ dropped from ca. 167 °C to 165, 162 and 157 °C, respectively. As the temperature increased further no other peaks were observed showing that the $T_{m,HS}$ is non-reversible (Liff et al. 2007). For the second cooling phase the PULap 1 to 5 samples each displayed a single $T_{c,SS}$ peak, in a similar position to that during the first cooling, 112, 113 and 121 °C, respectively, still displaying a minor decrease in intensity as the Laponite content increased. However the PULap 5 sample shows a peak broadening effect, possibly displaying two peaks, and a larger intensity decrease compared to the PULap 1 and 2 samples.

Sample Description	$T_{c,SS}$, °C (1st, 2nd)	$T_{m,SS}$, °C (1st, 2nd)	$T_{m,HS}$, °C (1st, 2nd)
PULap 0	77, 77	155, 167	240, -
PULap 1	112,112	155, 165	238, -
PULap 2	115,113	155, 162	233, -
PULap 5	119,121	155, 157	228, -

Table 5.5: DSC thermal properties of interest for the PULap 0 to 5 samples. – denotes no result recorded.

These results correspond well to results presented by Lin and Chen (1998), Liff et al., (2007) and Mishra et al., (2008) who found similar DSC thermal events apart from the decrease to lower temperatures of the $T_{m,HS}$ as Laponite content increased. This was possibly because fewer samples with low Laponite contents were analysed; therefore the shift of $T_{m,HS}$ to lower temperatures may have been lost due to the intensity and shifts of other peaks. The Laponite appears to favourably interact with the HS rather than the SS as evidenced by the first heating phase, figure 5.15 A, where the $T_{m,SS}$ was not shifted but the $T_{m,HS}$ was reduced to lower temperatures as Laponite content increased. It was seen that the $T_{c,SS}$ peak shifted to higher temperatures as Laponite content increased, indicating an effect of Laponite on the SS crystallinity. These results correspond well with the TGA and ATR-FTIR results which suggested a preference for the Laponite to reside within the HS but there was some present in the SS.

5.2.3. Mechanical Results

5.2.3.1. Dynamic Mechanical Analysis

To explore the thermomechanical properties of the PULap 0 to 5 samples, DMA was used to obtain the storage modulus, loss modulus and tan δ, figure 5.16. The peak maximum of the tan δ was used to determine the T_g, this is the general literature standard for determining T_g of a material when using DMA (Liu et al., 2002). DMA results of interest are summarised in table 5.6. Prior to DMA each sample, PULap 0 to 5, was heated to 150 °C to remove thermal history.

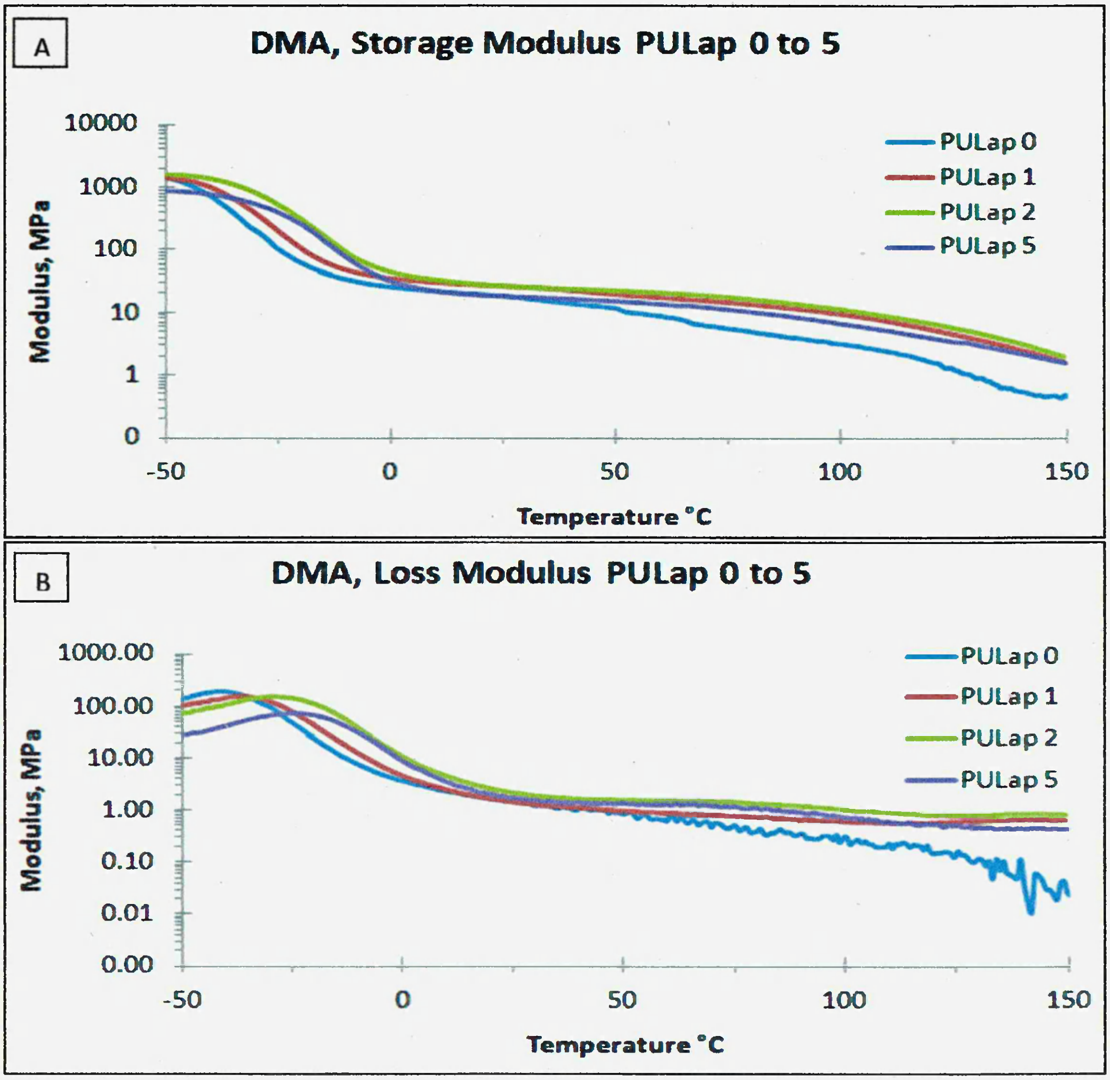

Figure 5.16: DMA of the PULap 0 to 5 samples, A) storage modulus, B) loss modulus and C) tan δ.

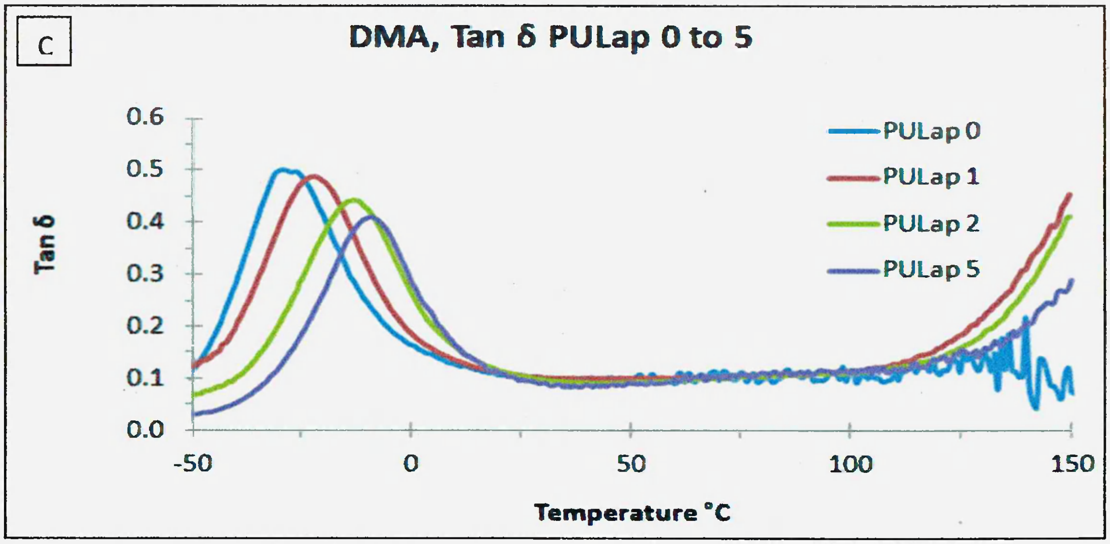

Figure 5.16: DMA of the PULap 0 to 5 samples, A) storage modulus, B) loss modulus and C) tan δ.

The PULap 0 sample shows an initial storage modulus, figure 5.16 A, of 1439 MPa, as temperature increases, from -50 to -25 °C, the storage modulus drops steeply to 102 MPa due to a $T_{g\alpha}$ transition from a glassy solid to a rubber. This demonstrates an almost two order magnitude drop in storage modulus. It has been suggested by Tsai et al., that a sharp, at least one order of magnitude drop in storage modulus indicates that a polymer system will demonstrate SME (Tsai et al., 2008, Du and Zhang, 2010). From -25 to 0 °C a quasi-rubbery plateau state is reached at ca. 26 MPa, this gradually drops to 12 MPa as temperature increases to 50 °C, whereupon the PULap 0 sample begins to soften and the modulus begins to steadily decrease. At ca. 150 °C the modulus has reduced to almost nothing, 0.5 MPa. The tan δ maximum for PULap 0, caused by the $T_{g,SS}$, occurred at -28.39 °C and exhibited an intensity of 0.50 tan δ. It has also been suggested by Chun et al., that a high intensity tan δ peak indicates that a SMP will behave more like an elastomer and experience a higher shape recovery rate (Chun et al., 2002, Tsai et al., 2008). No other tan δ peaks were observed for the PULap 0 sample. The rise in the tan δ baseline, between 125 and 150 °C, indicates that the PULap 0 sample is softening, it has been reported that Elasthane will start to flow and can be processed at ca. 170 to 197 °C (MatWeb, 2011).

Each sample, PULap 1 to 5, shows a similar DMA profile to the PULap 0 sample. As the Laponite content increases, 1 to 2 wt%, there was an increase in initial storage modulus, from 1439 MPa to 1445 and 1648 MPa, respectively, this then decreased to

907 MPa at 5 wt%. As the temperature increases from -50 to -25 °C, the storage modulus drops steeply to 201, 521 and 394 MPa, respectively, this shows that as the Laponite content increases there is an initial increase followed by a drop in storage modulus during the $T_{g\alpha}$ transition. All the PULap 1 to 5 samples demonstrated an almost two order of magnitude drop in storage modulus, similar to the PULap 0 sample, therefore each should demonstrate SME (Tsai et al., 2008, Du and Zhang, 2010). From -25 to 0 °C a quasi-rubbery plateau state is reached at 34, 45 and 31 MPa, respectively, which gradually drops to 19, 22 and 15 MPa, respectively, as temperature increases to 50 °C, whereupon the PULap 1 to 5 samples begin to soften and the modulus begins to decrease more steadily. At ca. 150 °C, the modulus for each of the PULap 1 to 5 samples has reduced to 2 MPa. The tan δ peaks for the PULap 1 to 5 samples occur at -22, -14 and -10, respectively, with corresponding intensity values of 0.49, 0.44 and 0.41 with no other tan δ peaks observed. It was however observed that between 125 and 150 °C all samples began to soften as indicated by the rise in the tan δ baseline.

Sample Name	Storage Modulus, MPa						T_g, °C	Tan δ_{max}
	-50 °C	-25 °C	0 °C	50 °C	100 °C	150 °C		
PULap 0	1439	102	26	12	3	0.5	-28	0.50
PULap 1	1445	201	34	19	9	2	-22	0.49
PULap 2	1648	521	45	22	11	2	-14	0.44
PULap 5	907	394	31	15	6	2	-10	0.41

Table 5.6: Storage modulus, loss modulus and tan δ values for the PULap 0 to 5 samples obtained from DMA.

These results indicate that as the Laponite content increases above 2 wt% the SME of the Elasthane will decrease. However it also seems that as Laponite increases up to 2 wt%, there is ca. a 15 % increase in the storage modulus. Mishra et al., (2008) reported a similar trend with incorporation of 5 wt%, amine modified, Laponite into a polyether PU attributing the effect to the higher clay loading causing filler–filler interactions. The filler-filler interactions dominate over the polymer–filler interactions causing a general decrease of the storage modulus in both glassy and rubbery regions.

It is also observed that as Laponite content increases the tan δ peak shifts to higher temperatures, this indicates that the Laponite is influencing the SS and not just the HS.

The shift of the $T_{g,SS}$ to higher temperatures was not observed by either Liff et al., or Mishra et al. However a shift of the $T_{g,SS}$ towards higher temperatures was observed by Seydibeyoglu et al., (2010).

Combined with the DSC data, it can be seen that Laponite content has a clear effect on the HS and SS of Elasthane, with minor changes occurring at small loadings, 1 wt% Laponite, which generally become more pronounced with larger loadings, 5 wt% Laponite. The Laponite certainly affects the way in which the SS re-crystallise after melting, as shown by the DSC, while DMA has revealed that Laponite alters the SS, $T_{g,SS}$, as well as increasing the PU's ability to retain its storage modulus at higher temperatures.

5.2.4. Shape Memory Properties

5.2.4.1. Unconstrained Shape Memory Effect Evaluation

Evaluation of the SME was carried out in order to assess whether adding 1 to 5 wt% Laponite enhances or reduces the shape memory effect of Elasthane, figure 5.17. As reported by Lendlein and Kelch (2002) a PTMO/MDI/BDO type PU is a class III SMP, with a $T_{trans} = T_g$. This is therefore Elasthane's SMP class. However in previous work carried out by Lin and Chen (1998) it was found that using a PTMO (MW 1,000 g mol^{-1}) SS and MDI/BDO HS in the ratio of 60.5:39.5 caused the PU to display SME but at a different temperature range to the others within the study, which were not reported on. Lendlein and Kelch (2002) found that that certain PU SMP class III can develop a mixed T_g state, this is when the PU contains a HS and SS which are not fully phase separated due to a short switching segment. This has been observed in short PTMO chains, MW 250 and 650 g mol^{-1}, but not in longer PTMO chains, MW 2000 and 2900 g mol^{-1}. Therefore with Elasthane having a PTMO chain of MW 1,000 g mol^{-1} it potentially can show the mixed T_g phenomenon. Therefore an appropriate SME temperature range needs to be adopted, in this case as the mixed T_g will be between the $T_{g,SS}$, ca. -28 °C, and the $T_{g,HS}$, will occur at ca. 90 to 100 °C (Lin and Chen 1998), having a T_{low} at 0 to 5 °C and a T_{high} at 90 °C should provide an adequate SME range. In order to only view the effect of Laponite on the SME ability of the PULap 0 to 5 samples, each was annealed at 150 °C for 15 minutes prior to being tested to remove any previous thermal history. The PULap 0 to 5 samples were deformed and their recovery analysed, section 2.1.6, figure 2.14.

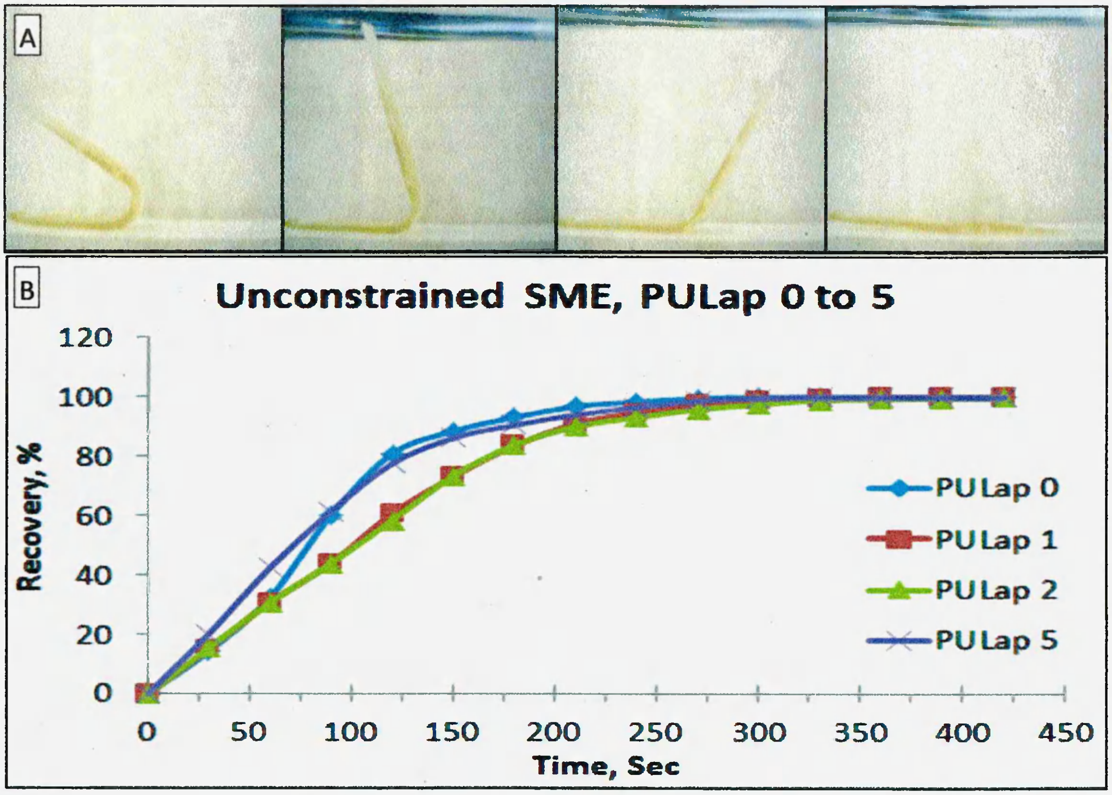

Figure 5.17: Unconstrained SME testing of PULap 0 to 5 samples, from temporary to permanent shape, A) still images of PU/Lap SMP at sequential intervals, B) plotted against time at a fixed temperature, ca. 90 °C.

The unconstrained SME evaluation results, θ_{Max} %, θ_{Fixed} %, $\theta_{1/2Final}$ %, θ_{Final} % and $\theta_{1/2Final}$ % and θ_{Final} % recovery times are summarised in table 5.7. The PULap 0 sample exhibited a θ_{Max} of 100 %, demonstrating that it is elastic enough to accommodate a high level of deformation stress. After the deformation constraint was removed, the sample was left at room temperature ca. 22 °C, during which an amount of recovery strain occurred, leading to a θ_{Fixed} of ca. 89 %.

Unconstrained shape memory recovery was carried out at 90 °C and the $\theta_i(T)$ was recorded every 30 seconds until the PULap 0 sample reached its θ_{Final}, 100 %. This demonstrates that although PULap 0 cannot store 100 % of the deformed strain at room temperature, there is still sufficient energy to return it to its permanent shape.

In order to further assess the PULap 0 sample shape memory ability the $\theta_{1/2\ Final}$ and θ_{Final} time of recovery, 80 and 270 seconds, respectively, were recorded. These results indicate that Elasthane recovers 50 % in ca. one third of the full recovery time,

demonstrating that the majority of the energy stored in the SS is used quickly whilst the remaining recovery strain slowly recovers the permanent shape.

The PULap 1 to 5 samples all showed a θ_{Max} of 100 %, demonstrating that the Laponite content does not significantly affect the elastic ability of the SS to accommodate a high level of deformation stress. This suggests that Laponite interactions in the SS are minimal as elasticity would generally decrease if there was clay in the SS (Liff et al., 2007). After the deformation constraint was removed, and the samples were left at room temperature, each displayed an amount of recovery strain, leading to a θ_{Fixed} of 91, 93 and 95 %, respectively. This implies that although Laponite is most likely interacting with the HS, observed using DSC and ATR-FTIR, there is only a minor increase in θ_{Fixed} % compared to the PULap 0 sample.

Shape memory recovery was carried out and the $\theta_i(T)$ were recorded every 30 seconds until the PULap 0 to 5 samples reached their θ_{Final}, 100 %. These results demonstrate that the Laponite at up to 5 wt% loading does not interfere with the Elasthane ability to return to the permanent shape. The $\theta_{1/2\ Final}$ and θ_{Final} time of recovery for the PULap 1 to 5 samples were evaluated giving times of 102, 104 and 70 seconds and 330, 360 and 270 seconds, respectively. These results indicate that the PULap 1 to 5 samples recover 50 % in ca. one third of the full recovery time, the same as the PULap 0 sample.

Sample Description	θ_{Max}, %	θ_{Fixed}, %	$\theta_{1/2Final}$, %	θ_{Final}, %	$\theta_{1/2Final}$ time, Sec	θ_{Final} time, Sec
PULap 0	100	89	50	100	80	270
PULap 1	100	91	50	100	102	330
PULap 2	100	93	50	100	104	360
PULap 5	100	95	50	100	70	270

Table 5.7: Summary of unconstrained SME evaluation results observed from the PULap 0 to 5 samples, recording the θ_{Max} %, θ_{Fixed} %, $\theta_{1/2Final}$ %, and θ_{Final} %.

These results show that $\theta_{1/2\ Final}$ time of recovery for the PULap 1 and 2 samples was retarded but was quickened for the PULap 5 sample, while the θ_{Final} time of recovery was increased with any wt% Laponite loading. This suggests that at 1 and 2 wt%

Laponite, reinforcement of the HS occurs, as evidence by the increase of θ_{Fixed} %, causing the SS to be held in place more tightly, increasing $\theta_{1/2\ Final}$ and θ_{Final} time of recovery. The PULap 5 sample appears to reinforce the HS, supported by the increase of θ_{Fixed} %, but decreases the $\theta_{1/2\ Final}$ time of recovery. This effect may occur because the Laponite platelets increase the amount of deformation stress that can be stored within Elasthane, allowing an increase of initial shape return, however this does not appear to affect the overall shape return.

These results demonstrated that the PTMO/MDI/BDO based Elasthane is a class III SMP with a mixed T_g, as evidence for shape fixity at room temperature, ca. 22 °C and a SME displaying at 90 °C, a temperature much higher than the $T_{g,SS}$, the supposed T_{trans} (Lendlein and Kelch, 2002). This result also contradicts the findings of Liu et al., (2007), who described this SMP as a type IV with a T_{trans} as the T_m of the PTMO chain between 0 and 46 °C, with a PTMO chain of ca. 1,000 g mol^{-1} this would imply that the SME onset would occur at ca. 24 °C (Lin and Chen, 1998), however as all the PULap 0 to 5 samples show shape fixity at ca. 22 °C this is not the case.

The SME evaluation results correspond to those predicted by the DMA results which suggested that the PULap 0 to 5 samples will show shape memory ability and that there will be a reduction in the shape memory recovery rate with incorporation of Laponite as shown by the decreased intensity of the tan δ peaks as Laponite content increased.

5.3. Conclusions

The effects of incorporating Laponite, into PU, Elasthane, were studied to assess if an intercalated or exfoliated nanocomposite could be formed, and if any improved shape memory properties were conferred. This was to contribute to the aim of creating a mechanically and thermally stable SMP packaging solution.

Overall the Elasthane demonstrated that it has reasonable mechanical, thermal and shape memory properties, which can be partially tailored with the incorporation of exfoliated Laponite platelets. These results indicate that Laponite can be fully dispersed within Elasthane at low contents, 1 and 2 wt% Laponite, and partially dispersed at higher contents, 5 wt% Laponite. The HS and SS of the Elasthane can be influenced almost separately depending on the Laponite loading, and that the SME can also be affected in the same manner. This is a significant result, as depending on the desired application of the SMP, a consistent SME can be employed by utilising 1 and 2 wt% Laponite loading or an initial rapid SME effect could be used with a 5 wt% Laponite loading. However as Laponite content increases there was a decrease in thermal stability at lower temperatures as seen in the TGA thermograms, therefore impacting the use of the PULap nanocomposites for higher temperature applications. It would appear that although the PULap 0 to 5 samples are mechanically suitable for the purpose, displaying reasonable shape memory ability, their T_{trans}, and SME onsets are high. In this respect a SMP should have a T_{trans} more towards room temperature to be of service in the packaging industry, therefore an alternative should be sought.

5.4. References

CHUN, B.C., et al. (2002). Enhanced dynamic mechanical and shape-memory properties of a poly(ethylene terephthalate)-poly(ethylene glycol) copolymer crosslinked by maleic anhydride. Journal of Applied Polymer Science, **83** (1), 27-37.

DAI, XH., et al. (2004). Study on structure and orientation action of polyurethane nanocomposites. Macromolecules, **37** (15), 5615-5623.

DU, H.Y., and ZHANG, J.H., (2010). Shape memory polymer based on chemically cross-linked poly(vinyl alcohol) containing a small number of water molecules. Colloid and Polymer Science, **288** (1), 15-24.

CLEMITSON I.R., (2008). Castable Polyurethane Elastomers. Boca Raton (FL): CRC Press, Taylor and Francis Group.

FERGUSON, J., and PETROVIC, Z., (1976). Thermal stability of segmented polyurethanes. European Polymer Journal, **12** (3), 177-181.

FINNIGAN, B., et al. (2004). Morphology and properties of thermoplastic polyurethane nanocomposites incorporating hydrophilic layered silicates. Polymer, **45** (7), 2249-2260.

GUNES, I.S., CAO, F., and JANA, S.C., (2008). Effect of thermal expansion on shape memory behavior of polyurethane and its nanocomposites. Journal of Polymer Science Part B-Polymer Physics, **46** (14), 1437-1449.

GUNES, I.S., CAO, F., and JANA, S.C., (2008). Evaluation of nanoparticulate fillers for development of shape memory polyurethane nanocomposites. Polymer, **49** (9), 2223-2234.

HE, Z., et al. (2011). Remote controlled multishape polymer nanocomposites with selective radiofrequency actuations. Advanced Materials, **23** (28), 3192.

HU J.L., (2007). Shape memory polymers and textiles. Cambridge: Woodhead publishing limited.

HU, J.L., JI, F.L., and WONG, Y.W., (2005). Dependency of the shape memory properties of a polyurethane upon thermomechanical cyclic conditions. Polymer International, **54** (3), 600-605.

IJDO, W.L., KEMNETZ, S., and BENDERLY, D., (2006). An infrared method to assess organoclay delamnination and orientation in organoclay polymer nanocomposites. Polymer Engineering and Science, **46** (8), 1031-1039.

JEONG, E.H., et al. (2007). Effective preparation of montmorillonite/polyurethane nanocomposites by introducing cationic groups into the polyurethane main chain. European Polymer Journal, **43** (6), 2286-2291.

JEONG, H.M., et al. (2001). Miscibility and shape memory property of poly(vinyl chloride)/thermoplastic polyurethane blends. Journal of Materials Science, **36** (22), 5457-5463.

KIM, B. K., LEE, S. Y., and XU, M., (1996). Polyurethanes having shape memory effects. Polymer, **37** (26), 5781-5793.

LEE, BS., et al. (2001). Structure and thermomechanical properties of polyurethane block copolymers with shape memory effect. Macromolecules, **34** (18), 6431-6437.

LENDLEIN, A., and KELCH, S., (2005). Shape-memory polymers as stimuli-sensitive implant materials. Clinical hemorheology and microcirculation, **32** (2), 105-116.

LIFF, S. M., KUMAR, N., and MCKINLEY, G.H., (2007). High-performance elastomeric nanocomposites via solvent-exchange processing. Nature Materials, **6** (1), 76-83.

LIN, J.R., and CHEN, L.W., (1998). Study on shape-memory behavior of polyether-based polyurethanes. I. influence of the hard-segment content. Journal of Applied Polymer Science, **69** (8), 1563-1574.

LIN, J.R., and CHEN, L.W., (1998). Study on shape-memory behavior of polyether-based polyurethanes. II. influence of soft-segment molecular weight. Journal of Applied Polymer Science, **69** (8), 1575-1586.

LIU, C., QIN, H., and MATHER, P.T., (2007). Review of progress in shape-memory polymers. Journal of Materials Chemistry, **17** (16), 1543-1558.

LIU, C.D., et al. (2002). Chemically cross-linked polycyclooctene: Synthesis, characterization, and shape memory behavior. Macromolecules, **35** (27), 9868-9874.

MARTIN, D.J., et al. (1999). The influence of composition ratio on the morphology of biomedical polyurethanes. Journal of Applied Polymer Science, **71** (6), 937-952.

MATWEB, (2011). DSM-PTG Elasthane™ 80A Thermoplastic Polyether Urethane. [online]. Last accessed 10 August 2011 at:http://www.matweb.com/search/DataSheet .aspx?MatGUID=61a633b7094b4983a20d5fa2c450e68d&ckck=1

MISHRA, A.K., NANDO, G.B., and CHATTOPADHYAY, S., (2008). Exploring preferential association of laponite and cloisite with soft and hard segments in TPU-clay nanocomposite prepared by solution mixing technique. Journal of Polymer Science Part B-Polymer Physics, **46** (21), 2341-2354.

PAN, G.H., et al. (2008). The glass transition temperature of polyurethane shape memory polymer reinforced with treated/non-treated attapulgite (playgorskite) clay in dry and wet conditions. Smart Materials & Structures, **17** (4), 045007.

PATTANAYAK, A., and JANA, S.C., (2005). Properties of bulk-polymerized thermoplastic polyurethane nanocomposites. Polymer, **46** (10), 3394-3406.

PATTANAYAK, A., and JANA, S.C., (2005). Synthesis of thermoplastic polyurethane nanocomposites of reactive nanoclay by bulk polymerization methods. Polymer, **46** (10), 3275-3288.

REZANEJAD, S., and KOKABI, M., (2007). Shape memory and mechanical properties of cross-linked polyethylene/clay nanocomposites. European Polymer Journal, **43** (7), 2856-2865.

PURRC, (2005). Polyurethane Recycling. [Online] Article from Center for the Polyurethanes Industry of the American Chemistry Council last accessed 24 August 2011 at: www.polyurethane.org/recycling

ROCKWOOD SPECIALTIES INC., (2009). Laponite. [Leaflet] Cheshire: Rockwood Additives Limited

ROUSSEAU, I.A., (2008). Challenges of shape memory polymers: A review of the progress toward overcoming SMP's limitations. Polymer Engineering and Science, **48** (11), 2075-2089.

SEYDIBEYOGLU, M.O., et al. (2010). Preparation of Polyurethane/Hectorite, Polyurethane/Montmorillonite, and Polyurethane/Laponite nanocomposites without organic modifiers. Journal of applied polymer science, **116** (2), 832-837.

SHIEH, Y.T., et al. (1999). Thermal degradation of MDI-based segmented polyurethanes. Journal of Polymer Science Part A-Polymer Chemistry, **37** (22), 4126-4134.

TIEN, Y.I., and WEI, K.H., (2001). High-tensile-property layered silicates/polyurethane nanocomposites by using reactive silicates as pseudo chain extenders. Macromolecules, **34** (26), 9045-9052.

TIEN, Y.I., and WEI, K.H., (2001). High-tensile-property layered silicates/polyurethane nanocomposites by using reactive silicates as pseudo chain extenders. Macromolecules, **34** (26), 9045-9052.

TSAI, Y., et al. (2008). Shape memory effects of poly(ethylene terephthalate-co-ethylene succinate) random copolymers. European Polymer Journal, **44** (2), 550-554.

YEH, F., et al. (2003). In-situ studies of structure development during deformation of a segmented poly(urethane-urea) elastomer. Macromolecules, **36** (6), 1940-1954.

VICENTE, I., (2010). Hectorite in Polyurethane Composites. PhD, Universitat Rovira I Virgili.

WARD, B., (2008). New Possibilities with Polyurethanes: How new biostable polyurethanes can satisfy the materials requirements of tomorrow's medical devices. Berkeley (CA). DSM PTG, Part of DSM Biomedical.

Chapter 6: Exploration of Polyurethane/PVC Blends and Composites as SMP

6. Introduction

With SMP, including PU, there are still challenges to be overcome. When compared to SMAs SMP have low mechanical strength and low shape recovery stress as well as showing hysteresis after repeated deformation-recovery cycles (Rousseau, 2008).

In order to improve the abilities of SMP, the concept of physically blending two or more existing polymers is an attractive solution as it is an effective method to obtain new or desirable attributes in polymer systems.

In recent years polymer blends have become the focus of many research groups, with important research being carried out to investigate the relationships between composition, morphology and properties of various blends (Coleman et al., 1988, Jeong et al., 2001, Han and Huang, 2010).

Using the blending method a series of copolymers with variable properties can be easily formed by careful selection of the components and composition to match the demands of various applications. PU has been shown to be compatible with several polar thermoplastics such as PVC (Jeong et al., 2001), polycarbonate (Feng et al., 2009), acrylonitrile-butadiene-styrene (Ha et al., 1997) and phenoxy resin (Jeong et al., 2001).

Therefore in order to improve the performance of SMP PU another polymer should be blended with it. For example, blending a high molecular weight material with polynorbornene enhances its physical entanglements and reduces its hysteresis during shape memory cycle (Jeong et al. 2001) while recently Ratna and Karger-Kocsis (2011) have shown that blending poly(ethylene oxide) and crosslinked poly(MMA), improves its shape fixity while providing a reasonable shape memory response. A suitable candidate for blending with a PU SMP is a polymer which can potentially improve its SME, therefore it should have a certain amount of shape memory ability itself. Certain amorphous polymers can show SME due to physical entanglements acting as HS. These include PVC, poly(MMA), and polycarbonate.

The blending of PU and PVC has been studied previously in the literature (Xiao et al., 1987, Ha et al., 1998, Pielichowski and Hamerton, 2000), with different types of polyurethanes e.g. polyether and/or polyester based, being blended with varying amounts of PVC. These novel polymer blends have given rise to materials with considerable technological value and scientific interest, since chlorine containing polymers have been reported to interact with oxygen containing polymers, e.g. PU, increasing fire retardance through vapour phase inhibition and increased char formation (Xiao et al., 1991). The blending of PU with PVC has provided materials with a broader range of hardness, abrasion resistance, permanence, low temperature flexibility, and impact resistance and has led to the blends being studied for their commercial importance as good candidates for cable jacketing, tubing, hose, and shoe sole applications (Takahiko, 1982).

However blends of PUs and PVC been reported to be difficult to mix on conventional polymer processing equipment and would command significant premiums within industry to produce (Parnell and Min, 2005). Although it is possible to melt blend softer grades of PU and PVC, the high processing temperatures, ca. 190 °C, and melt viscosities required to homogenize such blends often result in partial PVC degradation, even in the presence of thermal stabilizers. Several techniques are available to avoid PVC degradation including solution blending which although eliminates many of the problems associated with melt blending is not a commercially viable mixing technique due to the large amounts of solvent to be removed.

In order to overcome the processing and mixing difficulties associated with blended PU/PVC systems an alternative blending technique would be advantageous. In the synthesis of semi-interpenetrating polymer networks and dynamic vulcanizates, polymer blending is often achieved by mixing an already polymerized high polymer with miscible monomers or oligomers of a second polymer that are subsequently polymerized. Such a reactive blending technique offers an attractive method for overcoming the previously mentioned melt blending problems. Several other advantages that such a reactive blending technique might offer include reduced costs and a means of controlling final blend morphology (Parnell and Min, 2005).

Previously in the literature the majority of work has concentrated on the compatibility of different PU with varying wt% of PVC polymer, while the specific study of the shape memory ability of PU/PVC blend materials is not well known. Ha et al., previously carried out work on the fracture toughness of PU/PVC blends (Ha et al. 1998), whilst Parnell and Min (2005) worked on the reactive blending of PU and PVC in situ. Other authors such as Xiao et al., (1991) have considered the morphology, modulus-composition relations and compatibility of PVC with different SS of PU. Other than Jeong et al., (2001) who previously synthesized a range of PU/PVC blends using selected hard and soft PU segments before characterising the mechanical, thermal and SME of these blends, no authors have considered PU/PVC shape memory abilities.

The objective of the work in this chapter is to expand on the limited work on the SME of PU/PVC, to synthesize a range of PU/PVC blends and study the influence of PVC on the mechanical, thermal and shape memory properties of PU. It may be expected that blends of PU and PVC will exhibit improved shape memory ability due to the shape memoy capability of PVC (Jeong et al. 2001). The solvent-exchange method developed by Liff et al. (2006), described in chaper 5, was used to dissolve the PU and combine it with PVC to form PU/PVC blends. Properties studied include miscibility, storage and loss modulus, tan δ, thermal stability, and SME.

6.1. Experimental

All characterisation methods were carried out in MERI at Sheffield Hallam University.

6.1.1. Materials

The materials described in section 5.1.1. PVC, (ca. 10,000g mol^{-1}), were used as received from Sigma-Aldrich.

6.1.2. Elasthane/PVC Blends Preparation

In order to effectively and uniformly blend Elasthane with PVC a solution mixing method was used, figure 6.1. Elasthane and PVC were both dissolved separately in DMAc, the solutions were stirred using a PTFE-coated, magnetic, spin-bar on a hot plate stirrer with a moderate stir speed (lv 6) for 24 hours at 45 °C. Both Elasthane and PVC solutions were mixed together and stirred for another 24 hours at 45 °C.

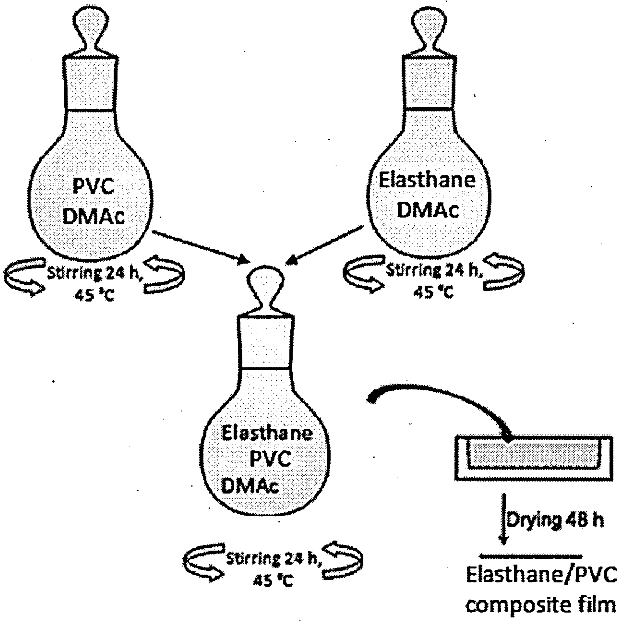
PVC
DMAc
Stirring 24 h, 45 °C
Elasthane
DMAc
Stirring 24 h, 45 °C
Elasthane
PVC
DMAc
Stirring 24 h, 45 °C
Drying 48 h
Elasthane/PVC composite film

Figure 6.1: Solution mixing procedure of Elasthane and PVC composites.

The Elasthane/PVC-DMAc polymer solutions, table 6.1, were cast in a pre-heated polytetrafluoroethylene, PTFE, mould, 40 x 60 x 18 mm, and the solvent was removed by controlled evaporation in an oven for 48 hours at 70 °C. After controlled evaporation an Elasthane/PVC blend film, 0.20±0.05 mm thick, was formed and removed. The Elasthane/PVC blends were analysed using ATR-FTIR, TGA, DSC, DMA and SME testing.

Sample Description	Short Description	Elasthane, g	PVC, g	PVC, wt%	DMAc, g
Elasthane 100 wt% / PVC 0 wt%	PU100/PVC0	0.75	0.00	0	60
Elasthane 80 wt% / PVC 20 wt%	PU80/PVC20	0.60	0.15	20	60
Elasthane 60 wt% / PVC 40 wt%	PU60/PVC40	0.45	0.30	40	60
Elasthane 40 wt% / PVC 60 wt%	PU40/PVC60	0.30	0.45	60	60
Elasthane 20 wt% / PVC 80 wt%	PU20/PVC80	0.15	0.60	80	60
Elasthane 0 wt% / PVC 100 wt%	PU0/PVC100	0.00	0.75	100	60

Table 6.1: PU/PVC blend formulations for solution casting to produce thin films.

6.1.3. PU/PVC 0 to 5 wt% Laponite Composites Preparation

The Laponite was dispersed into the PU60/PVC40 blend via the delamination procedure, developed by McKinley et al., to fully disperse Laponite layers within an organic solvent, figure 6.2 (Liff et al., 2007).

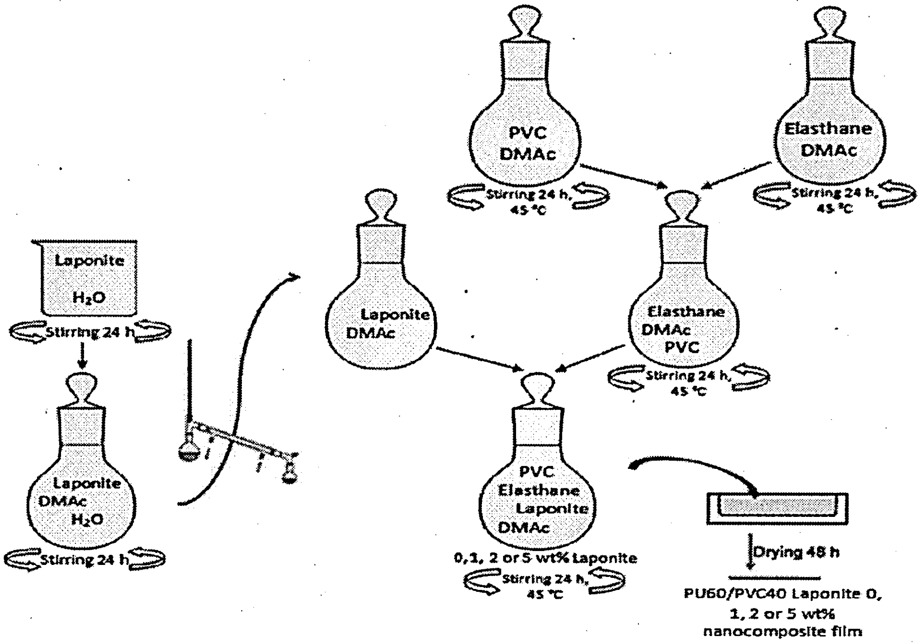
PVC
DMAc
Stirring 24 h, 45 °C
Elasthane
DMAc
Stirring 24 h, 45 °C
Laponite
H₂O
Stirring 24 h
Laponite
DMAc
Elasthane
DMAc
PVC
Stirring 24 h, 45 °C
Laponite
DMAc
H₂O
Stirring 24 h
PVC
Elasthane
Laponite
DMAc
0, 1, 2 or 5 wt% Laponite
Stirring 24 h, 45 °C
Drying 48 h
PU60/PVC40 Laponite 0, 1, 2 or 5 wt% nanocomposite film

Figure 6.2: The delamination of Laponite and its subsequent dispersal into the PU60/PVC40 blend to produce PU60/PVC40 composites containing 1 to 5 wt% Laponite.

1 g of Laponite was mixed with 100 g of deionised water. The solution was stirred using a PTFE-coated, magnetic, spin-bar on a hot plate stirrer with a moderate stir speed (lv 6) for 24 hours. 200 g DMAc was added to the solution and stirred at the same speed for 48 hours. The liquid-vapour phase equilibrium of the binary solvent system was utilized in order to evaporate off all the water from the solution. A distillation setup was used to remove the water. Elasthane and PVC were both

dissolved separately in DMAc, figure 6.2, the solutions were stirred using a PTFE-coated, magnetic, spin-bar on a hot plate stirrer with a moderate stir speed (lv 6) for 24 hours at 45 °C. Both Elasthane and PVC solutions were mixed together and stirred for another 24 hours at 45 °C, creating a Elasthane/PVC/DMAc solution.

Sample Description	Short Description	Elasthane, g	PVC, g	Laponite/DMAc suspension, g	DMAc ,g
PU/PVC/Laponite 0 wt%	PU/PVC/Lap 0	0.450	0.300	0.00	30.00
PU/PVC/Laponite 1 wt%	PU/PVC/Lap 1	0.446	0.297	5.27	24.73
PU/PVC/Laponite 2 wt%	PU/PVC/Lap 2	0.441	0.294	10.54	19.46
PU/PVC/Laponite 5 wt%	PU/PVC/Lap 5	0.428	0.285	26.36	3.64

Table 6.2: Formulations for solution casting of the PU/PVC/Laponite composites to create thin films.

The Elasthane/PVC/DMAc solution was infused with pre-weighed amounts of Laponite/DMAc dispersion. The PU/PVC/Laponite/DMAc polymer solutions, table 6.2, were cast in a pre-heated PTFE, mould 40 x 60 x 18 mm, and the solvent was removed by controlled evaporation in an oven for 48 hours at 70 °C. After controlled evaporation PU/PVC/Lap 0 to 5 composite films, 0.2±0.05 mm thick, were formed and removed. These were analysed using XRD, ATR-FTIR, TGA, DSC, DMA and SME testing.

6.1.4. Techniques

All techniques used, XRD, ATR-FTIR, TGA, DSC, DMA and unconstrained SME evaluation have been previously described in section 5.1.3.

6.2. PU/PVC Blend Results

6.2.1. Homogeneity

6.2.1.1. ATR-FTIR Spectroscopy

ATR-FTIR spectra, 500 to 3500 cm^{-1}, of the PU/PVC blended samples are presented in figure 6.3. This was carried out to observe the effects of PVC on Elasthane, specifically on the NH and CO bonding, figure 6.4.

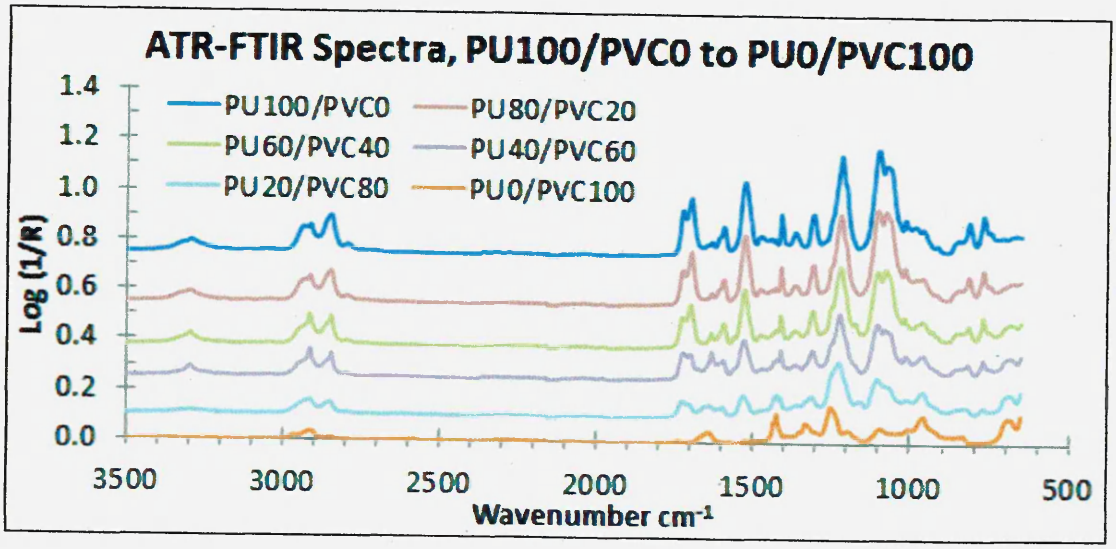

Figure 6.3: ATR-FTIR spectra of PU100/PVC0 to PU0/PVC100

The spectrum of the PU homopolymer, PU100/PVC0 blend, was described in section 5.2.1.2. For the PU0/PVC100 blend, in the high frequency region, ca. 3400 to 2700 cm^{-1}, only aliphatic C-H stretch vibrations were observed at 2920 cm^{-1}. At lower frequencies, ca. 1800 to 1000 cm^{-1} only C-H bend vibrations were observed, 1550, 1420, 1325, 1250 and 1090 cm^{-1}. In the 900 to 600 cm^{-1} region C-H rock vibrations were observed at 950 and 820 cm^{-1} along with an alkyl halide C-Cl stretch vibration at 780 cm^{-1}.

The PU/PVC blends all showed infra-red spectra between those of the homopolymers Elasthane and PVC as expected. In the region 3500 to 3000 cm^{-1} the major NH absorption peaks from the HS of the PU are observed, 2 peaks are displayed, both related to NH stretch vibrations, a major peak at 3310 cm^{-1}, related to the hydrogen-bonded NH, with a shoulder, on the higher wavelength side, at 3330 cm^{-1}, related to the free NH, figure 6.4 A. As the amount of PU decreases the amount of free NH reduces and disappears completely in the PU40/PVC60 blend while the hydrogen-bonded NH intensity remains relatively constant. Once PVC has increased to 80 wt% the 3310 cm^{-1} peak is considerably reduced with none present in the pure PVC sample,

as expected. These results show that the majority of the NH groups are hydrogen-bonded, and that the intensity of the free NH is severely reduced by addition of >20 wt% PVC, demonstrating that PVC is interacting with the HS domains, bonding with the free NH groups. However only at PVC levels >60 wt% is hydrogen bonding between HS segments disrupted (Xiao et al., 1987). This could be caused by the PVC physically blocking the formation of large HS volumes or because the PVC is having a dilution effect on the PU at >60 wt%, reducing the size of the HS domains. However as ATR-FTIR only penetrates 4 to 6 μm into the surface this is not conclusive.

In the carbonyl stretch region, 1780 to 1640 cm^{-1}, there are two well resolved peaks of similar intensity observed at ca. 1730 and 1700 cm^{-1} both from the PU HS. These peaks can be attributed to the free and bonded carbonyl groups, respectively, figure 6.4 B.

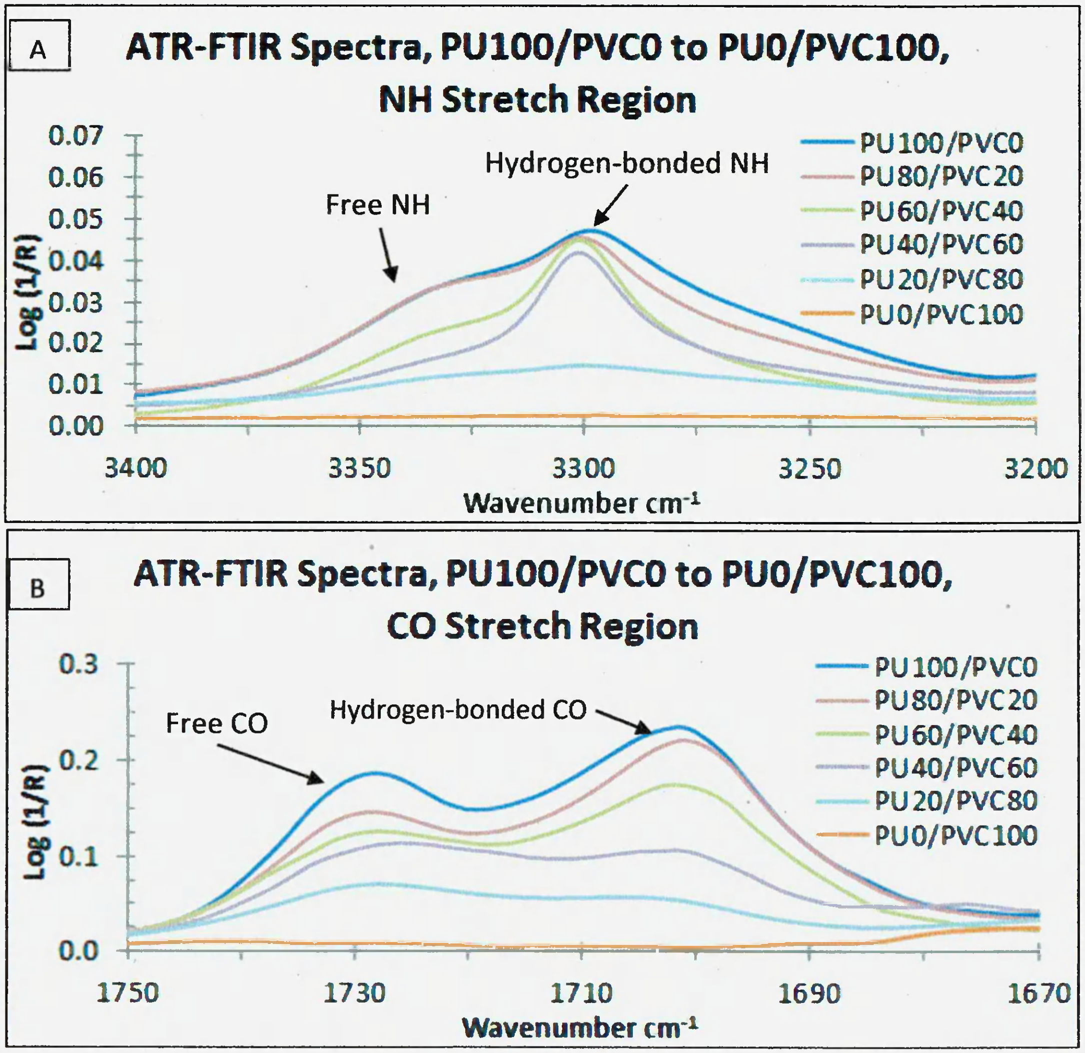

Figure 6.4: ATR-FTIR spectra for PU/PVC blends A) NH bend vibrations, 3200 to 3400 cm^{-1}, B) CO stretch vibrations, 1670 to 1750 cm^{-1}.

In the PU100/PVC0 blend the peak for the bound carbonyl is of greater intensity than that of the free carbonyl. However as the PVC content increases there is a reduction in blend intensity for both bound and free carbonyls until blend PU40/PVC60, when the free carbonyl intensity becomes greater than that for the bound carbonyls. These results indicate as PVC increases it reduces the intensity of both the bonded and free CO. At PVC contents >40 wt% the amount of bonded CO decreases below the amount of free CO, this indicates the PVC is interfering with the hydrogen bonding between adjacent HS but is not bonding directly with the CO in the HS. Parnell and Min (2005) reported similar results, including that at PVC content <20 wt%, PVC cannot interrupt the carbonyl bonding in the HS domains. In the alkyl halide stretch region, 800 to 650 cm^{-1}, there was no C-Cl peak in the pure PU, however as the PVC content increases the intensity of the C-Cl peak, ca. 780 cm^{-1}, increases, confirming the presence of the PVC in the PU/PVC blends.

These results suggest that PVC is disrupting the HS hydrogen bonding and forming new bonds with the NH groups, suggesting that PVC is potentially miscible with Elasthane. The reduction in hydrogen bonding in the HS also suggests that the HS domains will be smaller because of reduced attraction to each other, and potentially more isolated from the PTMO SS due to physical blocking by the PVC. This potentially increases the phase separation of the PU HS and SS (Xiao et al., 1987). However ATR-FTIR only allows a small penetration depth, 4 to 6 µm, so the effects of PVC on PU may only be occurring at the surface of the PU/PVC blends. Therefore if there are greater PVC concentrations at the surface of the PU/PVC blends this interpretation is potentially inaccurate. Further analysis by other techniques is certainly required before an informed conclusion can be drawn.

6.2.2. Thermoanalytical Results

6.2.2.1. Thermogravimetric Analysis

The TGA thermograms and their derivatives, obtained on heating the PU/PVC blends prepared in this study are shown in figure 6.5 and the temperatures of interest are summarized in table 6.3.

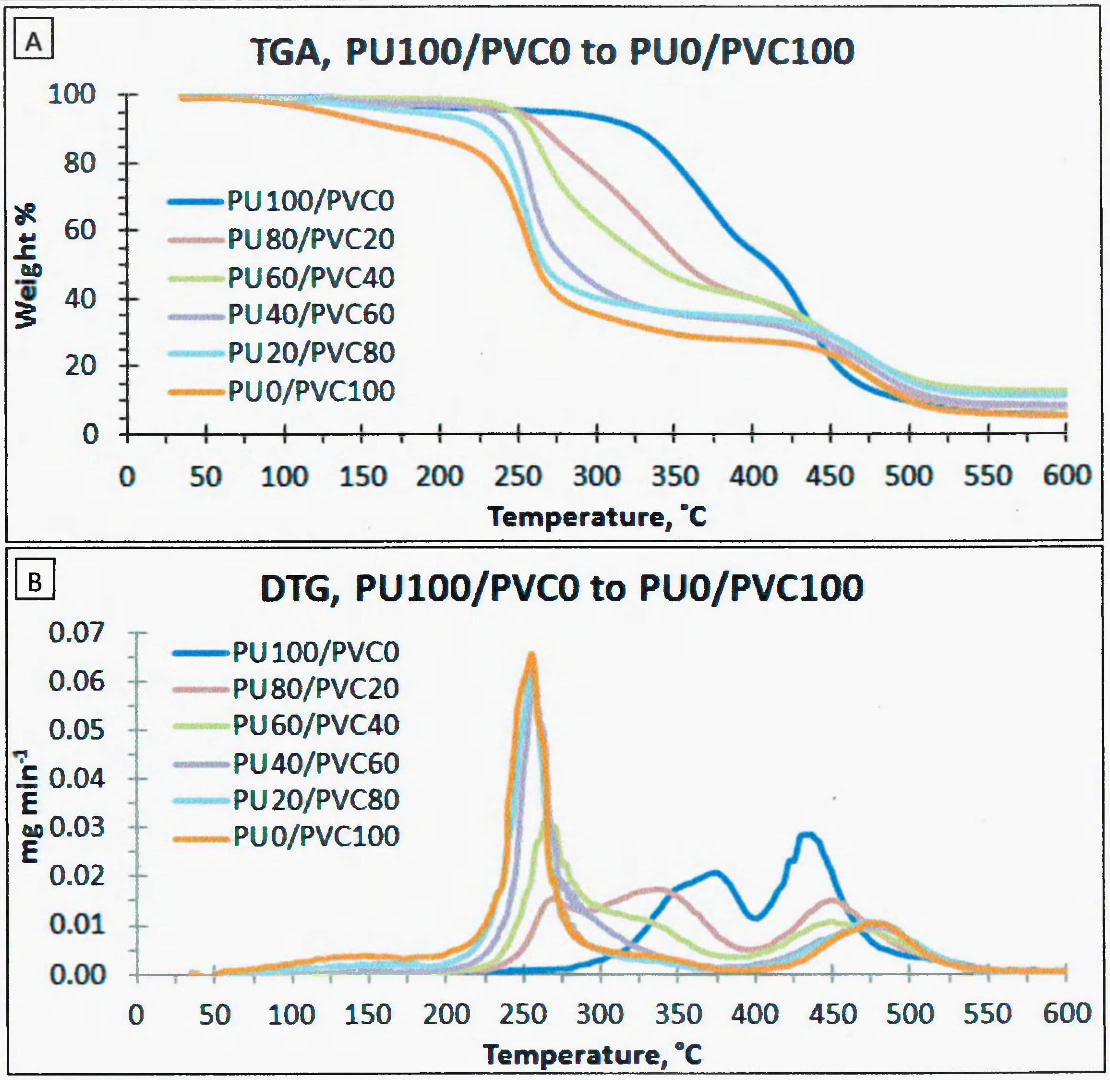

Figure 6.5: PU/PVC blends A) TGA and B) DTG thermograms.

The PU homopolymer, PU100/PVC0 blend was described in section 5.2.2.1. The PU0/PVC100 blend exhibits a three stage decomposition, with an initial broad degradation at ca. 140 °C, $T_{max(1)}$, a steep weight loss at 255 °C, $T_{max(2)}$ and a third degradation stage at 475 °C, $T_{max(4)}$. Above 600 °C the polymer is fully degraded with only some minor carbon or char residue remaining. $T_{max(1)}$ at ca. 140 is caused by minor thermally induced dehydrochlorination, THCL. THCL is the process of chain stripping of PVC, the loss of small volatile molecules by a reaction that “strip” side chain substituents from the main PVC chain forming HCl (Fisch and Bacaloglu, 1995). The $T_{max(2)}$ at 255 °C, is attributed to major chain stripping of PVC and the major production of HCl. This process initiates, via autocatalysis, internal cross-linking of the main PVC chain enhancing char formation producing a carbon rich, hydrogenated char residue. The $T_{max(4)}$ at 475 °C is the hydrogenated char breaking down via a chain scission reaction, this occurs at higher temperatures as the char formed by the chain stripping effect is more compact and less easily volatilized (Wilkes et al., 2005).

All PU/PVC blends show either a two or three stage degradation sequence depending on composition, with degradation stages occurring between those observed for Elasthane and PVC homopolymers. As the PVC content increases in Elasthane $T_{max(4)}$ reduces in intensity and shifts to a higher temperature up to 453 °C at blend PU60/PVC40. In the PU40/PVC60 blend only the PVC degradation stage at 375 °C, $T_{max(4)}$ is observed. As PVC content increases, the peak $T_{max(3)}$, reduces in intensity and shifts to lower temperatures reaching ca. 295 °C for blend PU40/PVC20. At blend PU20/PVC80 the $T_{max(3)}$ is no longer visible, these results are comparable to those of Ha et al., (1997) who also found a decrease in thermal stability of PU with increasing PVC content.

At the PU0/PVC100 blend, the $T_{max(2)}$ peak is observed, this remains stationary as PVC content decreases to blend PU40/PVC60. At the PU60/PVC40 blend the $T_{max(2)}$ decreases in intensity and shifts to higher temperatures, up to 274 °C at blend PU80/PVC20. It is also observed that as PVC content decreases, the $T_{max(1)}$ peak decreases rapidly, disappearing at blend PU40/PVC60.

Sample Description	$T_{5\%}$, °C	$T_{Max(1)}$, °C	$T_{Max(2)}$, °C	$T_{Max(3)}$, °C	$T_{Max(4)}$, °C
PU100/PVC0	271	---	---	375	434
PU80/PVC20	250	---	274	340	448
PU60/PVC40	246	---	270	330	453
PU40/PVC60	230	---	255	295	475
PU20/PVC80	182	150	255	---	475
PU0/PVC100	128	140	255	---	475

Table 6.3: TGA thermal properties of the PU/PVC blends, including the degradation onset temperature, $T_{5\%}$, defined as the temperature at which the sample weight decreases by 5 wt% and the peak centres in the DTG traces, $T_{Max\ (1)}$ to $T_{Max\ (4)}$.

The results of the PU/PVC blends thermograms show that the majority, with the exceptions of PU0/PVC100 and PU20/PVC80 which display early onset THCL, are thermally stable up to ca. 200 °C which is usually high enough for commercial processing, 174 to 194 °C (MatWeb, 2011). It is also observed that as the PVC content increases, the thermal stability of Elasthane decreases at lower temperatures as shown by the decrease of the $T_{max\,(3)}$ peak. These results suggest that PVC is reducing the HS thermal stability, which corresponds to ATR-FTIR results. Although ATR-FTIR data was only collected at room temperature the results indicated a decrease in hydrogen bonding of HS which would most likely result in a decrease in structural stability as temperatures increased. This observation was also observed by Hu (2007) who found that with reduction of urethane linkages, due to PU dilution, caused a reduction in the intra-domain cohesion of PU, causing reduced thermal stability. This effect could potentially be the result of a dilution effect caused by addition of increasing PVC.

6.2.2.2. Differential Scanning Calorimetry

The DSC thermograms obtained on heating of PU/PVC blends used in this study are shown in figure 6.6 and the relevant data is summarized in table 6.4.

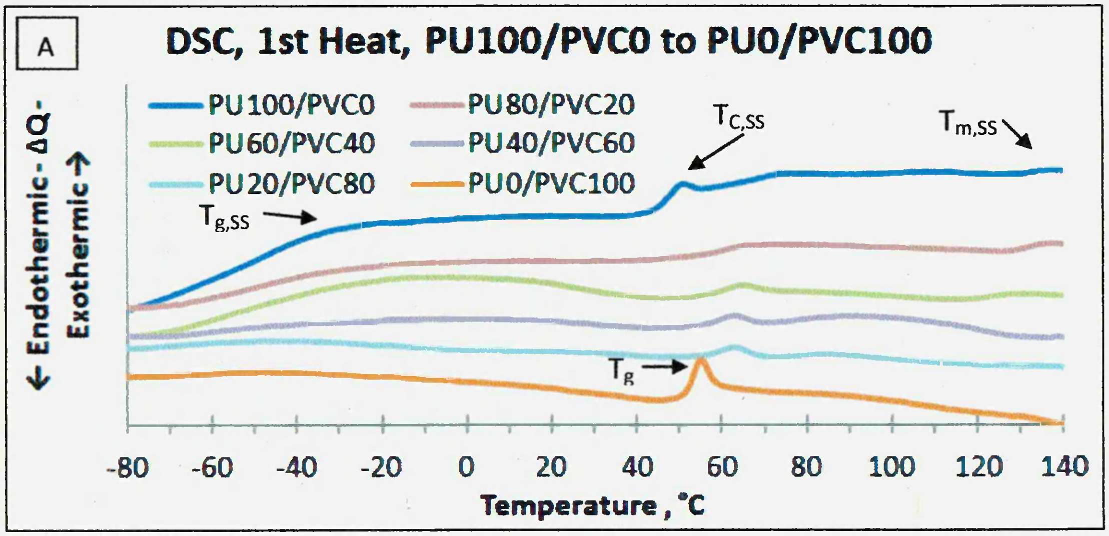

Figure 6.6: DSC thermograms, -80 to 140 °C, of PU/PVC blends A) 1st heating, B) 2nd heating, C) 1st cooling and D) 2nd cooling.

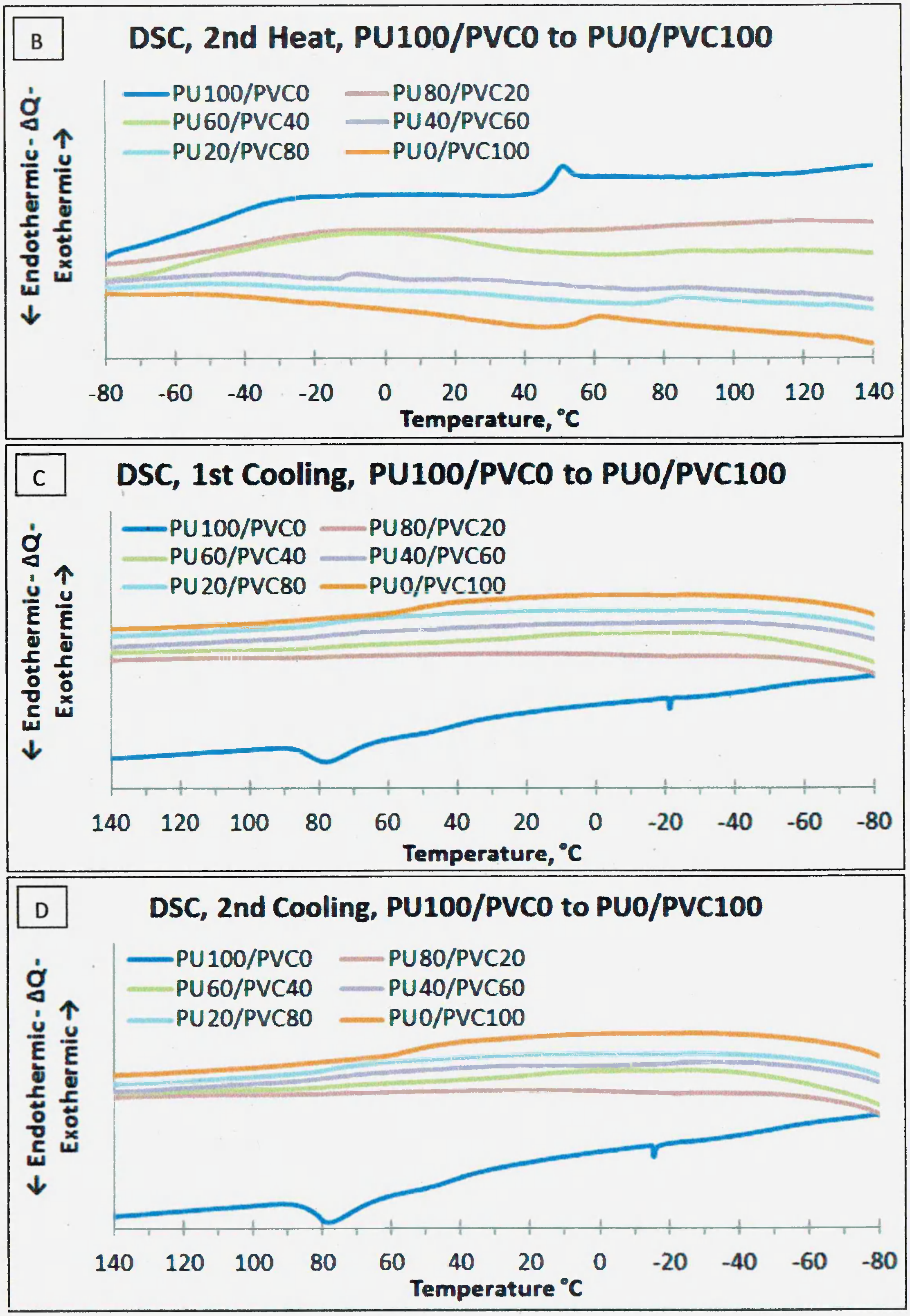

Figure 6.6: DSC thermograms, -80 to 140 °C, of PU/PVC blends A) 1st heating, B) 2nd heating, C) 1st cooling and D) 2nd cooling.

The PU homopolymer, PU100/PVC0 blend, was described in section 5.2.2.2, however the $T_{g,SS}$ can be seen as a lower start temperature was used. During the 1st heating the

PVC homopolymer displays a sharp single T_g at ca. 55 °C with no other peaks up to 140 °C.

The PU/PVC blends during the 1st heating stage display thermal transitions from both homopolymers, Elasthane and PVC, which vary, depending on composition.

As PVC content increases from blend PU100/PVC0 to PU0/PVC100, a reduction in intensity and broadening of the $T_{g,SS}$ occurs between blends PU80/PVC20 to PU40/PVC60, displaying $T_{g,SS}$ at -26, -10 and 0 °C, respectively. The PU20/PVC80 and PU0/PVC100 blends do not show any evidence for the $T_{g,SS}$ of Elasthane. As the PVC is incorporated the $T_{c,SS}$ at 50 °C disappears almost immediately at blend PU80/PVC20 and the emergence of the PVC T_g at 67, 65, 63, 62 and 55 °C, respectively, occurs. This indicates that the PVC is interacting with the PU SS, retarding the PTMO from forming ordered crystalline domains. This disappearance/severe reduction in crystallinity of the PU SS was also observed when Jeong et al., (2001) introduced low levels of PVC into a polyester-based PU.

As the PVC content increases, the suspected $T_{M,SS}$, appears to become broader and shifts to lower temperatures for blends PU80/PVC20 to PU20/PVC80 at 129, 124, 80 and 75 °C, respectively. These results possibly suggest that the PVC is interacting with the SS causing a shift to higher temperatures of the $T_{g,SS}$, a retardation of the SS crystallisation and an earlier onset of the $T_{M,SS}$. These results indicate a partial miscibility of both PVC and PU, due to the shifts of the thermal events, rather than full miscibility, where a single T_g would form and move with composition.

Sample Description	$T_{g,SS}$ °C (1st, 2nd)	$T_{C,SS}$ °C (1st, 2nd)	T_g°C (1st, 2nd)	$T_{M,SS}$ °C (1st, 2nd)
PU100/PVC0	-30, -29	50, 52	---, ---	132, ---
PU80/PVC20	-26, -16	---, ---	67, ---	129, ---
PU60/PVC40	-10, -5	---, ---	65, ---	124, ---
PU40/PVC60	0, ---	---, ---	63, 85	80, ---
PU20/PVC80	---, ---	---, ---	62, 81	75, ---
PU0/PVC100	---, ---	---, ---	55, 62	---, ---

Table 6.4: DSC thermal properties, 1st and 2nd heating and cooling, of PU/PVC blends.

During the 1st cooling phase, figure 6.6 C, as PVC is added to the Elasthane homopolymer, at any content, the crystallisation becomes unobservable. The PVC homopolymer shows a thermal event, possibly a crystallisation of micro-crystal HS domains within the PVC, at 65 °C, this can also be slightly observed in the PU20/PVC80, but is broader and shifted to a higher temperature, 75 °C. At blend PU40/PVC60 the PVC crystallisation becomes unobservable.

On the 2nd heating the PVC homopolymer again showed its characteristic T_g, however it had become broader and the peak had shifted to a higher temperature, 62°C. The shift of the PVC T_g to higher temperatures could imply that it has undergone some mild stripping of the side-chains, initiating the formation of internal double bonds strengthening the main chain at 110 °C. Xiao (1988) observed that the T_g of PVC increases upon annealing, and after 3 hours the T_g = 78 °C.

The PU/PVC blends, during the 2nd heating show thermal transitions from both homopolymers again, blends PU80/PVC20 and PU60/PVC40, show a broadened $T_{g,SS}$ at -16 and -5 °C ,respectively, but it is no longer observed for blend PU40/PVC60. As before in the 1st heating, the PU20/PVC80 blend acts more like the PVC homopolymer, as expected, displaying a PVC T_g. However the T_g is broader, has a reduced intensity and has been shifted to a higher temperature, 62 °C, compared to the T_g of the homopolymer, 55 °C. This trend continues as PVC content decreases down to the PU40/PVC60 blend. No other transitions, including $T_{m,SS}$, were observed during the second heating for any of the PU/PVC blends. During the 2nd cooling similar results to the 1st cooling of PU/PVC blends were recorded.

These results show that as PVC content increases the $T_{g,SS}$ increases, the $T_{C,SS}$ disappears, the PVC T_g appears and the $T_{m,SS}$ shifts to lower temperatures. The appearance of the $T_{C,SS}$ has also been observed in Polyether PU by Hu (2007) and Lin and Chen (1998). This has led to some contradictory discussion regarding polyether PUs, with Hu (2007) reporting it to be an indicator of good phase separation of the HS and SS domains while Lin and Chen (1998) suggested that it as an indicator of poor phase separation of the HS and SS domains. However, the Elasthane homopolymer, section 5.2.4, has a high probability of containing a mixed T_{trans} (Lendlein and Kelch, 2002), which requires a moderately poor phase separation between HS and SS domains, therefore supporting the results of Lin and Chen (1998).

The PVC may contain micro-crystal domains evidenced by the appearance of the re-crystallisation peak occurring during cooling. This was also observed by Yalcin and Cakmak (2004). Potentially the crystallites in PVC can act as HS while the amorphous chains act as SS explaining how it can show shape memory ability. The DSC results for the PU/PVC blends, show that the polymers are partially but not fully miscible. If they were fully miscible a single T_g for each polymer system would be observed that shifts to higher or lower temperature depending on the composition. Therefore as the individual $T_{g,SS}$ and PVC T_g shift to higher and lower temperatures compared to the homopolymers partial mixing appears to have occurred. This corresponds to the ATR-FTIR results which potentially indicated that PVC is interfering via bonding with the PU HS or possibly by diluting the PU HS, as seen by the reduction of the free NH groups in the HS.

6.2.3. Mechanical Properties

6.2.3.1. Dynamic Mechanical Analysis:

The storage modulus, loss modulus and tan δ of the PU/PVC blends, are plotted in figure 6.7 as a function of temperature, -90 to 150 °C, while the dynamic mechanical properties are summarized in table 6.5.

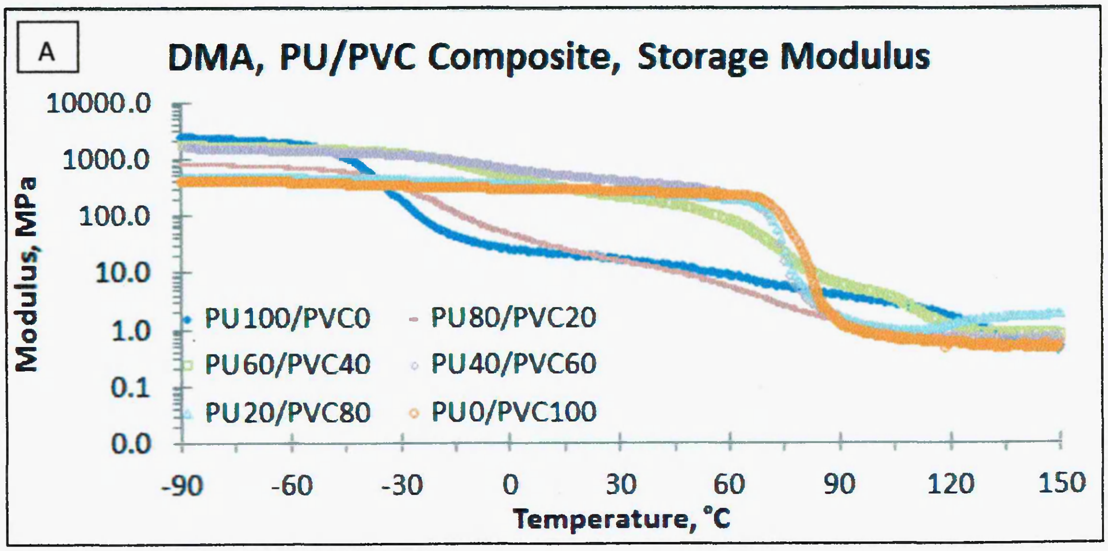

Figure 6.7: DMA data: temperature dependance of A) storage modulus, B) loss modulus and C) tan δ of PU/PVC blends over the temperature range -100 to 150 °C.

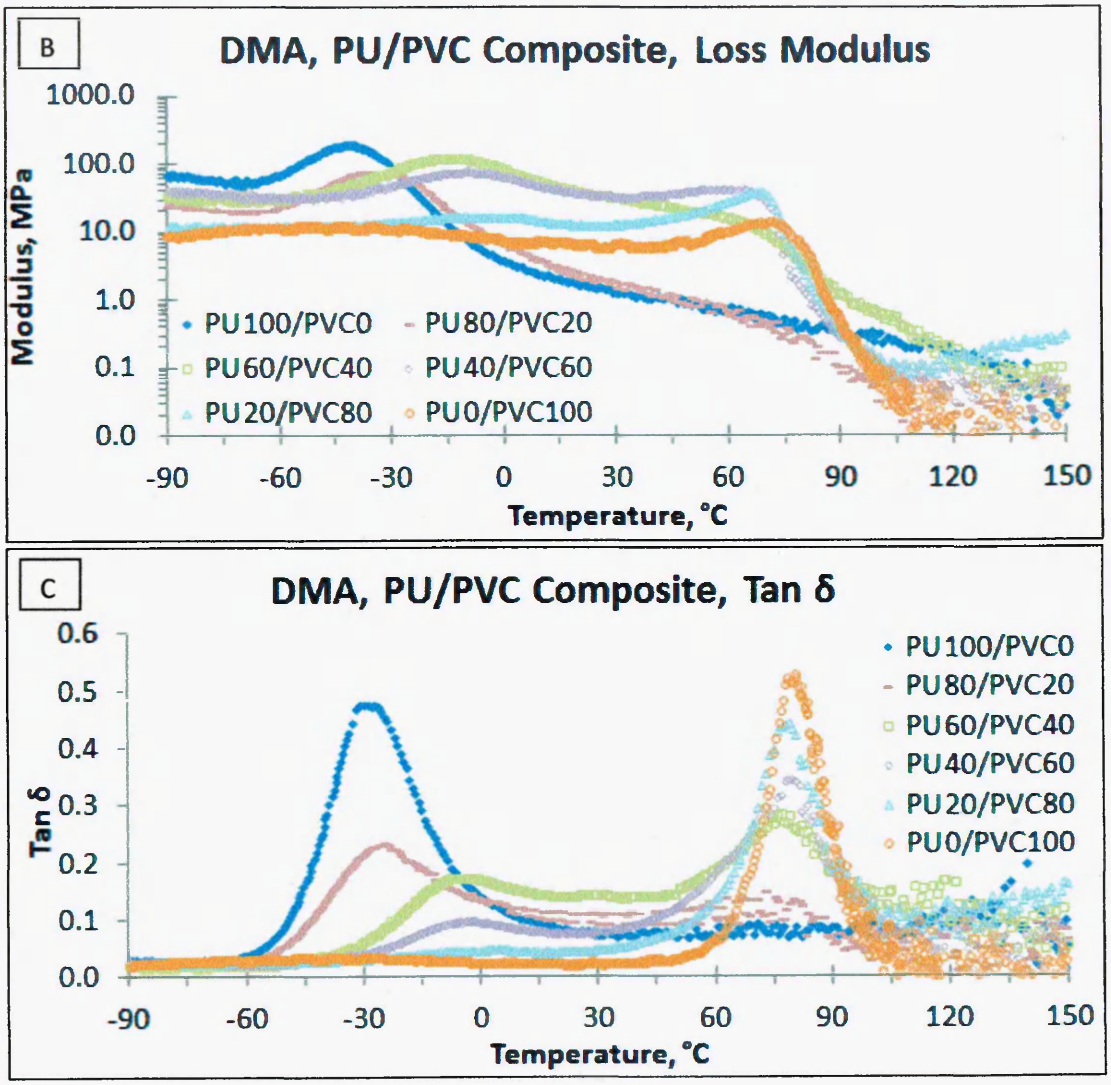

Figure 6.7: DMA data: temperature dependance of A) storage modulus, B) loss modulus and C) tan δ of PU/PVC blends over the temperature range -100 to 150 °C.

The PU homopolymer, PU100/PVC0 blend, was described in section 5.2.3.1.

The PU0/PVC100 blend shows an initial modulus of 412 MPa, significantly lower than that of PU100/PVC0. As temperature increases, from -90 to 70 °C, the storage modulus decreases gradually to 181 MPa. Between 70 and 110 °C the PU0/PVC100 blend undergoes a $T_{g\alpha}$ transition, $T_{g\alpha(2)}$,where the modulus steeply falls to 0.7 MPa. This demonstrates more than two orders of magnitude drop in storage modulus indicating that it will demonstrate SME (Tsai et al., 2007, Du and Zhang, 2010). From 110 to 150 °C the modulus continues to fall reaching, 0.5 MPa. The PU0/PVC100 blend tan δ, tan $\delta_{max(2)}$, was recorded at 81 °C and the intensity was 0.53 tan δ suggesting that a faster shape recovery rate than the PU100/PVC0 blend will occur (Chun et al., 2002, Tsai et al., 2008). No other tan δ peaks were observed.

Sample Description	Storage Modulus, MPa							$T_{g\alpha(1)}$	Tan $\delta_{max(1)}$	$T_{g\alpha(2)}$	Tan $\delta_{max(2)}$
	-90,°C	-50,°C	-10,°C	30,°C	70,°C	110,°C	150,°C				
PU100/PVC0	2414	1439	35	17	6	3	0.5	-29	0.48	---	---
PU80/PVC20	857	677	85	17	4	0.9	0.6	-24	0.23	73	0.15
PU60/PVC40	1723	1479	710	219	39	2	0.9	-5	0.17	77	0.28
PU40/PVC60	1583	1340	850	416	116	0.9	0.8	-2	0.10	78	0.34
PU20/PVC80	493	453	383	269	135	1	2	1	0.05	79	0.44
PU0/PVC100	412	374	310	273	181	0.7	0.5	---	---	81	0.53

Table 6.5: A summary for PU/PVC blends dynamic mechanical values of interest obtained from DMA over temperature range of -90 to 150 °C.

Each PU/PVC blend sample exhibits a DMA profile comparable to its major homopolymer constituent, although each exhibits transitions of both homopolymers to varying degrees of intensity depending on composition. As PVC content increases, from blend PU100/PVC0 to PU0/PVC100, there was a decrease in initial storage modulus from 2414 MPa to 857, 1723, 1583, 493 and 412 MPa, respectively. As the temperature increases from -90 °C, the storage modulus of each blend, PU80/PVC20 to PU20/PVC80, gradually drops until the $T_{g\alpha(1)}$ transition phase is reached where there is a marked loss in storage modulus. All PU/PVC blends demonstrate at least a one order magnitude drop in storage modulus, suggesting each should demonstrate SME (Tsai et al., 2007, Du and Zhang, 2010). After the $T_{g\alpha(1)}$ transition a rubbery plateau is reached where the modulus continues to drop gradually, leading to the $T_{g\alpha(2)}$ transition, where there is another notable loss of storage modulus. After each blend, PU80/PVC20 to PU20/PVC80, passes the $T_{g\alpha(2)}$ transition, the modulus continues to decrease gradually and by 150 °C, is reduced to almost nothing, 0.6, 0.9, 0.8 and 2 MPa, respectively. The tan $\delta_{max(1)}$ and tan $\delta_{max(2)}$ for the blends PU80/PVC20 to PU20/PVC80 were caused by the $T_{g,SS}$ and T_g of the Elasthane and PVC homopolymers, respectively, with tan $\delta_{max(1)}$ values of 0.23, 0.17, 0.10 and 0.05 and tan $\delta_{max(2)}$ intensity values of 0.15, 0.28, 0.34 and 0.44 tan δ, respectively. These results show that as the PVC content is increased the tan $\delta_{max(1)}$ is reduced in intensity and the tan $\delta_{max(2)}$ gradually increases in intensity, as expected. This suggests that the majority of shape recovery will occur due to the phase with the more intense tan δ peak in the system. Chun et al., (2002) observed that the greater the intensity of the tan δ peak the better the shape recovery rate will be.

The DMA values for the storage modulus, loss modulus and tan δ suggest that addition of PVC causes a reduction of the initial storage and loss modulus for the PU100/PVC0 blend but from the PU60/PVC40 blend onwards, after the tan $\delta_{max(1)}$ transition, the storage modulus remains higher than that for the PU100/PVC0 blend up to the $\delta_{max(2)}$ transition after which the storage modulus decreases significantly. This could indicate that although the PU/PVC blends cannot store as much energy as the Elasthane homopolymer, they do retain a larger energy in the intermediate rubbery plateau between 0 and 60 °C, the proposed working range of the polymer, before $\delta_{max(2)}$. The tan δ results indicate PU/PVC blends will demonstrate SME and that although Elasthane is not fully miscible with PVC, they are partially miscible as evidenced by the movement of the individual tan δ peaks to higher or lower temperatures depending on composition. This observation corresponds well with the previous DSC results which also indicated partial miscibility. Parnell and Min (2005), reported that some polyether PU, PTMO based SS, when mixed with PVC could be characterised as partially blended i.e. where two components spontaneously mix but do not form a single, thermodynamically stable phase. Xiao et al., (1988) made similar observations with regards to incorporation of PVC into a PTMO based PU suggesting that only a limited amount of PVC can be miscible with the PU, specifically the PU SS domains, leaving the rest to form separate PVC domains. This relates to results from Jeong et al., (2001), who found that when polyester PUs are blended with phenoxy resin, a miscible polymer, there will be a drop in glassy modulus and rubbery modulus of the host polymer due to some of the HS being dissolved into the SS. This effect could explain the drop in glassy modulus of the PU/PVC blends as PVC content increases.

6.2.4. Shape Memory Effect Testing

6.2.4.1. Unconstrained Shape Memory Effect Evaluation

SME was carried out in order to assess whether increasing the PVC content enhances or reduces the SME of Elasthane, figure 6.8. As previously described in section 5.2.4, Elasthane can display mixed T_g phenomenon; therefore an appropriate SME temperature range needs to be adopted. For Elasthane the mixed T_g will be between the $T_{g,SS}$, ca. -29.4 °C, and the $T_{g,HS}$, ca. 90 to 100 °C (Lin and Chen, 1998), having a T_{low}

at 0 to 5 °C and a T_{high} at 90 °C should provide an adequate SME range for all the PU/PVC composites, as the T_{high} is also above the PVC T_g. In order to view only the PVC effect on the shape memories of each PU/PVC blend, the PU/PVC blends were annealed at 150 °C for 15 minutes prior to being tested. Each blend was deformed and their recovery determined as described in the section 2.1.6, figure 2.15. The SME properties of interest are summarized in table 6.6.

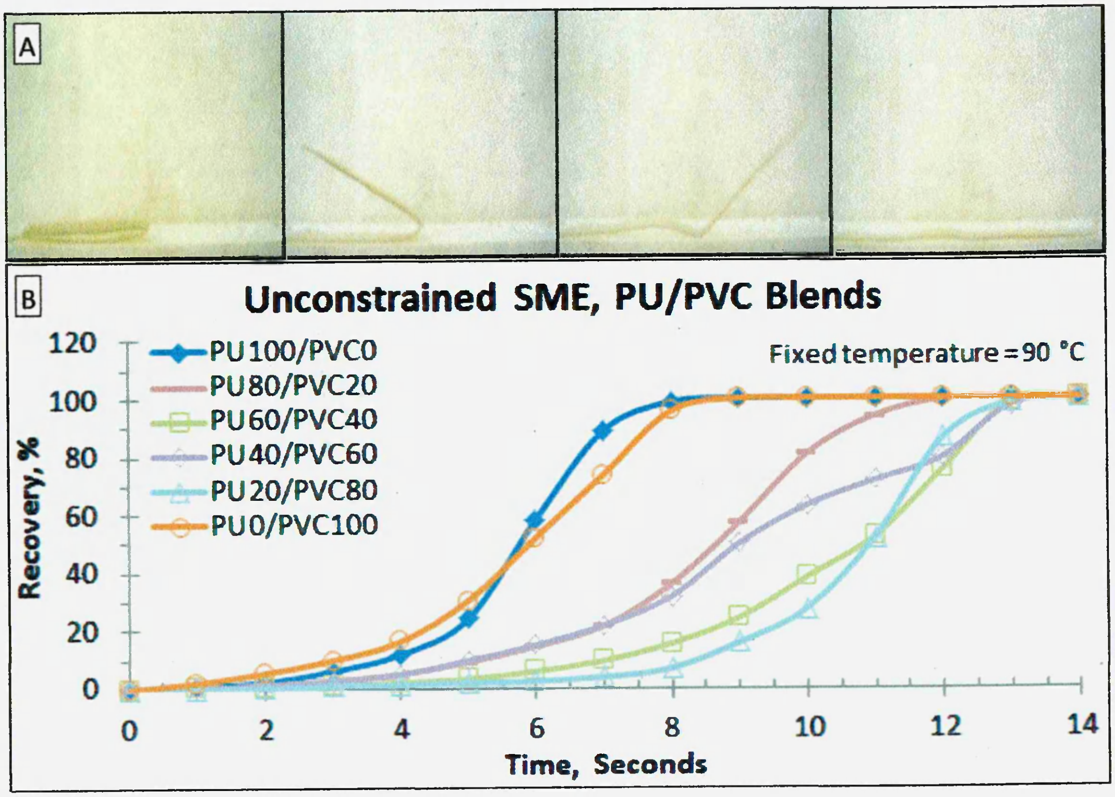

Figure 6.8: Unconstrained SME testing of PU/PVC blends 0 to 100 wt% PVC, from temporary to permanent shape, A) still images of a PU/PVC blended SMP at sequential intervals, B) plotted against time at a fixed temperature, 90 °C.

The PU100/PVC0 blend exhibited a $\theta_{Max,}$ of 100 %, demonstrating that it is elastic enough to accommodate a high level of deformation stress, a desirable property for a SMP. After the deformation constraint was removed, the sample was left at room temperature ca. 22 °C, an amount of recovery occurred, leading to a θ_{Fixed} of ca. 87 %. This demonstrates that the PU100/PVC0 blend is not strong enough to maintain the full load of stored stress within the SS at room temperature, and potentially means that shape memory recovery will be high (Jang et al., 2008).

The $\theta_i(T)$ was recorded every 1 second until the PU100/PVC0 blend reached its θ_{Final}, 100 %. This demonstrates that although not all the deformed strain was stored at room temperature, there is still enough to return it to its original shape during SME evaluation.

In order to further assess the PU100/PVC0 blend shape memory ability the $\theta_{1/2\ Final}$ and θ_{Final} time of recovery, 5.7 and 8.0 seconds, respectively, were recorded. These results indicate that the SME of the PU100/PVC0 blend recovers 50 % in ca. ¾ of the full recovery time. These results are different to the prior results obtained for Elasthane homopolymer, section 5.2.4, this indicates that the rate of recovery of shape memory varies depending on sample thickness. This however appears to not affect the θ_{Max}, θ_{Fixed} or θ_{Final} results as there were no significant changes to the Elasthane homopolymer when compared to a previous SME test, section 5.2.4, except for rate of recovery.

The PU0/PVC100 blend was deformed to a θ_{Max} of 100 %, after deformation strain was applied and the deformation constraint was removed the θ_{Fixed} was recorded at 100 %. These results indicate that, like Elasthane, PVC demonstrates an elastic characteristic that allows maximum deformability. It also displayed an improved ability over Elasthane to maintain the temporary shape, potentially caused by the finely dispersed crystallite like HS dispersed in the amorphous SS like phase (Yalcin and Cakmak, 2004), which Jeong et al., (2001) reported allows increased shape retention in SMP. The $\theta_i(T)$ was recorded every 1 second until PVC reached its maximum θ_{Final}, 0 %. Overall PVC demonstrated that it can sustain a temporary shape at room temperature and return to its original shape when SME evaluation is carried out. PVC $\theta_{1/2\ Final}$ and θ_{Final} time of recovery were also recorded, at 6.0 and 8.0 seconds, respectively, demonstrating that like the PU100/PVC0 blend it also takes ca. ¾ of the overall shape memory recovery time to recover 50% of the original shape.

The PU80/PVC20 to PU20/PVC80 blends displayed a θ_{Max} of 100 %, the same as the homopolymers indicating that regardless of PVC content Elasthane displays no reduction in elasticity or ability to accommodate a high level of deformation stress. The θ_{Fixed} values were recorded at, 92, 99, 100 and 100 %, respectively, which suggests that as the PVC content increases it positively affects shape retention.

There are several potential explanations for this with the most likely being that the PVC has partially mixed with the PU SS and has raised the $T_{g,SS}$, as seen in the DMA and

DSC results, allowing a better retention of applied stress at room temperature. Alternatively with increasing PVC content, the HS bonding is reduced, causing smaller HS domains to be formed, increasing the amount of HS distributed in the SS, this finer distribution of HS previously reported by Jeong et al., (2001) causes an enhanced fixed structure throughout the polymer matrix. Another possibility is that the regions of pure PVC, which have a higher T_g, are forming a continuous network which, due to a higher T_g, adds additional constraints to the SS chain motion of the polymer blend, resulting in an enhanced shape retention (Meng and Hu, 2009).

The $\theta_{1/2Final}$ and θ_{Final} time of recovery vary dramatically from the homopolymers, with $\theta_{1/2Final}$ times of 8.5, 11.0, 9.0 and 11.0 seconds, respectively and θ_{Final} times of 12.0, 13.0, 13.5 and 13.5 seconds, respectively. The $\theta_{1/2Final}$ time and θ_{Final} time of recovery results seem to indicate that when PVC is blended with PU, PVC actively retards the SME of PU, while when PU is blended with PVC, the PU also retards the SME of PVC. This suggests that both PU and PVC are interfering with each other, possibly by altering the amount of energy that can be released for shape memory recovery, possibly due to altering shape retention abilities (Jeong et al., 2001, Meng and Hu, 2009). However as PU or PVC content increases it does not appear to hinder the overall shape recovery, as each sample returned to its original shape.

Sample Description	θ_{Max}, %	θ_{Fixed}, %	$\theta_{1/2Final}$, %	θ_{Final}, %	$\theta_{1/2Final}$ Time, sec	θ_{Final} Time, sec
PU100/PVC0	100	87	50	0	5.5	8.0
PU80/PVC20	100	92	50	0	8.5	12.0
PU60/PVC40	100	99	50	0	11.0	13.0
PU40/PVC60	100	100	50	0	9.0	13.5
PU20/PVC80	100	100	50	0	11.0	13.5
PU0/PVC100	100	100	50	0	6.0	8.0

Table 6.6: Summary of unconstrained SME evaluation results observed from the PU/PVC blends, recording the θ_{Max} %, θ_{Fixed} %, $\theta_{1/2Final}$ %, and θ_{Final} %, plotted against time at a fixed temperature, 90°C.

The results observed from unconstrained SME evaluation showed that overall addition of any PVC content to Elastane causes an increase in θ_{Fixed} and an increase in $\theta_{1/2Final}$ and θ_{Final} time. Under standard circumstances it would be expected for the PU80/PVC20 to PU20/PVC80 blends, to have results between the two homopolymers, as anticipated from the T_g behavior of table 6.4 and 6.5. However the PU80/PVC20 to PU20/PVC80 blends showed greater resistance than the homopolymers to the external temperature before recovering their original shape, this could possibly be explained by the blended samples maintaining a higher average level of storage modulus, as seen in the DMA results, throughout the temperature range, -90 to 150 °C, compared to either homopolymer, possibly indicating that energy will be retained to a greater degree during SME. Alternatively as reported in the literature, due to the blending of both homopolymers the shape fixity is increased and therefore the release of energy for SME recovery is retarded (Jeong et al., 2001, Meng and Hu, 2009). The SME results correspond to the results predicted from the DMA data which suggested that the PU80/PVC20 to PU20/PVC80 blends will show SME and that the blended samples will display a reduction in the shape memory recovery rate as shown by DMA, figure 6.7, with the decreased intensity of the tan $\delta_{max(1)}$ and tan $\delta_{max(2)}$ peaks, which has been suggested by Chun et al., (2002) who observed that the greater the intensity of the tan δ peak the better the shape recovery rate will be.

6.3. PU/PVC Blend Summary

The effects of blending PVC with Elasthane, PU, was studied to assess if addition of PVC would improve or reduce the shape memory properties of PU, in order to fulfil the aim of creating a mechanically and thermally stable SMP packaging solution. The resulting blends were characterised for homogeneity, thermal and mechanical properties including SME.

Overall blending Elasthane with PVC was found to be beneficial as it appears to create a more thermally stable polymer system that shows good shape memory ability while exhibiting a greater overall storage modulus compared to the original homopolymers. However the PU/PVC blended samples still show the classic shortcomings of SMP, especially when compared to SMAs i.e. low mechanical strength.

One of the immediate methods to reinforce the SMP blend is by using high modulus fillers i.e. clay. Incorporation of Laponite into Elasthane, chapter 5, allowed the thermal and mechanical properties to be tailored. However the effect of dispersing Laponite into a blend of Elasthane and PVC may provide significantly different results. In order to evaluate the effects of clay reinforced PU/PVC blends, the PU60/40PVC blend, which displayed enhanced thermal properties, greater overall storage modulus compared to the parent homopolymers with improved shape fixity and good shape memory recovery, was chosen as the host polymer in which to incorporate Laponite with the aim to produce a SMP blend nanocomposite.

6.4. PU/PVC/Lap Composite Results

6.4.1. Homogeneity

6.4.1.1. X-Ray Diffraction

The XRD trace in the region 2 to 45 ° 2θ for the PU/PVC/Lap 0 to 5 composites, were carried out in order to assess the state of dispersion of Laponite in the PU/PVC host polymer matrix, figure 6.9.

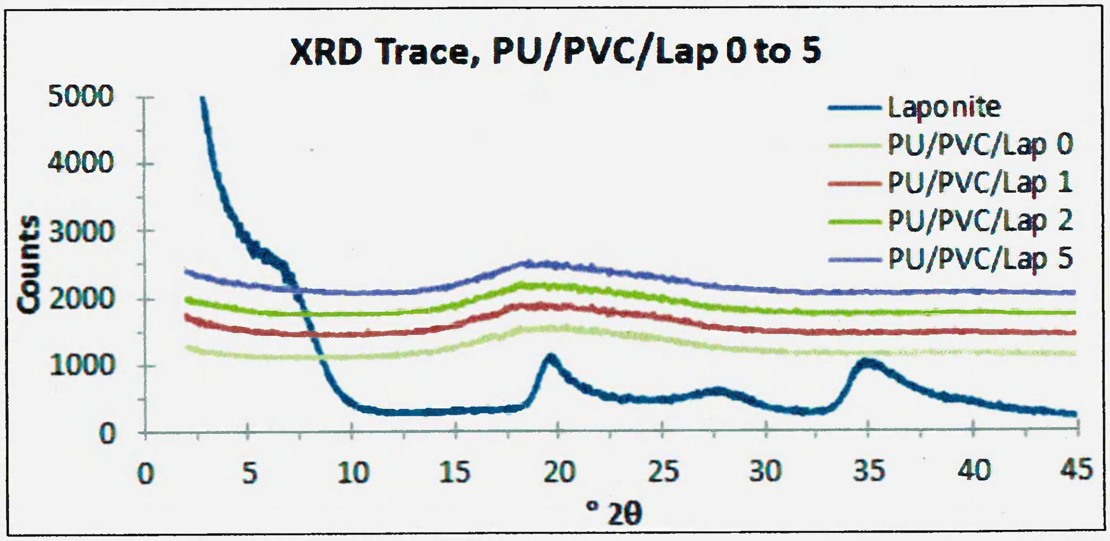

Figure 6.9: XRD trace of PU/PVC/Lap 0 to 5 composites.

The XRD trace of Laponite powder displayed peaks at, 6.0 °2θ (14.7 Å), 19.8 °2θ (4.7 Å), 28.0 °2θ (3.3 Å) and at 35.2 °2θ (2.6 Å), these peaks correspond to d001, 110, 101, and 130 reflections, respectively. This is what would be expected from an unorientated Laponite (Mishraet al., 2008, Vicente et al., 2010). The XRD trace of the PU/PVC/Lap 0 composite shows a broad peak, observed from 12.5 (7.1 Å) to 29.2 (3.1 Å) with no other observable peaks. This diffraction pattern is similar to that of pure Elasthane, section 5.2, figure 5.7, where a broad peak, from 2θ value 15 (5.9 Å) to 37° (2.4 Å) with no other peaks observed, caused by its overall amorphous or quasi crystalline nature.

The XRD traces for the PU/PVC/Lap 1 to 5 composites exhibit XRD-silent traces. As Laponite is small in size, ca. 25 nm, and has weak reflections due to imperfect platelet registration the 110, 101 and 130 peaks would be expected to be hidden by the broad diffraction halo of the PU60/PVC40 blend host matrix. The absence of diffraction peaks in the PU/PVC/Lap 1 to 5 composites indicates that the clay is well dispersed in the polymer blend host. Previous literature, regarding PVC nanocomposites, where Na-

MMT was dispersed into PVC and reported no clay peaks at up to 7.5 wt% (Yang et al., 2006) and PU nanocomposites, where Laponite was dispersed into an Elasthane host and showed no clay peaks at up to 4 wt% Laponite content. Overall the Laponite appears to be well dispersed within the PU60/PVC40 blend host polymer with results suggesting that Laponite dispersal is greater than in the Elasthane homopolymer previously studied.

6.4.1.2. ATR-FTIR Spectroscopy

ATR-FTIR spectra for the PU/PVC/Lap 0 to 5 composites, concentrating on the major NH absorption peaks, ca. 3315 cm^{-1}, and carbonyl peaks, ca. 1700 cm^{-1}, are presented in figure 6.10. This work was carried out in order to assess the state of clay delamination in the PU/PVC host polymer.

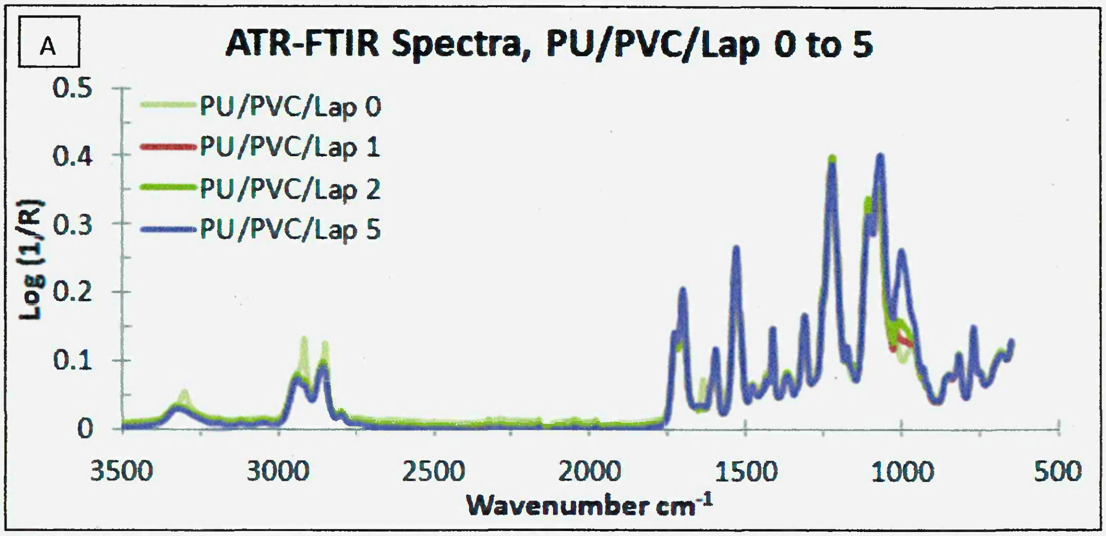

Figure 6.10: ATR-FTIR spectra of the PU/PVC/Lap 0 to 5 composites, A) full ATR-FTIR spectrum, B) SiO stretching region, C) NH stretching vibration absorption, and D) Carbonyl stretching vibration absorption.

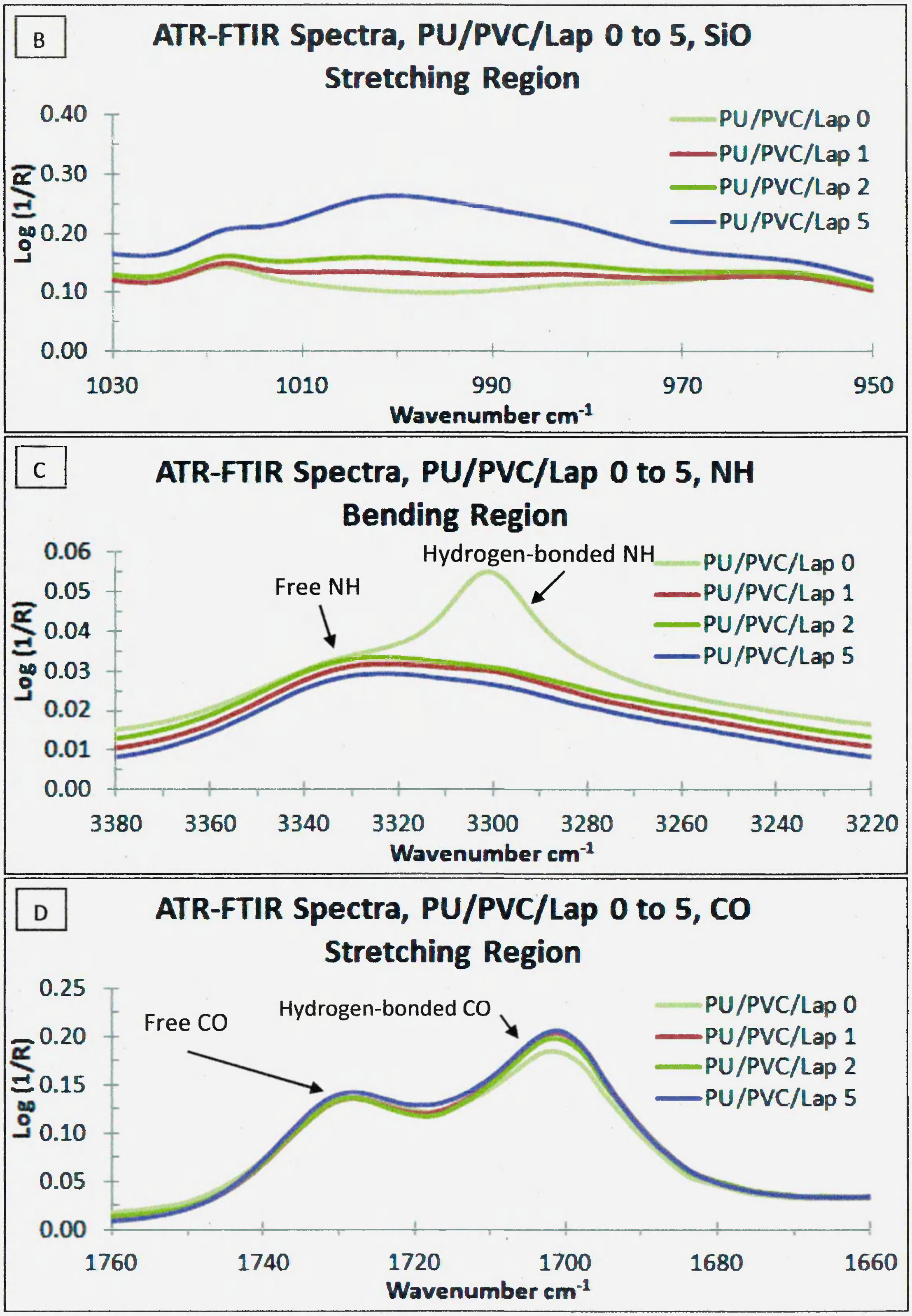

Figure 6.10: ATR-FTIR spectra of the PU/PVC/Lap 0 to 5 composites, A) full ATR-FTIR spectrum, B) SiO stretching region, C) NH stretching vibration absorption, and D) Carbonyl stretching vibration absorption.

For the PU/PVC/Lap 0 composite, in the high frequency region, ca. 3400 to 2700 cm^{-1} the peaks of interest are the NH absorption peaks relating to the hydrogen-bonded NH, ca. 3298 cm^{-1}, and the free NH, ca. 3332 cm^{-1}. At lower frequency, ca. 1800 to 1000 cm^{-1} the peaks of interest are the carbonyl stretching peaks relating to the free, 1728 cm^{-1}, and bonded, 1702 cm^{-1}, carbonyl groups. At frequencies, 900 to 600 cm^{-1}, IR bands due to aromatic C-H bend, minor aliphatic C-C stretch and PVC alkyl halide C-Cl stretch, 780 cm^{-1}, vibrations are observed.

As Laponite increases from 0 to 1 wt% the free NH intensity displays no significant change while the hydrogen-bonded NH considerably reduces becoming a small shoulder on the free NH peak. It was found previously, section 5.2, figure 5.11 A, that as Laponite content increased in an Elasthane homopolymer, the hydrogen-bonded NH peak decreased in intensity gradually, but remained more intense than the free NH peak, which remained constant. In the PU/PVC/Lap composites, with addition of 1 wt% Laponite, there is a marked decrease in hydrogen-bonded NH, below the intensity of the free NH, with no further changes in intensity with additional Laponite content. These results suggests that even with a low loading of Laponite there is a greater influence on the NH bonding ability of the HS of Elasthane in the PU60/PVC40 blend than in the Elasthane homopolymer. This result may be caused by the combination of the PVC and Laponite platelets interfering with the HS bonding. Both PVC and Laponite retard the HS hydrogen bonding individually (Xiao et al., 1987) so together a commutative effect may occur causing a greater drop in hydrogen-bonded NH intensity.

As Laponite content increases the free, 1728 cm^{-1}, and bonded 1702 cm^{-1}, carbonyl groups do not significantly alter in intensity, similar to the Elasthane nanocomposites, section 5.2.1.2, figure 5.11 B. This indicates that the Laponite is having no greater effect on the CO stretching when Elasthane is incorporated with PVC. In the silicon oxygen, Si-O, stretch vibration region, ca. 1000 cm^{-1}, due to masking by the PU/PVC host polymer, there is only a single peak observed, figure 6.10 B. As reported by Ijdo et al., (2006) stacking of clays causes broadening of the Si-O peaks causing an overlap of the in-plane and out-of-plane Si-O bands, generating a single broad peak. Conversely, the absorption bands narrow as the clay platelets become delaminated and the individual absorption bands become better resolved, generating two narrow peaks.

Therefore in order to clarify the dispersion of the clay platelets the PU/PVC/Lap 0 spectrum was subtracted from the PU/PVC/Lap 1 to 5 spectra, figure 6.11.

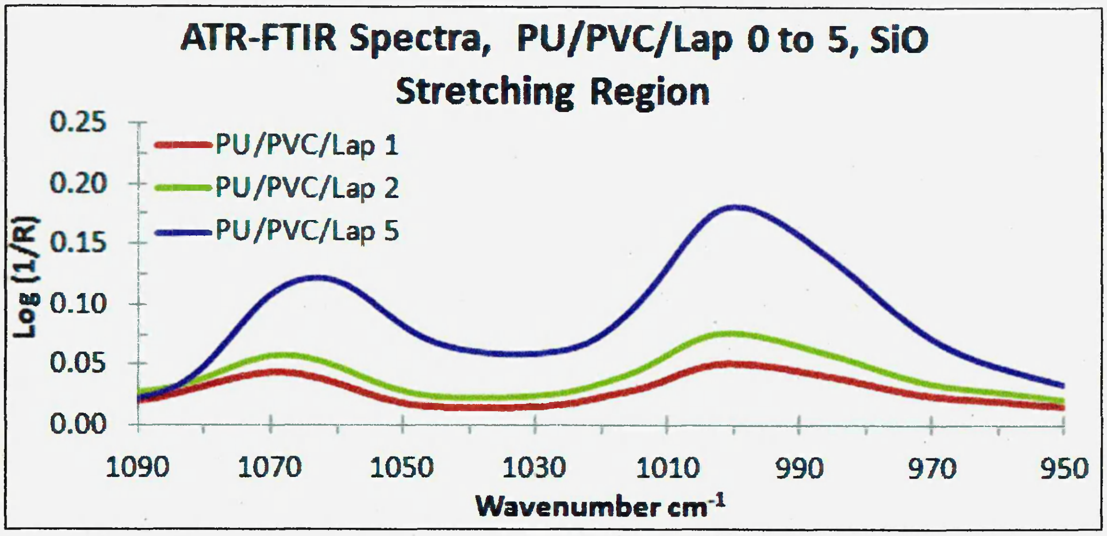

Figure 6.11: ATR-FTIR subtracted spectra of the PU/PVC/Lap 1 to 5 composites SiO stretch region, in-plane and out-of-plane Si-O absorption.

The subtracted spectra revealed two individual peaks for each PU/PVC/Lap 1 to 5 composite, Si-O bonds, in-plane and out-of-plane, ca. 1000 and ca. 1068 cm^{-1}, respectively, rather than a single broad peak. Ijdo observed that for hectorite clay layers to be fully delaminated the distance at the FWHM for the in-plane Si-O peak should be ca. 28 to 29 cm^{-1} (Ijdo et al., 2006). The FWHM for PU/PVC/Lap 1 to 5 was 31.0, 32.0 and 36.0 cm^{-1}, respectively, which corresponds to ca. 65, 55, and 37 % clay delamination. These results indicate that as Laponite content increases the delamination decreases, however Ijdo et al., also reports the IR technique is not very sensitive to high levels of delamination but more so at low levels. These results demonstrate that the PU/PVC/Lap 1 and 2 composites are partially exfoliated, and the PU/PVC/Lap 5 composite is intercalated (Ijdo et al., 2006).

It was also observed that as Laponite content increases, 1 to 5 wt%, the out-of-plane Si-O peak shifts to a lower wavelength, 1074, 1070 and 1064 cm^{-1}, respectively, this was not observed as Laponite content increased in the Elasthane homopolymer. These results indicate that there is a significant effect of PVC on the dispersion of Laponite in Elasthane. This could possibly be due to Laponite, which reportedly is hydrophilic and therefore compatibilises with more polar polymers (Essawy et al., 2008), preferentially

incorporating in the polar HS of the PU first, then the intermediate polar PVC followed by the SS of the PU.

The ATR-FTIR results overall suggest that in the PU60/PVC40 matrix, the PVC has a definite impact on the way Laponite is dispersed in the Elasthane HS and SS phase due to the intermediate polarity of the PVC (Essawy et al., 2008). This is evident by the differing effects of Laponite on the NH bending vibrations as well as the SiO stretching vibrations which all differ to the effect of Laponite observed in the Elasthane homopolymer. PVC also appears to affect how well Laponite is dispersed at 1 wt%, as ATR suggests that less delamination occured in the PU/PVC/Lap composites compared to the PU/Lap composites.

6.4.2. Thermoanalytical Results

6.4.2.1. Thermal Gravimetric Analysis

To study the effects of thermal degradation on the PU/PVC/Lap 0 to 5 composites, TGA thermograms and their derivatives are presented in figure 6.12 and the temperatures of interest are summarized in table 6.7.

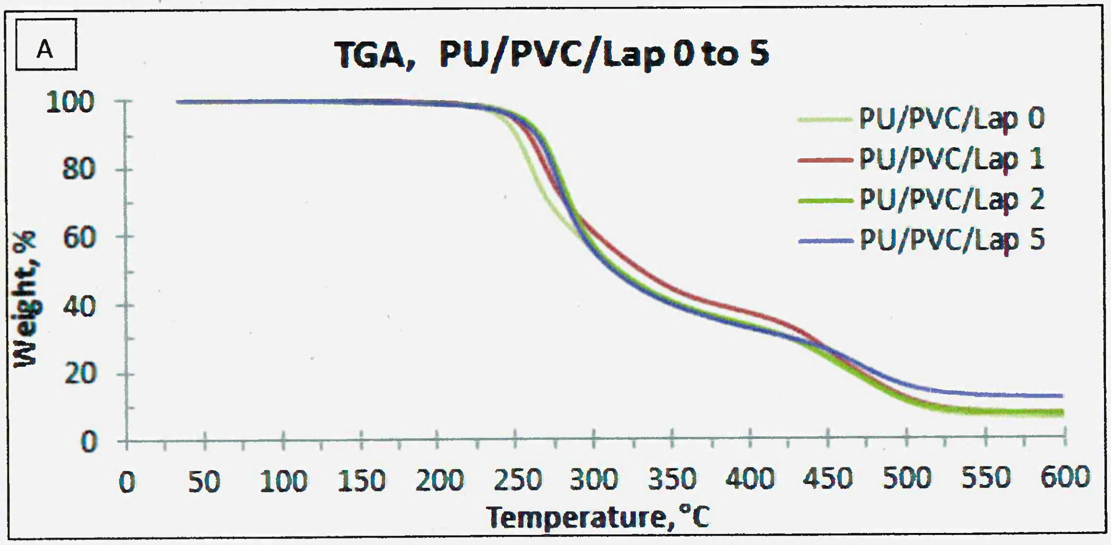

Figure 6.12: PU/PVC/Lap 0 to 5 composites A) TGA and B) DTG thermograms, from 35 to 600 °C.

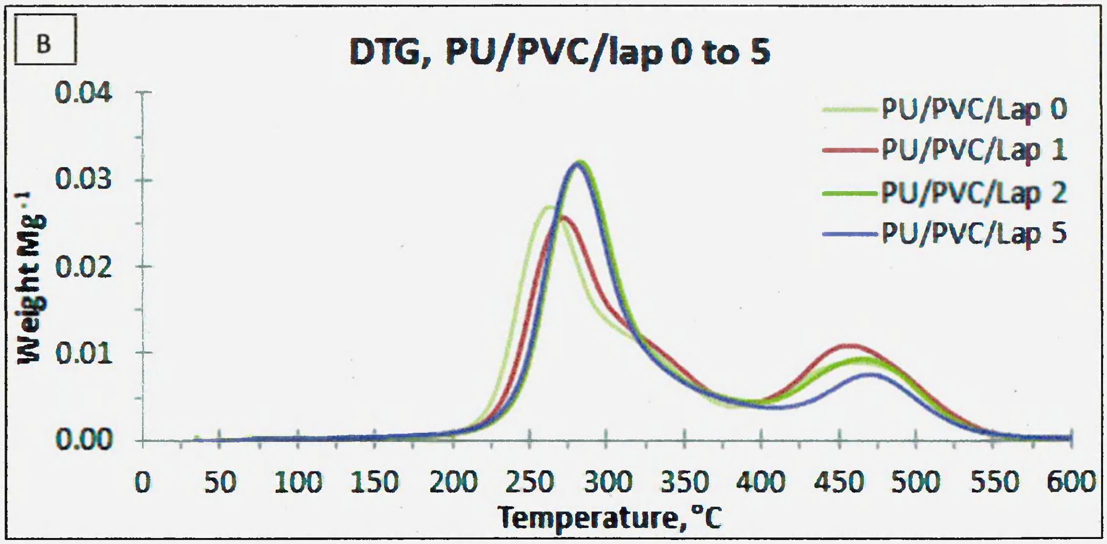

Figure 6.12: PU/PVC/Lap 0 to 5 composites A) TGA and B) DTG thermograms, from 35 to 600 °C.

The DTG for the PU/PVC/Lap 0 composite shows a three step, $T_{Max(1)}$ to $T_{Max(3)}$, decomposition profile, at 265, 320 and 472 °C respectively, and displays no signs of early onset THCL, typically observed with the PVC homopolymer, ca. 100 °C to 200 °C, while the $T_{5\%}$ is observed at 241 °C. The 1st degradation stage is due to the rapid weight loss of the PVC phase caused by major chain stripping, this process initiates internal cross-linking of the main PVC chain enhancing char formation producing a carbon rich, hydrogenated char residue (Fisch and Bacaloglu, 1995, Wilkes, et al., 2005). The 2nd degradation stage is attributed to the degradation of the Elasthane HS. The final, 3rd, degradation stage is caused by a combination of the PVC phase hydrogenated char degradation and the complete degradation of the Elasthane SS phase which both occur in a similar temperature range (Ferguson and Petrovic, 1976, Shieh et al., 1999).

All the PU/PVC/Lap 1 to 5 composites show a similar thermal profile to the PU/PVC/Lap 0 composite, all showing no signs of THCL and having either a two or three-step decomposition profile. The PU/PVC/Lap 1 composite shows a similar profile as the PU/PVC/Lap 0, having a three step thermal decomposition profile, but also displays a later onset of $T_{5\%}$, 248 °C, a higher $T_{Max(1)}$, 274 °C, and $T_{Max(2)}$, 325 °C, as well as a lower temperature, but more intense, peak at $T_{Max(3)}$, 455 °C.

Both the PU/PVC/Lap 2 and 5 composites were also comparable to the PU/PVC/Lap 0 composite but both only have a two-step thermal decomposition profile. Both PU/PVC/Lap 2 and 5 composites, respectively, have an increased $T_{5\%}$, 252 and 249 °C, an increased $T_{Max(1)}$, 281 and 281 °C, and a lower temperature, but a more intense peak at $T_{Max(3)}$, 461 and 461 °C.

Sample Description	$T_{5\%}$, °C	$T_{Max(1)}$, °C	$T_{Max(2)}$, °C	$T_{Max(3)}$, °C
PU/PVC/Lap 0	241	265	320	472
PU/PVC/Lap 1	248	274	325	455
PU/PVC/Lap 2	252	281	---	461
PU/PVC/Lap 5	249	281	---	461

Table 6.7: TGA and DTG thermograms, 35 to 600 °C, thermal properties of interest of the PU/PVC/Lap 0 to 5 composites.

These results show that as Laponite content increases it reinforces the PU/PVC polymer matrix at lower temperatures as evidenced by the shift to higher temperatures of $T_{5\%}$, $T_{Max(1)}$ and $T_{Max(2)}$, but at higher temperatures does not, as shown by the reduced intensity and shift to lower temperatures of the $T_{Max(3)}$ peak. The reduction and shift of the $T_{Max(3)}$ peak is opposite to the effect observed by Mishra et al., (2008) and Liff et al., (2007) when Laponite was dispersed in a polyether PU. This potentially demonstrates the effects of blended PVC. As Laponite content increases, the $T_{Max(2)}$, degradation of the HS, is pushed to higher temperatures at 1 wt% Laponite but becomes unobservable at 2 and 5 wt% Laponite, demonstrating that at 1 wt% Laponite there was an enhancement of the thermal stability of the Elasthane HS. The disappearance of the $T_{Max(2)}$ peak in the PU/PVC/Lap 2 and 5 composites suggests that the Laponite has caused a reduction in the thermal stability of the Elasthane HS phase causing it to be hidden by the $T_{Max(1)}$ peak. This corresponds to the ATR-FTIR results which indicated a decrease in hydrogen bonding of the HS and therefore potentially structural stability. However the ATR-FTIR results were gathered at ca. 22 °C and may not reflect the polymer structure at higher temperatures, as seen with the TGA data. Hu (2007) observed that with fewer urethane linkages, therefore reduced hydrogen bonding, caused the intra-domain cohesion of PU to decrease, reducing its thermal stability. This could potentially be a result of the dilution effect caused by the PVC content and addition of increasing amounts of Laponite. These results also correspond to pure polyurethane nanocomposites; Mishra et al., (2008) and Liff et al., (2007) found that as the Laponite content increased the $T_{Max(2)}$ decreased. Also it was found in

PVC nanocomposites by Awad et al., (2009) that as hectorite content increased the internal cross-linking of the main PVC chain was retarded which corresponded to a rise in thermal stability of $T_{Max(1)}$. However as the Laponite content increases it causes a slight reduction in the $T_{Max(3)}$ peak, This indicates that Laponite is most probably interacting with the PVC phase, potentially causing the shift of $T_{Max(3)}$ to lower temperatures due to the retardation of the initial internal cross-linking of the main PVC chain. This would have caused less hydrogenated char to be produced and the chain scission reaction that occurs at higher temperatures ca. 445 °C would easily volatilize the less compacted hydrogenated char present (Awad et al., 2009, Wilkes et al., 2005). As expected the amounts of char remaining at 600 °C increased as the Laponite wt% increased.

6.4.2.2. Differential Scanning Calorimetry

The DSC thermograms obtained on heating and cooling of the PU/PVC/Lap 0 to 5 composites used in this study are presented in figure 6.13 and the thermal properties of interest are summarized in table 6.8.

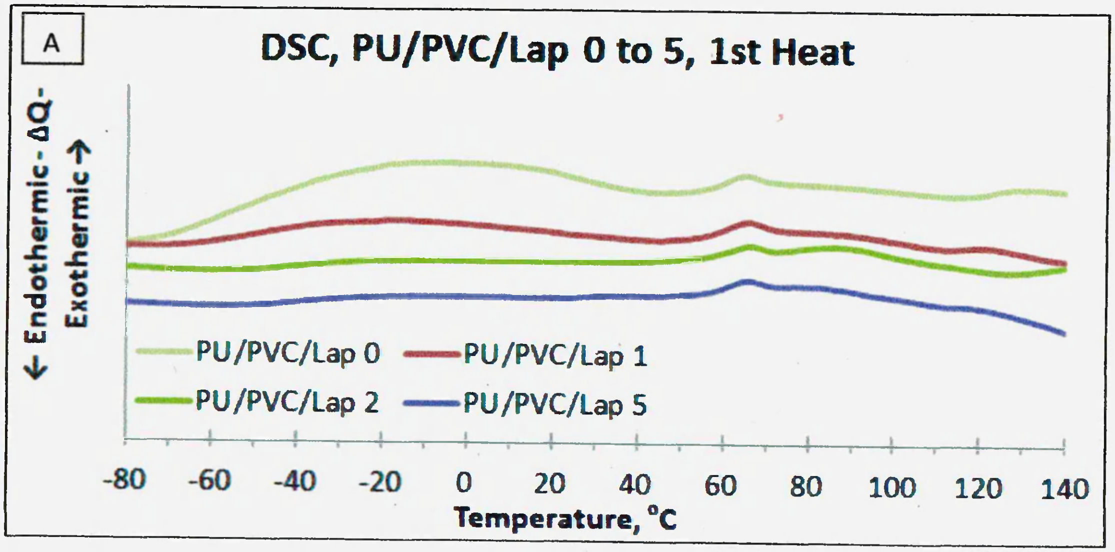

Figure 6.13: DSC thermograms of the PU/PVC/Lap 0 to 5 composites obtained on heating and subsequent cooling, -80 to 140 °C, A) 1st Heating, B) 2nd Heating, C) 1st Cooling and D) 2nd Cooling.

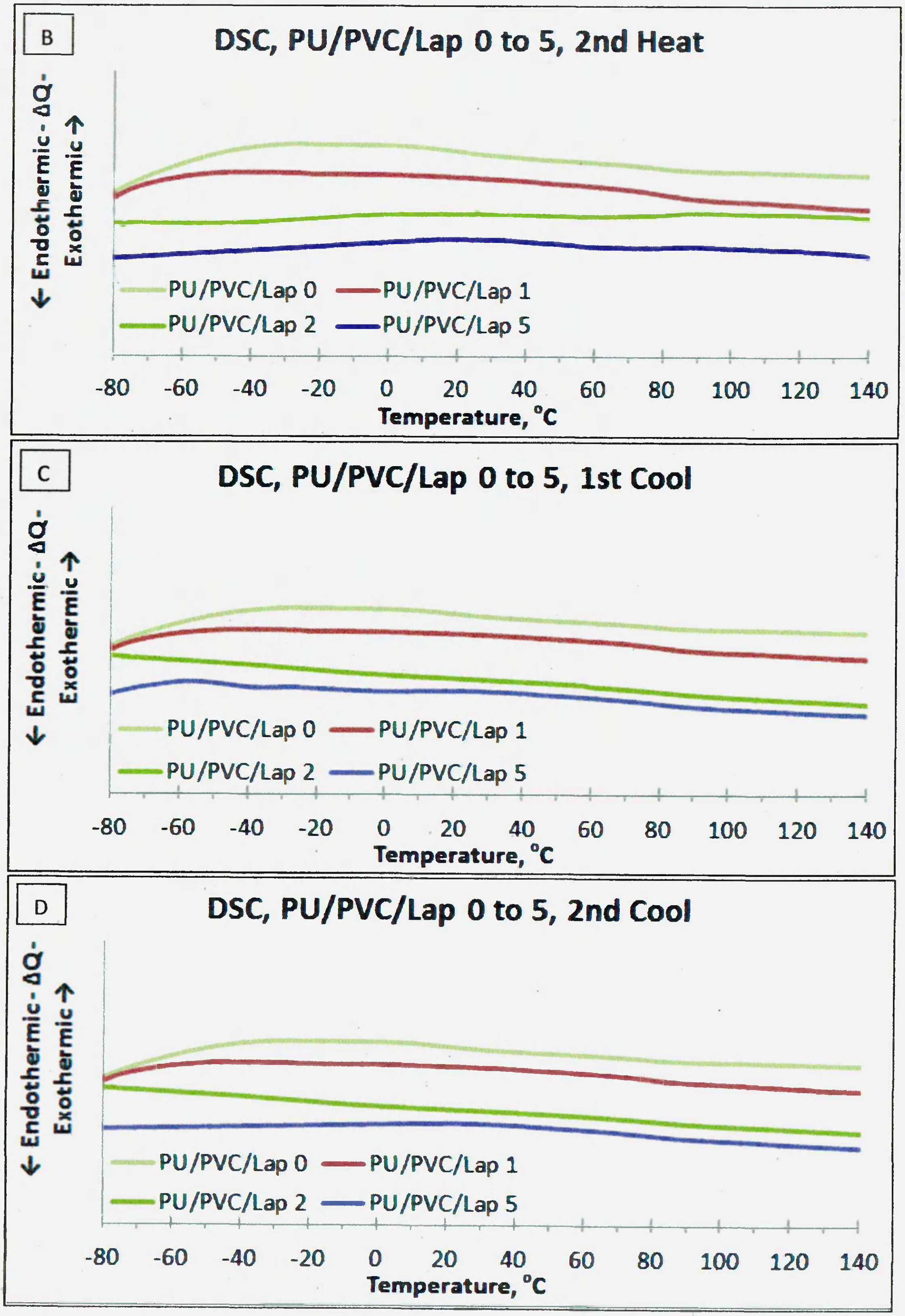

Figure 6.13: DSC thermograms of the PU/PVC/Lap 0 to 5 composites obtained on heating and subsequent cooling, -80 to 140 °C, A) 1st Heating, B) 2nd Heating, C) 1st Cooling and D) 2nd Cooling.

During the 1st heating stage, -80 to 140 °C, the PU/PVC/Lap 0 composite displayed a very broad exothermic $T_{g,SS}$ of the Elasthane phase at -8 °C while another exothermic peak, representing the T_g of the PVC phase was observed at 65 °C. The onset of the Elasthane SS T_M, $T_{M,SS}$, at ca. 126 °C was also observed.

The PU/PVC/Lap 1 to 5 composites during the 1st heating stage displayed similar thermal transitions as the PU/PVC/Lap 0 composite. As Laponite content increased the endothermic peak of the $T_{g,SS}$ decreases in intensity almost becoming unobservable at 5 wt% and is shifted to lower temperatures, -17, -24 and -26 °C, respectively. The endothermic peak of the PVC phase observed at 65 °C, does not appear to alter in intensity or position as the Laponite content increases. The $T_{M,SS}$, at ca. 126 °C was observed to shift to lower temperatures, ca. 121 and 95 °C, respectively, as the Laponite increases from 0 to 2 wt%, and becomes unobservable at 5 wt% Laponite. During the 1st cooling stage, 140 to -80 °C, the PU/PVC/Lap 0 to 5 composites display no peaks.

Sample Description	$T_{g,SS}$, °C (1st, 2nd)	T_g, °C (1st, 2nd)	$T_{M,SS}$, °C (1st, 2nd)
PU/PVC/Lap 0	-8, -14	65 , ---	126 ,---
PU/PVC/Lap 1	-17, ---	65 ,---	111 ,---
PU/PVC/Lap 2	-24, ---	65 ,---	95 , ---
PU/PVC/Lap 5	-26, ---	65 ,---	---, ---

Table 6.8: DSC, -80 to 140 °C, thermal properties of interest, T_g, $T_{g,SS}$, $T_{g,HS}$ and $T_{M,SS}$ for the PU/PVC/Lap 0 to 5 composites.

During the 2nd heating stage, -80 to 140 °C, the PU/PVC/Lap 0 composite displayed a very non-distinct, very broad $T_{g,SS}$ of the Elasthane phase, ca. -14 °C, but no peaks were observed for the PVC phase T_g or Elasthane phase $T_{M,SS}$. As Laponite increases, 0 to 1 wt%, the Elasthane phase $T_{g,SS}$ reduces in intensity and cannot be observed. No other peaks were observed for any of the PU/PVC/Lap 1 to 5 composites. The 2nd cooling phase revealed no observable peaks.

These results demonstrate that Laponite has a significant effect in the PU60/PVC40 composite, most significantly altering the $T_{g,SS}$, as also reported by Liff et al., (2007) while appearing not to affect the PVC T_g, which corresponds to Awad et al., (2009) who previously reported that hectorite does not alter the PVC T_g significantly. These results suggest that the Laponite has incorporated into the Elasthane HS and SS phases and has also potentially entered the PVC phase as well. However unlike in the Elasthane homopolymer where the Laponite, up to 5 wt%, only appeared to affect the HS, the Laponite at any wt% appears to affect both the SS and HS significantly. These results indicated that the PU and PVC may be merging with increasing Laponite content, as the individual PU $T_{g,SS}$, $T_{m,SS}$ and PVC T_g appear to shift towards each other while the peaks become broader and less distinct. These results correlate well with the previous ATR-FTIR and TGA data.

6.4.3. Mechanical Properties

6.4.3.1. Dynamic Mechanical Analysis

To further view the thermomechanical properties of the PU/PVC/Lap 0 to 5 composites, DMA was used to obtain the storage modulus, loss modulus and tan δ, figure 6.14. The peak maximum of the tan δ was used to determine the T_g, this is the general literature standard for determining T_g of a material when using DMA (Liu et al., 2002). DMA results of interest are summarised in table 6.9.

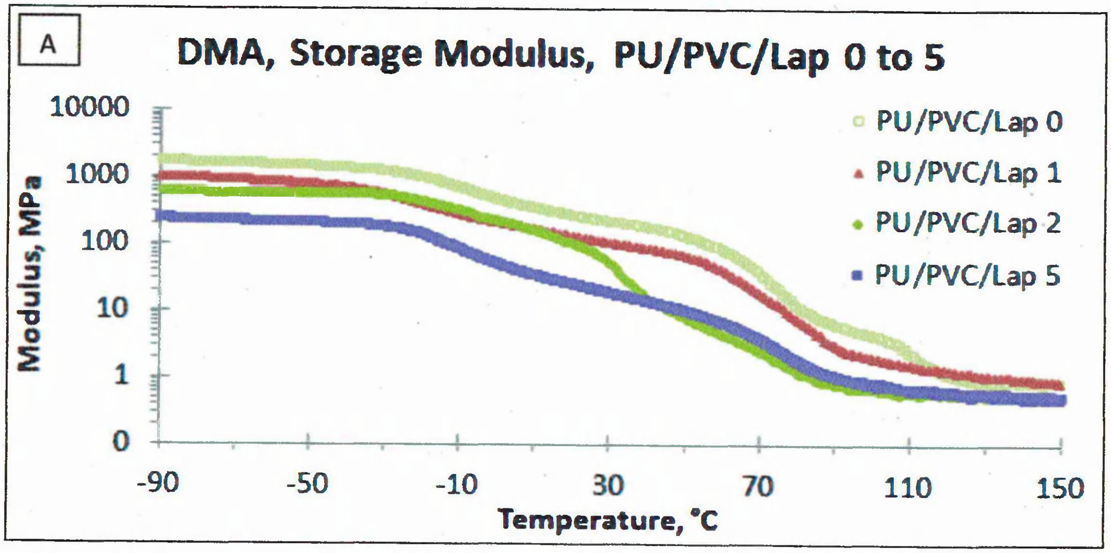

Figure 6.14: DMA traces of the PU/PVC/Lap 0 to 5 composites A) storage modulus, B) loss modulus and C) tan δ, plotted as a function of temperature, -90 to 150 °C.

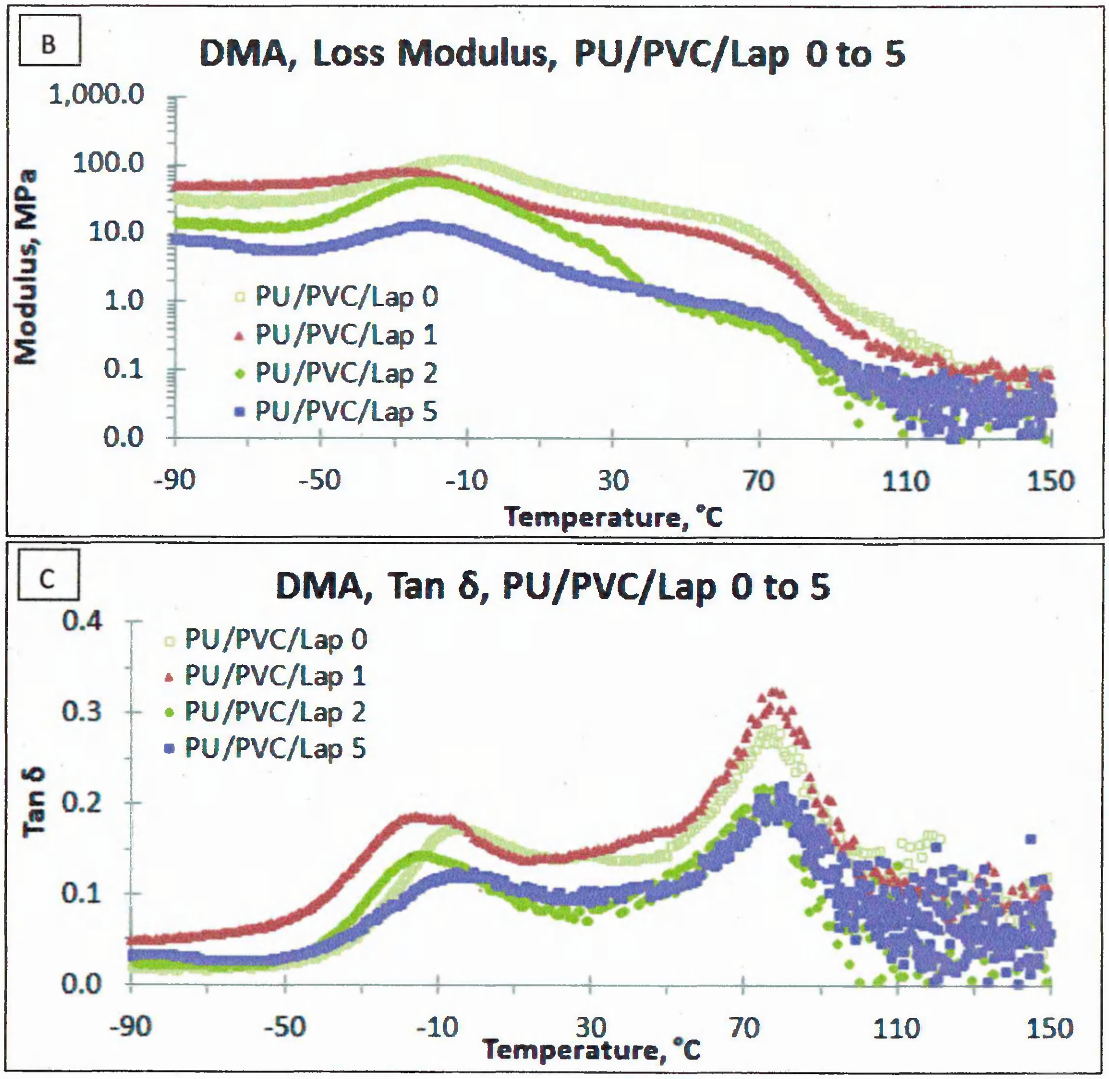

Figure 6.14: DMA traces of the PU/PVC/Lap 0 to 5 composites A) storage modulus, B) loss modulus and C) tan δ, plotted as a function of temperature, -90 to 150 °C.

The PU/PVC/lap 0 composite displays an initial storage modulus, figure 6.14 A, of 1720 MPa, as temperature increases, from -90 to -50 °C, the storage modulus drops gradually to 1479 MPa, from -50 to -10 a $T_{g\alpha(1)}$ transition from a glassy solid to a rubber occurred, where the modulus steeply falls to 697 MPa. This demonstrates a half order of magnitude drop in storage modulus. It has been suggested by Tsai et al., (2007) that a sharp, at least one order of magnitude drop in storage modulus is necessary to indicate that a polymer system will demonstrate SME (Du and Zhang, 2010). After the $T_{g\alpha(1)}$ transition, from -10 to 30 °C a quasi-rubbery plateau is reached, the storage modulus during this period gradually drops to 215 MPa. After the plateau the $T_{g\alpha(2)}$ transition occurs at 77 °C, where there is another marked loss of storage modulus dropping to ca. 17 MPa. The $T_{g\alpha(2)}$ transition demonstrates a greater than two order of magnitude drop in storage modulus, therefore indicating that the PU/PVC/lap 0 composite will have SME ability. From 77 to 150 °C the modulus continues to fall and is reduced to almost nothing, 0.9 MPa. The tan $\delta_{max(1)}$ was recorded at -6 °C and the intensity was 0.17 tan δ, this was attributed to the PU $T_{g,SS}$. The tan $\delta_{max(2)}$ was recorded at 77 °C and the intensity was 0.28 tan δ, this was attributed to the PVC T_g. No other tan δ peaks were observed.

Sample Description	Storage Modulus, MPa							$T_{g\alpha(1)}$	Tan $\delta_{max(1)}$	$T_{g\alpha(2)}$	Tan $\delta_{max(2)}$
	-90,°C	-50,°C	-10,°C	30,°C	70,°C	110,°C	150,°C				
PU/PVC/Lap 0	1720	1479	697	215	33	2	0.9	-6	0.17	77	0.28
PU/PVC/Lap 1	1021	801	278	106	19	2	0.8	-13	0.19	77	0.32
PU/PVC/Lap 2	603	572	321	49	3	0.6	0.5	-15	0.14	77	0.22
PU/PVC/Lap 5	241	210	85	19	4	0.7	0.5	-7	0.12	77	0.22

Table 6.9: DMA thermal properties of interest for the PU/PVC/Lap 0 to 5 composites.

The PU/PVC/lap 1 to 5 composites displayed initial storage moduli, figure 6.14 A, of 1021, 603 and 241 MPa, respectively. As temperature increased from -90 to -50 °C the storage moduli dropped gradually to ca. 801, 572 and 210 MPa, respectively. From -50 to ca. -10 °C the storage moduli continued to drop until the $T_{g\alpha(1)}$ transition occurred at -13, -15 and -7 °C, respectively. All the composites demonstrate a greater drop in storage modulus than the PU/PVC/Lap 0 composite, ca. 1 order of magnitude indicating that each Laponite loaded composite will demonstrate SME (Tsai et al,. 2007, Du and Zhang, 2010). After the $T_{g\alpha(1)}$ transition, from -10 to 30 °C, a quasi-rubbery plateau state is reached, the storage modulus during this interval gradually drops to 106, 49 and 19 MPa, respectively. From 30 to 70 °C the storage moduli continue to drop until the $T_{g\alpha(2)}$ transition occurred at 77 °C, where there is another marked loss of storage modulus, with each composite dropping to ca. 18, 2 and 3 MPa, respectively. The $T_{g\alpha(2)}$ transition demonstrates a greater than one order of magnitude drop in storage modulus for each composite, therefore indicating SME ability (Du and Zhang, 2010). From 77 to 150 °C the modulus continues to fall and is reduced to almost nothing, 0.8, 0.5 and 0.5 MPa, respectively. The PU/PVC/lap 1 to 5 composites tan $\delta_{max(1)}$ was recorded at -13, -15 and -7 °C and the intensity was 0.19, 0.14 and 0.12 tan δ, respectively, this was caused by the PU $T_{g,SS}$, while the tan $\delta_{max(2)}$ was recorded at

77, 77 and 77 °C and the intensity was 0.32, 0.22 and 0.22 tan δ, respectively, this was caused by the PVC T_g. No other tan δ peaks were observed.

The DMA results demonstrate that addition of any Laponite content causes a reduction of PU/PVC/Lap 0 initial storage and loss modulus in the glassy and rubbery phases. This indicates PU/PVC/Lap 1 to 5 nanocomposites cannot store as much initial energy as the PU/PVC/Lap 0 composite however as each displayed ca. a 3 order drop in magnitude of storage modulus all composites are predicted to display SME (Tsai et al., 2007, Du and Zhang, 2010). The tan δ results show that both the tan δ peaks associated with PU $T_{g,SS}$ and PVC T_g, reduce in intensity as the Laponite content increases with the exception of PU/PVC/Lap 1 which demonstrated a higher intensity peak, suggesting it has a greater shape memory recovery ability than the PU/PVC/Lap 0 composite (Chun et al., 2002, Tsai et al., 2008). The tan δ results also indicate that Laponite is not acting as a compatibilizer between PU and PVC as no significant shift of the tan δ peaks towards each other was observed as seen with partially miscible blends of PU/PVC in the literature (Xiao et al., 1987, 1998 and 1991, Parnell and Min, 2005). These results correspond to some of the literature trends observed for the individual PU or PVC nanocomposites, but not all, as there are many contradictions within the literature. Awad et al., (2009) reports that addition of a hectorite clay to PVC causes an increase in storage modulus below and above the T_g while not significantly altering the T_g position. Rhoney et al., (2003) observed that addition of C30B and Cloisite 6A into a polyether PU caused an increase of storage modulus in both the glassy and rubbery phase while not affecting the $T_{g,SS}$. However Essawy et al., (2008) and Yalcin and Cakmak (2004) found that smectite clays cause the PVC T_g to shift to lower temperatures potentially due to the clay disturbing the continuity of the PVC network structure. Korley et al., (2006) and Liff et al., (2007) found that Laponite content in a polyether PU although causing increased toughness and initial modulus also caused a shift of the $T_{g,SS}$ to lower temperatures. Overall our results do not fit exactly with the results reported for the homopolymer nanocomposites as there was no increase, but a loss of storage modulus in both the glassy and rubbery phases. The PU/PVC/Lap 1 composite appears to have a beneficial gain on shape memory properties as demonstrated by tan δ peaks of greater intensity when compared to the PU/PVC/Lap 0 composite. As there was no apparent trend to the position of the $T_{g,SS}$ of PU and the PVC T_g remained constant, our results correlate to those of Awad et al., (2009), partially agree with Korley et al., (2006) and Liff et al., (2007) but do not agree with Yalcin and Cakmak (2004), Rhoney et al., (2003) or Essawy et al., (2008).

6.4.4. Shape Memory Effect Testing

6.4.4.1. Unconstrained Shape Memory Effect Evaluation

SME was carried out in order to assess whether Laponite content enhances or reduces the SME of the PU60/PVC40 blend, figure 6.15. As previously carried out in section 5.2.4, having a T_{low} at 0 to 5 °C and a T_{high} at 90 °C will provide an adequate SME range for all the PU/PVC/Lap 0 to 5 composites. In order to view only the Laponite effect on shape memory ability each composite, PU/PVC/Lap 0 to 5, was annealed at 150 °C for 15 minutes prior to being evaluated. The PU/PVC/Lap 0 to 5 composites were deformed and their recovery determined as described in section 2.1.6, figure 2.15. The unconstrained SME evaluation results, θ_{Max} %, θ_{Fixed} %, $\theta_{1/2Final}$ %, θ_{Final} % and $\theta_{1/2Final}$ % and θ_{Final} % recovery times are summarised in table 6.10.

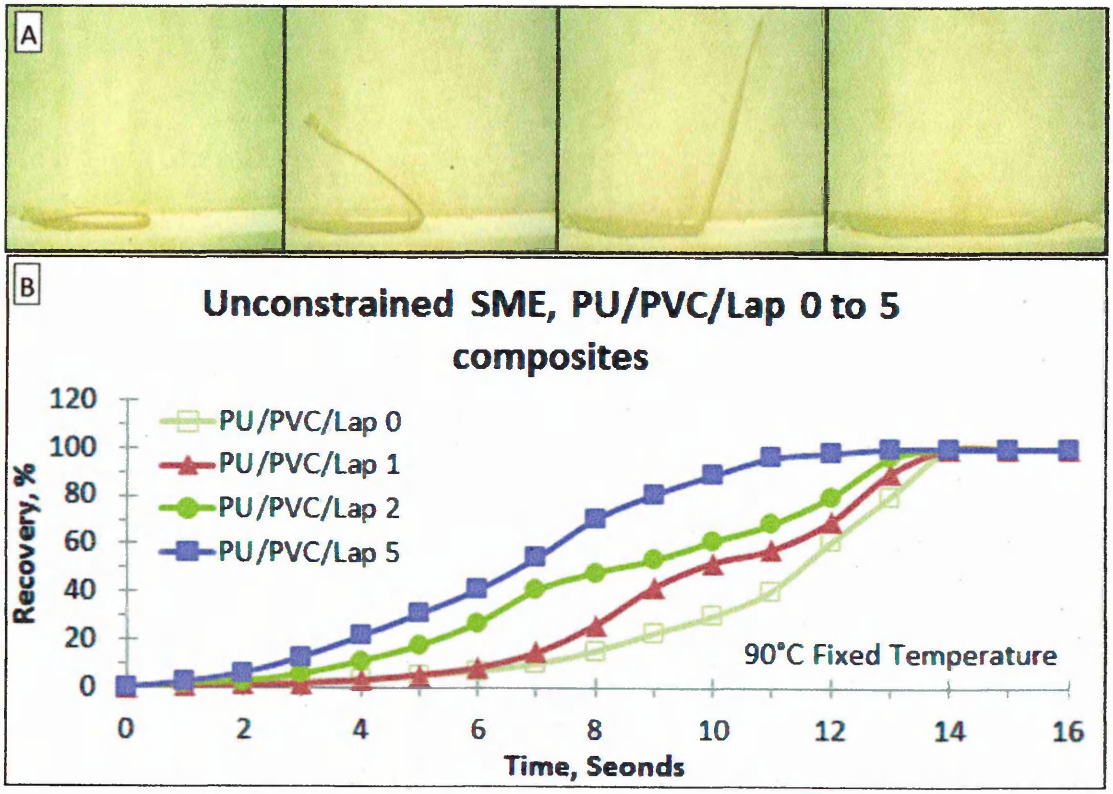

Figure 6.15: Unconstrained SME testing of PU/PVC/Lap 0 to 5 composites, from temporary to permanent shape, A) still images of a PU/PVC/Lap composite SMP at sequential intervals, B) plotted against time at a fixed temperature, 90 °C.

The PU/PVC/Lap 0 composite exhibited a θ_{Max} of 100 %, demonstrating that it is elastic enough to accommodate a high level of deformation stress. After the deformation constraint was removed, the composite was left at room temperature ca. 22 °C, a negligible amount of recovery strain occurred, leading to a θ_{Fixed} of 99 %. This demonstrates that the PU/PVC/Lap 0 composite is able to maintain almost the full load of stored stress at room temperature. Shape memory recovery was carried out at 90 °C and the $\theta_i(T)$ was recorded every second until θ_{Final} was reached. The PU/PVC/Lap 0 composite demonstrated, by achieving a θ_{Final} 100 %, that it can store almost all of the deformed strain at room temperature and return to its original shape when SME is activated. In order to further assess the shape memory ability of the PU/PVC/Lap 0 composites the $\theta_{1/2\ Final}$ and θ_{Final} time of recovery, 12.5 and 15 seconds, respectively, were recorded. These results demonstrate that the PU/PVC/Lap 0 composite recovers 50 % in ca. 5/6th of the full recovery time. These results vary to prior results obtained for the PU60/PVC40 composite, section 6.2.4, which suggests that there is a degree of error occurring during repeated SME evaluations. This could be due to slightly differing sample heterogeneity which may have occurred during the drying procedure of the polymer film i.e. slightly differing sample thickness, 0.2±0.05 mm.

The PU/PVC/Lap 0 to 5 composites exhibited a θ_{Max} of ca. 100 %, demonstrating that as Laponite content increases the composites can still accommodate a high level of deformation stress. After the deformation constraint was removed, the composites were left at room temperature ca. 22 °C, where little to no recovery occurred, leading to θ_{Fixed} results of ca. 100 %. This demonstrates that the PU/PVC/Lap 1 to 5 composites are able to maintain almost all the stored stress at room temperature. Shape memory recovery was carried out at 90 °C and the $\theta_i(T)$ was recorded every second until their respective θ_{Final} results were achieved. The PU/PVC/Lap 1 to 5 composites demonstrated, by achieving a θ_{Final} 100 %, that as Laponite content increases it does not hinder the overall shape return when SME is activated. The $\theta_{1/2\ Final}$ time of recovery, 11, 10 and 8 seconds, respectively, and θ_{Final} time of recovery, 15, 15 and 14 seconds, respectively, were recorded. These results demonstrate that that SME initially recovers faster as Laponite content increases but does not significantly alter the overall shape recovery time.

Sample Description	θ_{Max}, %	θ_{Fixed}, %	$\theta_{1/2Final}$, %	θ_{Final}, %	$\theta_{1/2Final}$ Time, sec	θ_{Final} Time, sec
PU/PVC/Lap 0	100	99	50	100	12.5	15.0
PU/PVC/Lap 1	100	100	50	100	11.0	15.0
PU/PVC/Lap 2	100	100	50	100	10.0	15.0
PU/PVC/Lap 5	100	100	50	100	8.0	14.0

Table 6.10: Summary of unconstrained SME evaluation results observed from the PU/PVC/Lap 0 to 5 composites, recording the θ_{Max} %, θ_{Fixed} %, $\theta_{1/2Final}$ %, and θ_{Final} %.

The PU/PVC/Lap 0 to 5 composites all possess shape memory ability, demonstrating maximum shape deformity, practically maximum shape fixity and full shape recovery. These results correspond well to the predicted DMA results that suggested all composites will demonstrate SME and that the PU/PVC/Lap 1 composite would display a slightly increased shape memory recovery rate as shown by the increase in intensity of the tan $\delta_{max(1)}$. However the PU/PVC/Lap 2 and 5 composites also displayed a faster recovery rate. It was observed that as Laponite content increased the $\theta_{1/2Final}$ time decreased and no change occurred to the θ_{Final} time. This means the Laponite is selectively enhancing the initial recovery of the SMP, possibly by storing additional internal elastic strain during the deformation process that is released during shape memory recovery, providing a faster initial recovery (Gall et al., 2002). Another potential explanation is the Laponite fraction present in the PVC increases the continuity of the crystallite physical cross-link network therefore aiding in local stress transfer to the attached chains during shape fixing and recovery process, which potentially would lead to an initially faster shape memory response (Yalcin and Cakmak, 2004). This same form of increased network continuity was proposed by Meng and Hu (2009), for PUs where Na-MMT was incorporated, adding more constraints to chain motion within the PU and increasing the shape memory. However it has been commented within the literature that excess clay will lead to adverse effects on the SME properties in PVC and PU (Yalcin and Cakmak, 2004, Jang et al., 2008), but there appear to be no adverse effects on the shape memory ability of PU60/PVC40 with up to 5 wt% Laponite.

6.5. Conclusions

The effects of incorporating Laponite into a PU/PVC composite, was studied to assess if addition of Laponite would improve or reduce the shape memory properties of PU60/PVC40, in order to fulfil the aim of creating a mechanically and thermally stable SMP packaging solution. The resulting PU/PVC nanocomposites were characterised for homogeneity, thermal and mechanical properties including shape memory ability. Overall the addition of Laponite to PU60/PVC40 was found to be beneficial as it appears to create a more thermally stable polymer system that shows good shape memory ability that can be partially tailored with the incorporation of low level amounts of exfoliated Laponite platelets. However the PU/PVC/Lap composite methodology i.e. solvent blending and casting, although suitable for a laboratory has many potential problems when being considered for a commercial production line. The main concern of up-scaling this type of production method is the long dissolving time, dispersion issues, solvent quantity and drying times involved, as they are not commercially viable. Although this polymer system appears to be a good SMP that can be further tailored, with Laponite, it is doubtful that it will be made commercially and therefore a different SMP system will be required to fulfil the aim of creating a mechanically and thermally stabile SMP packaging solution. Candidates that may be suitable are thermally curable acrylate SMP, styrene based thermoset SMP resin systems, biodegradable SMP such as PLA, or polymer systems formed from renewable sources such as corn oils and fish oils.

6.6. References

AWAD, W.H., et al. (2009). Material properties of nanoclay PVC composites. Polymer, **50** (8), 1857-1867.

CHUN, B.C., et al. (2002). Enhanced dynamic mechanical and shape-memory properties of a poly(ethylene terephthalate)-poly(ethylene glycol) copolymer crosslinked by maleic anhydride. Journal of Applied Polymer Science, **83** (1), 27-37.

COLEMAN M.M., et al. (1988). Amorphous polyurethane polyether blends. Polymer, **29** (9), 1659-1663.

DU, H.Y., and ZHANG, J.H,. (2010). Shape memory polymer based on chemically cross-linked poly(vinyl alcohol) containing a small number of water molecules. Colloid and Polymer Science, **288** (1), 15-24.

ESSAWY, H.A., EL-WAHAB, N.A., and EL-GHAFFAR, M.A., (2008). PVC-laponite nanocomposites: Enhanced resistance to UV radiation. Polymer Degradation and Stability, **93** (8), 1472-1478.

FENG Y., et al. (2009). Synthesis and characterization of poly(carbonate urethane) networks with shape-memory properties. Journal of Applied Polymer Science, **112** (1), 473-478.

FERGUSON, J., and PETROVIC, Z., (1976). Thermal stability of segmented polyurethanes. European Polymer Journal, **12** (3), 177-181.

FISCH, M.H:, and BACALOGLU, R., (1995). Kinetics and mechanism of the thermal degradation of poly(vinyl chloride). Journal of Vinyl & Additive Technology, **1** (4), 233-240.

GALL, K., et al. (2002). Shape memory polymer nanocomposites. Acta Materialia, **50** (20), 5115-5126.

HA, C.S. et al. (1998). Fracture toughness and properties of plasticized PVC and thermoplastic polyurethane blends. Polymer, **39** (20), 4765-4772.

HAN, J., and HUANG, H., (2011). Preparation and characterization of biodegradable Polylactide/Thermoplastic polyurethane elastomer blends. Journal of Applied Polymer Science, **120** (6), 3217-3223.

HU J.L., (2007). Shape memory polymers and textiles. Cambridge: Woodhead publishing limited

IJDO, W.L., KEMNETZ, S., and BENDERLY, D., (2006). An infrared method to assess organoclay delamnination and orientation in organoclay polymer nanocomposites. Polymer Engineering and Science, **46** (8), 1031-1039.

JANG, M.K., HARTWIG, A., and KIM, B.K., (2009). Shape memory polyurethanes cross-linked by surface modified silica particles. Journal of Materials Chemistry, **19** (8), 1166-1172.

JEONG, H.M., AHN, B.K., and KIM, B.K., (2001). Miscibility and shape memory effect of thermoplastic polyurethane blends with phenoxy resin. European Polymer Journal, **37** (11), 2245-2252.

JEONG, H.M., et al. (2001). Miscibility and shape memory property of poly(vinyl chloride)/thermoplastic polyurethane blends. Journal of Materials Science, **36** (22), 5457-5463.

KIM, B.K., LEE, S.Y., and XU, M., (1996). Polyurethanes having shape memory effects. Polymer, **37** (26), 5781-5793.

KIM, B.K., LEE, S.Y., and XU, M., (1996). Polyurethanes having shape memory effects. Polymer, **37** (26), 5781-5793.

KORLEY, L.T.J., et al. (2006). Preferential association of segment blocks in polyurethane nanocomposites. Macromolecules, **39** (20), 7030-7036.

LENDLEIN, A., and KELCH, S., (2005). Shape-memory polymers as stimuli-sensitive implant materials. Clinical Hemorheology and Microcirculation, **32** (2), 105-116.

LIFF, S.M., KUMAR, N., and MCKINLEY, G.H., (2007). High-performance elastomeric nanocomposites via solvent-exchange processing. Nature Materials, **6** (1), 76-83.

LIN, J. R., and CHEN, L. W., (1998). Study on shape-memory behavior of polyether-based polyurethanes. I. influence of the hard-segment content. Journal of Applied Polymer Science, **69** (8), 1563-1574.

LIN, J.R., and CHEN, L.W., (1998). Study on shape-memory behavior of polyether-based polyurethanes. II. influence of soft-segment molecular weight. Journal of Applied Polymer Science, **69** (8), 1575-1586.

LIU, C.D., et al. (2002). Chemically cross-linked polycyclooctene: Synthesis, characterization, and shape memory behavior. Macromolecules, **35** (27), 9868-9874.

MATWEB, (2011). DSM-PTG Elasthane™ 80A Thermoplastic Polyether Urethane. [online]. Last accessed 10 August 2011 at: http://www.matweb.com/search/DataSheet.aspx?MatGUID=61a633b7094b4983a20d5fa2c450e68d&ckck=1

MENG, Q.H., and HU, J.L., (2009). A review of shape memory polymer composites and blends. Composites Part A-Applied Science and Manufacturing, **40** (11), 1661-1672.

MISHRA, A.K., NANDO, G.B., and CHATTOPADHYAY, S., (2008). Exploring preferential association of laponite and cloisite with soft and hard segments in TPU-clay nanocomposite prepared by solution mixing technique. Journal of Polymer Science Part B-Polymer Physics, **46** (21), 2341-2354.

PARNELL, S., and MIN, K., (2005). Reactive blending of thermoplastic polyurethane in situ with polv(vinvl chloride). Polymer Engineering and Science, **45** (6), 876-887.

PIELICHOWSKI, K., and HAMERTON, I., (2000). Compatible poly(vinyl chloride)/chlorinated polyurethane blends: Thermal characteristics. European Polymer Journal, **36** (1), 171-181.

RATNA, D., and KARGER-KOCSIS, J., (2011). Shape memory polymer system of semi-interpenetrating network structure composed of crosslinked poly (methyl methacrylate) and poly (ethylene oxide). Polymer, **52** (4), 1063-1070.

RHONEY, I. et al., (2004). Influence of processing method on the exfoliation process for organically modified clay systems. I. polyurethanes. Journal of Applied Polymer Science, **91** (2), 1335-1343.

ROCKWOOD SPECIALTIES INC., (2009). Laponite. [Leaflet] Cheshire: Rockwood Additives Limited.

ROUSSEAU I.A., (2008). Challenges of shape memory polymers: A review of the progress toward overcoming SMP's limitations. Polymer Engineering and Science, **48** (11), 2075-2089.

SHIEH, Y.T., et al. (1999). Thermal degradation of MDI-based segmented polyurethanes. Journal of Polymer Science Part A-Polymer Chemistry, **37** (22), 4126-4134.

TAKAHIKO, KATSUHISA, HIDEKI and TAKAKI, (1982). Japan Patent; 57-450027

TSAI, Y., et al. (2008). Shape memory effects of poly(ethylene terephthalate-co-ethylene succinate) random copolymers. European Polymer Journal, **44** (2), 550-554.

VICENTE, I., (2010). Hectorite in Polyurethane Composites. PhD, Universitat Rovira I Virgili.

WILKES C.E., SUMMERS J.W., and DANIELS C.A., (2005). PVC Handbook. Müchen Germany: Carl Hanser Verlag.

XIAO F., SHEN D., ZHANG X., HU S., and XU M., (1987). Studies on the morphology of blends of poly(vinyl chloride) and segmented polyurethanes. Polymer (guilford), **28**, 2335-234.

XIAO F., SHI L., XU M., (1991). Modulus composition dependence for blends of PVC with segmented polyurethanes of different soft segments. Chinese Journal of Polymer Science, **9** (1), 55-64.

XIAO F., ZHANG X., HU S., MA D., LUO X., and XU M., (1988). Compatibility of PVC with polyurethanes of different soft segments. Chinese Journal of Polymer Science, **6** (1).

YANG, D.Y., et al. (2006). Structure and thermal properties of exfoliated PVC/layered silicate nanocomposites via in situ polymerization. Journal of Thermal Analysis and Calorimetry, **84** (2), 355-359.

Chapter 7: Conclusions and Future Work

7. Conclusions

This project aimed to investigate shape memory polymers and explore the feasibility of producing a SMP packaging solution for the pharmaceutical and general consumer market.

Investigations into SMP overall showed that a simple technique, DMA, could be used to predict whether polymers would demonstrate useful shape memory ability. It was found that a polymer would likely demonstrate a useful shape memory effect when there was a drop in storage modulus of at least 1 decade, with the speed of the transition depending on the shapeness of the tan δ peak, the sharper the peak the faster the transition. Other factors influencing the shape memory ability included the structure of the polymer network and the amount of netpoints or cross-links. Another observation was that less substituted linear chain networks demonstrated a faster shape recovery with less cross-links compared to branched chain networks which demonstrated a faster recovery with increased cross-links. It was also found that the quantity of netpoints or cross-links in any given system altered the shape memory recovery i.e. introducing clay, hence increasing the quantity of netpoints, increased shape memory recovery. However introducing too many netpoints did not appear to improve the shape memory ability. This effect was however more prominent in class IV SMP than class I SMP.

The initial SMP packaging study was started by examining the combination of tBA cross-linked with PEGDMA, with the objective to establish the most suitable composition ratio of tBA to PEGDMA in order to produce a thermally stable SMP packaging solution.

The tBA-co-PEGDMA networks proved to be fully polymerised, thermally stable, offered good mechanical properties and most provided a shape memory response.

The t90/P10 network was found to be most suitable for the proposed application, but maintained some of the classic shortcomings of SMP, especially when compared to SMAs i.e. low mechanical strength.

Clay was incorporated into the tBA-co-PEGDMA networks and was found to retain the polymers' good shape memory properties and did not increase brittleness or fracturing during large deformations. The most ideal loading of clay was found to be 1 wt%. This formulation was coated onto packaging substrates and studied further. A significant difference in shape memory abilitiy was observed between different substrates, PET and Sulpak paper, with notable differences between the recovery rate and θ_{Final} recovery. Overall the coated PET film provided a faster and greater recovery of the permanent shape compared to the coated Sulpak paper.

Both samples were sent to Chesapeake for further cure testing but due to the tBA's low flash point, 18 °C, the polymer was not suitable for large scale production.

A series of acrylate monomers were studied to find a suitable replacement for the tBA monomer. The acrylates IBoA, IBoMA and tBMA were found to be the most suitable. Each acrylate was cross-linked with PEGDMA in differing ratios and characterised with emphasis on mechanical properties and shape memory abilities.

The results indicated that IBoA was the most likely substitute for tBA and was sent to Chesapeake for evaluation on their UV curing system.

Two acrylate networks, I90/P10 and I80/P20, were coated, 76 µm thick, onto PET and Sulpak substrates and cured. However each required seven passes through the UV curing machine conveyer, UV dose of ca. 150 mJ/cm^2 per pass. For a commercially viable coating process a standard cure in two passes was the maximum.

A series of experiments was carried out where additional photoinitiators and oxygen inhibitors were introduced to form a photoinitiator 'cocktail' with the aim to produce a full cure in two passes on the UV cure instrument.

It was discovered that the main cause of a slow cure was due to oxygen inhibition which had previously not occurred because all the samples had either been prepared in a closed mould system or in a nitrogen atmosphere.

To prevent significant oxygen inhibition from occurring during curing a chemical method of prevention would be most suitable. Therefore TPO-L, ITX, EHA, DEA and TEA were investigated as additions and replacements to the photoinitiator cocktail for curing the IBoA-co-PEGDMA network.

A photoinitiator formulation, C09, allowed the IBoA-co-PEGDMA network to be cured in air in 2 passes on the industrial UV curing machine. However the C09 cocktail caused unwanted effects on the mechanical and shape memory properties of the produced network. The C09 combination of TPO-L, ITX, EHA and TEA caused a general reduction in storage modulus, an earlier onset of shape memory recovery and a possible loss of recovery force associated with a reduction of the tan δ_{max} peak intensity.

Therefore a new formulation, D07, was created with an altered combination of TPO-L, ITX, EHA and TEA which minimalized the unwanted effects on mechanical and shape memory abilities. It was found that it contained similar mechanical properties as the original C00 IBoA-co-PEGDMA network but with a reduced shape memory onset temperature causing it to be outside the working onset temperature range, ca. 18 to 22 °C, for a SMP packaging solution and in order to overcome this obstacle a different SMP monomer with a higher T_g was required, IBoMA was identified.

Previously the IM80/P20 and IM70/P30 networks were found to have good storage modulus, T_g, and SME abilities, therefore using the D07 photoinitiator formulation polymer films were created and investigated for mechanical and shape memory abilities.

It was established that the D07 IM80/P20 and IM70/P30 networks had adequate storage modulus, T_g temperatures and SME abilities for shape memory packaging solutions, thus they were coated onto PET and Sulpak substrates and tested for curing at Chesapeake.

Both the D07 IM80/P20 and IM70/P30 networks did not fully cure when exposed to Chesapeake's UV lamp. This was potentially caused by the methacrylate double bond being less reactive than the acrylate double bond causing the networks to be more susceptible to oxygen inhibition. Therefore in order to assess the SME abilities of the D07 IM80/P20 and IM70/P30 networks they were cured in a nitrogen atmosphere.

Both networks cured completely and were found to show shape memory ability as well as demonstrate relatively good shape fixity and excellent permanent shape recovery. From these results it was concluded that if the oxygen inhibition effect could be overcome, the D07 IM80/P20 and IM70/P30 networks would be very suitable as SMP packaging solutions.

In order to further evaluate SMP for potential packaging applications the other limit of the SMP classes was utilised, class IV. This investigation was carried out in order to assess whether a class IV SMP, Elasthane, and its (nano)composites could contribute information towards the target of creating a SMP packaging solution.

It was found that Elasthane had reasonable mechanical, thermal and shape memory properties, which could also be tailored with the incorporation of exfoliated/intercalated Laponite platelets, more so than the class I SMP i.e. tBA, IBoA, tBMA and IBoMA –co-PEGDMA.

This was a significant result as various shape memory recovery speeds could be implemented using different Laponite loadings, inferring allowing specific recovery speeds to SMP packaging. However it was observed that at higher Laponite loadings some unwanted properties developed including a reduced thermal stability at lower temperatures. It was also found that the shape memory onset temperature of Elasthane was too high for standard packaging solutions and would probably be more suitable for a specific, higher temperature, type of packaging.

To further investigate and potentially improve the abilities of the class IV, PU, SMP, it was physically blended with PVC, a quasi-SMP. Blending two or more existing polymers is a well-established method used in polymer technology to obtain enhanced or new properties from materials.

The effects of blending PU with PVC were studied to assess if addition of PVC would improve or reduce the shape memory properties of PU.

The PU/PVC blends were generally found to be more thermally stable, demonstrated good shape memory ability and exhibited greater overall storage modulus compared to the original homopolymers. The most enhanced blend was PU60/40PVC. However the classic shortcomings of SMP were still apparent i.e. low mechanical strength.

Therefore Laponite was incorporated into the PU60/40PVC blend. Previously incorporation of clay had demonstrated the ability to tailor the thermal and mechanical properties of SMP PU.

The resulting PU60/PVC40 blend (nano)composites were found to be more thermally stable, show good mechanical and shape memory ability that could be tailored by altering the amounts of exfoliated Laponite platelets.

However the shape memory onset temperature was too high for standard packaging solutions, as observed for the PU SMP, and would probably be more suitable for higher temperature packaging.

The aim of producing a SMP packaging solution for the pharmaceutical and general consumer market was explored by assessing both extremes of the four classes of SMP, class I and IV. It could be argued that for standard packaging solutions e.g. food and general household products packaging, the class I SMP would be most suitable. Unlike the class IV SMP the formulations are easily made and can be applied relatively easily onto substrates as well as the opportunity to tailor the transition temperature over a wide range by simple composition variations. Class I SMP also provide good mechanical and shape memory abilities. Class IV SMP which are more difficult to prepare and are hard to apply directly to substrates, would probably be more suitable for low quantity, specialised packaging solutions e.g. aerospace and heavy industry applications. In these areas higher temperatures and more uncommon environments are more likely to be encountered. From both SMP classes explored and assessed a range of potential packaging solutions could be developed however further work is still required within some areas. In regards to the acrylate based SMP further investigation into overcoming oxygen inhibition during curing is required. While for the PU based SMP greater improvements into the casting process should be considered before they can become commercially viable.

7.1. Future Work

The project did not fully achieve its aim of creating a SMP packaging solution. Due to time constraints it was not possible to fully explore the production of an ideal SMP packaging solution. The results gained from the project however are very promising especially with regards to the IBoA and IBoMA – co-PEGDMA formulations.

If more time was allocated to this research, carrying out experiments into forming a blend of IBoA and IBoMA cross-linked with PEGDMA would be very beneficial. Using the latest photoinitiator cocktail, D07, and ca. 60 wt% IBoA, 20 wt% IBoMA and 20 wt% PEGDMA, a fast curing, mechanically strong polymer network with very useful shape memory abilities could potentially be produced. This would be possible because the majority of the network would be fast curing acrylate monomer which would cure with little difficulty in air, as IBoA demonstrated in section 4.9, while the minor methacrylate monomer would provide beneficial mechanical and thermal properties. Previously when IBoA was cured with D07 the T_g onset temperature was ca. 5 °C, by blending ca. 20 wt% IBoMA the T_g of the blend will increase by ca. 15 to 20 °C. Therefore using the D07 photoinitiator cocktail with the blend of IBoA and IBoMA would suggest that the overall network will have a T_g onset temperature in the range of 20 to 25 °C. This would be a suitable onset/working temperature for a packaging application. The network would probably also contain good mechanical properties as the IBoMA will contribute a higher rubbery modulus value to the IBoA network, this would potentially increase the amount of recovery force that would be generated during shape memory recovery.

Further exploration into the current SMP materials should be also undertaken if more time was available. Aspects that should be given priority would be research into the reaction kinetics of the acrylate networks and into shape memory evaluation testing, possibly with access to more sophisticated instrumentation.

Learning more about the reaction kinetics of the acrylate networks would potentially allow a more refined photoinitiator cocktail to be developed as well as provide valuable information on specific times required for a full cure to be achieved.

Further work into the exploration of the acrylate reaction kinetics may also aid with overcoming oxygen inhibition issues that arise during curing. It was found previously that oxygen inhibition was the primary cause for slowness/incompleteness of curing and further research into preventing this would be of considerable benefit.

With new equipment e.g. an Instron tensile tester equipped with a thermo-chamber, a procedure could be developed, similar to section 1.4.1, where more reproducible and reliable SME evaluations could be produced. This again would provide further insight into SMP e.g. how an SMP network will react when exposed to much more rigorous conditions than a simple bending test could provide.

With more time, specific SMP packaging solutions could be considered and researched appropriately e.g. SMP milk bags. There would be several new facets of the material to consider if used for this application, including the effects of possible long term storage, effects of prolonged moisture exposure and possible chemical leaching. In order to evaluate these possibilities a range of new analytical techniques would need to be employed, although DMA could possibly be used to evaluate both long term storage and effects of moisture.

Another growing issue that should be addressed is the present concern of biodegradability and sustainability of packaging materials. With greater time and utilising different SMP monomer materials e.g. PLA, corn and fish oil derived polymers, investigations into sustainable and biodegradable SMP systems should be carried out. Gaining these abilities would further add to the commercialisation appeal of SMP packaging materials.

A1. Award and presentation in seminar and conferences:

1. 1st Prize Winner for "The Best Oral Presentation" at MERI Research Student Day, Sheffield Hallam University-UK, 26th May 2010.
2. Michael Barwood, Chris Breen "THE EFFECT OF (ORGANO)CLAY ADDITION ON THE PROPERTIES AND USES OF POLYVINYLCHORIDE/POLYURETHANE SHAPE MEMORY POLYMER BLENDS", Oral Presentation at EUROCLAY 2011 Conference, Antalya, Turkey, 26th June - 1st July 2011.
3. Michael Barwood, Francis Clegg, Chris Breen, Carol Hammond "THE EFFECT OF (ORGANO)CLAY ADDITION ON THE PROPERTIES AND USES OF UV POLYMERISED ACRYLATE SHAPE MEMORY POLYMERS", Poster Presentation at Trilateral Meetings on Clays, Seville, Spain, 8 - 11th June, 2010.
4. Michael Barwood, Francis Clegg, Chris Breen, Carol Hammond "THE EFFECT OF (ORGANO)CLAY ADDITION ON THE PROPERTIES AND USES OF UV POLYMERISED ACRYLATE SHAPE MEMORY POLYMERS", Poster Presentation at Macro Group Young Research Meeting 2010, Nottingham, UK, 29 - 30th April 2010.
5. Michael Barwood, Chris Breen "THE EFFECT OF (ORGANO)CLAY ADDITION ON THE PROPERTIES AND USES OF SHAPE MEMORY POLYMERS", Oral Presentation at MERI Research Student Day, Sheffield Hallam University-UK, 26th May 2010.
6. Michael Barwood, Francis Clegg, Chris Breen "THE EFFECT OF (ORGANO)CLAY ADDITION ON THE PROPERTIES AND USES OF SHAPE MEMORY POLYMERS", Poster Presentation at the XIV International Clay Conference, Italy, 14 - 20th June 2009.
7. Michael Barwood, Francis Clegg, Chris Breen "EFFECT OF ORGANOCLAYS ON THE PROPERTIES AND USES OF SHAPE MEMORY POLYMERS", Poster Presentation at MERI Research Student Day, Sheffield Hallam University-UK, 20th May 2009.

A2. Conference and seminars attended:

1. The 197th Infra Red and Raman Discussion Group Christmas Meeting, London, UK, 20th December 2011.
2. EUROCLAY 2011 Conference, Antalya, Turkey, 26th June - 1st July 2011.
3. MERI Research Student Day, Sheffield Hallam University, UK, 25th May 2011.
4. The 194th Infra Red and Raman Discussion Group Christmas Meeting, London, UK, 16th December 2010.
5. Seminar on Bio-Plastic Food Packaging, Newport Shropshire, UK, 23rd June 2010.
6. The TMC "Trilateral Meeting on Clays": General Meeting and Symposium in Seville, Spain, 8 - 11th June 2010.
7. MERI Research Student Day, Sheffield Hallam University, UK, 26th May 2010.
8. Macro Group Young Research Meeting 2010, Nottingham, UK, 29 - 30th April 2010.
9. The Futuroclays Meeting, Newcastle, UK, 14 - 16th December, 2009.
10. The XIV International Clay Conference, Italy, 14 - 20th June 2009.
11. MERI Research Student Day, Sheffield Hallam University, UK, 20th May 2009.
12. Weekly MERI and PCAS Seminars, Sheffield Hallam University, UK, October 2008 - to date.